Novel Modeling Technology For UAS-S4 and UAS-S45 Flight Dynamics

by

Maxime Alex Junior KUITCHE

MANUSCRIPT-BASED THESIS PRESENTED TO ÉCOLE DE TECHNOLOGIE SUPÉRIEURE IN PARTIAL FULFILLMENT FOR THE DEGREE OF DOCTOR OF PHILOSOPHY
PH.D.

MONTREAL, 14TH JANUARY 2020

ÉCOLE DE TECHNOLOGIE SUPÉRIEURE
UNIVERSITÉ DU QUÉBEC

BOARD OF EXAMINERS

THIS THESIS HAS BEEN EVALUATED

BY THE FOLLOWING BOARD OF EXAMINERS

Mrs. Ruxandra Mihaela Botez , Thesis Supervisor
Department of Automated Production Engineering at École de technologie supérieure

Mr. Mohammad Jahazi , President of the Board of Examiners
Department of Mechanical Engineering at École de technologie supérieure

Mr. Guy Gauthier, Member of the jury
Department of Automated Production Engineering at École de technologie supérieure

Mr. Adrian Hiliuta, External Evaluator
CMC Electronics

THIS THESIS WAS PRENSENTED AND DEFENDED

IN THE PRESENCE OF A BOARD OF EXAMINERS AND PUBLIC

THE 6TH DECEMBER 2019

AT ÉCOLE DE TECHNOLOGIE SUPÉRIEURE

ACKNOWLEDGMENT

First and Foremost, I would like to express my dearest and deepest gratitude to Professor Ruxandra Mihaela Botez. She gave me the opportunity to work on challenging projects as part of LARCASE team. Her constant guidance, support and encouragement throughout the project helped me to perform the best work I could.

Many thanks are also due to the Hydra Technologies Team in Mexico for their continuous support especially Mr. Carlos Ruiz, Mr. Eduardo Yakin and Mr. Alvaro Gutierrez.

Special thanks are due to the LARCASE team. I learned a lot from each of you mainly what it feels to be part of a research team and to have an impact in the research domain. Thank you to Georges Ghazi, Marine Segui, Manuel Flores Salinas, David Communier, Alejandro Murieta and Oscar Carranza Moyao.

A great thank you to my family in Cameroon for their incommensurable support, for helping me travel the world to follow my dreams, for always encouraging even when they did not understand and to make me feel their love even thousand kilometers away.

Last, but not least, a huge thank you to my friends. I met you throughout my journey and have become my second family. Thank you to Yvan Tondji, Ted Tchinde and Hassanatou Diakite.

Nouvelle technologie de conception de la dynamique de vol de l'UAS-S4 et de l'UAS-S45

Maxime Alex Junior KUITCHE

RÉSUMÉ

La croissance rapide des systèmes de vol autonome dans le domaine arien ainsi que l'intérêt grandissant de la préservation environnementale, poussent les constructeurs d'aéronefs à s'intéresser de plus en plus à des techniques d'amélioration de performance. Améliorer la performance consiste, dans ce cas, à réaliser un vol optimal tout en réduisant la quantité de carburant consommé. Cependant, la validation d'une technique d'amélioration de performances peut être très couteuse en termes d'argent et de temps et également, causer la destruction de l'appareil. Pour répondre à ces problèmes de réduction ressources financières et environnementales nécessaires à la validation de techniques d'amélioration de performance et à la certification des aéronefs, cette thèse propose la réalisation d'un modèle de simulation de vol de grande précision. Les principaux objectifs de ce travail sont : 1) réaliser un modèle dynamique de vol capable d'estimer de manière précise le comportement des UAS-S4 et UAS-S45 conçus par Hydra Technologies ; 2) s'assurer que le modèle de dynamique de vol permette de tester des techniques d'amélioration de performance et implémenter une nouvelle loi de contrôles.

Cette thèse se rapporte, ainsi, essentiellement à la modélisation de la dynamique de vol des aéronefs ainsi qu'à la stabilité et au contrôle des aéronefs. Elle s'articule autour de quatre contributions. La première contribution est centrée sur les méthodologies d'obtention du modèle de vol de l'UAS-S4 et l'UAS-S45. La méthode proposée consiste à diviser l'architecture global de chaque aéronef en sous-modèles. Par la suite, chacun des sous-modèles est estimé en utilisant des méthodes numériques et expérimentales. Cette contribution montre que la méthodologie proposée ne nécessite qu'un minimum de données pour les calculs.

La deuxième contribution est liée à l'utilisation de méthodes numériques pour l'estimation d'un modèle aérodynamique des UAS-S4 et UAS-S45. Malgré les diverses méthodes de calcul aérodynamiques existantes, la méthode proposée, qui est basé sur un réseau de vortex non linéaire, permet d'obtenir des résultats de haute-fidélité en un temps abordable. Pour vérifier les résultats, des analyses expérimentales ont été réalisées sur un modèle réduit de l'aile de l'UAS-S45 dans la soufflerie subsonique Price-Païdoussis.

La troisième contribution examine la précision des méthodes d'analyses de dynamique de fluide ainsi que d'une amélioration de la théorie des éléments de pales pour l'estimation des performances aérodynamiques de l'hélice de l'UAS-S4 et UAS-S45. Les deux méthodes numériques proposées ont été validé à partir d'une étude expérimentale en soufflerie ouverte.

La quatrième contribution est liée à l'étude de la stabilité et du contrôle de l'UAS-S45. Dans cette contribution une nouvelle méthode de contrôle, utilisant une approche LQR et un contrôleur PI avec une action anticipatrice, est proposée. La robustesse du système est également assurée grâce à un observateur d'état étendu. Par la suite, un réseau neuronal flou est utilisé pour le séquencement de gain.

Mots-clés : Modélisation d'UAS, dynamique de vol, modélisation aérodynamique, modélisation de la propulsion, essais en soufflerie, commandes de vol, observateur d'états étendus

Novel modeling technology for UAS-S4 and UAS-S45 flight dynamics

Maxime Alex Junior KUITCHE

ABSTRACT

The rapid development of unmanned flight systems in the aviation domain and the growing interest in environmental preservation are driving aircraft manufacturers to focus more and more on performance improvement techniques. In this case, improving the performance consists in achieving an optimal flight while reducing the amount of fuel consumed. However, the validation of a performance improvement technique can be very demanding in terms of money and time and can also lead to the destruction of the aircraft. To respond to these problems of financial and environmental resource reduction for the validation of performance improvement techniques and aircraft certification, this thesis proposes the design of a high precision flight simulation model. The main objectives are: 1) to design a dynamic flight model capable of accurately estimating the behaviour of UAS-S4 and UAS-S45 manufactured by Hydra Technologies; and 2) to ensure that the flight dynamics model allows the testing of performance improvement techniques and the implementation of a new control law.

This thesis relates essentially to the modeling of the flight dynamics of aircraft as well as to aircraft stability and control. It is articulated around four contributions. The first contribution focuses on the methodologies for obtaining the UAS-S4 and the UAS-S45 flight models. The proposed method divides the overall architecture of each aircraft into sub-models. Subsequently, each of the sub-models is estimated using numerical and experimental methods. This contribution shows that the proposed methodology requires only a minimum of data for the flight dynamics calculations.

The second contribution is related to the use of numerical methods for estimating the aerodynamic model of the UAS-S4 and the UAS-S45. In contrast to the various aerodynamic calculation methods available, the proposed method, which is based on nonlinear vortex lattices, provides high-fidelity results in an affordable time. To verify these results, experimental analyses were carried out on a model of the UAS-S45 wing in the Price-Païdoussis subsonic wind tunnel.

The third contribution examines the accuracy of fluid dynamics analysis methods as well as an improved blade elements theory for estimating aerodynamic propeller performance of the UAS-S4 and the UAS-S45. The two proposed numerical methods were validated using an experimental study in an open test section wind tunnel.

The fourth contribution proposes a new control method, using an LQR approach and a PI with reference feedforward controller for the stability and control of the UAS-S45. The robustness of the system is ensured using to an extended state observer. A fuzzy neural network was subsequently used for gain scheduling.

Keywords: UAS modeling, flight dynamics, aerodynamic modeling, propulsion modeling, wind tunnel testing, flight control, general extended state observer

TABLE OF CONTENTS

Page

LIST OF TABLES

Page

LIST OF FIGURES

Page

LIST OF ABREVIATIONS

ANFIS	Adaptive Neuro-Fuzzy Inference System
BET	Blade Element Theory
CAS	Control Augmentation System
CFD	Computational Fluid Dynamics
DATCOM	DAta COMpendium
ETS	École de Technologie Supérieure
FEM	Finite Element Method
GDP	Gross Domestic Product
GESO	Generalized Extended State Observer
ISE	Integral Square Error
ITAE	Integral of Time-weighted Absolute Error
LARCASE	Laboratory of Applied Research in Active Control, Avionics and Aeroservoelasticity
LQR	Linear Quadratic Regulator
MALE	Medium Altitude Large Endurance
MRF	Multi Reference Frame
MT	Momentum Theory
PID	Proportional Integral Derivative
RANS	Reynolds Average Navier-Stokes
RDS	Raymer's Design System
SAS	Stability Augmentation System
SST	Shear Stress Transport

STOVL	Short Take-off and Vertical Landing
UAS	Unmanned Aerial System
UAV	Unmanned Aerial Vehicle
USAF	United States Air Force
VLM	Vortex Lattice Method

LIST OF SYMBOLS

AR	Aspect ratio
c	Chord
c_l	Airfoil lift coefficient
c_m	Airfoil pitch moment coefficient
cv	Specific heat at constant volume
C_D	Aircraft drag coefficient
C_f	Skin friction coefficient
C_h	Hinge moment coefficient
C_L	Aircraft lift coefficient
C_{Lq}	Lift derivative with respect to pitch rate
C_m	Aircraft pitch moment coefficient
C_{mq}	Moment derivative with respect to pitch rate
C_P	Power coefficient
C_Q	Torque coefficient
C_T	Thrust coefficient
d	Diameter
D	Drag force
e_b	Back electromagnetic force
e_a	Armature voltage
f	Friction of the motor / Bending moment / Frequency
G_v	Production of turbulent viscosity
h	Static enthalpy / cell's height

h_0	First cell's height
H	Total enthalpy
i_a	Armature current intensity
I_x	Inertia about the x-axis
J	Advance ratio
J_x	Inertia
k	Turbulent kinetic
L	Lift force
L_a	Armature inductance
m	Mass
$\dot{m}$	Mass rate
Ma	Mach number
N_b	Blade number of the propeller
P	Pressure
P_k	Turbulent kinetic energy
P_{rt}	Turbulent Prandtl number
Q	Torque
R_a	Armature resistance
Re	Reynolds number
RPM	Rotational speed of the propeller
S_e	Control surface area
S_w	Wing area
Δs	First cell height

t/c	Thickness to chord ratio
T	Temperature
T_{hr}	Thrust
Throt	Throttle position
U_i	Velocity component of the flow
U_∞	Free stream velocity
U_{fric}	Frictional velocity
V	Aircraft velocity
V_E	Effective resultant velocity
W_i	Ideal work
W_o	Gross weight
W_w	Wing weight
x_{cg}	x-location of the center of gravity
x_p	x-location of the propeller
y^+	Distance to the wall
Y_v	Destruction of turbulent viscosity
α	Angle of attack
α_0	Zero-lift angle of attack
α_{0f}	Fuselage zero lift angle of attack
α_i	Induced angle of attack
β	Prandtl Glauert-correction factor / pitch angle
ϕ	Helix angle
ρ	Air density

Γ	Vortex intensity
η	Propeller efficiency
μ	Molecular viscosity
μ_{eff}	Effective viscosity
Φ_{TE}	Turbulent viscosity
δ_{ij}	Kronecker delta function
γ	Specific heat ratio
ω	Specific rate of dissipation / Angular velocity
Ω	Angular velocity
θ	Angular displacement
Λ	Sweep angle
ε	Downwash angle / Turbulence energy
λ	Taper ratio / Thermal conductivity
ν	Molecular kinematic viscosity

INTRODUCTION

Mankind had long dreamed of traveling the skies like birds. Many forerunners such as Leonardo da Vinci or George Cayley attempted to replicate the flight mechanism of birds, but it was not until 1891 when the first controlled flight was achieved, directed by Otto Lilienthal. Since then, the field of aviation has undergone continuous progress. In 2018, the Gross Domestic Product (GDP) of the aerospace industry was close to 2700 billion dollars (3.6% of the global GDP), making it a key player in economic development (Air Transport Action Group, 2014). Among the sectors of the aerospace industry, UAVs (Unmanned Aerial Vehicles) show a rapid dynamic evolution. A UAV or an autonomous flight system is an aircraft, programmed or remotely controlled and equipped with one or more onboard systems and payloads.

Although they have been around for almost a century, UAVs have long developed in the shadow of conventional aviation. More recent progress in the fields of robotics, optronics, miniaturization of electronic components and computer science have made UAVs essential for various civil and military applications. The UAV market is expected to reach $16 billion dollars in 2025 (Perrin *et al*., 2017).

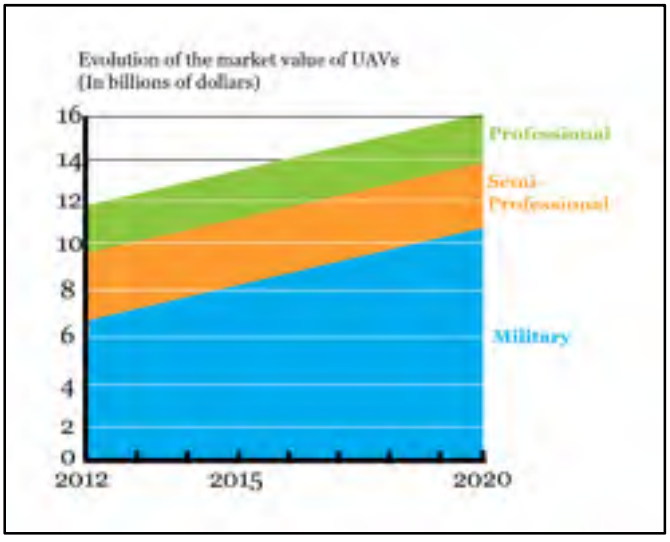

Figure 0.1 Evolution of the UAVs market value

UAVs have become essential tools to control information, as well essential players in the realization of many operations. As a result, several industrial and economic issues are emerging regarding their use. These issues are conditioned by the response of UAVs to some specific needs, in particular:

- The growing need of UAVs for increasingly dangerous or hostile missions.

The increase in the number of autonomous flight systems is strongly linked to their ability to perform missions in dangerous areas. The increase in investments related to autonomous flight systems is thus huge, especially in the military field. UAVs allow strategic missions to be conducted and provide tactical support in hostile or disaster areas as part of first aid missions. Nevertheless, the use of an autonomous flight system in dangerous zones generally causes its destruction. According to a study of US UAVs accidents, more than 400 UAVs have crashed in the world since 2001 (David and Panhaleux, 2015). The malfunctions, the cause of most of these accidents, were mainly due to poor weather conditions, loss of air-ground connection, and mechanical or electrical breakdown related to the environment. Given the cost of a drone (16.9 million dollars for the MQ-9 Reaper) (Perrin *et al.*, 2017), the financial losses were enormous.

Therefore, the ability to estimate in a preliminary way the behaviour of a UAV in hostile conditions is very important.

- The need to improve the performance of UAVs

Numerous advancements in computer science, mechanical systems and electronics have made possible the integration of new performance-enhancing technologies on autonomous flight systems. The morphing wing technique, a multidisciplinary optimization methodology designed to reduce fuel consumption and to increase flight performance, is one example. The validation of such new concepts for UAVs requires a high number of flight tests for validation; these are expensive both financially and environmentally. For example, the cost per flight hour of the MQ-9 Reaper is estimated at $6,800, while its average fuel consumption is 67 kg/hour (Perrin *et al.*, 2017). Reducing the number of flight tests required to certify unmanned flight systems will be a definite advance.

- The need for pilot training and strategic forecasts.

Unmanned flight systems require qualified pilots to facilitate tactical collaboration and to adapt to airworthiness rules. It should be noted that 25% of the causes of autonomous flight system losses are due to human error (David and Panhaleux, 2015). This highlights the importance of thorough pilot training before each mission, as this would make it possible to strategically plan the actions and the tasks of the autonomous flight systems.

To respond to these challenges, the solution proposed in this thesis is the use of a flight simulation model for unmanned aerial systems. A flight simulation model is a digital device that makes it possible to obtain the behaviour of an aircraft from its input data (speed, altitude, control surface position, etc.). This flight simulation modelling is done for the Unmanned Aerial Systems S4 Éhecalt and S45 Balàam designed and manufactured by Hydra Technologies. The UAS-S4 and UAS-S45 are unmanned aerial systems created to provide tactical support for surveillance and security for both military and civilian missions. The general characteristics of each unmanned aerial system are presented in Tables 0.1 and 0.2.

Table 0.1 General Characteristics of the UAS-S4

Specification	**Value**
Wingspan	4.2 m
Wing Area	2.3 m²
Total length	2.5 m
Mean Aerodynamic Chord	0.57 m
Empty Weight	50 kg
Maximum Take-off Weight	80 kg
Loitering Airspeed	35 knots
Maximum Airspeed	135 knots
Operating Ceiling	15, 000 ft
Operating range	120 km

Figure 0.1 UAS-S4 Éhecatl of Hydra Technologies

Table 0.1 General Characteristics of the UAS-S45

Specification	Value
Wingspan	6.11 m
Wing Area	2.72 m²
Total length	3.01 m
Mean Aerodynamic Chord	0.57 m
Empty Weight	57 kg
Maximum Take-off Weight	79.6 kg
Cruise Airspeed	55 knots
Operating Ceiling	20, 000 ft
Operating range	120 km

Figure 0. 2 UAS-S45 Balàam of Hydra Technologies

The realization of a flight simulation model for unmanned aerial systems raises two issues. The first is that the designed model must be capable of accurately predicting the flight dynamics of the UAS-S4 and the UAS-S45. The model will have to allow the development of new research; therefore, it will need to have a high level of certification (accuracy). The second aspect is that the model must allow for the integration of performance improvement techniques, such as new control laws or a morphing wing technique.

This thesis is structured into several chapters. The first chapter is devoted to a literature review of the different topics covered in this thesis, namely to a comprehensive description of unmanned aerial systems as well as of the various modelling methods applied to them. The synthesis of the methodologies used for new flight control law modelling are also discussed in this first chapter. The second chapter highlights the issues, objectives and the original contributions of this thesis. The various papers published or submitted in scientific journals are presented in Chapters 3, 4, 5 and 6. The design methodology of the UAS-S4 and UAS-S45 autonomous flight system simulation models is presented in Chapter 3. Chapter 4 proposes a methodology for estimating the aerodynamic model of the S45 unmanned aerial system based on a Nonlinear Vortex Lattice Method and a Computational Fluid Dynamics. Chapter 5 presents an improved Blade Element Momentum Theory, Computational Fluid Dynamics and experimental analyses of the UAS-S4 and UAS-S45 propeller. Chapter 6 presents a low-order robust controller for stabilization, tracking and disturbance rejection of the unmanned aerial systems. Finally, a conclusion is presented at end of the thesis, as well as an investigation of future work to build on the research completed to date.

CHAPTER 1

LITERATURE REVIEW

This UAS flight dynamics design thesis involves several disciplines whose central focus is “modeling and simulation”. “Modeling” involves collecting and compiling information about a system and expressing it in a form that allows its numerical computation (Diston, 2010). “Simulation”, which is subsequent to modelling, consists in performing tests in order to make the model intelligent or predictive.

Several methods exist for the design of simulation models of autonomous flight systems or aircraft. This chapter reviews the literature on this subject. The control law synthesis approaches that may be applied to unmanned aerial systems are also investigated.

Before addressing the different methods of flight dynamics modeling, it is important to present a comprehensive review of the “Unmanned Aerial System” concept.

1.1 The Unmanned Aerial System

Although they have experienced a real boom in recent years, the first projects related to UAVs date from nearly a century ago. Since the launch in 1917 of the first autonomous air vehicle, the “Kettering Bug”, capable of reaching a target, the evolution of drones has been closely linked to military needs (Fahlstrom and Gleason, 2012). In 1960, during the Vietnam War, the “Firebee drone” was used for reconnaissance and targeting missions. In the 1970s, the "compass code" program made it possible to set up the first HALE (High Altitude Long Endurance) drone (Fahlstrom and Gleason, 2012). One of the turning points in the history of drones was the year 1973, with the integration of real-time intelligence to facilitate the decision of drone design and manufacturing. This integration gave birth to the drones “Scout” and “Aquilla” (Tsach *et al*., 2010). From the 1980s, real-time intelligence began to be widespread in design, especially for drones performing tactical missions. These drones included the “IAI/TRW Hunter”, the “IAI/AAI Pioneer” and the “AAI Shadow”. In the 1990s, a new drone class was developed, the MALE drones (Medium Altitude Long Endurance), which included the “IAI-Heron” and the “RQ-1A Predator” (Tsach *et al*., 2010). Since then, technological

advances in various engineering disciplines have led to drones being used in many areas, such as film production, transportation of emergency equipment, mapping and surveillance.

Drones are autonomous vehicles with aerodynamic, structural and propulsive systems (Fahlstrom and Gleason, 2012). Drones can be categorized in several ways depending on their mission, size, endurance, area of operation, etc. The most common method classifies drones according to their maximum attainable altitude, their maximum take-off weight and their airspeed, as follows (U.S. Army, 2010):

- Group 1: maximum mass less than 20 lb, a maximum altitude less than 1200 ft and an airspeed of less than 100 kts;
- Group 2: maximum mass between 21 and 55 lb, a maximum altitude of less than 3,500 feet and airspeed less than 250 kts;
- Group 3: maximum mass less than 1320 lb, a maximum altitude of less than 18,000 ft and airspeed less than 250 kts;
- Group 4: maximum weight exceeding 1320 lb, a maximum altitude of less than 18,000 ft and airspeed exceeding 205 kts; and
- Group 5: maximum weight exceeding 1320 lb, a maximum altitude exceeding 18,000 ft.

Two type of UAVs, such as a quadrotor and the RQ-1 Predator, can be very different (David and Panhaleux, 2015). Nevertheless, when one evokes a set consisting of an unmanned aircraft, multiple sensors, communication systems, a control station, launching and recovery systems as well as several possible payloads (luggage, missiles, etc.), this set is called an Unmanned Aerial System. An unmanned aerial system is then a “UAV system”.

1.2 Modeling Methods for Unmanned Aerial Systems

There are several methods to obtain the model of a system. Depending on the prior knowledge of the system (Bosch and Klauw, 1994 ; Jategaonkar, 2015), these methods are classified as follows:

- The “white box method”. The white box method allows a model of a system to be designed solely from the laws of physics. This results in a “phenomenological model”.

- The “black box method”. The black box method only uses system observations to design its model. Estimation algorithms such as the Least Square Method, Neural Networks, etc., are used to correlate the observations with its behaviour. A “behavioural model” is then obtained. Black boxes are easier to obtain than white boxes, especially for complex systems. However, the parameters obtained for a behavioural model do not necessarily have a physical meaning, such as the weights of a Neuron Network or the Least Squares model parameters (Boely *et al*., 2011 ; Hamel, 2014).

A compromise of these two methods is the “gray box method”. It uses both the laws of physics and observations of the system. This is the methodology used throughout this thesis.

Since unmanned aerial systems can be associated with aircraft, they can be modeled using the same procedures. Designing the model or performing the simulation of an aircraft can lead, under certain conditions, to wrong results due to numerical instabilities due to the successive accumulation of errors.

To cope with this difficulty, the UAS model was divided into sub-models. The general model of the UAS is a function of its geometry, installed systems and environmental factors. As a result, the UAS is mainly composed of aerodynamics, structure, actuation and propulsion systems.

The realization of an unmanned aerial system model thus proceeds through the design of its different sub-systems and their interactions.

1.2.1 The Aerodynamic Sub-Model

The first studies of aerodynamics date back centuries with Aristotle (384-322 BC) who set the first definitions of continuity and air resistance. The 17th century was a time of rapid evolution in the field (Anderson, 2010). Several scientists have contributed to the definitions of the fluid dynamics laws and of aerodynamics in particular.

Isaac Newton (1642-1727) established the first definition of drag as being proportional to dynamic pressure. Newton also established a relationship of proportionality between the shear stress inside a fluid and the velocity gradient, which is a peculiarity of so-called "Newtonian"

fluids (Anderson, 2010). David Bernoulli (1700-1782) established Bernoulli's principle: in a fluid flow, the higher the speed is, the lower the pressure is. Bernoulli's principle, as well as the resulting Bernoulli equation, subsequently opened the doors to hydrodynamics (Anderson, 2010). Euler (1707-1783) determined the laws of motion of a non-viscous fluid, as he drew up a mathematical formulation of its motion, and thus allowed the quantitative analysis of aerodynamic problems. Louis Marie Henri Navier (1785-1836) and George Gabriel Stokes (1819-1903) independently determined the famous Navier-Stokes equations. They introduced the notion of viscosity into the fluid motion equations previously established by Euler. Osborne Reynolds (1842-1912) made advancements in the study of the transition between laminar and turbulent flow. He established a constant, called the Reynolds number, allowing the characterization of the flow. Wilhelm Kutta (1867-1944) and Nikolai Zhukovsky (1847-1921) independently established a mathematical relation allowing the calculation of the lift of a wing airfoil. This equation was a revolution in theoretical aerodynamics because it allowed for the first time the calculation of the lift with mathematical precision (Anderson, 2010). Ludwig Prandtl (1875-1953) described the concept of a boundary layer and made a great contribution to the field of aerodynamics. His work has defined the transition zone from laminar to turbulent regimes and its corresponding transition point.

During the first half of the 20th century, wind tunnel testing was the only way to obtain an accurate aerodynamic model of an aircraft, because the Navier-Stokes equations were difficult to solve and computers of that time were still rudimentary. The wind tunnel remains the best experimental way for aerodynamic analysis validation, especially for problem involving complex phenomena that cannot be easily modelled using computers.

Koreanschi *et al*. (2016) proposed a methodology to study the aero-elastic effect of a morphing wing tip during wind tunnel testing. Their analysis was focused on the flutter phenomenon. They made a wing equipped with a composite flexible skin which was optimized to obtain the best structural and aerodynamic performances during the morphing process. The analyses were performed in the subsonic wind tunnel of the National Research Council of Canada for a range of speeds from 50 m/s to 85 m/s, a range of angles of attack from -3° to -1.5° and a range of aileron deflection angles from -2° to 5°. The authors showed that no flutter phenomenon would

occur due to the composite flexible skin, and furthermore, that the skin allowed enough rigidity for the wing, which guaranteed that no damages would occur during the morphing process.

Mosbah *et al*. (2016) performed a validation of a hybrid method for the prediction of aerodynamic coefficients of an ATR-42 scaled wing model using wind tunnel experimental tests. The methodology of estimation was based on using Support Vector Machines (SVM), with parameters that were optimised using the Extended Great Deluge algorithm. The experimental tests were performed in the Price-Païdoussis subsonic wind tunnel. The results showed the perfect agreement of the experimental data with the estimated data.

In addition to wind tunnel testing, analytical methods began to be well known and used for aerodynamic calculation. These analytical methods relied on collections of semi-empirical equations (Williams and Vukelich, 1979). One of the most famous procedures, still used today, is the DATCOM procedure (Williams and Vukelich, 1979). The USAF Stability and Control DATCOM or DATCOM procedure is one of the best compilations of semi-empirical methods for calculating aerodynamic coefficients and their stability derivatives for an aircraft flying mainly in the subsonic regime. It allows the analytical prediction of the aerodynamic coefficients of an aircraft under different configurations (Wing, Wing-fuselage, Wing-tail etc.) and flight conditions. Its methodology is based on the addition of the aerodynamics contributions of the different surfaces of the aircraft by considering their interferences. The DATCOM semi-empirical procedure combines theoretical methods, charts and equations based on wind tunnel and flight test data (Popescu, 2009). The DATCOM procedure is widely used in industry and academia for the calculation of aerodynamic coefficients.

A research team from the Aerospace Faculty of Delft University of Technology developed a Cessna Citation 500 flight simulator based on the DATCOM procedure (Baarspul and Mulder, 1993). The results have shown that an aerodynamic model designed using DATCOM made it possible to reduce the number of flight tests needed for its certification.

Kuitche *et al*. (2017) and Segui *et al*. (2017) estimated the longitudinal aerodynamics coefficient of the UAS-S4 Ehecatl from its geometrical data. The computations were made for several flight conditions expressed in terms of altitudes (5,000 to 10,000 ft), airspeeds (45 knots to 50 knots) and angles of attack (-2° to 10°). The results showed that the lift, drag and

moment coefficients obtained with the DATCOM procedure were accurately predicted in comparison to those obtained with a CFD analysis using ANSYS Fluent.

An improved version of the DATCOM procedure, called Fderivatives, was developed at the Laboratory of Applied Research Active Controls, Avionics and AeroServoElasticity (LARCASE). This new code overcame some of the weaknesses of DATCOM, particularly in estimating the slope of the wing airfoil lift, the angle of attack and the pitching moment for zero-lift for a wing airfoil, the angle of attack for zero-lift for asymmetric fuselages, and the maximum lift coefficient for a wing. Fderivatives is also a collection of semi-empirical methodologies used to determine the aerodynamic coefficients and their stability derivatives coefficients for an aircraft (Anton *et al.*, 2009a).

Anton and Botez (2010, 2011) used the Fderivatives code to determine the aerodynamic model of the Hawker 800 XP business aircraft and of the X-31 military aircraft. They have shown, from a comparison between their aerodynamic models and the experimental data, that Fderivatives gave accurate results for the realization of an aircraft simulation model.

During the 1960s, the Vortex Lattice Method (VLM) (Hess and Smith, 1967) had a strong impact in the field of aerodynamics. The VLM is very effective in solving incompressible, irrotational and non-viscous flow problems (Jeffery and Docksey, 2008). This method is based on the resolution of Laplace's equations as follows:

$$\nabla^2 V = 0 \tag{1.1}$$

where V is the velocity vector of the flow.

For an incompressible and non-viscous flow, a wing can be designed as a set of panels that generates lift. Each panel contains a vortex. When the panels are considered planar, the Biot-Savart law can be used to calculate the influence of vorticity-induced velocity by taking into account its strength and orientation using the following expression (Bertin and Smith, 1998) :

$$\boldsymbol{V} = \frac{\Gamma}{4\pi} \frac{\boldsymbol{r}_1 \times \boldsymbol{r}_2}{\left|\boldsymbol{r}_1 \times \boldsymbol{r}_2\right|^2} \left[\boldsymbol{r}_0 \left(\frac{\boldsymbol{r}_1}{\left|\boldsymbol{r}_1\right|} - \frac{\boldsymbol{r}_2}{\left|\boldsymbol{r}_2\right|} \right) \right] \tag{1.2}$$

where Γ is the vortex intensity, $\boldsymbol{r_1}$ and $\boldsymbol{r_2}$ are the vectors of the start and end points of the vortex segment to the random point in space, and $\boldsymbol{r_0}$ is the vector located along the vorticity segment. For each panel, the speeds induced by all the other panels are summed, which leads to a set of equations satisfying the boundary "no-flow condition". The local velocities calculated by these equations are used to calculate the pressure differences between the upper and lower surfaces of the lifting surfaces. The integration of these pressures makes it possible to obtain the aerodynamic forces and moments. The efficiency of the VLM lies in the fact that the flow field does not require a meshgrid to be designed, and therefore its computation time is reduced.

The VLM is widely used today for the preliminary design of aircraft. At the Innovation Center of the Faculty of Mechanics of the University of Belgrade, the VLM has been used for the preliminary aerodynamic design of a light aircraft (Kostić *et al*., 2014). This study has shown that even though the VLM is limited to incompressible flows (the VLM is not accurate enough in estimating the drag), it still gives good results for subsonic flows and angles of attack located in the linear zone of the lift variation with the angle of attack. A comparison was made between the results obtained with the VLM and those obtained with a CFD analysis. These results have shown a perfect match between the two results obtained with these methods.

Segui *et a*l. (2018) developed an aerodynamic model of the Cessna Citation X based on the VLM using OpenVSP software. The model was designed with the aim to perform a morphing wing design on the aircraft. The computations were performed for the Mach numbers from 0.6 to 0.9, which correspond to the cruise regime speeds of the Cessna Citation X. The lift and drag coefficients obtained were compared to those provided by a Level D Research Aircraft Flight Simulator. The results showed a good agreement of these data for Mach numbers equal to 0.6 and 0.7, and angles of attack varying from -5° to 12°. The VLM does not consider the influence of the transonic regime on the drag, and for this reason, results were only obtained for Mach numbers smaller than 0.7.

Şugar Gabor *et al*. (2016) proposed a new nonlinear definition of the VLM. From the classical VLM approach (Katz, 1991), a correction factor $\Delta\Gamma$ was added to each vortex's intensities and becomes:

$$\Gamma \rightarrow \Gamma + \Delta\Gamma \tag{1.3}$$

where Γ is the vortex intensity, and the correction factor is $\Delta\Gamma$. Thus, the nonlinear VLM approach was obtained from the following expression:

$$\left(\boldsymbol{V}_{\infty} + \sum_{j=1}^{N} (\Gamma_j + \Delta\Gamma_j)\boldsymbol{v}_{ij} + \boldsymbol{V}_i^T \right).\boldsymbol{n}_i = 0 \tag{1.4}$$

where $\boldsymbol{V}_{\infty}$ is the freestream velocity, N is the number of panels over the wing, $\boldsymbol{v}_{ij}$ is the velocity induced the unit vortex j at the i^{th} panel, $\boldsymbol{V}_i^T$ is the modulus of the surface transpiration velocity, and $\boldsymbol{n}_i$ is the surface normal vector calculated at the i^{th} panel.

Aubeelack and Botez (2017) investigated the efficiency of the nonlinear VLM analyses when optimizing the lift to drag ratio of the UAS-S4 wing. The analysis consisted of determining the accuracy that can be obtained using the nonlinear VLM analysis for a wing sweep optimization. This analysis was compared with a RANS simulation and showed, for angles of attack $\alpha = 0°$ and $\alpha = 2°$, for Reynolds numbers $R_e = 1.0\text{x}10^6$ and $R_e = 1.5\text{x}10^6$, and for a wing sweep angle varying from -12° to 12°, that there is a very good agreement between the results obtained from both methodologies. The maximum percentage of difference calculated was 2.9%.

Computational Fluid Dynamics (CFD) began to be used in aerodynamic modelling thanks to the revolution in the field of computer science. The CFD method is based on the resolution of both Euler and Navier-Stokes equations (Argyropoulos and Markatos, 2015). It allows, theoretically, to fully describe the aerodynamic phenomena of an aircraft, and thus, can be considered as the most powerful and accurate aerodynamic modelling method. However, it requires integration and discretization-adapted schemes to integrate the Navier-Stokes equations. The computational requirements for the direct resolution of Navier-Stokes equations as a function of time for turbulent flows at high Reynolds numbers are very large, and cannot be realized with the current computing power (Nelson et Zingg, 2004). As a result, the CFD method generally uses turbulence models based on the Reynold Averaged Navier-Stokes equations (RANS) (Argyropoulos and Markatos, 2015).

$$\frac{\partial \rho}{\partial t} + \frac{\partial}{\partial x_j}\left(\rho U_j\right) = 0 \tag{1.5}$$

$$\frac{\partial}{\partial t}(\rho U_i)+\frac{\partial}{\partial x_j}(\rho U_j U_i)=-\frac{\partial P}{\partial x_i}+\frac{\partial}{\partial x_i}\left[\mu_{eff}\left(\frac{\partial U_i}{\partial x_j}+\frac{\partial U_j}{\partial x_i}\right)-\frac{2}{3}\mu_{eff}\frac{\partial U_k}{\partial x_k}\delta_{ij}\right] \quad (1.6)$$

$$\frac{\partial}{\partial t}(\rho H)-\frac{\partial P}{\partial t}+\frac{\partial}{\partial x_j}(\rho U_j H)=\frac{\partial}{\partial x_j}\left[\lambda\frac{\partial T}{\partial x_j}+\frac{\mu_t}{Pr_t}\frac{\partial h}{\partial x_j}\right]$$
$$+\frac{\partial}{\partial x_j}\left\{U_i\left[\mu_{eff}\left(\frac{\partial U_i}{\partial x_j}+\frac{\partial U_j}{\partial x_i}\right)-\frac{2}{3}\mu_{eff}\frac{\partial U_k}{\partial x_k}\delta_{ij}\right]+\mu\frac{\partial k}{\partial x_j}\right\} \quad (1.7)$$

Silisteanu and Botez (2010) have used a CFD method to estimate the laminar-turbulent transition zone on a NACA 2415 wing airfoil from its friction coefficient. They proposed a new methodology based on turbulence simulation over the entire flow domain by using RANS simulation. Comparison of the results obtained using the CFD method with the results obtained experimentally give a maximum error of 4%.

Regarding the previous work related to the UASs, Oliviu *et al*. (2015) performed an aerodynamic analysis of the UAS-S4 using the CFD approach in order to investigate its performance improvement in a morphing wing situation. The morphing methodology consisted of determining the optimized airfoil shapes using a coupling of the Artificial Bee Colony (ABC) and the Broyden-Fletcher-Goldfarb-Shanno algorithms. Navier-Stokes equations were used to estimate the aerodynamic coefficients of the morphed airfoil. The results showed that the morphing wing lift-to-drag ratio (L/D) increases up to 4%, compared to the L/D original geometry.

Kuitche and Botez (2017) proposed methodologies to estimate the aerodynamic coefficient of the UAS-S4 using its geometrical characteristics. The approaches presented were the DATCOM procedure using the “Digital Datcom” code, the VLM method using TORNADO code and the CFD analysis using ANSYS Fluent software. The three methodologies were compared, and their results showed a good agreement for the lift, drag and pitch moment coefficients.

1.2.2 The Propulsion Sub-Model

In the 100 years since the first controlled flight by the Wright brothers, propulsion systems have undergone a great evolution. The major role of "propulsion" in aircraft performance has made it a major discipline in aeronautics.

All type of propulsion systems produce thrust in the same way. An air mass is accelerated after passing through the propulsion system. The acceleration of the air movement subsequently creates a reaction that is called "thrust" (Phillips, 2009). The thrust increases as a function of the air flow entering the propulsion system, while the efficiency of a propulsion system decreases as a function of the outlet air speed. Therefore, a propulsion system will have an optimal efficiency if the air flow is maximum and the speed is minimum. However, the increase in air absorption capacity leads to an increase in the total mass of the propulsion system. Thus, there is a trade-off between the thrust (or the amount of air entering) and the mass of the propulsion system (Phillips, 2009).

Propeller engines are the type most often used for aircraft flights in the subsonic regime because they offer a good ratio of thrust to the mass of the propulsion system. Jet engines, however, are more efficient for transonic and supersonic flights. Turboprop engines, meanwhile, are a compromise between jet engines and propeller engines.

The UAS-S4 and UAS-S45, in particular, use two piston-propeller engines. The first use of this type of propulsion was made by the Wright brothers in 1903 (Phillips, 2009). In 1907, Traian Vuia built an aircraft powered with a 25-horsepower internal combustion engine (Gibbs-Smith, 1960). The "Coandă-1910" aircraft designed by Henri Coandă in 1910 used a ducted fan composed of a piston engine driving a multi-bladed centrifugal blower which exhausted into a duct (Winter, 1980). The "A. Vlaicu Nr. I, II and III", manufactured and designed by Aurel Vlaicu from 1910 to 1914, used a rotary engine equipped with a propeller (Taylor, 1989). Elie Carafoli designed a fighter prototype called the "IAR CV 11" in 1930 (Grey and Bridgman, 1930). The aircraft was powered using a coupling of a 500-horsepower piston engine and a 2-bladed variable pitch propeller. The "IAR CV 11" was able to reach 319 km/h top speed, which was very impressive for that time.

Propellers are the most important part of propeller engines. Each blade of a propeller is modelled with one or more airfoils. The rotational movement of the propeller creates an airflow around each blade, and thus produces a lift and drag that are components of the thrust (Gudmundsson, 2013a).

Because of the complex interactions occurring between the rotational speed of the propeller, its geometry and the aircraft speed, several methods have been developed to estimate the thrust. The most famous of these methods are:

- The Momentum Theory (MT)

This method allows to quickly estimate the propeller's performance, even though the results are generally optimistic. The momentum theory (Stepniewski and Keys, 1984) is based on the following assumptions: the propeller is replaced by a thin disc; the flow passes through the disc uniformly; the stagnation pressure of the flow outside the streamtube is constant; the streamlines in the far-field of the disk are parallel; the flow is inviscid, irrotational and incompressible (Gudmundsson, 2013a).

The momentum theory assumes that the propeller, replaced by a disc, moves uniformly in the fluid by exerting a thrust. Its displacement is accompanied by an acceleration of the fluid and a pressure variation. The thrust is therefore deduced from the momentum equation (Gudmundsson, 2013a):

$$T = \int_S \rho V(\vec{V}.\vec{n})dS \tag{1.8}$$

where V is the velocity of the flow, S is the area of the disk and ρ is the density of the air. The momentum theory is an excellent method for the preliminary estimation of propeller performance. However, due to of all the assumptions, and in particular to the incompressible and uniform flow assumption, as well as to the neglection the geometry of the propeller, generally, optimistic results are obtained. Therefore, the MT is often associated with the blade elements theory in order to obtain better results than by applying only one of these methods.

- The Blade Elements Theory (BET)

The Blade Elements Theory (BET) allows to estimate the thrust by dividing the propeller into several blade elements(Gudmundsson, 2013a). On each blade element airfoil, the aerodynamic parameters are calculated according to the conditions of its surrounding flow, as follows:

$$dL = \frac{1}{2}\rho V_E^2 c(r) C_l dr \tag{1.9}$$

$$dD = \frac{1}{2}\rho V_E^2 c(r) C_d dr \tag{1.10}$$

where *dL* and *dD* are obtained from the lift and drag of each blade element, *c*(*r*) is the chord of the blade element located at the *r*-position, ρ is the density of the air, and V_E is the effective velocity of the flow expressed by:

$$V_E = \sqrt{(v_i + V_0)^2 + (\omega r)^2} \tag{1.11}$$

where ω is the speed of rotation of the propeller, V_0 is the speed of the airplane and v_i is the induced speed calculated from momentum theory. C_l and C_d are the lift and drag aerodynamic coefficients of the blade element.

The aerodynamic parameters are subsequently added to obtain the thrust and the torque generated by the propeller.

$$T = N_B \int_{R_{hub}}^{R} dL\cos(\varphi + \alpha_i) - N_B \int_{R_{hub}}^{R} dD\sin(\varphi + \alpha_i) \tag{1.12}$$

$$Q = N_B \int_{R_{hub}}^{R} r.dL\sin(\varphi + \alpha_i) - N_B \int_{R_{hub}}^{R} r.dD\cos(\varphi + \alpha_i) \tag{1.13}$$

where *T* and *Q* are the thrust and torque produced by the helix, N_B the number of blades, *R* the radius at the tip and R_{hub} the radius at the hub of the helix.

The BET is generally used in the literature. Khan and Nahon (2015) developed a propulsion model capable of predicting all aerodynamic forces and moments for a cruise condition. Their methodology combined momentum theory with the blade elements theory in order to determine the speeds and the angles of attack induced. The proposed model has been validated

with experimental tests carried out in a wind tunnel. The results have shown a perfect concordance between the realized model and its experimental data.

MacNeill and Verstraete (2017) used the BET to study the performance of APC propellers. Their methodology also used the momentum theory for the estimation of induced velocities, as well as the equations of Viterna and Corrigan (1982) for the estimation of aerodynamic effects for high angles of attack. The obtained results were in perfect agreement with the experimental results from wind tunnel testing.

Similarly, Phillips (2009) established a methodology for the determination of the aerodynamic effects of propellers from the VLM. This methodology was combined with the BET and led to the accurate thrust calculations of the propellers from their geometrical characteristics.

1.2.3 The Structural Sub-Model

The structural sub-model is generally used to estimate the mass and moments of inertia of an aircraft according to its flight conditions. Methodologies for estimating masses and moments of inertia can be divided into three categories (Dababneh et Kipouros, 2018):

- Empirical and Semi-Empirical Methods

Empirical and semi-empirical methods use equations developed from statistical data. Empirical methods are the most popular methods in the aeronautical field. The most famous are the equations of Howe (2000), Raymer (1989), Roskam (1985a) and Torenbeek (2013).

Glatt (1974) proposed a method for calculating the masses of the components of an aircraft. The method was based on a statistical analysis using the historic record of the components' masses similar to the component whose mass must be determined.

Empirical methods are generally used for preliminary design, but they may have some limitations due to the quantity or quality of data available, as well as due to the conditions in which they were developed. For example, the Torenbeck equations provide good results, but are limited to subsonic flights.

- Analytical and Quasi-Analytical Methods

Analytical methods are the least present in the literature. Ritter (1960) established a methodology for accurately estimating the mass of a wing by structural analysis. His method

consisted in determining the mass needed to satisfy the structural stiffness and bending requirement of the wing. Udin and Anderson (1992) established a wing mass estimation method for a simplified model of a subsonic aircraft wing. They divided a wing into several components, and then performed an analysis of its loads to obtain its mass as a function of the bending moment, the torsion and the shear forces. Elham *et al.* (2013) carried out a quasi-analytical method to estimate the mass of a wing. Their methodology used basic wing sizing techniques to calculate the amount and distribution of the material needed to withstand the applied loads. Their proposed wing weight prediction method was validated using data collected from different aircraft wings of various sizes, categories and manufacturers. The results have shown that the calculation time was considerably reduced.

- Finite Elements Methods (FEMs)

FEMs allow the structural analysis problems of an aircraft to be solved numerically by using partial differential equations (PDEs). Hürlimann *et al.* (2011) proposed a multidisciplinary approach based on a Computer Aided Design and a Computer Aided Engineering (CAD/CAE) procedure to estimate the mass of wing structures. Their methodology used CATIA V5 for the design of the wing and for the application of different loads on it. Following the application of the FEM, the results obtained were excellent, although the method required a high computation time.

Sensmeier *et al.* (2006) conducted a methodology to generate an aircraft structural model for the preliminary estimation of its mass. This methodology consisted of creating an FEM by defining a parametric structure to facilitate its deformation. The model thus obtained was further optimized in order to obtain the appropriate geometry of the aircraft. The results showed that the proposed method was more accurate than the empirical methods for estimating aircraft mass.

Regarding the works related to UASs, Tondji and Botez (2014, 2017) performed a numerical and experimental analysis on the UAS-S4 to determine its mass, center of gravity and inertia. The numerical analysis methodology was conducted through Raymer and DATCOM statistical-empirical methods coupled with mechanical calculations. The pendulum method was proposed as the experimental methodology. The comparison of the two methods showed very good results with an average error of 7.8%.

1.2.4 The flight dynamics Sub-Model

Flight dynamic analysis allows to obtain an aircraft's motion based on the flight conditions and the flight data. Flight dynamics analysis is linked to stability and control analysis. Although aircraft geometry is an essential part of stability and control studies, modern theories also consider interactions between actuators and control systems (Diston, 2010). As a result, obtaining the flight dynamics model requires several mechanical assumptions. The equations of motion for a flight dynamics model were established by Bryan (1911) and Lanchester (1907). The aircraft was considered as a rigid object with six degrees of freedom subject to several forces. These forces are generally divided into three categories: gravitational, propulsive and aerodynamic. These equations allowed the flight dynamics of the aircraft to be defined mathematically. Other equations took into account the aeroelastic effects, the dynamics of the control systems and the atmospheric disturbances (Diston, 2010).

Using the Bryan and Lanchester flight dynamics equations, Ghazi (2014) developed a simulation model for the Cessna Citation X business aircraft. This simulation model was found to be accurate through its comparison with data obtained using a certified level D simulator of CAE Inc.

1.3 The Control Laws

The stability and control of an aircraft is one of the most important issues in aviation. To address this issue, it is necessary to use theories of control adapted to an aircraft. Designing an internal control law is equivalent to applying methods that guarantee very good flight qualities. Thus, the synthesis of a control law passes through the definition of manoeuvrability qualities as constraints to be satisfied by the aircraft, and through the choice of a control architecture.

1.3.1 Manoeuvrability qualities

Manoeuvrability qualities are "those qualities or characteristics of an airplane that govern the ease and precision with which the pilot is able to perform the required tasks" (Cooper and

Harper, 1969). Therefore, the pilot gives qualitative opinions following several flight tests, which are further converted into quantitative data. The qualities of manoeuvrability can be of several types: modal, temporal and frequency. Most of the specifications used in the field of aviation are mentioned in "*The U.S Military Specification for the Flying Qualities of Piloted Airplanes*" (US Military, 1980). Although they are military specifications, these same criteria are also mentioned by many authors such as Gibson (1995), Hodgkinson (1999) and Nelson (1997), and are adapted to civil aviation.

1.3.2 Aircraft Control Architectures

The general architecture of a control loop that is needed to satisfy the qualities of manoeuvrability is composed of a Stability Augmentation System (SAS) and a Control Augmentation System (CAS) (Stevens and Lewis, 2003; Tewari, 2011).

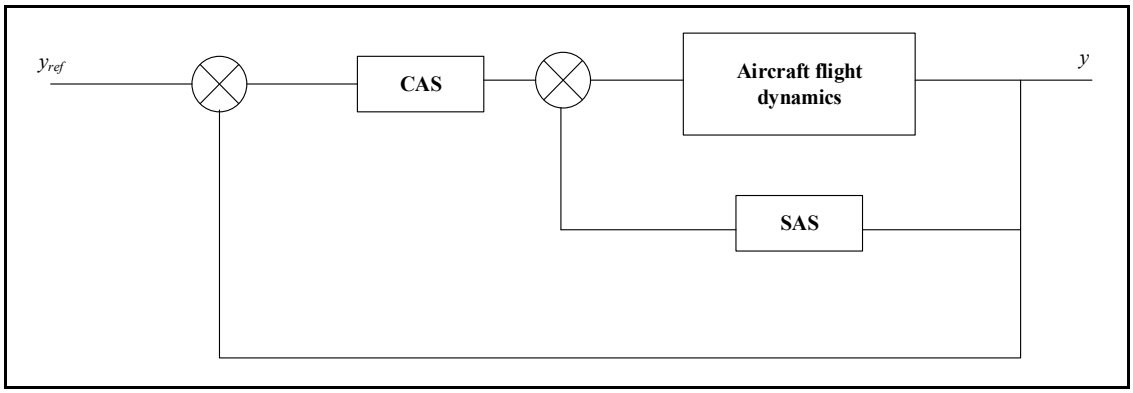

Figure 1.1 The general architecture of an aircraft control loop

There are several theories regarding flight control synthesis. Based on the work of (Balas, 2003; Pratt, 1999), the main methods are the following:

- Classical approaches

The classical control law methodologies are the most famous in the literature (Nelson, 1997; Stevens and Lewis, 2003; Tewari, 2011). These methodologies are based in most cases on the synthesis of a PID controller or on a controller in advance or phase-delayed. These

methodologies are generally based on a “pole placement” or on the “direct tuning of parameters” from a Bode diagram.

Sufendi *et al*. (2013) designed a PID controller for a drone using the Zeigler-Nichols method. The PID controller ensured longitudinal and lateral stability, including control of angular velocity, attitude and altitude. The response time of their system was improved as well as the reduction overshoot for a step response in comparison to the uncontrolled system.

Barbosa *et al*. (2004) proposed a methodology for adjusting a PID based on an ideal Bode transfer function. The controller parameters were determined by minimizing the errors between the time responses of the desired model using the ideal Bode transfer function, and the responses of the system to be controlled with the PID. The results showed that the obtained system was very robust to gain variations.

- Optimal Control

Unlike conventional approaches, Optimal Control methods allow multivariable systems to be handled more efficiently. The most common method is the Linear Quadratic Regulator (LQR) method (Kwakernaak and Sivan, 1972). The LQR method allows the stability of a system to be ensured while guaranteeing a minimum of effort required by the actuators. It is based on the resolution of the performance index (Kwakernaak and Sivan, 1972):

$$J = \int_0^\infty \left(\Delta x^T Q \Delta x + \Delta \eta^T R \Delta \eta \right) dt \tag{1.14}$$

where x is the system state vector, η is the control vector, Q is the system state weighting matrix, and R is the control weighting matrix. The LQR method and its other variants (Linear Quadratic Gaussian Control, Linear Quadratic Integral Compensator, etc.) are generally used in the literature.

Ashraf *et al.* (2018) proposed an LQR method for controlling the lateral dynamics of an F-16. The control matrix was calculated from the performance index by choosing the appropriate weighting matrices. The resulting controller was compared to a conventional pole placement approach. The results showed that the LQR method gave better performance and was more robust to disturbances than the conventional pole placement method.

Boughari *et al*. (2017) also carried out an LQR method, but for the control of the Cessna Citation X business aircraft. Their methodologies consisted in calculating the weighting matrices using a meta-heuristic algorithm to satisfy the chosen manoeuvrability qualities. They showed that their method significantly reduced the time, therefore the cost of designing control laws.

- The H_∞ Synthesis and the μ-Synthesis Methods

H_∞ synthesis methodology was developed to address disturbance rejection and robustness issues. Briefly, it is a question of decreasing the impact of disturbances on the behaviour of a system. The H_∞ standard method then allows to minimize the maximum value of the ratio between the finite energy of the output and the finite energy input (D. A. Saussié, 2010).

$$\left\|G(s)\right\|_\infty = \sup_{\omega \in \square} \bar{\sigma}\left(G(j\omega)\right) = \sup_{U(s)\neq 0 \in L_2} \frac{\left\|Y(s)\right\|_2}{\left\|U(s)\right\|_2} \tag{1.15}$$

Saussié *et al*. (2006) proposed a synthesis approach of a robust controller of the longitudinal dynamics of a challenger CL-604. Their approach used a H_∞ synthesis capable of anticipating the mass and balance variations while satisfying the desired manoeuvrability. The controller thus developed had very good robustness with respect to the variation of the mass and balance. The authors also applied a modal reduction method to reduce the order of the controller while maintaining its performance.

The μ-synthesis provides a general framework for studying the robustness of a system that has some modelling errors. Modelling errors can be uncertainties of physical parameter values or uncertainties due to poorly-known dynamics. Amato et Iervolino (2004) used the μ-synthesis for the design of a commercial aircraft model controller for disturbance rejection and robustness improvement.

- Intelligent Control

Intelligent Control combines the control systems methods with artificial intelligence techniques. The integration of artificial intelligence solves not only conventional control problems such as system uncertainties or environmental disturbances, but also other problems related to the lack, inconsistency and/or unreliability of sensor information or actuator malfunctions (Burns, 2001). There are several methods of intelligent control. Mengali (2000)

proposed a method for designing a non-linear controller based on fuzzy logic. Calise and Sharma (2001) used a neural network to increase the performance of linear controllers. Grigorie and Botez (2015) used data fusion associated with fuzzy logic to improve the performance of an inertial navigation system in a scenario in which sensors returned noisy data.

CHAPTER 2

RESEARCH METHODOLOGY AND THESIS ORGANIZATION

As shown in the literature review, flight systems modeling methods are very diverse. These methods depend primarily on the point of view of the modeller, but also on the phenomena that the modeller seeks to identify (Jategaonkar, 2015). The desired level of precision is also very important. The two main axes that guided the model development of the unmanned aerial system proposed in this thesis were: to be able to faithfully estimate the flight dynamics of the unmanned aerial system so that the simulation model could be certified; and to be able to validate a performance improvement technique using the model. For this second axis, the selected performance improvement methods were a new internal control law and a morphing wing technology. Morphing wing technology, in particular, consists of modifying the shape of the wing of an aircraft in order to reduce its drag and increase its lift. The simulation model is therefore designed to promote the integration of a morphing wing and it will be able to do so in real time to improve the aircraft's performance.

These issues then helped to formulate the preliminary questions of this research work:

- How to design an unmanned aerial system model with a very high level of certification?
- How to promote the integration of the morphing wing technique to the model of the unmanned aerial system?
- How to define a new control law for the obtained model?

The following research methodology was established to respond to these three questions.

2.1 Research Methodology

The research methodology is based on the decomposition of the global model of the UAS into sub-models in order to reduce the numerical instabilities due to the successive increase of the errors. The design of the UAS-S4 and S45 models consists of the realization of their various sub-models of their aerodynamics, propulsion, structure and actuators. A stability study and a study of the internal control laws were then conducted. The integration of the different sub-models was done under MATLAB/SIMULINK (MathWorks, 2005). MATLAB is a software

for system design and analysis that allows several types of scientific problems to be solved. SIMULINK is a MATLAB tool for continuous domain simulation. This tool makes it possible to create models in the form of a block diagram, which facilitates the design of complex systems. MATLAB/SIMULINK is generally used in research and industry, and is therefore an appropriate tool for this thesis.

2.2 Aerodynamic Sub-Model Design

The aerodynamic sub-model was designed to analyse or modify each component of the UAS separately. Therefore, each UAS will be divided into four parts (Figure 2.1): the "Wing-Body" part, the "tail" part, the "control surface" part, and the "propulsion" part. A final "ground effect" part can also be added. The equations of flight mechanics complete the total model. This separation of the aircraft into several elements also favourizes the integration of the morphing wing technique.

In the "Wing-Body" part, the aerodynamic coefficients of the wing are calculated separately, then they are added to the aerodynamic coefficients of the fuselage while taking into account the interactions. Thus, any deformation of the wing will involve a modification of its aerodynamic coefficients, and the new estimation of the "wing-fuselage" part's contribution.

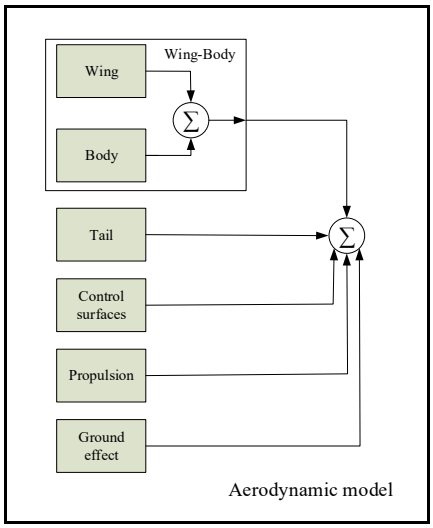

Figure 2.1 Aerodynamic sub-model of the UAS.

The methods chosen for the design of the aerodynamic sub-model were semi-empirical methods using Fderivatives, DATCOM software, the VLM using TORNADO software, and CFD methods using ANSYS Fluent software. Fderivatives, DATCOM and the VLM only require a small computation time. These methods also gave a good estimate of the aerodynamic coefficients of an aircraft for a subsonic flight and were applied on the UAS-S4 and UAS-S45. The CFD method, which is the most accurate and computational intensive, was mainly used to validate the results obtained with the other three methods.

2.3 Propulsion Sub-Model Design

The UAS-S4 and the UAS-S45 both have a front and a rear propulsion system. Each propulsion system consists of a two-stroke engine and a propeller.

The first study was the aerodynamic analysis of the propeller. The purpose of this study was to evaluate the thrust produced by the propeller as a function of the atmospheric data and of its rotational speed. The numerical analysis was carried out using the CFD method on ANSYS Fluent, and by the BET. Subsequently, a test bench was constructed in order to perform experimental tests in the wind tunnel. These tests validated the numerical analysis.

The second study was the design and analysis of the engines. An engine model was made by considering the pressure-volume diagram of the Otto cycle of a two-stroke engine. Each of the Otto cycle phases was represented by an equation. The torque and the power produced by the engine were calculated by solving all of these equations. The engine model was then optimized using the manufacturer's data and Nelder-Mead's nonlinear optimization algorithm. The last study involved the redesign of the propulsion system from the results of the analysis of its propellers and engines.

2.3.1 Actuator and Structural Sub-Models' Design

The structural sub-model dealt with the estimation of the mass, the center of gravity and the inertia of each aircraft. The structural sub-model was divided into six parts corresponding to the following six aircraft surfaces: wings, fuselage, engines, vertical tail, horizontal stabilizer

and landing gear. Each surface was decomposed into basic shapes, such as triangles, rectangles and trapezoids to facilitate the calculation of the aircraft center of gravity and mass. Using these configurations, semi-empirical Raymer equations were applied to each surface in order to estimate its mass and center of gravity. The inertia of the aircraft was estimated using the DATCOM procedure, and the numerical results were validated with experimental data.

This sub-section was also devoted to the realization of the UAS-S4 and S45's actuation system. This actuation system allows for the control surfaces' deflections and is also used for the propulsion system's throttle control. Each actuation system consists of a servomotor coupled to a lever arm. The actuation system was then modelled using the geometrical characteristics of the control surfaces, the servomotor manufacturer's data, and the mechanical equations.

2.3.2 Control Law Design

The stability analysis was carried out using the control law design. The purpose of this analysis was to determine the control settings (control surfaces and throttles) necessary for the UAS to perform an accurate flight under different flight conditions. The procedure used for this analysis can be found in several publications (Cook, 2013; Nelson, 1997; Phillips, 2009). Once this procedure was established, a study of the small disturbances around the equilibrium position of the aircraft was performed. The data thus obtained was subsequently used to establish the control laws.

The established control architecture includes a stability augmentation system (SAS) and a controllability augmentation system (CAS). The SAS was realized using an LQR approach, while the controllability augmentation system uses a PI corrector associated with an extended state observer. The parameters of the control matrices were optimized so that the system obeys the desired manoeuvrability and flight qualities. Subsequently, a Gain Scheduling methodology was proposed based on a fuzzy adaptive neuron network.

2.4 Originality of the thesis

Studies focused on the UAS-S45 and on this type of unmanned system in general are not very present in the literature. Regarding the UAS-S4, the only aerodynamic and the structural analyses available were performed by authors from the same environment as the LARCASE (Kuitche and Botez, 2017; Oliviu *et al*, 2015; Segui, *et al*. 2017; Tondji and Botez, 2016). The results from this work on the UAS-S4 and S45 are thus a major contribution to the academic and industrial field.

The originality of the thesis has four aspects. The first aspect is related to the numerical methodologies proposed to design each UAS model. Each methodology, which was a completely in-house method, used only the geometrical data to estimate each sub-model with a guarantee of a high level of accuracy. The UAS-S45 aerodynamic sub-model estimation methods, for example, required only a minimum of geometrical data and showed a very good agreement with the experimental data. The paper derived from this work was published in the Special Edition for CJA 30th Anniversary, Volume 32, Issue 1, of the *Chinese Journal of Aeronautics.*

The second aspect is related to the innovation of each sub-model estimation method. The aerodynamic model was developed with a new code called Fderivatives, which was modified to predict the accurate aerodynamic coefficients for the UAS. This method had not been available in the literature and, thus, can lead to the development of new research goals. The methodology proposed to estimate the propulsion sub-model using a piston-engine model designed from the Otto cycle and the propeller performance model designed from a CFD analysis were also innovations. The conventional methodologies proposed in the literature were electrical propulsion and a propeller analysis performed using the Blade Element Theory. The methodology proposed is more accurate than those proposed in the literature.

The third aspect is related to the proposed flight dynamic model of each UAS. The proposed flight dynamic model was designed with the aim of testing performance improvement techniques. The research was focussed on the “morphing wing technique”. The UAS model allows to apply and validate in real time any planform wing morphing parameters (span, chord

and sweep angle morphing) or airfoil morphing. This type of flight dynamics model is not present in the literature.

The fourth aspect is related to the design of the UAS-S45 robust low-order controller. The proposed methodology was divided into 1) stability and tracking improvements and 2) robustness improvement. The stability and tracking improvements were performed using a composite controller combining an LQR approach, for which the weight matrices were calculated using a metaheuristic optimisation algorithm, and a Proportional Integral controller with a feedforward compensation. A Generalised Extended State Observer (GESO) was applied for robustness improvement. The GESO is a good alternative to design a robust controller since it allows the estimation and the compensation of the disturbances and uncertainties. Thus, an intelligent gain scheduling method based on an Adaptive Neuro-Fuzzy Inference System (ANFIS) was proposed. The presented methodology is new, as it was not available in the literature, and showed better performance for aircraft control than the other control methodologies.

2.5 Thesis Organisation

The four journal papers in Chapter 3 to Chapter 6 are the results of the research performed in the thesis. Their main author is the author of this thesis. One of the journal papers has been published and three are currently under review.

Prof. Ruxandra Mihaela Botez, as co-author for all the papers, supervised the realization and the progress of the research. In the second paper, Mr. Arthur Guillemin, Internship student, worked as a co-author by contributing to the aerodynamic analysis of the UAS-45 Bàlaam using ANSYS Fluent. Mr. David Communier, PhD student, worked as a co-author by contributing to wind tunnel testing on the UAS-S45 reduced scale wing in the second paper. In the third paper, Mr. Remi Visio, Internship student, and Dr. Oscar Carranza Moyao worked as co-authors by contributing to the design and manufacture of the bench test of the UAS-S45 propeller. Mr. Jean Christophe Maunand, Internship student, worked as co-author by contributing to the aerodynamic analysis of the UAS-45 propeller using ANSYS Fluent. In the

fourth paper, Hugo Yañez Badillo, Internship student, worked as co-author by contributing to the implementation of the generalised extended state observer to the UAS-S45 controller.

2.5.1 The first journal paper

Chapter 3 presents the journal paper entitled “Novel Modeling Methodologies for Unmanned Aerial Systems - Applications to the UAS-S4 Ehecatl and the UAS-S45 Bálaam” published in the *Chinese Journal of Aeronautics*, Special Edition for CJA 30th Anniversary ,Vol. 32, Issue 1, in January 2019. This chapter highlights the design methodology of the simulation models for the Unmanned Aerial System UAS-S4 and S45. The procedure consists of dividing their model architecture into aerodynamic, propulsion, structure and actuator sub-models. The aerodynamic sub-model was estimated using the in-house Fderivatives code. The propulsion sub-model consists of a two-stroke engine model, based on the thermodynamic Otto cycle equations; the propeller performance sub-model was done using the blade elements and the momentum theories. The structural sub-model, designed to determine the mass and moment of inertia, was performed using Raymer's semi-empirical equations. Finally, the actuators sub-model consisted of the design of a servomotor controlled by a PID that satisfied the specifications of the manufacturer. The validation of the Unmanned Aerial Systems S4 and S45 models was made by comparison of each estimated sub-model with its numerical and experimental data. For this purpose, the data from the aerodynamic sub-model were compared to those obtained from the DATCOM procedure, the VLM and a CFD analysis. The two-stroke engine model constituting the propulsion sub-model was compared to the manufacturer's data, while the propeller performance data was compared to the data obtained by the CFD analysis. The structural sub-model was compared to experimental data obtained from the pendulum method. The results of these comparisons showed that the presented methodology was very efficient and allowed to obtain a high level of precision for the UAS-S4 and S45 simulators.

2.5.2 The second journal paper

Chapter 4 presents the journal paper “Aerodynamic Modelling of Unmanned Aerial System through Nonlinear Vortex Lattice Method, Computational Fluid Dynamics and Experimental Validation - Application to the UAS-S45 Bàlaam”. This paper has been submitted for publication to the *Aeronautical Journal* in September 2019. This chapter shows a procedure to design an aerodynamic model for the UAS-S45 Bàlaam based on a new non-linear Vortex Lattice Method. This procedure calculates the viscous forces from the strip theory, and the forces generated by the vortex rings from the vortex lifting law. The chapter also describes a CFD analysis performed on the UAS-S45. For this purpose, a FEM was firstly used to design a structured mesh for investigating the flow occurring in the airfoil boundary layer. The Reynolds Averaged Navier-Stokes (RANS) equations, in addition to a k-ω turbulence model, were then used to estimate the behaviour of the flow around the airfoil. Secondly, the overall geometry of the UAS-S45, instead of its airfoil, was analysed. An unstructured mesh was chosen for this analysis to reduce the computation time. The parameters of the mesh grid were determined using a convergence study. The Spalart-Allamaras equations were chosen as the turbulence model.

The validation of the airfoil behaviour was performed using experimental data. For this purpose, a reduced-scale model of the wing was manufactured and then tested in the Price-Païdoussis subsonic wind tunnel. The validation of the complete UAS model was carried out using the results obtained by means of the semi-empirical DATCOM and Fderivatives procedures. These comparisons revealed the accuracy of the new non-linear Vortex Lattice Method proposed.

2.5.3 The third journal paper

Chapter 5 contains the journal paper entitled “UAS-S45 Bàlaam Propeller: Improved Blade Element Momentum Methodology and Wind Tunnel Test Performance Evaluation”. This paper has been submitted for publication to the *Journal of Aerospace Engineering* in September 2019. This paper presents an improved Blade Element Momentum Method to

estimate the propeller performance of the Unmanned Aerial System UAS-S4. The methodology used a rotation effect model and a high angle of attack lift coefficient correction model to increase the accuracy of the results. In addition to Blade Element Momentum Method, a CFD analysis was also performed. The geometry was modelled using unstructured mesh. A fluid dynamics simulation was performed using the Reynolds Averaged Navier-Stokes (RANS) equations and the k-ε turbulence model. The Multiple Reference Approach (MRF) was used on ANSYS Fluent to reduce computation time, and thus to facilitate convergence with respect to other models. The validation of the obtained results was performed by comparing the data obtained through the CFD analysis and the blade elements theory with experimental data obtained in the wind tunnel. The paper also presents the design methodology of the test bench and the experimental procedure.

2.5.4 The fourth journal paper

Chapter 6 presents the journal paper "Low-Order Robust Controller for Stabilization, Tracking and Disturbance Rejection of the Unmanned Aerial System UAS-S45 Bálaam". This paper has been submitted for publication to the *Aeronautical Journal* in September 2019. This chapter shows a novel procedure to design an UAS-S45 controller able to reject unknown and random environmental effects while guaranteeing the best performance. The procedure considered a composite controller combining a feedback Linear Quadratic Regulators (LQR) system for stability augmentation, and a Proportional Integral controller with reference feedforward compensation for tracking improvement. A Generalized Extended State Observer (GESO) was implemented for disturbance rejection and to provide robustness to the closed loop system. Furthermore, a gain scheduling method was performed to obtain the controller parameters for certain unknown trim conditions within a given flight domain. The gain scheduling method was based on an Adaptive Neuro-Fuzzy Inference System (ANFIS). The results showed the proposed procedure was highly efficient and required minimum effort on the control input.

CHAPITRE 3

MODELING NOVEL METHODOLOGIES FOR UNMANNED AERIAL SYSTEMS – APPLICATIONS TO THE UAS-S4 EHECATL AND THE UAS-S45 BÁLAAM

Maxime Alex Junior Kuitche, Ruxandra Mihaela Botez
LARCASE Laboratory of Applied Research Active Controls,
Avionics and AeroServoElasticity,
Ecole de Technologie Supérieure, 1100 Notre Dame West,
Montreal, H3C1K3, Québec, Canada

Article publié dans le *Chinese Journal of Aeronautics*, en Janvier 2019,
Special edition for issue for CJA 30th anniversary, Volume 32, Issue 1, DOI :
10.1016/j.cja.2018.10.012

Résumé

La demande croissante de systèmes aériens sans pilote (UAS) pour effectuer des tâches dans des environnements hostiles a mis en évidence la nécessité de disposer de modèles de simulation pour les évaluations préliminaires de leurs missions. L'efficacité d'un modèle d'un UAS est directement liée à sa capacité à estimer sa dynamique de vol avec un minimum de ressources de calcul. La littérature décrit plusieurs techniques permettant d'estimer une dynamique de vol précise. La plupart d'entre eux sont basés sur l'identification des systèmes. Cet article présente une méthodologie alternative pour obtenir un modèle complet des systèmes aériens sans pilote S4 et S45. Les modèles des UAS-S4 et UAS-S45 ont été divisés en quatre sous-modèles, chacun correspondant à une discipline spécifique: aérodynamique, propulsion, masse et inertie et actionneur. Le sous-modèle « aérodynamique » a été construit en utilisant le code, fait-maison, Fderivatives, qui est une amélioration de la procédure classique DATCOM. Le sous-modèle « propulsion » a été obtenu en associant un modèle de moteur à deux temps, basé sur le cycle idéal d'Otto et sur une analyse de la théorie des éléments de pale (BET) de l'hélice. Le sous-modèle « masse et inertie » a été conçu en utilisant les méthodologies de Raymer et DATCOM. Un sous-modèle d'actionneur, qui utilise les caractéristiques du servomoteur, a été ajouté pour compléter le modèle. Le modèle global a

ensuite été vérifié en validant chaque sous-modèle avec des données numériques et expérimentales. Les résultats indiquent que le modèle obtenu était précis et pouvait être utilisé pour concevoir un simulateur de vol.

Abstract

The rising demand for Unmanned Aerial Systems (UASs) to perform tasks in hostile environments has emphasized the need for their simulation models for the preliminary evaluations of their missions. The efficiency of the UAS model is directly related to its capacity to estimate its flight dynamics with minimum computational resources. The literature describes several techniques to estimate accurate aircraft flight dynamics. Most of them are based on System Identification. This paper presents an alternative methodology to obtain complete model of the S4 and S45 Unmanned Aerial Systems. The UAS-S4 and the UAS-S45 models were divided into four sub-models, each corresponding to a specific discipline: aerodynamics, propulsion, mass and inertia, and actuator. The "aerodynamic" sub-model was built using the Fderivatives in-house code, which is an improvement of the classical DATCOM procedure. The "propulsion" sub-model was obtained by coupling a two-stroke engine model based on the ideal Otto cycle and a Blade Element Theory (BET) analysis of the propeller. The "mass and the inertia" sub-model was designed utilizing the Raymer and DATCOM methodologies. A sub-model of an actuator using servomotor characteristics was employed to complete the model. The total model was then checked by validation of each sub-model with numerical and experimental data. The results indicate that the obtained model was accurate and could be used to design a flight simulator.

3.1 Introduction

During recent years, interest in Unmanned Aerial Systems (UAS) has shown an enormous growth in both military and civil aviation. The increased demand has led engineers and designers to search for methods to improve flight performance (Liu *et al*., 2017), especially for long endurance reconnaissance and intelligence missions. However, the validation of a

performance improvement technique requires a high number of flight tests, which can be very demanding in terms of both time and money. A high-level simulation model provides an alternative solution, allowing engineers to perform numerical calculations to test new aircraft designs or any modifications to existing ones in a simulation environment (Kamal *et al*., 2016).

Designing a model or realizing an aircraft simulator may, under certain conditions, result in aberrant results, including numerical instability due to the successive error increases. To cope with this difficulty, the aircraft model is divided into sub-models. The general model of the aircraft depends on its geometry, its systems and the environmental factors. Therefore, its overall architecture is composed of aerodynamics, propulsion and actuation systems, as well as its mass and inertia. Thus, the modelling procedure for an aircraft is a collection of methods for estimation of each sub-model. Several studies have been conducted to examine this methodology.

Jodeh *et al.* (2006) developed a nonlinear simulation model to estimate the flight dynamics of the Rascal 110, with its aerodynamic model designed using the DATCOM procedure. The propeller model was based on the airfoil characteristics while the engine model consisted of a linear lookup table. The mass and inertia analyses were conducted by the experimental pendulum method. Al-Radaideh designed and built a test bed for the ARF60 AUS-UAV (Al-Radaideh *et al*., 2009). The model was constructed under Simulink using Aerosim and Aeroblockset to facilitate the flight control system development. The aerodynamics was modelled using linear estimation based on the aircraft's geometry. The propulsion model used a transfer function with the throttle command as input, and the RPM of the engine and the thrust produced by the propeller as outputs. This model was used to test autopilot behaviour. The results have shown that the outputs were very close to the command values.

A procedure to model small unmanned vehicles at high angles of attack was presented by Selig (2014). This methodology was developed for UAV/Radio-controlled aircraft. The UAV/RC was divided into basic components, such as wing, horizontal tail and vertical tail, in order to evaluate their interaction effects. The aerodynamic analysis was performed using strip theory while the propeller model was estimated from Blade Element Momentum Theory using

PROPID code (Selig, 2012). The aircraft model was implemented in the Flight Simulator FS-1 to determine its flight dynamics at stall condition.

Elharouny *et al*. (2012) provided a procedure for modelling small UAV. This procedure was applied on a Sky Raider Mach 1. The aerodynamic modelling was performed by coupling Xfoil (Drela, 1989) to determine the airfoil aerodynamics characteristic and DATCOM to estimate the overall aerodynamic model of the UAV. The propulsion model consisted of evaluating the thrust performance of the UAV. It was estimated experimentally using a spring scale to measure the thrust force along with a set of throttle command and incoming wind speed. The moment of inertia and the center of gravity were obtained from a pendulum method while the mass was determined using a balance. The resulting model was used for control design tasks.

Kamal *et al*. (2016) presented a flight simulation model for a small commercial off-the-shelf Radio-Controlled UAV, the "tiger Trainer". The structural model consisted in determining the mass, the center of gravity and the moment of inertia of the UAV. The mass was obtained using an accurate digital scale and the center of gravity was estimated from a moment balance about the nose wheel. The pendulum method was thus applied to experimentally evaluate the UAV moment of inertia. The propulsion system consisted of a piston-propeller engine. The propulsion modelling was separated into the propeller analysis and the engine dynamic estimation. The propeller analysis was performed experimentally in a low speed wind tunnel to measure thrust and power performance from static condition to windmill regime. The engine dynamic was built from a black box using pulse on the throttle as input and engine rotation speed as output. The aerodynamic characteristics were obtained, in the first step, by analysing the similarity of the wing airfoil with conventional airfoil as Clark-Y. In the second step, DATCOM was used to obtain aerodynamic behaviour of the entire UAV. The actuator was modelled from an identification process on a servomotor. This methodology required a time history of the rotational angle of the servomotor as function of a signal inputs which were measured experimentally. The complete six DoF nonlinear model of the UAV was assembled using MATLAB/SIMULINK. The model was verified, for a horizontal steady flight, on its longitudinal and lateral dynamic. The results showed a good agreement with the experimental flight test.

RAYMER (1979) developed a code called RDS, dedicated to the development and analysis of aerospace vehicles. It contained a sizing code based on Roskam (Roskam, 1985a, 1985b, 1998) and features analysis modules for the aerodynamics, mass and inertia and propulsion models. The program was applied on a STOVL jet aircraft (Raymer et McCrea, 2010). Aerodynamic behaviour was estimated using classical techniques from (Roskam, 1985a), while the drag, the maximum lift and the control derivatives were estimated using the DATCOM procedure (Williams et Vukelich, 1979). The mass and inertia properties were obtained using a statistical method based on the type of aircraft and were further adjusted based on the aircraft composite materials and systems. The propulsion models were estimated from a default engine data on which corrections were applied. These corrections were defined as the differences between the reference and the actual inlet recovery pressure, the actual bleed coefficient, and the installed inlet drag.

The Systems Engineering and Aircraft Design Group of Delft University of Technology developed a knowledge-based design software called the Design Engineering Engine (DEE) (Rocca et Tooren, 2009) . The software includes a tool, the Flight Mechanics Model (FMM), which analyses the flight dynamics of an aircraft. The FMM combines sub-models for aerodynamics, structure and propulsion analysis into one single aircraft model. These sub-models are physical-based or empirical. The DEE has been used in several academic and industrial research projects. In the European project MOB (Multidisciplinary Optimisation of a Blended wing-body), the DEE was used to achieve a distributed computational design framework for the multidisciplinary design and optimisation of a blended wing-body freighter (Morris, 2002) . The Tail Optimization and Redesign in a Multi Agent Task Environment (TAILORMATE) project (Cerulli *et al.*, 2006 ; Schut and Tooren, 2007) a collaboration project with Airbus, used the DEE software for the fully automatic redesign of the vertical tail of a large passenger aircraft.

The Simulating Aircraft Stability And Control Characteristics for Use in Conceptual Design (SimSAC) (Rizzi, 2011) project was a FP6 European project with the aim of developing a tool for modelling and simulating aircraft stability and control. The Computerized Environment for Aircraft Synthesis and Integrated Optimization Methods, CEASIOM was the resulting software of this project. CEASIOM is a framework tool that integrated multi-discipline

methods dedicated to the modelling and the analysis of fixed-wing aircraft. CEASIOM contains 8 significant modules: The Aircraft Builder (AcBuilder) and the Surface Modeller (SUMO) allows to build geometry for aerodynamic calculation. These tools can generate surface and volume mesh useful for CFD analysis. The weight and balances module estimates the mass the inertia and the position of the center of gravity using the geometry data of the aircraft. Four methods are provided to estimate mass and inertia: the Howe (2000), Torenbeek (2013), Raymer (1989) and the DATCOM methods. The Aerodynamic Model Builder module combines computational, analytical and semi-empirical methods to obtain the aerodynamic model of the aircraft. Depending on the accuracy needed, the user can choose between low cost methods as DATCOM and Vortex Lattice Method, and time demanding methods as Euler and Reynolds Averaged Navier-Stokes (RANS) analysis, to perform aerodynamics calculation. The Next generation Aero-Structural Sizing (NeoCASS) module perform an aero-structural analysis by giving a complete understanding of aerodynamic, structure and aero elastic interaction for several flight conditions. The propulsion module uses the thrust data as a function of Mach number and altitude to construct a propulsion database useful for stability and control analysis. The Simulation and Dynamic Stability Analyser (SDSA) module provides stability analysis with eigenvalues estimation of the linearized model and it also provides a six degree of freedom flight simulation. The Flight Control System Design Toolkit (FCSDT) is useful to design a Stability Augmentation System (SAS) and a flight control system based on a LQR approach. These modules generate enough data to build a six Degree of Freedom flight simulator. The Ranger 2000 trainer was modelled using CEASIOM (Rizzi, 2011) to study the rudder free effect at low attitude and speed when a lateral gust is encounter. The results show that at low attitude and speed, the oscillation of the rudder and the sideslip cannot be damped by the yaw rate. Thus, the aircraft loses altitude until it crashes. These results were confirmed by experimental flight tests.

Table 3.1 shows the different aircraft modelling procedures and the corresponding methodologies. This paper describes a procedure for modelling the both Unmanned Aerial System UAS-S4 and UA-S45, designed and manufactured by Hydra Technologies. They provide surveillance and security capabilities for military and civilian purposes (Sugar Gabor,

2015). General information regarding the UAS-S4 and the UAS-S45 is presented in Tables 3.2 and 3.3, respectively, and Figures 3.1 and 3.2 show their respective images.

Table 3.1 Aircraft modelling methods.

Reference	**Aircraft**	**Method**			
		Aerodynamic	**Propulsion**	**Structure**	**Actuator**
Jodeh (N. M. Jodeh, 2006)	Rascal 110	DATCOM	Airfoil analysis	Pendulum	
Al-Radaideh et al. (Al-Radaideh et al., 2009)	ARF60 AUS-UAV	Linear estimation from aircraft geometry	1st order transfer function	Pendulum	
Selig (Selig, 2014)	UAV/RC	Strip theory	BET		
Elharouny et al. (Elharouny et al., 2012)	Sky Raider Mach 1	Xfoil, DATCOM	Experimental measurement	Balance measurement, pendulum	
Kamal et al. (A. M. Kamal et al., 2016)	Tiger Trainer	Airfoil analysis, DATCOM	Wind tunnel test, black box identification	Balance measurement, pendulum	Black box identification
Raymer and McCrea (Raymer & McCrea, 2010)	STOVL Jet Aircraft	Roskam, DATCOM, VLM	Default engine corrected	Statistical	
Rizzi (Rizzi, 2011)	General Aircraft	DATCOM, VLM, RANS, EULER	Interpolation from database	Howe, Torenbeek, Raymer, DATCOM	

Table 3.2 General Characteristics of the UAS-S4

Specification	Value
Wing span (m)	4.2
Wing area (m^2)	2.3
Total length (m)	2.5
Mean aerodynamic chord (m)	0.57
Empty weight (kg)	50
Maximum take-off weight (kg)	80
Loitering airspeed (knots)	35
Maximum speed (knots)	135
Service ceiling (ft)	15000
Operational range (km)	120

Table 3.3 General Characteristics of the UAS-S45

Specification	Value
Wing span (m)	6.11
Wing area (m^2)	2.72
Total length (m)	3.01
Mean aerodynamic chord (m)	0.57
Empty weight (kg)	57
Maximum take-off weight (kg)	79.6
Loitering airspeed (knots)	55
Service ceiling (ft)	20000
Operational range (km)	120

Figure 3.1 Hydra technologies UAS-S4 Ehecatl

Figure 3.2 Hydra technologies UAS-S45 Bàlaam

In this paper, the architecture of each UAS integrates sub-models to evaluate the aerodynamics, propulsion, actuation, the mass and inertia. The aerodynamic sub-model was obtained with Fderivatives code, an improvement of the DATCOM procedure. This code was developed in-house at our Research Laboratory in Active Controls, Avionics and Aeroservoelasticity (LARCASE) of the ETS. Its main advantage is related to the need of a minimum number of geometrical data to estimate the aircraft aerodynamic coefficients and their corresponding stability derivatives (Anton *et al.*, 2011) . The aerodynamic coefficients of each UAS, obtained using Fderivatives code, were compared with those calculated with the DATCOM procedure, the Vortex Lattice Method (VLM) on TORNADO and the Computational Fluid Dynamics (CFD) (Hua *et al.*, 2018) analysis on ANSYS Fluent.

The propulsion sub-model was obtained by coupling two-stroke engine modelling and a numerical analysis of the propeller. The two-stroke model is based on the Otto cycle thermodynamic equation, and on the geometrical characteristics of the engine. The torque produced by the engine as well as the fuel consumption and the rotation speed of the crankshaft were determined. The propeller analysis estimated the thrust and propeller efficiency as a function of the advance ratio from an in-house blade element theory code. The two-stroke engine model was compared to the manufacturer's data, and the propeller analysis was compared to a CFD analysis on ANSYS Fluent.

Each UAS model was completed with the sub-model of an actuator. Each actuator is a servomotor; therefore, a controlled DC motor was used for its modelling. The structural sub-model was calculated using the Raymer and the DATCOM methodologies. The aerodynamic sub-model is explained in Section 3.2, the propulsion sub-model in Section 3.3, the actuator sub-model in Section 3.4, and the structural model in Section 3.5. Results are given in Section 3.6 and are followed by a conclusion section. Results have been validated using different modelling and simulation approaches including experimental data (for actuator and structure) for-each sub-model of the UAS.

3.2 Aerodynamic sub-model

The aerodynamic sub-model deals with the estimation of an aircraft's aerodynamic behaviour. To accurately predict the aerodynamic forces and moments that act on an aircraft in flight, it is necessary to describe the pattern of flow around the aircraft configuration (Bertin and Smith, 1998).

The DATCOM procedure is one of the best collections of semi-empirical equations for aerodynamic coefficients and stability derivative calculations. This tool is used for the evaluation of aerodynamic coefficients for preliminary aircraft design, and provides equations for various aircraft configurations and flight regimes (Anton *et al.*, 2009b). The calculation method used in DATCOM is based on the summation of the contributions of all of an aircraft's components along with their interaction effects. Although the DATCOM procedure can create a good aerodynamic model, it also presents some weaknesses. This procedure does not provide

a methodology for estimating the zero-lift angle of attack or the zero-lift pitch moment for an airfoil or for an asymmetrical fuselage. The procedure does not take into account the aerodynamic twist of the wing in the calculation of the lift-curve slope of the wing. In addition, the contribution of the engine nacelles is neglected.

In this context, our LARCASE team at ETS has developed a new code called Fderivatives. Fderivatives contains new equations and methods that have been added to DATCOM's classical procedure to improve the aerodynamic coefficients and stability derivative calculation for flying subsonic regime (Anton *et al*., 2010, 2011 ; Anton *et al*., 2009a, 2009b).

3.2.1 Fderivatives' improvements

Fderivatives is an in-house code designed as a collection of semi-empirical methodologies for determining aerodynamic coefficients and stability derivatives. The code includes a number of procedures such as those in DATCOM, with improvements in both the theoretical equations and in calculation methodologies. All of the improvements and the description of the code are given in (Anton *et al.*, 2010, 2011 ; Anton *et al.*, 2009a, 2009b ; Popescu, 2009). The main improvements proposed in the Fderivatives code with respect to the DATCOM procedure are realised in the calculation of the airfoil lift-curve slope $c_{L\alpha}$, the zero-lift angle of attack α_0 and the zero-lift pitch moment c_{m0}, in the zero-lift angle of attack α_{0f}, for an asymmetrical fuselage, and in the maximum lift coefficient of the wing $C_{L\max.}$

3.2.1.1 Lift-curve slope, zero lift angle of attack and zero lift pitching moment of airfoil

The lift-curve slope of the airfoil, $c_{L\alpha}$, is one of the most important parameters for the calculation of an aircraft's aerodynamic coefficients. In Fderivatives, the lift-curve slope (lift coefficient derivative with respect to α) is estimated for an ideal flow, and then is corrected for viscous and compressible flow conditions.

$$c_{L\alpha} = \frac{1.05}{\beta_{PG}}\left[\frac{c_{L\alpha}}{(c_{L\alpha})_{theory}}\right](c_{L\alpha})_{theory} \tag{3.1}$$

where $(c_{L\alpha})_{\text{theory}}$ is the lift-curve slope of the airfoil for inviscid and incompressible flow. Then,

$$\left(c_{L\alpha}\right)_{theory} = 6.28 + 4.7\left(\frac{t}{c}\right)_{max}\left(1 + 0.00375\Phi_{TE}\right) \tag{3.2}$$

where $\left(\frac{t}{c}\right)_{\max}$ is the maximum thickness of the airfoil, and Φ_{TE} is the trailing edge angle calculated in degree.

The following factors are incorporated to correct for the compressible and viscous flow conditions:

β_{PG} is the Prandtl-Glauert correction factor for compressible flow, and it depends upon the Mach number *Ma* according to the following expression:

$$\beta_{PG} = \sqrt{1 - Ma^2} \tag{3.3}$$

$\frac{c_{l\alpha}}{(c_{l\alpha})_{\text{theory}}}$ is a correction factor for viscous flow that is a function of the Reynolds number *Re* and of the trailing edge geometry of the profile (Kinsey and Bowers, 1971):

$$\frac{c_{l\alpha}}{\left(c_{l\alpha}\right)_{theory}} = 1 - \left(ln\frac{Re}{10^5}\right)^n\left[0.232 + 1.785tan\left(\frac{\Phi_{TE}}{2}\right) - 2.95tan^2\left(\frac{\Phi_{TE}}{2}\right)\right] \tag{3.4}$$

where the term *n* can be found with:

$$n = -1 + \frac{5}{2}tan\left(\frac{\Phi_{TE}}{2}\right) \tag{3.5}$$

The zero lift angle of attack α_0 and the zero lift pitching moment c_{m0} are obtained by utilizing the theory developed by Pankhurst (Pankhurst, 1944) . Pankhurst established a calculation procedure in which α_0 and c_{m0} are written as linear combinations of their values of the y-axis Z_e values of an airfoil's upper surface, and of the Z_i values of its lower surface. The parameters Z_e and Z_i correspond to a finite number of chosen points.

$$\begin{cases} \alpha_0 = -\sum_j A_j \left(Z_e + Z_i\right)_j \\ c_{m0} = -\sum_j B_j \left(Z_e + Z_i\right)_j \end{cases} \tag{3.6}$$

where A_j and B_j are correlation coefficients depending on their x-axis values on the chord (Anton et al., 2010 ; Popescu, 2009). The compressibility, and the Reynolds number effects on the zero lift angle of attack α_0 and on the zero lift pitching moment c_{m0} are neglected as specified in (Jacobs, 1933).

3.2.2 Maximum lift coefficient of the wing

Derivatives code uses two methods to estimate a wing's maximum lift coefficient, depending on the type of the wing.

In the "first" method, for a constant airfoil configuration, the wing is divided into ten sections. For each section, a lift coefficient distribution is calculated thereby allowing its non-linear twisted wing values to be taken into account (Anton *et al*., 2011). The maximum lift coefficient of the airfoil, $c_{L\max}$, is calculated in the section where the lift coefficient has the highest value. The equation developed by Phillips and Alley (2007) is then used:

$$C_{L\max} = \left(\frac{c_l}{c_{l\max}} \right)_{\substack{\theta=0 \\ \Lambda=0}} k_{L\Lambda} \left(c_{l\max} - k_{L\theta} C_{L\alpha} \theta \right) \tag{3.7}$$

where θ is the twist of the wing, Λ is the sweep angle of the wing, $k_{L\Lambda}$ and $k_{L\theta}$ are respectively the sweep and the twist correction factor, $c_{L\max}$ is the maximum lift coefficient of the airfoil calculated in the section where the lift coefficient has the highest value, $C_{L\alpha}$ is the lift-curve slope of the wing, and $\left(\frac{c_l}{c_{l\max}}\right)_{\substack{\theta=0 \\ \Lambda=0}}$ is a correction factor of the maximum lift coefficient for unswept and untwisted wing sections.

In the "second" method, for a wing whose airfoil changes along the span, Roskam's method (Roskam, 1985a, 1998) is applied. The maximum lift coefficient of the wing is assumed to be proportional to the average of maximum lift coefficient of the airfoil at the tip and at the root of the wing:

$$C_{L_{max}} = f\cos(\Lambda_{c/4})\left(\frac{\left(c_{L_{max}}\right)_{tip} + \left(c_{L_{max}}\right)_{root}}{2}\right) \tag{3.8}$$

where $(c_{L\max})_{tip}$ and $(c_{L\max})_{root}$ are the maximum lift coefficients of the airfoil at the tip and at the root of the wing, $\Lambda_{c/4}$ is the quarter chord sweep angle, and f is a correction coefficient dependent upon the taper ratio r:

$$f = -0.117r + 0.997 \tag{3.9}$$

3.2.2.1 Zero-lift angle of attack of an asymmetrical fuselage

The procedure to estimate the zero lift angle of attack, α_{0f}, is based on the thin airfoil theory. Jacobs (1933) proposed an equation for the determination of α_{0f} by using the mean camber line:

$$\alpha_{0f} = \int_0^l \frac{\xi(x)}{l} f\left(\frac{x}{l}\right) \tag{3.10}$$

where

$$f\left(\frac{x}{l}\right) = -\frac{1}{\pi}\frac{1}{\left(1-\frac{x}{l}\right)\sqrt{\frac{x}{l}-\left(\frac{x}{l}\right)^2}} \tag{3.11}$$

In Equation (3.10) and Equation (3.11), l is the length of the fuselage, x is the position on the mean camber line, and $\xi(x)$ is the mean camber line defined by:

$$\xi(x) = \frac{1}{2}\left[Z_i(x) + Z_e(x)\right] \tag{3.12}$$

Therefore, the fuselage can be replaced by a body of revolution with the same longitudinal distribution of the section as the original one (Whitcomb, 1952).

3.2.3 Fderivatives' logical scheme description

Fderivatives' graphical interface, produced at the LARCASE, ETS, allows users to calculate the aircraft stability from its geometrical data (Anton *et al*., 2011). Its main window with its sub-windows is presented in Figure 3.3. The Fderivatives code's logical scheme is given in two steps, as illustrated in Figure 3.4. The first step regards the selection of the aircraft configuration (Wing (W), Wing-Body (WB) or Wing-Body-Tail (WBT)), the type of planform (straight-tapered or non-straight tapered wing), and the flight conditions (altitude, Mach number and angle of attack) (Anton *et al*., 2009b). For each aircraft configuration, following parameters are needed: area, aspect ratio, taper ratio, and sweepback angle, for the wing, the horizontal and vertical tails, as well as their respective airfoil. The code also takes as inputs, the airfoil coordinates of the root, the tip and the mean aerodynamic chords as wells as the parameters for the fuselage and nacelle.

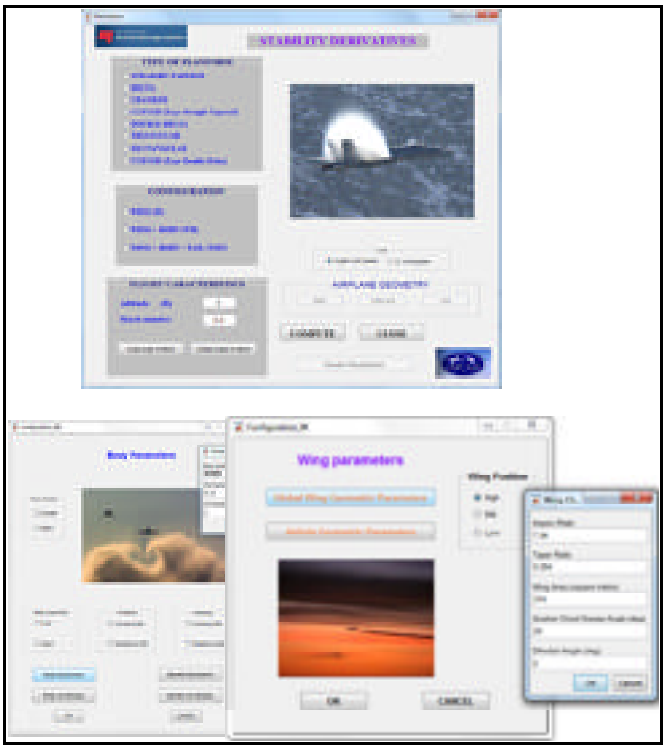

Figure 3.3 Main window and sub-windows
of Fderivatives code

Estimating the aerodynamic coefficients and the stability derivatives for a specific flight condition is the second step in the Fderivatives code. For each UAS, the wing-body-tail configuration was selected as the best one among the possible combinations (wing, wing-tail etc.) with the aim to obtain reliable results. The aerodynamic model was designed to analyse or to modify each component of the UAS separately, and their interactions effects. Therefore, each UAS will be divided into 5 components: the "Wing-Body", the "Tail", the "control surface", the "propulsion" and the “ground-effect” as shown in Figure 3.5. The Fderivatives code does not calculate the control surface derivatives, the ground and the propulsion effects. Therefore, these contributions were estimated using the DATCOM methodology (Williams and Vukelich, 1979).

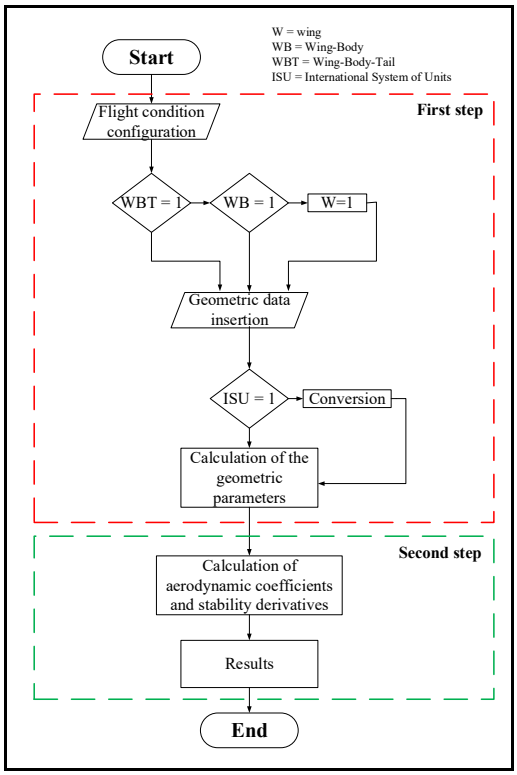

Figure 3.4 Logical scheme of Fderivatives code

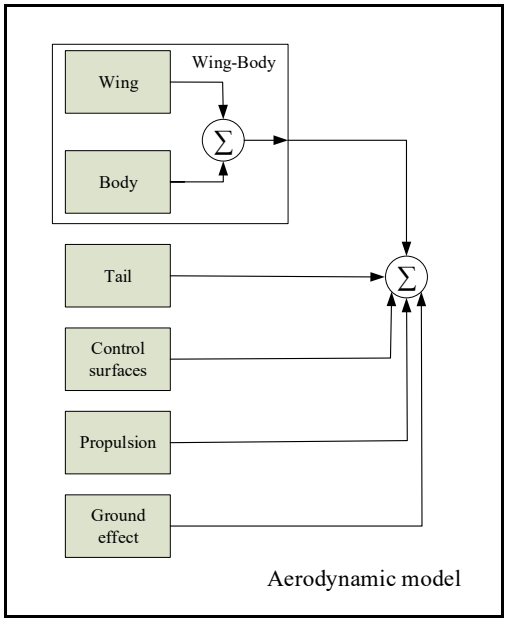

Figure 3.5 UAS aerodynamic model design

3.2.4 VLM using TORNADO code

The VLM is a numerical method to estimate flow dynamics around a generating lift surface. It is an effective method to solve problems of incompressible, irrotational and inviscid flows (Kuitche and Botez, 2017). The VLM is based on the lifting line surface theory. The lifting surfaces are modelled by a zero-thickness solid surface and represented by a grid on which horseshoe vortexes are superimposed at a control point (75% of the chord) (see Figure.3.6).

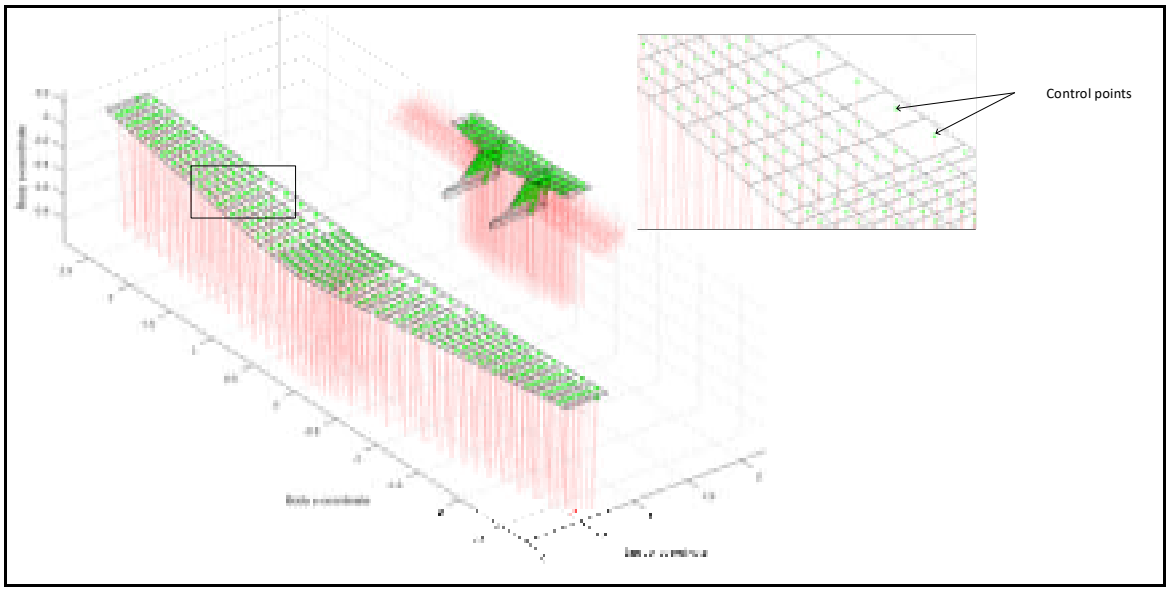

Figure 3.6 Panels and controls points modelling using the VLM

Because of the fact that each panel of the grid is considered as “planar”, the Biot-Savart law can be applied to calculate the velocity induced by each horseshoe(Şugar Gabor *et al*., 2016), with :

$$V = \frac{\Gamma}{4\pi} \frac{\boldsymbol{r}_1 \times \boldsymbol{r}_2}{\left|\boldsymbol{r}_1 \times \boldsymbol{r}_2\right|^2} \left[\boldsymbol{r}_0 \left(\frac{\boldsymbol{r}_1}{\left|\boldsymbol{r}_1\right|} - \frac{\boldsymbol{r}_2}{\left|\boldsymbol{r}_2\right|} \right) \right] \tag{3.13}$$

where Γ is the vortex intensity, $\boldsymbol{r}_1$ and $\boldsymbol{r}_2$ are the vectors from the starting and the ending points of the vortex segment to the random point in space, $\boldsymbol{r}_0$ is the vector along of the vortex segment.

For each of the control points in the lattice, the velocities induced by the other panels are summed, leading to a set of equations for the horseshoe vortex (located at the control point), that satisfies the boundary condition of "no flow through the wing" (Bertin and Smith, 1998). The local velocities calculated by these equations are used to further compute the pressure difference between the upper and lower surfaces of the airfoil. The integration of these pressures leads to the aerodynamics forces and moments.

The TORNADO code was used to apply the VLM to the UASs. TORNADO software is useful for research, education and teaching purposes. It uses VLM to model subsonic potential flow around a lifting surface. The general equations used in TORNADO code were developed by Moran (Moran, 1984). Since TORNADO computes inviscid flow equations, it does not model the boundary layer. Therefore, the code does not provide the skin friction component of the drag coefficient. In addition, since TORNADO uses a planar approximation of lifting surfaces, it does not take into account the aerodynamic contributions of an aircraft's fuselage.

3.2.5 CFD methodology with ANSYS Fluent

The CFD analysis in ANSYS Fluent was performed to obtain the aerodynamic sub-model of the UASs. In ANSYS Fluent, the fluid dynamics respects the fundamental principles of mass, momentum and energy conservation that are expressed through the Navier-Stokes equations. For the turbulent flows, the flow variables were decomposed into their time-average values and their fluctuating components. The Reynold stress tensor and the turbulent heat flux terms were related to the average flow variables using the Boussinesq eddy-viscosity hypothesis (Şugar Gabor *et al,* 2016). These assumptions lead to the following RANS equations:

$$\frac{\partial \rho}{\partial t} + \frac{\partial}{\partial x_j}\left(\rho U_j\right) = 0 \tag{3.14}$$

$$\frac{\partial}{\partial t}(\rho U_i)+\frac{\partial}{\partial x_j}(\rho U_j U_i)=-\frac{\partial P}{\partial x_i}+\frac{\partial}{\partial x_i}\left[\mu_{eff}\left(\frac{\partial U_i}{\partial x_j}+\frac{\partial U_j}{\partial x_i}\right)-\frac{2}{3}\mu_{eff}\frac{\partial U_k}{\partial x_k}\delta_{ij}\right] \tag{3.15}$$

$$\frac{\partial}{\partial t}(\rho H)-\frac{\partial P}{\partial t}+\frac{\partial}{\partial x_j}(\rho U_j H)=\frac{\partial}{\partial x_j}\left[\lambda\frac{\partial T}{\partial x_j}+\frac{\mu_t}{Pr_t}\frac{\partial h}{\partial x_j}\right]+\frac{\partial}{\partial x_j}\left\{U_i\left[\mu_{eff}\left(\frac{\partial U_i}{\partial x_j}+\frac{\partial U_j}{\partial x_i}\right)-\frac{2}{3}\mu_{eff}\frac{\partial U_k}{\partial x_k}\delta_{ij}\right]+\mu\frac{\partial k}{\partial x_j}\right\} \tag{3.16}$$

where ρ is the fluid density, U_i are the velocity components, P is the static pressure, μ_{eff} is the effective viscosity, which is the sum of the molecular viscosity μ and the turbulent viscosity μ_t, H is the total enthalpy, T is the fluid temperature, δ_{ij} is the Kronecker delta function, λ is the thermal conductivity, Pr_{t} is the turbulent Prandtl number, h is the static enthalpy and k is the turbulent kinetic energy.

The k-ω model was used as a closure of the RANS equations. This model achieves high accuracy for boundary layers with adverse pressure gradient, and can be easily integrated into viscous sub-layers without any additional damping function (Argyropoulos and Markatos, 2015 ; Menter, 1994) . Although the k-ω model has some weakness for flows with free stream boundaries, it can still give good estimation for general subsonic flows (Argyropoulos and Markatos, 2015).

The k-ω model estimates the turbulence kinetic energy k and the specific rate of dissipation ω by adding two more equations to the RANS equations (Wilcox, 2008; Menter, 1994).

$$\frac{\partial}{\partial t}(\rho k)+\frac{\partial}{\partial x_j}(\rho U_j k)=\rho P_k-\beta^*\rho\omega k+\frac{\partial}{\partial x_j}\left[(\mu+\sigma_k\mu_t)\frac{\partial k}{\partial x_j}\right] \tag{3.17}$$

$$\frac{\partial}{\partial t}(\rho\omega)+\frac{\partial}{\partial x_j}(\rho U_j\omega)=\frac{\gamma\omega}{k}P_k-\beta\rho\omega^2+\frac{\partial}{\partial x_j}\left[(\mu+\sigma_\omega\mu_t)\frac{\partial\omega}{\partial x_j}\right] \tag{3.18}$$

In Equations (3.17) and (3.18), ω is the specific rate of dissipation, P_k is the turbulent kinetic energy due to mean velocity gradients, and β, γ, σ_k, and σ_ω are the model's constants.

The CFD analysis using ANSYS Fluent was only performed on the UAS-S4. In order to use the partial differential Equations. (3.14) – (3.18), a structured and fine mesh of the UAS-S4 was performed using the ICEM-CFD software. The mesh was composed of 4424844 cells, and 4520132 nodes (Figure 3.7).

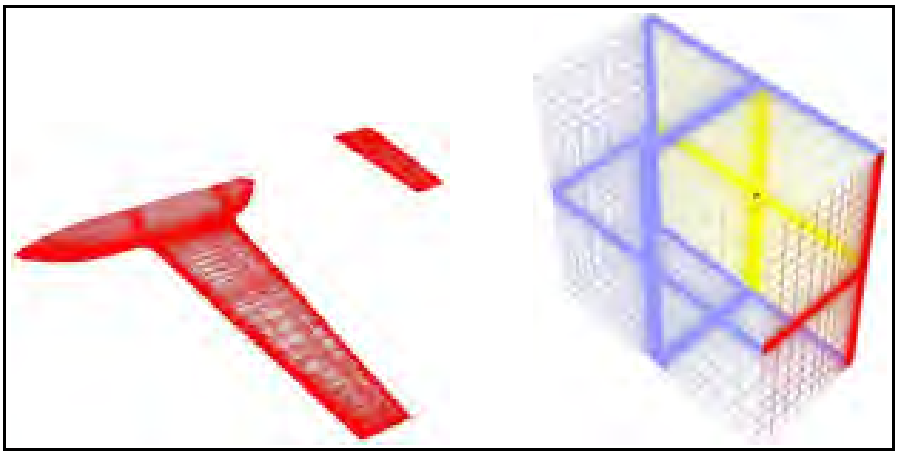

Figure 3.7 Mesh grid model of the UAS-S4 for CFD analysis in ANSYS Fluent

3.3 Propulsion system

Each of the UAS-S4 and the UAS-S45 use two propeller engines. Propellers are the most important parts of propulsion systems. Each blade of a propeller has an airfoil. Figure 3.8 shows the model proposed in order to estimate the propulsion system.

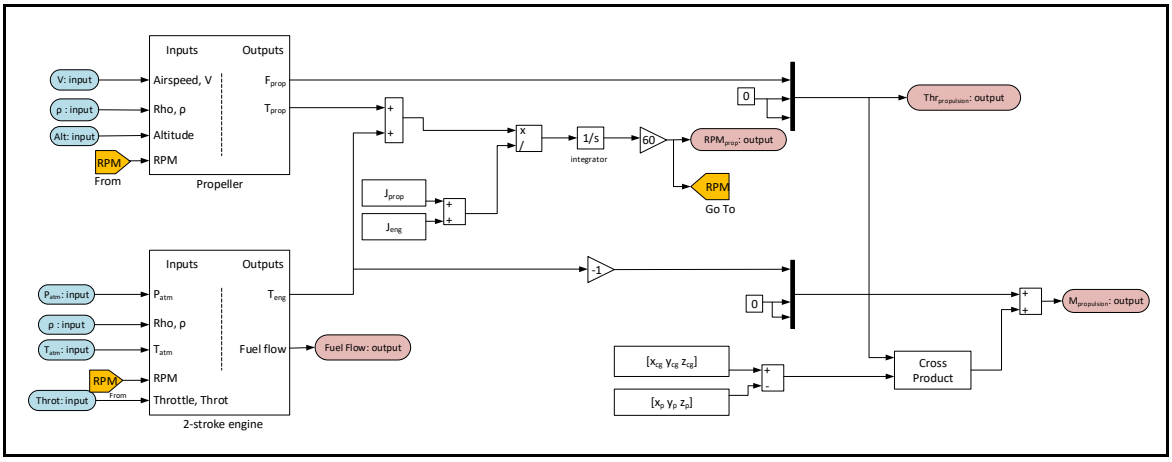

Figure 3.8 Model proposed for the propulsion system of each UAS

It is composed by two main boxes. The “2-stroke engine” box takes as inputs the atmospheric pressure and temperature, density of the air, the throttle positon and the rotational speed to estimate torque outputs produced by the engine and its fuel flow. The “propeller” box calculates the thrust and the torque outputs by using the airspeed, the rotational speed and the altitude of the flight inputs. The thrust produced by the propulsion system is the same as the thrust produced by the “propeller” box:

$$Thr_{propulsion} = F_{prop} \tag{3.19}$$

where $\mathrm{Thr}_{\mathrm{propulsion}}$ is the thrust produced by the propulsion system and F_{prop} is the thrust produced by the propeller.

The moment produced by the propulsion system is related to the torques output produced by the engine and the propeller using:

$$M_{propulsion} = \begin{bmatrix} x_{cg} - x_p \\ y_{cg} - y_p \\ z_{cg} - z_p \end{bmatrix} \times \begin{bmatrix} Q_{eng} \\ 0 \\ 0 \end{bmatrix} - \begin{bmatrix} Q_{prop} \\ 0 \\ 0 \end{bmatrix} \tag{3.20}$$

where x_{cg}, y_{cg}, z_{cg} define the 3D position of the center of gravity of the aircraft, x_p, y_p, z_p define the 3D position of the engine, Q_{eng} is the torque produced by the engine, and Q_{prop} is the torque produced by the propeller.

The rotational speed of the engine is calculated from the Newton's second law for the rotational motion:

$$RPMprop = 60\int \frac{(Q_{eng} + Q_{prop})}{(J_{eng} + J_{prop})} \tag{3.21}$$

In Equation (3.21), RPM_{prop} is the rotational speed of the propeller, J_{eng} and J_{prop} are respectively the inertia of the engine, and of the propeller.

The following sections detail the methodologies applied to determine the outputs of the propeller and the 2-stroke engine boxes.

3.3.1 Propeller analysis

The propellers' performance analyses were carried using the "blade element theory". The blade element theory is a methodology used to estimate the thrust of a propeller by dividing its blade into segments called "blade elements" (Gudmundsson, 2013a).

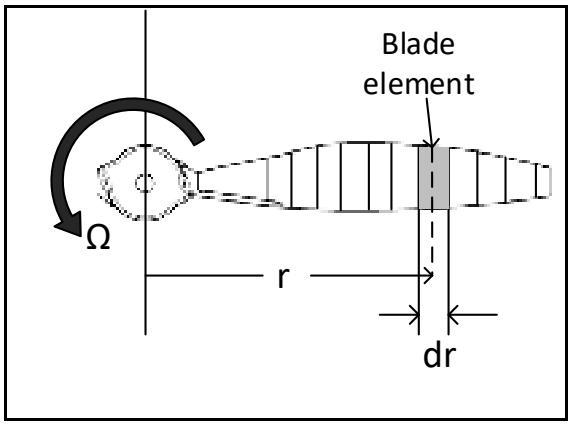

Figure 3.9 Blade element representation
used in the blade element theory

Each segment (blade element) is treated as an airfoil, for which the aerodynamic lift and drag forces are calculated according to the local flow conditions on the segment:

$$dL = \frac{1}{2}\rho V_E^2 c(r) C_l dr \tag{3.22}$$

$$dD = \frac{1}{2}\rho V_E^2 c(r) C_d dr \tag{3.23}$$

where dL and dD are the differential lift and drag forces on the blade element, $c(r)$ is the chord at the blade station r, ρ is the air density, and V_E is the effective resultant velocity which is given by:

$$V_E = \sqrt{\left(V_{in} + V\right)^2 + \left(\Omega r\right)^2} \tag{3.24}$$

where Ω is the angular velocity of the propeller and r is the distance from the hub to the blade element as seen on Figure 3.9; V is the airspeed of the aircraft and V_{in} is the induced velocity obtained from the momentum theory. C_L and C_D are respectively the airfoil lift and drag coefficients of the blade element.

Three-dimensional scanning was used to obtain the airfoil sections composing the propeller blade. The section lift and drag coefficients were then determined for a range of angles of attack from -10° to 10° and a range of Reynolds numbers from 5×10^4 to 100×10^4. These coefficients were estimated using Xfoil software (Drela, 1989), and are presented in Figure 3.10. The coefficients were evaluated for the angle of attack α:

$$\alpha = \beta - \varphi - \alpha_i + \alpha_0 \tag{3.25}$$

where β is the angle between the zero-lift line and the rotation plane, also called the pitch angle, ϕ is the helix angle, α_i is the induced angle of attack obtained from the momentum theory, α_0 is the zero-lift angle of attack of the airfoil, as seen on Figure 3.11.

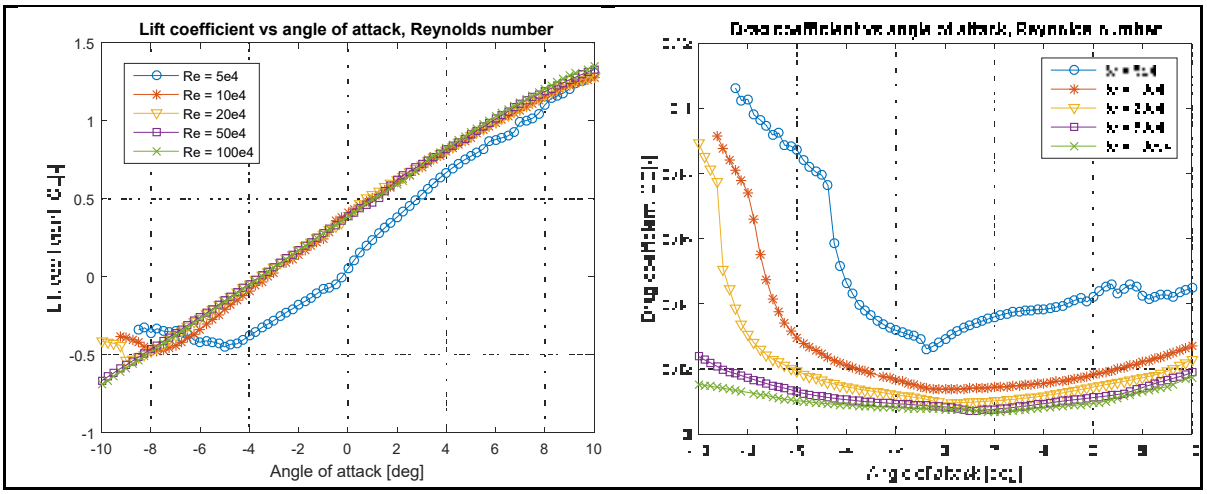

Figure 3.10 Lift and drag coefficients' variation with the angle of attack for the airfoil of the propeller

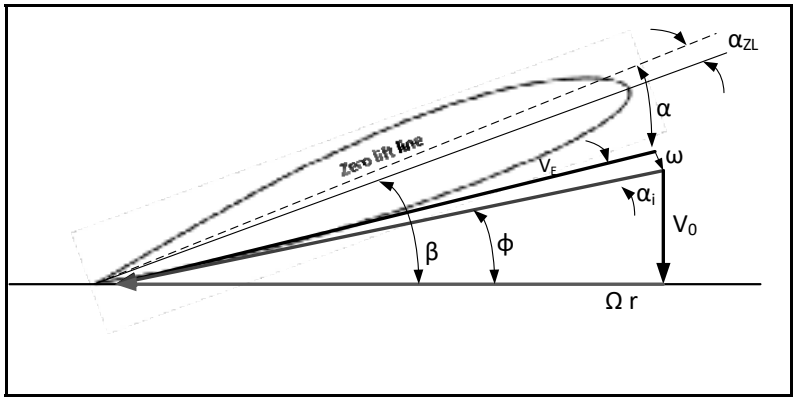

Figure 3.11 Angles and velocity of the propeller

The summation of the aerodynamic forces of each element allows to evaluate the properties of the complete propeller.

$$T = N_B \int_{R_{hub}}^{R} dL\cos(\varphi + \alpha_i) - N_B \int_{R_{hub}}^{R} dD\sin(\varphi + \alpha_i) \tag{3.26}$$

$$Q = N_B \int_{R_{hub}}^{R} r_d dL\sin(\varphi + \alpha_i) - N_B \int_{R_{hub}}^{R} r_d dD\cos(\varphi + \alpha_i) \tag{3.27}$$

where T and Q are the thrust and torque produced by the propeller, N_B is the number of blades, R is the tip radius and R_{hub} is the hub radius of the propeller. From the thrust and torque determined with Equations. (3.26) and (3.27), the thrust and torque coefficients as well as the efficiency of the propeller were obtained using the following Equations (3.28) – (3.30):

$$C_T = \frac{T}{\rho n^2 d^4} \tag{3.28}$$

$$C_Q = \frac{Q}{\rho n^2 d^5} \tag{3.29}$$

$$\eta = J \frac{C_T}{2\pi C_Q} \tag{3.30}$$

where n is the angular velocity of the propeller, d is the diameter of the propeller and J is the advance ratio expressed by Equation (3.31):

$$J = \frac{V}{nd} \tag{3.31}$$

where V is the airspeed. The thrust coefficient and the efficiency of the propeller obtained from the blade element theory were validated by comparing them with those obtained from a CFD analysis using ANSYS-Fluent (see Figure 3.12).

In the first step, the domain in which the calculations were performed was meshed. The chosen domain for the fluid flow is a cylinder, the most suitable and the most conventionally-used domain for a CFD analysis on a propeller. In order to reduce the execution time, the principle of the Multiple Reference Frame (MRF) approach was applied. This approach consists in adding a domain that rotates at the same speed as the propeller but in the opposite direction, thus a second cylinder was selected as this rotational domain. The simulation results remain the same. The real advantage of this method is that it reduces the computation time.

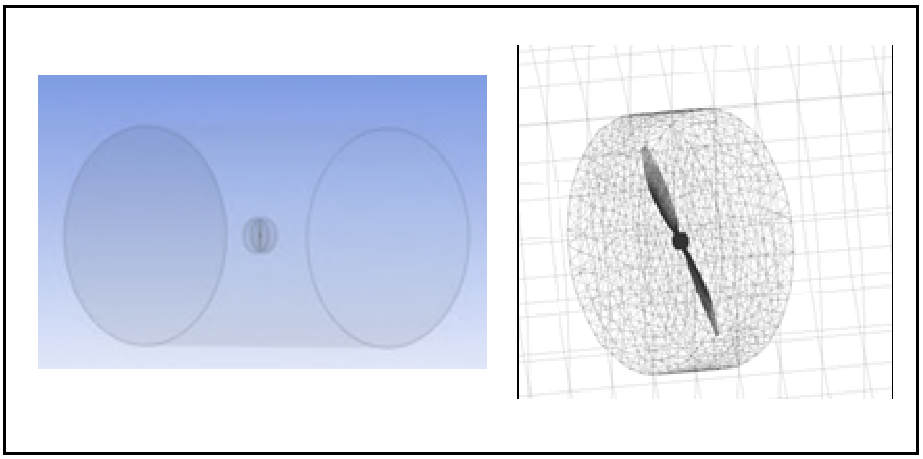

Figure 3.12 Flow domain and mesh grid of the propeller
for the CFD analysis

A structured grid with a fine sizing relevance centre was used to mesh the propeller, and the flow domain. The CFD simulation was then performed to simulate the flow past the propeller under specific flight conditions. The flow dynamics was modelled with the same Equations (3.14) – (3.16) as the flow for the UAS aerodynamic sub-model.

In the second step, the Shear Stress Transport (SST) k-ω model was used to estimate the flow around the propeller. This model has been validated, and gave good results for turbomachinery blades, wind turbines and strong adverse pressure gradients in the boundary layer due to its rotation (Argyropoulos and Markatos, 2015). Thus, the SST k-ω could be very accurate for propeller analysis, and its equations were solved using ANSYS Fluent solver.

3.3.2 2-stroke engine model

A 2-stroke engine is an internal combustion engine that produces torque or power from using a thermodynamic procedure. It is mainly composed by an inhaust system which is a carburettor, an exhaust system and a combustion chamber. The thermodynamic procedure that lead to the creation of torque happens in the combustion chamber (Figure 3.13).

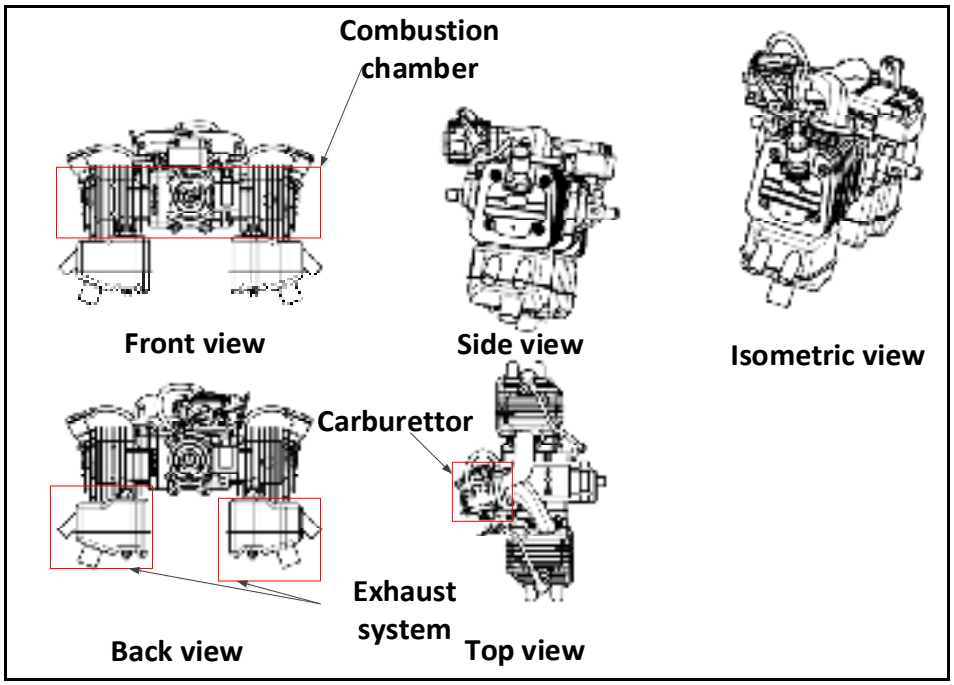

Figure 3.13 2-stroke engine description

In order to evaluate the performance of the two-stroke engine, the work produced has been separated into “ideal work” and “friction work”.

The ideal work produced per cycle was carried out on the piston by the force F created from the gas pressure p (Blair, 1996):

$$Ideal\ work\ \ per\ cyle = \int F dx = \int pA dx = \int p dV \tag{3.32}$$

where x is the distance covered by the piston and A is the piston area.

The ideal work of a two-stroke engine can be estimated from the Pressure-Volume diagram shown in Figure 3.14 as the enclosed area of the diagram corresponding to the ideal Otto cycle (Blair, 1996).

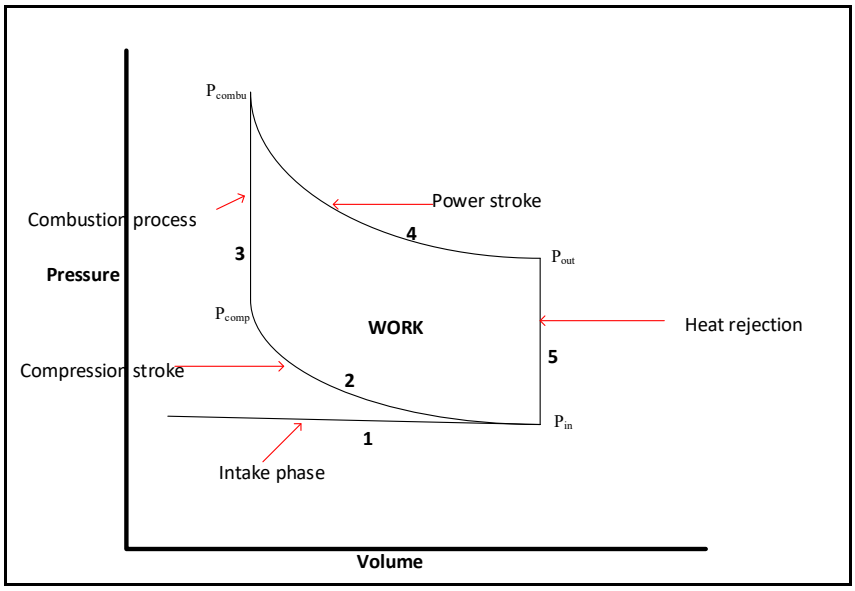

Figure 3.14 Pressure-Volume diagram for the ideal Otto cycle

The Otto cycle, shown in Figure 3.14, starts with the "intake phase" (1). The air flow passes through the carburettor where is mixed with fuel. The mix then enters into the combustion chamber to start the Otto cycle.

The pressure output of the carburettor which corresponds at the pressure at the intake phase is smaller than the atmospheric pressure depending on the admission valve opening controlled by the throttle. This pressure was estimated using:

$$P_{in} = \left[\left(P_{max} - P_{in} \right) Throt + P_{min} \right] \frac{P_0}{P_{SL}} \tag{3.33}$$

where P_{in} is the pressure at the intake phase, P_0 is the atmospheric pressure, Throt is the throttle position from 0 to 1, P_{SL} is the pressure at sea level, P_{max} and P_{min} are the maximum and the minimum pressure delivered by the carburettor that correspond to the pressure for full open throttle and closed throttle. P_{max} is equal to the pressure at the sea level and, P_{min} is obtained with:

$$P_{min} = \frac{d_{venturi}}{d_{throttle\_bore}} P_{max} \tag{3.34}$$

where d_{venturi} represents the diameter of the carburettor's Venturi, and $d_{\text{throttle\_bore}}$ is the diameter of the carburettor's throttle bore.

The mass rate of air mixture which enters in the combustion chamber is determined from:

$$\dot{m}_{air} = \rho A c = \rho A \left[\frac{2}{\gamma - 1} \left(\left(\frac{P_{in}}{P_0} \right)^{\frac{1}{\gamma}} - 1 \right) \right] \tag{3.35}$$

where A is the swept volume of the cylinder of the engine, c is the velocity of the air particle, γ is the specific heat ratio.

The second phase of the cycle is the "compression stroke" (2). The piston moves from the down position to the top position. This motion leads to the augmentation of the pressure and the reduction of the volume occupied by the air-fuel mixture. The ratio of the volume at the beginning of compression to the volume at the end of compression is called the compression ratio. It is related to the pressure and the temperature according to:

$$P_{comp} / P_{in} = r_c^{\gamma} \tag{3.36}$$

$$T_{comp} / T_{in} = r_c^{\gamma - 1} \tag{3.37}$$

where r_c is the compression ratio, P_{comp} is the compression stroke pressure, T_{comp} is the compression stroke temperature.

The compression stroke is followed by a constant-volume heat input process called the "combustion stroke" (3). During this combustion phase, a large amount of energy is added to the cylinder. This energy increases the temperature of the air to very high values. This increase in temperature during a closed constant-volume process also results in a large increase in pressure as seen also in:

$$T_{combu} = T_{comp} + \lambda Q / c_V \tag{3.38}$$

$$P_{combu} = P_{comp}(T_{combu} / T_{comp}) \tag{3.39}$$

where T_{combu} is the combustion temperature, P_{combu} is the combustion pressure, Q is the fuel heating value, c_{v} is the specific heat at constant volume, and λ is the air-fuel equivalence ratio, which is between 0.85 and 0.901 for the "octane". For the UAS' engine, the value of 0.85 was chosen.

The fuel flow per cycle and the fuel per time unit are thus estimated from:

$$\dot{m}_{fuelpercycle} = \dot{m}_{air}\left(\lambda / AFR_{stoich}\right) \tag{3.40}$$

$$\dot{m}_{fuel} = \dot{m}_{fuelpercycle}\omega\frac{1}{2\pi}N \tag{3.41}$$

where $\dot{m}_{\text{fuelpercycle}}$ is the fuel flow per cycle, $\dot{m}_{\text{fuel}}$ is the fuel flow per time unit, ω is the rotational speed of the engine, N is the number of cylinders of the engine, $\dot{m}_{air}$ is the mass rate of air, λ is the air-fuel equivalence ratio and AFR_{stoich} is the stoichiometric air fuel ratio, which is 15.05 for the octane.

The last phases of the Otto cycle are the "power stroke" (4) and the "heat rejection" (5). During the power stroke, the piston moves from the top position to the down position. The expansion ratio is the reciprocal of the compression ratio, and the same type of relationship can be used as the ones used during the compression stroke:

$$P_{out} / P_{combu} = r_c^{-\gamma} \tag{3.42}$$

$$T_{out} / T_{combu} = r_c^{1-\gamma} \tag{3.43}$$

At the "heat rejection" phase, the exhaust valve is opened and the residual passes through the exhaust system. The pressure is adjusted back to the intake pressure while the volume remains constant.

During the Otto cycle, the work is produced in the compression stroke and in the power stroke by the displacement of the piston. The work produced in a cycle is the difference between the work produced in the compression stroke and the work produced in the power stroke. The ideal work per cycle can thus be calculated using the difference of temperature between those phases:

$$W_i = c_v\left[\left(T_{combu} - T_{comp}\right) - \left(T_{in} - T_{out}\right)\right] \tag{3.44}$$

where W_i is the ideal work produced.

The ideal power and the ideal torque produced by the engine are then estimated:

$$P_i = W_i * cps \tag{3.45}$$

$$Q_i = P_i/\omega_r \tag{3.46}$$

where P_i is the ideal power produced by the engine, Q_i is the ideal torque produced by the engine, cps is the number of cycle per second and ω_r is the angular velocity.

The friction torque (and not the friction work) is calculated to obtain the torque produced by the engine. The friction torque is obtained by minimizing the error between the constructor data torque and the ideal torque as explained next. The proposed friction torque model is given in:

$$Q_f = k_1 + k_2\omega_r + k_3\omega_r^2 \tag{3.47}$$

where k_1, k_2, and k_3 are constants. The procedure to estimate these constants is divided into two steps. In the first step, a preliminary guess of these constants is obtained using the Least Square (LS) method. The results obtained are then used as initial conditions for the optimisation algorithm in the second step. This optimisation was used to find the constants k_1, k_2, k_3 for which the error between the constructor data and the ideal torque was minimized. The Nelder-Mead algorithm was used for this purpose.

Figure 3.15 shows the overall engine model proposed for the UAS propulsion system. The model estimates the torque, the power and the fuel flow using as input the atmospheric pressure and temperature P_0 and T_{in}, the throttle position T_{hr}, the air density ρ, and the rotational speed of the crankshaft RPM.

The results obtained for each engine of the UAS-S4 and UAS-S45 were compared to the constructor data and are presented in Section 3.7.

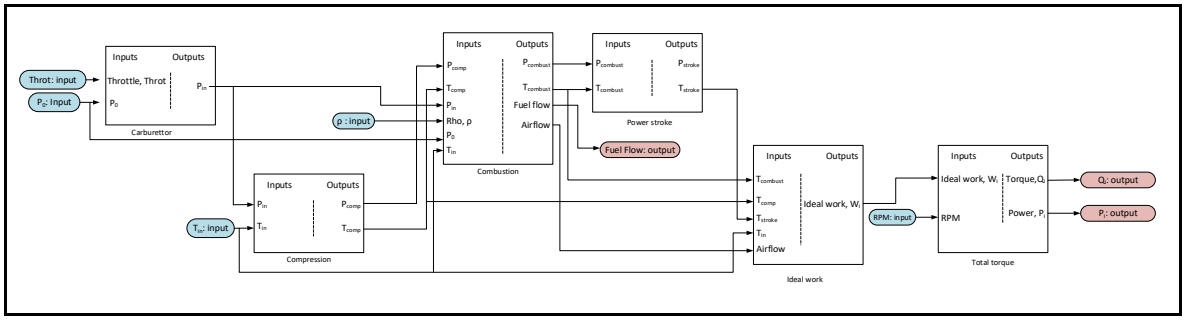

Figure 3.15 Engine model proposed for the propulsion system of each UAS

3.4 Actuator system

The actuator system of the UAS-S4 and of the UAS-S45 is an HS7954SH servomotor is a controlled DC motor. Figure 3.16 shows a schematic diagram of a DC motor.

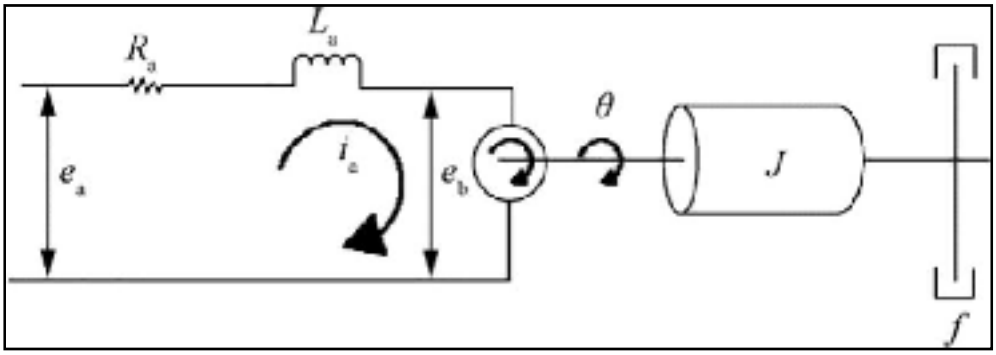

Figure 3.16 Schematic diagram of a DC motor.

The servomotor is controlled via the armature voltage e_a. The differential equation for the armature circuit is:

$$L_a \frac{di_a}{dt} + R_a i_a + e_b = e_a \tag{3.48}$$

where the armature current intensity is given by i_a, L_a is the armature inductance, R_a is the armature resistance, and e_b is the back electromagnetic force which is proportional to the angular velocity $d\theta/dt$:

$$e_b = K_b \frac{d\theta}{dt} \tag{3.49}$$

where K_b is the DC motor's back electromagnetic force constant and θ is the angular displacement of the motor shaft.

The armature current delivers the torque, Q, relates to the inertia and the friction by a second order differential equation as shown in :

$$J \frac{d^2\theta}{dt^2} + f \frac{d\theta}{dt} = Q \tag{3.50}$$

where J is the inertia of the motor and f is the friction of the motor. The torque Q produced by the servomotor is directly proportional to the armature current intensity i_a:

$$Q = K_a i_a \tag{3.51}$$

where K_a is the motor's torque constant.

Applying the Laplace transform on Equations. (3.48) - (3.51) leads to:

$$\left(L_a s + R_a\right) I_a(s) + E_b(s) = E_a(s) \tag{3.52}$$

$$\left(Js^2 + fs\right)\theta(s) = Q(s) \tag{3.53}$$

$$Q(s) = K_a I_a(s) \tag{3.54}$$

$$E_b(s) = K_b s\theta(s) \tag{3.55}$$

which can then be used to obtain the block diagram presented in Figure 3.17.

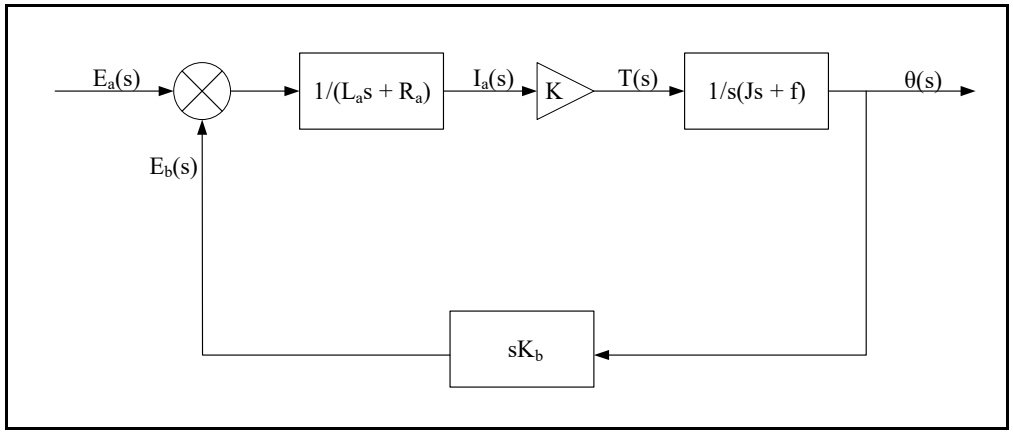

Figure 3.17 Block diagram of DC motor system for each actuator

A perturbation is added to the DC motor model which is the "hinge moment". The hinge moment is a resistive moment that the motor must overcome to move the control surface. It can be expressed using:

$$M_h = C_h \frac{1}{2} \rho V^2 S_e c_e \tag{3.56}$$

where V is the aircraft true airspeed, S_e is the area of the control surface, c_e is the chord of the control surface measured from the trailing edge of the flap and C_h is the hinge moment coefficient. The hinge moment coefficient is expressed by:

$$C_h = C_{h\alpha}\alpha + C_{h\delta}\delta \tag{3.57}$$

where $C_{h\alpha}$ is the hinge moment derivative due to the angle of attack, $C_{h\delta}$ is the hinge moment derivative due to the control surface deflection, δ is the control surface deflection and α is the angle of attack.

For the case of the elevator, the angle of attack is expressed by:

$$\alpha_t = \alpha_w - i_w - \varepsilon + i_t \tag{3.58}$$

where α_t is the angle of attack of the horizontal tail, α_w is the angle of attack of the wing, i_w is the incidence angle of the wing, i_t is the incidence angle of the horizontal tail, ε is the downwash angle.

All of the useful parameters such as the armature resistance, R_a, the armature inductance, L_a, the inertia, J, and the friction, f, of the motor, in the DC motor block diagram (Figure 3.16) can be found in manufacturers' datasheets. To obtain a servomotor model, a PID controller was added to the DC motor model (Figure 3.17). The PID controller was tuned such that the resultant servomotor model has the same operation speed as the one in the manufacturer's documentation in absence of perturbation. Therefore, for the PID tuning, the hinge moment M_h (normally considered as perturbation) was assumed to be zero.

In addition, the inductance armature L_a, is very small and can be neglected. The servomotor is also assumed to have no electromagnetic losses; thus, the torque constant K_a is equal to back electromagnetic force constant K_b:

$$K_a = K_b = K \tag{3.59}$$

The system of Eqs. (3.52)– (3.55) can be reduced to the opened loop transfer function:

$$\frac{\Theta(s)}{E_a(s)} = \frac{K}{s(R_a J)s + R_a f + K^2} = \frac{G}{s(T_s s + 1)} \tag{3.60}$$

where

$$G = \frac{K}{R_a f + K^2} \quad = \text{motor gain constant} \tag{3.61}$$

$$T_s = \frac{R_a J}{R_a f + K^2} \quad = \text{motor time constant} \tag{3.62}$$

The closed loop transfer function of the DC motor is obtained from Eq. (3.63) and is expressed by:

$$F(s) = \frac{\omega_a^2}{s^2 + 2\xi\omega_a s + \omega_a^2} \tag{3.63}$$

where, $\omega_a = \sqrt{\frac{kG}{T_s}}$ is the natural frequency of the system, and $\xi = \frac{1}{2T_s\omega_a}$ is the damping ratio of the system, k is the maximum voltage of the servomotor. It is added to convert the desired angle into a voltage.

The resulting servomotor block diagram is shown in Figure 3.18 and the tuning of the PID controller was performed using MATLAB/Simulink toolbox.

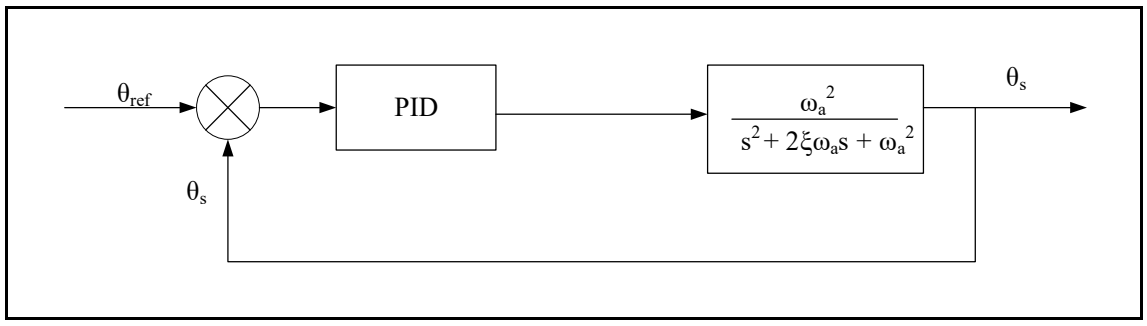

Figure 3.18 Block diagram of the servomotor system for each actuator

3.5 Structure system

The structural analysis includes the estimation of the mass, the center of gravity, and the inertia of each UAS. Numerical and experimental analyses to calculate the mass and the center of

gravity of the UAS-S4 were performed recently at our laboratory LARCASE, ETS and are explained in (Communier *et al*., 2015 ; Tondji and Botez, 2016, 2017). The experimental tests were used to validate the numerical code and analysis. The numerical code, following its experimental validation on the UAS-S4, was further applied on the UAS-S45.

The UAS-S45 structure was divided into six components: the wings, the fuselage, the power plants, the vertical tail, the horizontal tail and the landing gear. Each component was replaced by basic shapes such as triangles, rectangles and trapezoids to facilitate the calculation of its center of gravity and mass (Chahbani, 2015), see Figure 3.19. The reference system is given by (Oxyz)

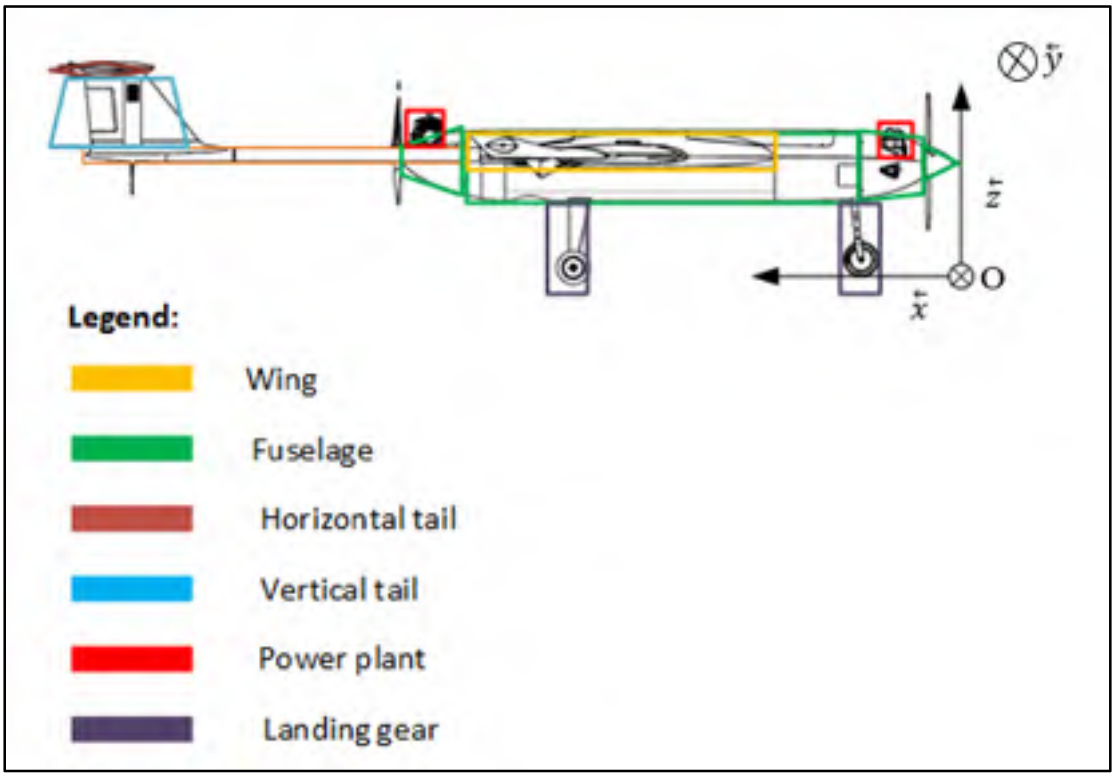

Figure 3.19 UAS-S45 decomposition using basic shapes

Using the classification of the UAS-S45, the equations provided by Raymer (1989) were applied on each of its components to estimate its weight.

The estimation of the wing mass is shown as an example. The UAS-S45 has a straight-tapered wing which can be approximated by a trapezoid on the top view, and a diamond-shaped on the side view (Figure 3.20).

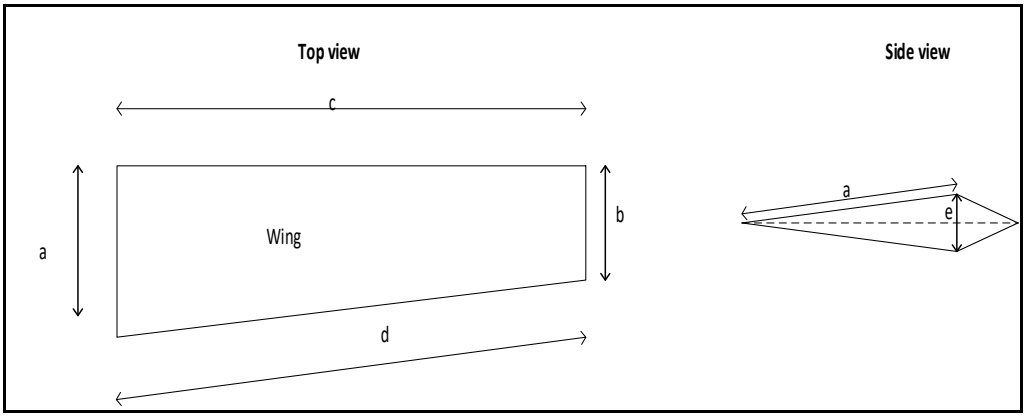

Figure 3.20 Top view and side view of the UAS-S45 wing using basic shapes.

The Raymer equation for the estimation of the wing mass W_w is given by:

$$W_W = 0.036 S_W^{0.758} \left(\frac{AR}{\cos^2(\Lambda_{c/4})} \right)^{0.6} q^{0.006} \lambda^{0.04} \left(\frac{100.t/c}{\cos(\Lambda_{c/4})} \right)^{-0.3} (n_z W_o)^{0.49} \quad (3.64)$$

where AR is the aspect ratio of the wing, $\Lambda_{c/4}$ is the wing sweep at 25% of the mean geometric chord, q is the dynamic pressure at cruise, t/c is the wing thickness to chord ratio, λ is the wing taper ratio, n_z is the ultimate load factor, which is 5 for a general class aviation airplane or default aircraft, and W_o is the designed gross weight.

The parameters such as AR, $\Lambda_{c/4}$, λ, and t/c are given by:

$$\lambda = \frac{a}{b} \quad (3.65)$$

$$\Lambda_{c/4} = \tan^{-1}\left(\frac{0.75(a-b)}{c} \right) \quad (3.66)$$

$$\frac{t}{c} = \frac{e}{a} \tag{3.67}$$

$$AR = 4\frac{c^2}{S_W} \tag{3.68}$$

The center of gravity location of each component was estimated using Mechanical Engineering calculations applied to the basic shapes. The center of gravity location of the whole UAS was then calculated using the weighted arithmetic mean of the center of gravity locations of each of its components.

$$x_{cg} = \frac{\sum x_{cgi} m_i}{\sum m_i} \tag{3.69}$$

$$y_{cg} = \frac{\sum y_{cgi} m_i}{\sum m_i} \tag{3.70}$$

$$z_{cg} = \frac{\sum z_{cgi} m_i}{\sum m_i} \tag{3.71}$$

where x_{cgi}, y_{cgi} and z_{cgi} are the center of gravity locations of each component of the UAS, and m_i is the mass of each component.

To obtain the inertia of the UAS-S4, Tondji and Botez (2017) developed a methodology based on the DATCOM code. The methodology consists of dividing the aircraft into five major components: wings, fuselage, horizontal stabilizer, vertical stabilizer and power plant. The inertia of each component was calculated about its center of gravity. The total aircraft inertia about its main axis is given by equations:

$$I_x = \sum \left(m_i x_{cgi}^2 + I_{oxi} \right) \tag{3.72}$$

$$I_y = \sum \left(m_i y_{cgi}^2 + I_{oyi} \right) \tag{3.73}$$

$$I_z = \sum \left(m_i z_{cgi}^2 + I_{ozi} \right) \tag{3.74}$$

where I_{oxi}, I_{oyi} I_{ozi} are the inertia values of each component about their center of gravity, and I_x, I_y I_z are the inertia values about the main axis of the UAS. The inertia about the center of gravity of the UAS can then be obtained from the Huygens theorem (Tondji and Botez, 2017). The same method was applied to estimate the inertia of the UAS-S45.

3.6 Results and discussion

Relative error: The relative error between a reference value x_a and an approximated value x_b is calculated as relative error $= \left| \frac{x_b - x_a}{x_a} \right| \times 100\%$.

3.6.1 Aerodynamic sub-model

Fderivatives in-house code does not take into account the parallel vertical tails and the winglets that are components of our UAS. The parallel vertical tails of each UAS were then replaced in this code by a single vertical tail with a double reference area. It was thus possible to use the CFD analysis to estimate the contributions of the parallel vertical tails. For the UAS-S45, the winglets were not modelled, and their contributions to the whole UAS have been neglected for the validation.

The flight conditions were considered as function of the altitudes, Mach numbers and angles of attack. The range of these parameter values associated with each flight condition is presented in Table 3.4. The unknown aerodynamic coefficients (lift, drag and pitch) can be found by interpolation, for any flight condition based on this range of flight conditions parameter values.

Table 3.4 Flight conditions for the aerodynamic coefficients determination

Altitude （ft）	***Ma***	**Angle of attack (°)**
0- 20000	0.1 – 0.2	−17 - 17

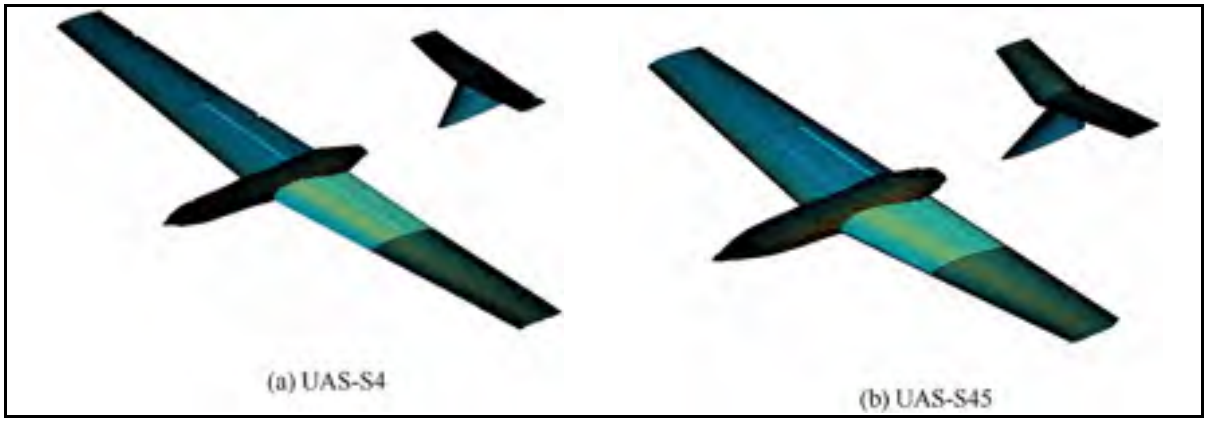

Figure 3.21 Model of the UAS-S4 and the UAS-S45 performed with Fderivatives code

Figure 3.22 shows the comparison of the lift, drag and pitch moment coefficients estimated with Fderivatives, DATCOM and TORNADO for the UAS-S4. The range of the angle of attack was reduced to [-8°, 12°] because the CFD analysis with ANSYS Fluent predicted the beginning of the stall at 10° while Fderivatives and DATCOM codes estimated a linear lift coefficient variation with angle of attack until 17°. The three semi-empirical methodologies (Fderivatives, DATCOM and TORNADO) gave very close results for C_L and C_m. In the same way as with the UAS-S45, the highest difference can be observed in the estimation of the pitching moment coefficient at high positive angles of attack with TORNADO code.

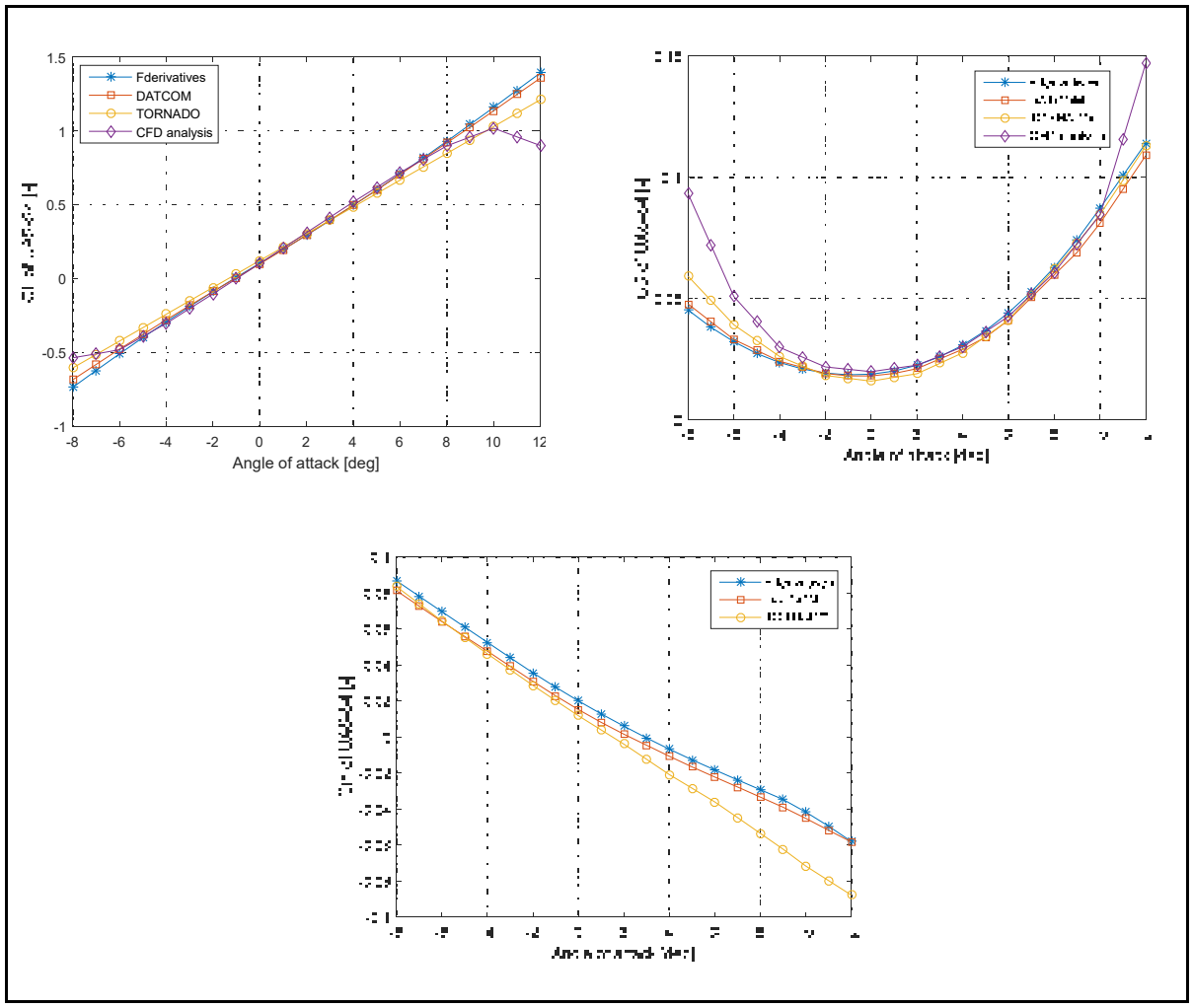

Figure 3.22 Lift, drag and pitch moment coefficient variation with the angle of attack for the UAS-S4 at altitude = 10000 ft and Mach number = 0.14

A comparison of the lift, drag and pitch moment coefficients estimated with Fderivatives, DATCOM and TORNADO codes for the UAS-S45 is shown in Figure 3.23. The estimation was performed for an altitude of 10000 ft. and a Mach number of 0.14. It can be seen that there is reasonable agreement between the three methodologies results on the lift and drag coefficients. The difference in results is associated with the estimation of the drag coefficient with TORNADO. This difference is probably due to no evaluation method for the contribution of the fuselage. Because of the lack of a method to evaluate the contribution of the fuselage in

TORNADO, the calculation of the longitudinal and lateral stability derivatives was validated using only DATCOM and Fderivatives codes.

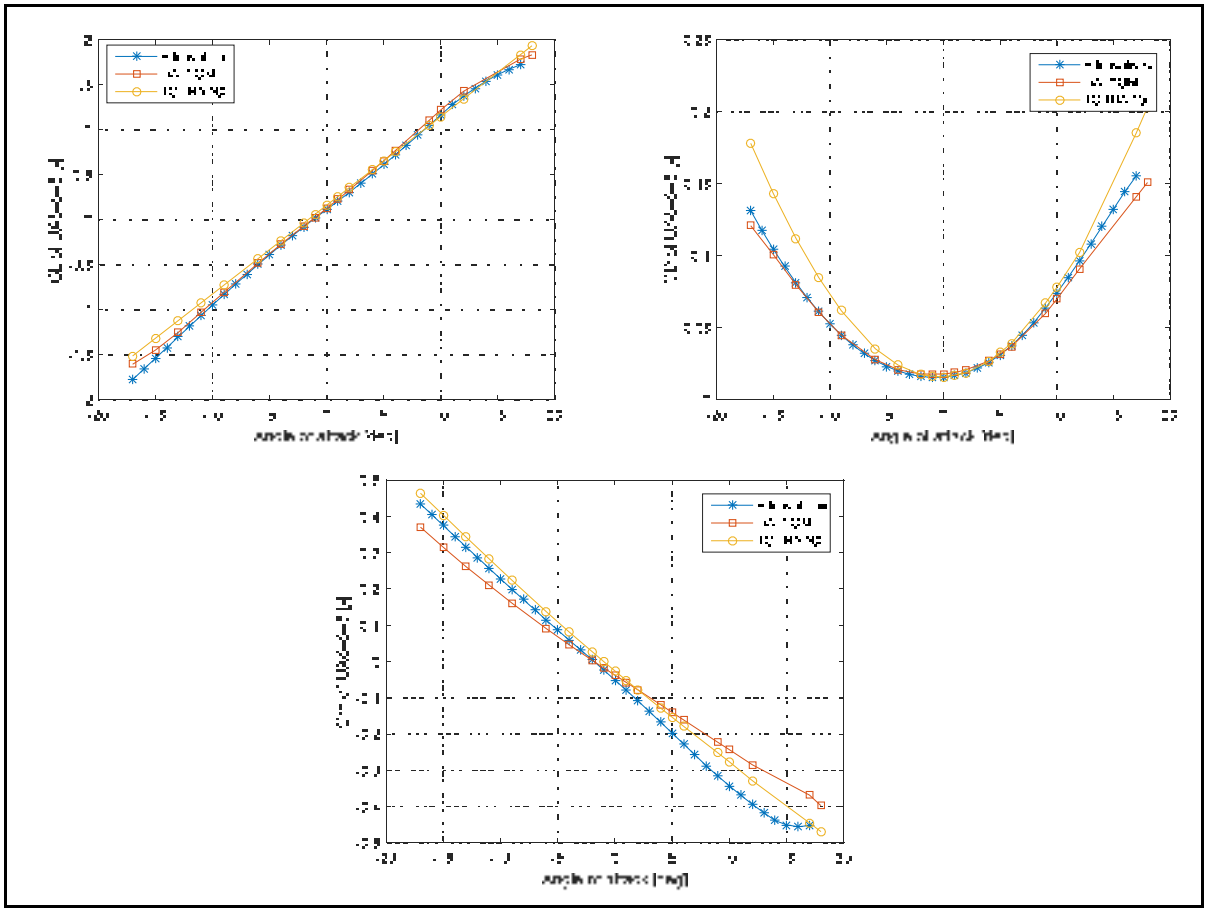

Figure 3.23 Lift, drag and pitch moment coefficient variation with the angle of attack for the UAS-S45 at the altitude = 10000 ft and Mach number = 0.14 .

Figure 3.24 displays the longitudinal lift and moment derivatives with respect to pitch rate in function of angle of attack, C_{Lq} and C_{mq} for the UAS-45 (Mach number of 0.18, altitude of 15000 ft). Both Fderivatives and DATCOM codes estimated constant lift and moment derivatives with respect to pitch rate. There is a rather good agreement between DATCOM and Fderivatives on the lift derivative with respect to pitch rate, C_{Lq}, with a difference of 6.36% equivalent to a relative error, but the difference is higher for the moment derivative with espect to pitch rate, C_{mq} (Figure 3.24).

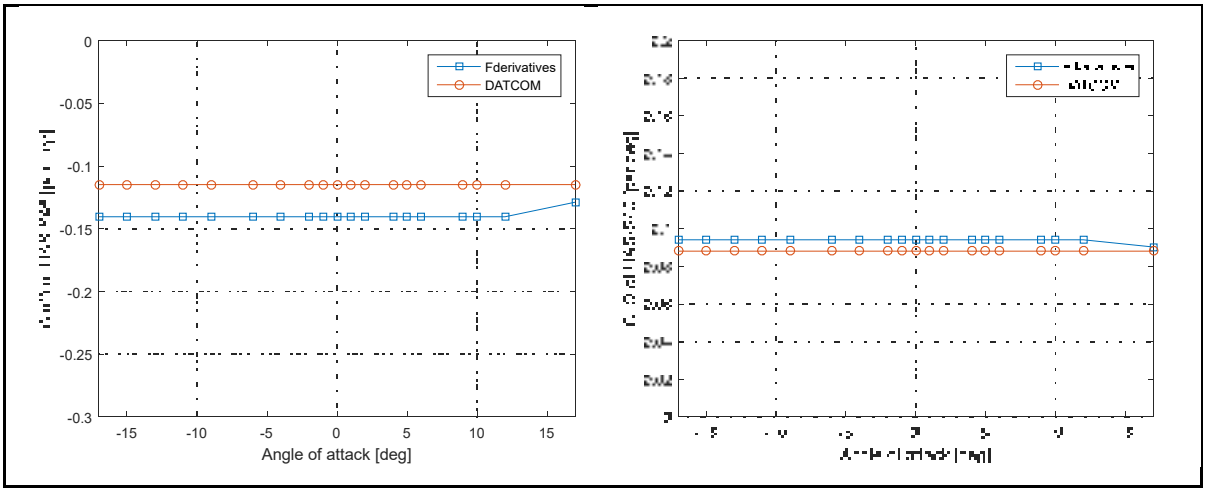

Figure 3.24 Lift and moment derivative with respect to pitch rate variation with the angle of attack for the UAS-S45 at altitude = 15000ft, Mach number = 0.18.

Figures. 3.25, 3.26, 3.27 and 3.28 show a comparison of lateral derivatives variations with angle of attack calculated with Fderivatives and DATCOM codes. These estimations were performed for an altitude of 15000 ft. and a Mach number of 0.18. Fderivatives code results clearly show a good agreement with the DATCOM results especially for angles of attack between -10° and 12°. The results remain the same for the other flight conditions.

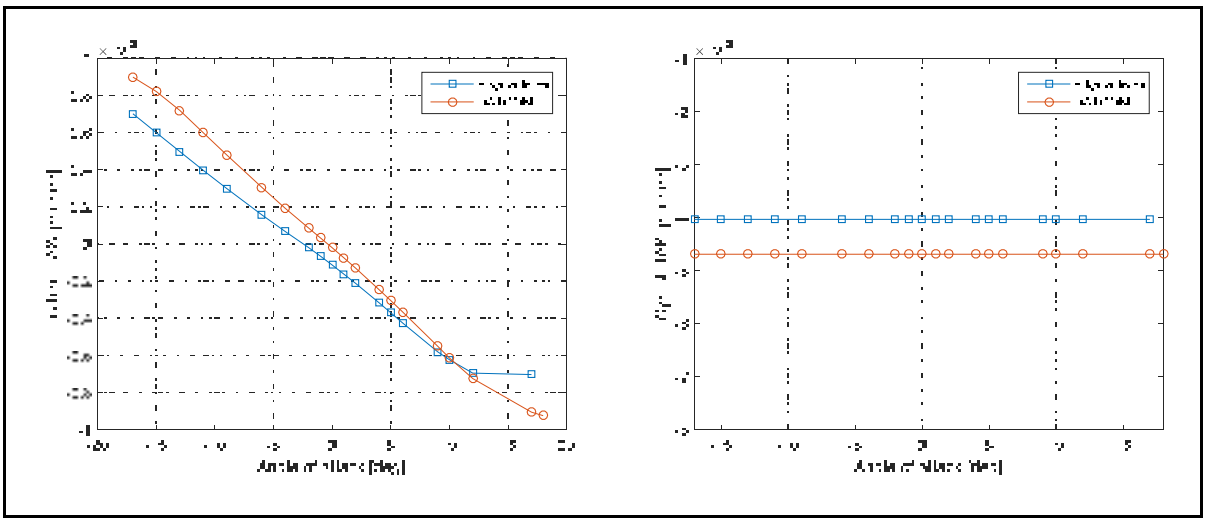

Figure 3.25 Side-force and rolling moment derivative coefficients with respect to sideslip angle, β, as function of angle of attack at altitude = 15000 ft, Mach number = 0.18

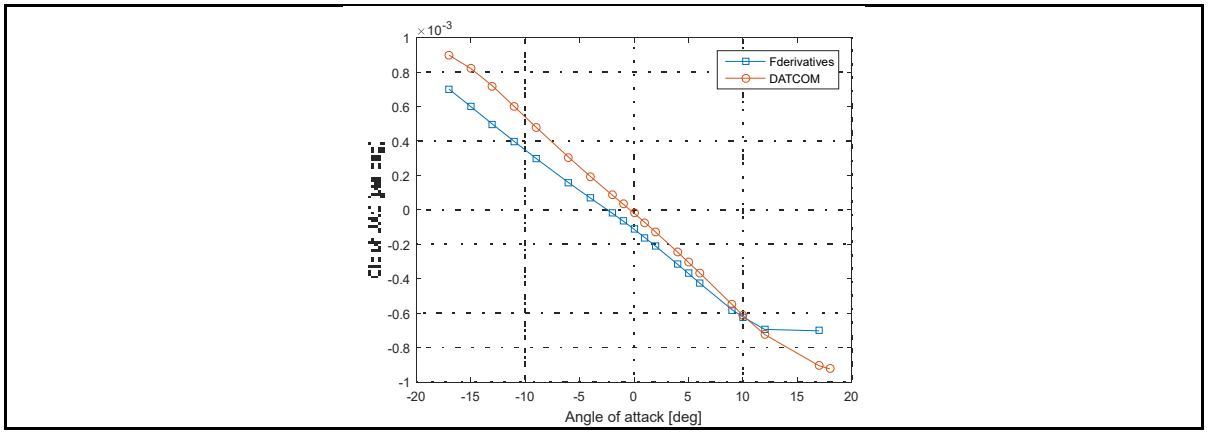

Figure 3.26 (Continued) Side-force and rolling moment derivative coefficients with respect to sideslip angle, β, as function of angle of attack at altitude = 15000 ft, Mach number = 0.18

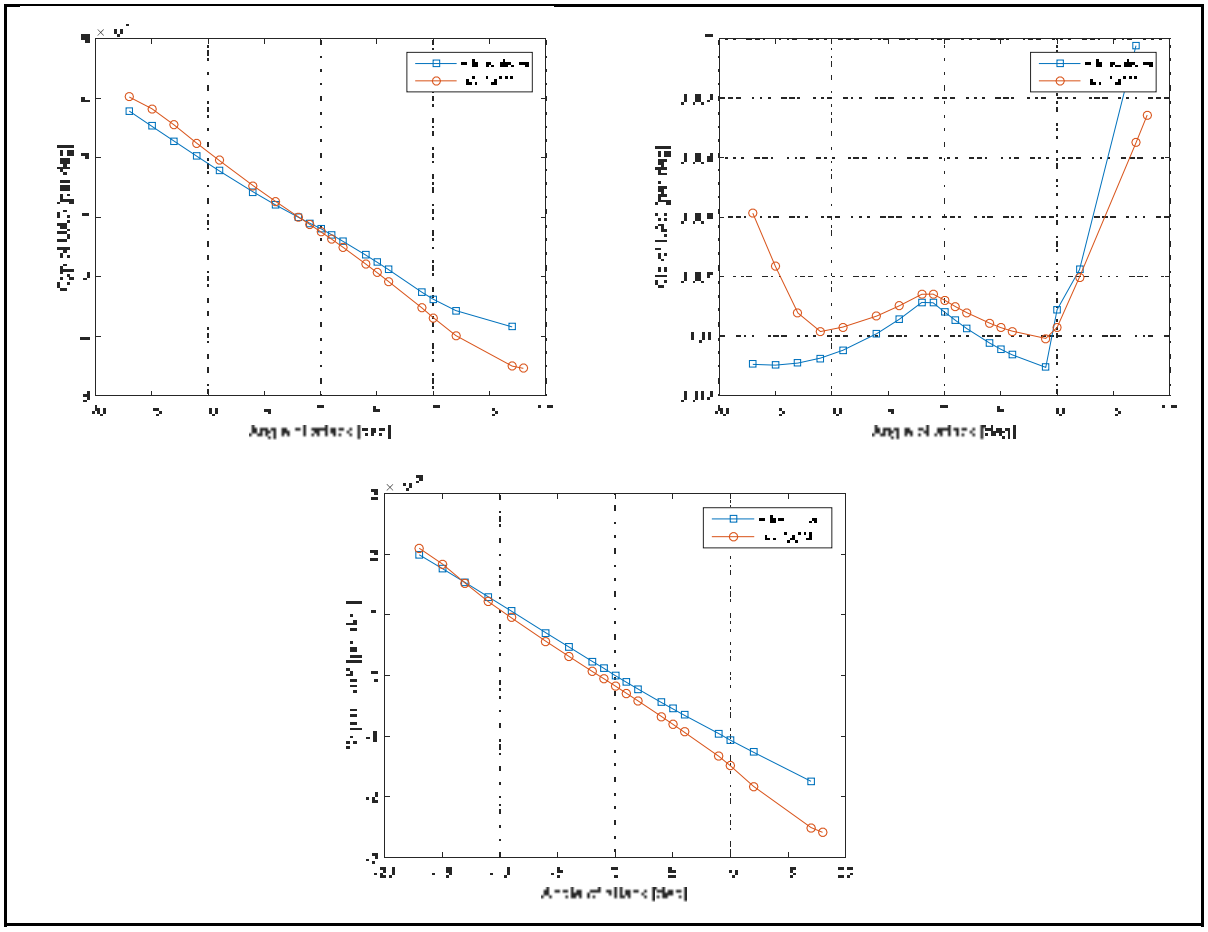

Figure 3.27 Side-force, rolling and yawing moment derivatives with respect to the roll rate as function of the angle of attack at altitude = 15000 ft, Mach number = 0.18

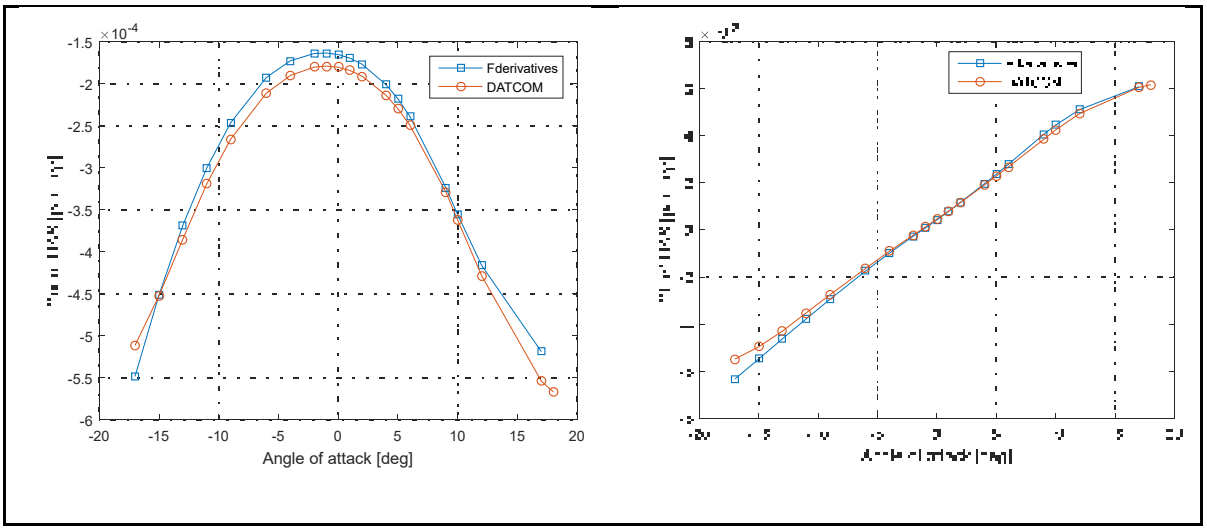

Figure 3.28 Rolling and yawing moment derivatives with respect to the yaw rate as function of the angle of attack at altitude =15000 ft, Mach number =0.18

3.6.2 Propulsion sub model

3.6.2.1 Propeller analysis

The UAS-S4 and the UAS-S45 use the same 18 inch MEJZLIK propeller. The Blade Element Theory (BET) was applied to the 18 inch propeller of each UAS for different values of speeds and attitudes. Figure 3.29 shows the variation of the thrust obtained as a function of the speed and the altitude. As seen on Figure 3.29, as both the altitude and the speed increase, the generated thrust decreases. The maximum thrust, also known as the static thrust, is obtained at the ground (altitude = 0 ft), thus at zero speed.

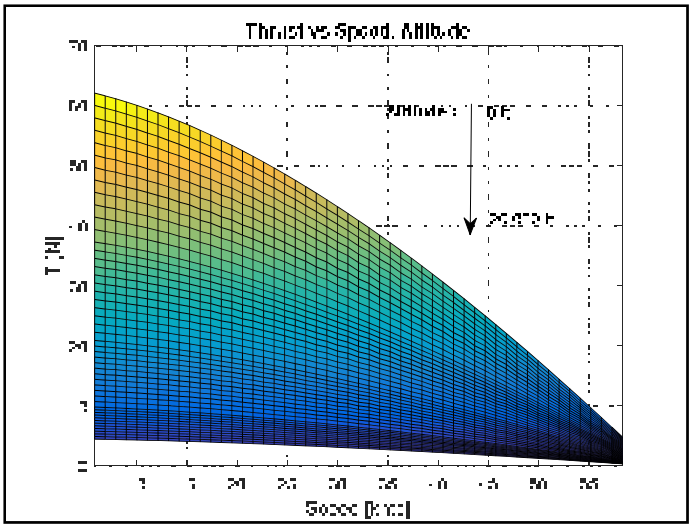

Figure 3.29 Thrust variation with speed and altitude

Figure 3.30 presents the thrust coefficient C_T and the propeller efficiency η variations with the advance ratio obtained with the BET, and with the CFD analysis using ANSYS Fluent. The results are obtained as function of the Advance Ratio, which is an adimensional parameter, defined as the ratio of the freestream fluid to the propeller tip speed and were evaluated at an altitude of 10000 ft as in Equation 3.31. Figure 3.30 shows that there is a reasonable agreement between these results obtained with two methodologies. The maximum relative error for the thrust coefficient is 5.6%, while for the propeller efficiency is 10.28%.

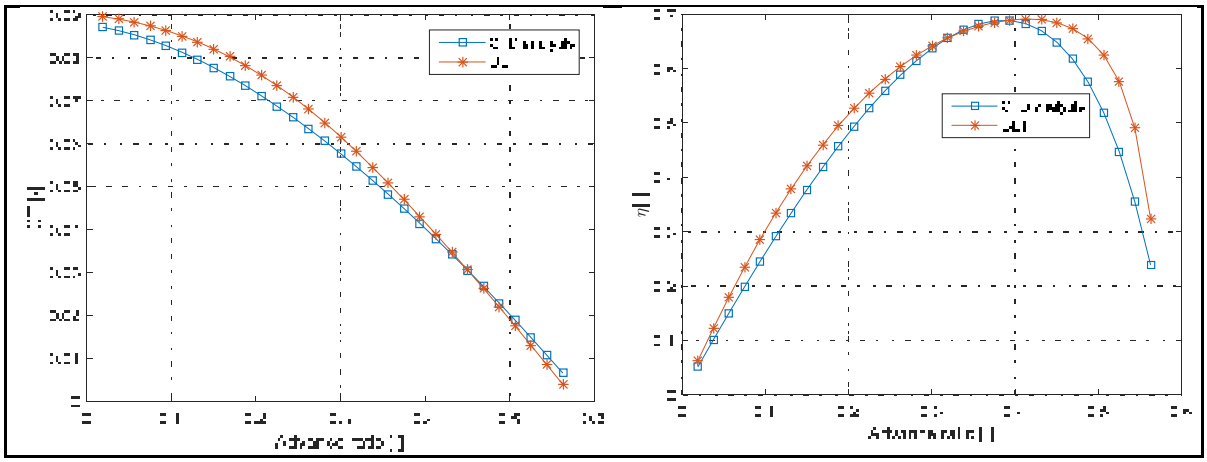

Figure 3.30 Thrust coefficient and propeller efficiency variation with the advance ratio for the altitude of 10,000ft

3.6.2.2 2-Stroke Engine Model

In the case of the 2-stroke engine, the torque produced by the proposed engine model (Figure 3.15) was compared to the torque provided by the manufacturer's documentation. Each UAS has two engines: the ZENOAH G800BPU at its front and the ZENOAH G620BPU at its rear. Figure 3.31 shows the comparison of the real values of the torque with their estimations for each engine given in Section 3.3.

Figure 3.31 demonstrates the close agreement between the estimated torque and its real value for each engine, with a mean relative error of 1.56% for the ZENOAH G800BPU, and 0.83% for the Zenoah G620BPU.

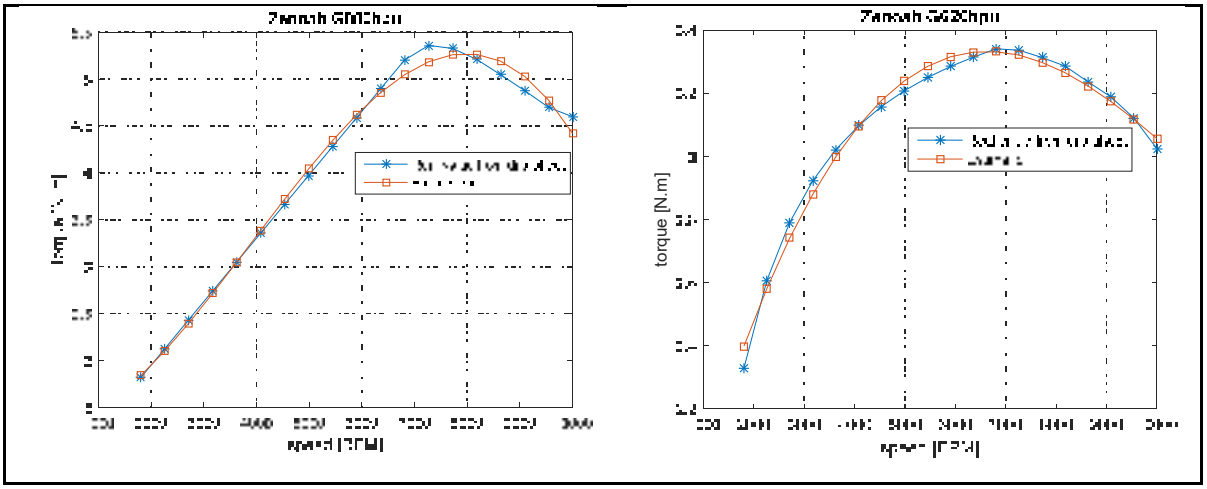

Figure 3.31 Torque variation with the speed for the ZENOAH G800BPU and ZENOAH620BPU

3.6.3 Actuator sub model

As specified in Section 3.4, the actuator sub-model, which is a servomotor, was estimated using controlled DC motor. The transfer function from Equation 3.63 was used with ω_a = 1.1636 rad/s and $\xi = 0.0163$ defining the system natural frequency and the damping ratio, respectively. The PID controller was tuned to obtain a desired operating speed when the hinge moment was

zero. The servomotor HS7954SH has an operating speed of 0.1 s/60°, as specified in the datasheet. To meet this specification, the tuning of the PID controller was performed using MATALB/Simulink toolbox.

Figure 3.32 shows the tuning of the PID controller, the operating time of servomotor, which is the servomotor to reach its final position, is similar to the settling time. For this purpose, the PID controller was tuned to obtain a settling time of 0.1 s. The estimated controller parameters were P=19.54, I= 241.81, D=0.37. A step response procedure was performed to validate the actuator sub-model. The settling speed of the servomotor was compared to the manufacturer's operation speed 0.1 s/60°.

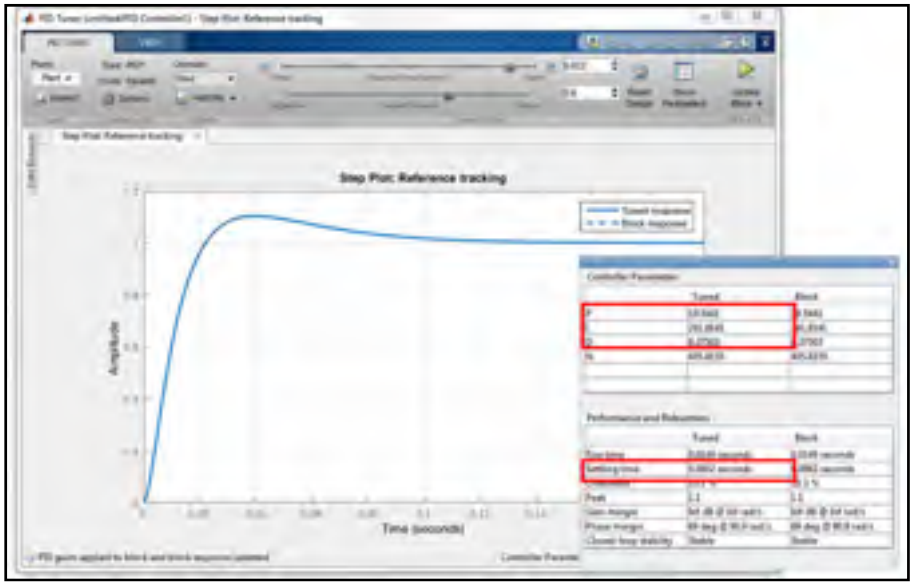

Figure 3.32 PID controller tuning using MATLAB/Simulink toolbox

Figure 3.33 shows the excellent results obtained for the step response of 60°. Therefore, the response time obtained was similar to the operating speed specified by the manufacturer s seen on Figure 3.33.

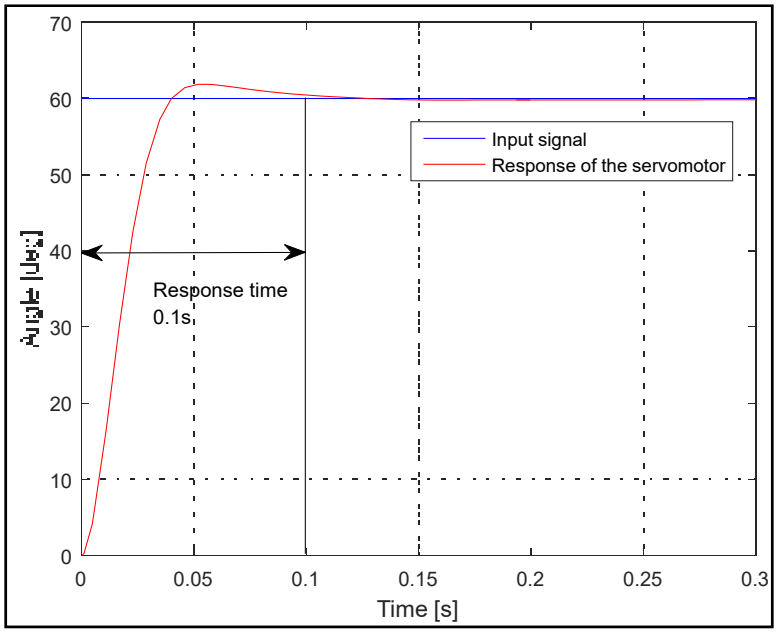

Figure 3.33 Step response of the servomotor model
for a signal of 60°

3.6.4 Structural analysis

Tondji and Botez (2017) performed a structural analysis of the Unmanned Aerial System UAS-S4. They estimated numerically the mass, position of the center of gravity and the moment of inertia numerically from the Raymer and DATCOM methods and further validated the results using and experimental pendulum method. The Raymer and DATCOM methods were applied to the UAS-S4 which was initially divided into components as fuselage, wing, and tail. Each component was approximated to basic shapes (triangle, square, circle etc.). The mass of each component as well as the mass of the entire UAS-S4 was then calculated by applying equations from the Raymer methods. The center of gravity results from the mass estimation using Equations (3.67) - (3.69). The moment of inertia of each component was calculated using DATCOM equations and then the overall UAS-S4 was computed from the Huygens theorem (Tondji and Botez, 2017). The mass of the UAS-S4 was validated experimental using results of an accurate scale. The center of gravity and the moment of inertia were validated using results from a pendulum method. For this purpose, the UAS-S4 was installed on a pendulum

and the rotational angle and speed were measured. The data measured led to the development of a nonlinear dynamic model for the rotational motion of the pendulum. The center of gravity and the moment of inertia were thus extracted from this model. The comparison between numerical and experimental data showed relative errors of 5.5%, 1.14% and 1.184% respectively for the *X, Y* and *Z* positions on the center of gravity. The moment of inertia from the DATCOM method was also compared to those obtained using the pendulum method. The relative errors were 15.69%, 1.84% and 2.05% for the inertia about the *X* axis, *Y* axis and *Z* axis.

The results obtained for the mass, the center of gravity and the inertia analyses are presented in Table 3.5. The unloaded mass of the UAS-S45 is 121.25 lb and its maximum mass is 153 lb. Thus, it allows 31.75 lb for the fuel, and for the extra load, such as a camera. To obtain the results presented in Table 3.5, the center of gravity and the inertia analyses were evaluated for a range of mass between the UAS-S45 maximum mass (167.79 lb) and its unloaded mass (117.79 lb) by changing adequately the fuel and the extra load masses. These considerations were made to avoid extrapolation when calculating values of center of gravity and inertia for a UAS-S45 mass near to the mass extremities such as the maximum mass or to the unloaded mass.

Table 3.5 Data obtained from the structural analysis for UAS-S45

Mass (lb)	X_{cg} **(in)**	Z_{cg} **(in)**	I_{xx} **(10^4lb.in^2)**	I_{yy} **(10^4lb.in^2)**	I_{zz} **(10^5lb.in^2)**
167.79	43.7676	16.5360	9.9266	6.7060	1.6695
157.79	44.0652	16.6620	9.9367	6.7797	1.675
147.79	44.3796	16.7952	9.9278	6.6898	1.6663
137.79	44.7396	16.9488	9.9187	6.5933	1.6570
127.79	45.1536	17.1240	9.9087	6.4885	1.647
117.79	45.6360	17.3292	9.874	6.1904	1.6201

By knowing the fuel flow of each UAS, any position of the center of gravity and inertia can be interpolated from Table 3.5. To validate the results obtained, the unloaded mass of the UAS-S45 and its corresponding position of the center of gravity for the unloaded mass were

estimated. The unloaded mass of the UAS-S45 was calculated by applying the Raymer's equations as specified in Section 5 in the absence of fuel and extra load. The corresponding center of gravity was interpolated using Table 3.5. These values were compared with real center of gravity data of the UAS-S45, as shown in Table 3.6. The estimated results show a very close agreement with the real data with a relative error of 0.07% for the mass and 5.7% for the *x*-position of the center of gravity.

Table 3.6 Comparison of mass and position of center of gravity estimated with the real values

Parameter	**Unloaded mass (lb)**	**X_{cg} (in)**	**Z_{cg} (in)**
Estimation	121.34	45.63	4.24
Real value from datasheet	121.25	48.43	4.15
Error (%)	0.07	5.7	2.1

3.7 Conclusion

A modelling procedure for the UAS-S4 and the UAS-45 was presented in this paper. The overall model of each UAS was divided into four sub-models, and the estimation methods of each sub-model were detailed. The aerodynamic sub-model was obtained from geometrical data using the in-house code Fderivatives, the DATCOM procedure, TORNADO and a CFD analysis on ANSYS-Fluent. The propulsion sub-model was estimated by coupling a two-stroke engine model based on the ideal Otto cycle with a blade element theory analysis on the propeller. The mass, the inertia and the position of the center of gravity were determined from the Raymer and the DATCOM methodologies. The actuator system was estimated from a DC servomotor model controlled with a PID controller.

A validation was performed for each sub-model. The aerodynamic sub-model obtained using Fderivatives was compared with CFD-Fluent analysis, a Vortex Lattice Method (VLM) and

the DATCOM procedure. The propeller sub-model estimate using the Blade Element Theory (BET) was compared with CFD-Fluent analysis. The engine sub-model, the actuator sub-model, the mass and the center of gravity was compared with experimental data. The results show good agreement for each sub-model with respect to its experimental sub-model. The complete UAS-S4 and UAS-S45 simulation models were assembled on Matlab/Simulink, and thus can be useful for efficient flight dynamics and control laws modelling and simulation technologies. The intent is to design a level D (highest level of flight dynamics) simulator for these UAS-S4 and US-S45 that will be validated with experimental flight test data.

3.8 Acknowledgements

Special thanks are dues to the Natural Sciences and Engineering Research Council of Canada (NSERC) for the Canada Research Chair Tier 1 in Aircraft Modelling and Simulation Technologies funding. We would also like to thank Mrs. Odette Lacasse and Mr. Oscar Carranza for their support at the ETS, as well as to Hydra Technologies' team members Mr. Carlos Ruiz, Mr. Eduardo Yakin and Mr. Alvaro Gutierrez Prado in Mexico.

CHAPTER 4

AERODYNAMIC MODELLING OF UNMANNED AERIAL SYSTEM THROUGH NONLINEAR VORTEX LATTICE METHOD, COMPUTATIONAL FLUID DYNAMICS AND EXPERIMENTAL VALIDATION - APPLICATION TO THE UAS-S45 BÀLAAM

Maxime Alex Junior Kuitche, Ruxandra Mihaela Botez, Arthur Guillemin and David Communier
LARCASE Laboratory of Applied Research Active Controls,
Avionics and AeroServoElasticity,
Ecole de Technologie Supérieure, 1100 Notre Dame West,
Montreal, H3C1K3, Québec, Canada

Article soumis dans *The Aeronautical Journal*, en Septembre 2019

Résumé

Cet article décrit une méthodologie permettant de prédire le comportement aérodynamique d'un système aérien sans pilote. La conception des aéronefs et la modélisation de la dynamique de vol concernent principalement l'aérodynamique. Par conséquent, son estimation nécessite un niveau élevé de précision. Les ressources informatiques et les coûts doivent être pris en compte lors de l'application de l'analyse numérique par dynamique des fluides. Le travail présenté ici montre une comparaison entre une nouvelle formulation non linéaire de la méthode classique du réseau de vortex et une analyse de la dynamique des fluides. La nouvelle méthode de réseau de vortex non linéaire a été réalisée en calculant les forces visqueuses à partir de la théorie des bandes et les forces générées par les anneaux de vortex à partir de la loi de portance des vortex. L'analyse de la dynamique des fluides a été faite à partir des maillages structurées et non structurées obtenues grâce a une étude de convergence de grille nécessaire pour prédire les coefficients aérodynamiques. Les modèles Spalart-Allmaras et k-ω été utilisés comme modèles de turbulence. Une validation expérimentale de la procédure a été réalisée à l'aide de données d'essais en soufflerie. Les résultats obtenus ont également été comparés à ceux obtenus à partir de méthodes semi-empiriques programmées à l'aide de DATCOM et de notre nouveau

code fait maison Fderivatives. Les résultats ont indiqué la précision des approches et ont montré qu'un modèle aérodynamique obtenu avec les coefficients aérodynamiques prédits avec ces méthodes pourrait être utile pour l'estimation de la dynamique de vol.

Abstract

This paper describes a methodology to predict the aerodynamic behaviour of an Unmanned Aerial System. Aircraft design and flight dynamics modelling are mainly concerned with aerodynamics, and thus its estimation requires a high level of accuracy. Computational resources and costs must be taken into account when applying Computational Fluid Dynamics analysis. The work presented here shows a comparison between a new non-linear formulation of the classical Vortex Lattice Method and a Computation Fluid Dynamics analysis. The new non-linear Vortex Lattice Method was performed by calculating the viscous forces from the strip theory, and the forces generated by the vortex rings from the vortex lifting law. The Computation Fluid Dynamics analysis used structured and unstructured grids obtained from a grid convergence study that is needed to predict the aerodynamic coefficients. The Spalart-Allmaras and the k-ω models were used as turbulence models. An experimental validation of the procedure was performed using wind tunnel test data. The obtained results were also compared to those obtained from semi-empirical methods programmed using DATCOM and our Fderivatives new in-house codes. The results have indicated the accuracy of the approaches and showed that an aerodynamic model obtained with the aerodynamic coefficients predicted with these methods could be useful for flight dynamics estimation.

4.1 Introduction

The focus of flight dynamics modelling is mostly related to its ability to accurately predict a suitable aerodynamic model. During the first half of the 20th century, wind tunnel testing was the core of aerodynamic research and it was the best way to obtain an accurate aerodynamic model of an aircraft (Nelson and Zingg, 2004). Aerodynamic semi-empirical analyses were performed using charts and equations from wind tunnel and flight tests, such as those presented

in the USAF DATCOM procedure (Williams and Vukelich, 1979). Computational Fluid Dynamics (CFD) analysis began to be considered in the last 50 years of the 20th century with the advancement of computing capabilities. In the 1960s, panel methods were the techniques of choice for aerodynamics studies, but they remained limited by their applicability only at low Mach numbers, incompressible and inviscid flows. Panel method does not use a mesh for the flow domain, and does not provide a prediction of the drag, which also limits the understanding of the fluid flow characteristics.

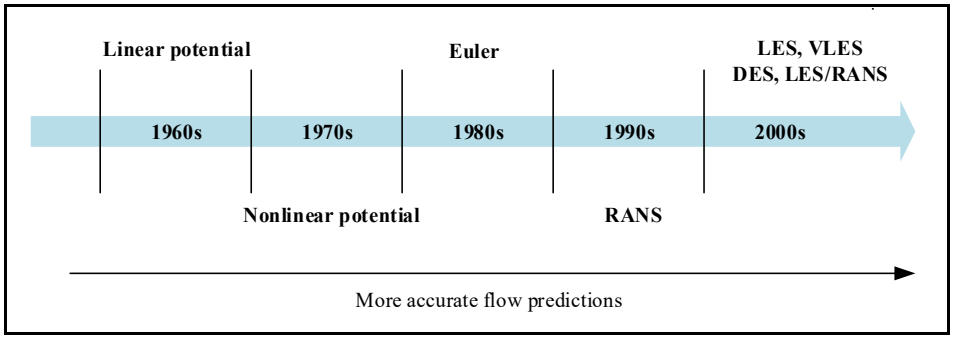

Figure 4.1 Historical development of CFD

Since the 1970s, the development of numerical algorithms has allowed a rapid progression of the CFD studies. From the Lax-Wendroff and MacCormack method for solving compressible Navier-stokes equations to the Spalart detached-eddy simulation (DES) (Nelson and Zingg, 2004), the CFD studies have evolved in many ways, including structured and unstructured meshing, implicit time-integration schemes, approximate factorization, total variation diminishing-like scheme, flux vector splitting, and flux difference splitting. Figure 4.1 shows the evolution of the CFD methods from the linear potential method, in the 1960s, to the Large Eddy-Simulation (LES), Very Large Eddy-Simulation (VLES), Detached-Eddy Simulation (DES) and Reynold Average Navier-Stokes (RANS) methods in the 2000s.

The success of the CFD in solving Navier-Stokes equations and in accurately predicting the dynamic flow around an aircraft has attracted the interest of many researchers. The CRIAQ MDO 505 (Botez *et al.*, 2015 ; Koreanschi *et al.*, 2016 ; Şugar Gabor *et al.*, 2016) project was realized in our Research Laboratory in Active Controls, Avionics and Aeroservoelasticity

(LARCASE) of the ETS in collaboration with the Ecole Polytechnique de Montréal, the University of Naples, Bombardier Aerospace, Thales Canada, Alenia Aeronautica, the IAR-NRC and the Italian Institute for Research in Aerospace CIRA. It dealt with the application of the morphing wing technique on a real wing of a Bombardier aircraft. The objective of this project was to demonstrate the aerodynamic and structural efficiency of a wing with a morphing upper surface. The wing characteristics were the following: span = 1.5m, root chord = 1.5m, sweep angle = 8deg.

The upper surface of the wing was modified between 20% and 60% of the chord by means of a flexible skin deformed by a mechanical system. The flexible skin (Pecora and Dimino, 2015 ; Salvatore *et al*., 2012) was composed of carbon fibre composite materials. The deformation system consisted of longitudinal members and ribs made from an aluminium alloy (Şugar Gabor *et al*., 2016). The numerical simulations were performed using a CFD analysis with a turbulence model able to predict the laminar-to-turbulent flow transition over the wing. This model included a fine mesh grid generation on the morphing surface that also had a grid convergence study. The Reynolds Averaged Navier-Stokes (RANS) equations with a k-ω SST model were applied for the flow analysis. Very good agreement was obtained between the numerical and the experimental results, with an average prediction error of the flow transition of approximately 5% of the chord. Both numerical and experimental results have shown that the morphing technique delayed the transition point location from 3% to 9% of the chord, which represented a considerable reduction in the total drag.

Boelens (2012) performed a CFD analysis while Anton *et al*. (2011) performed a fluid dynamics analysis on the X-31 aircraft at high angle of attack. The aim of the analysis was to determine whether or not the leading-edge details and the flap gaps needed to be taken into account for the X-31 wind tunnel model in order to properly simulate the flow around its configuration. A numerical investigation was made for three different geometries of the X-31 wind tunnel configuration with: 1) all leading-edge flap gaps, 2) only the longitudinal leading-edge flap gaps, and 3) no leading-edge flap gaps. The NLR's Cartesian mapping grid technique (Boelens *et al*., 2007) was used to generate a structured mesh for each geometry. This technique represents the geometry using "Cartesian blocks". The first layer of blocks around the geometry, and the field blocks in the physical space are automatically generated. The quality

of the grid can then be improved by using an elliptic smoothing algorithm. The solver ENSOLV (Boerstoel *et al*.,1996) was used for flow simulation. The turbulent model was a Turbulent Non-Turbulent (TNT) k-ω model (Kok, 2000). The numerical analysis results were compared to the experimental results for specific flight conditions: Mach number = 0.18, Reynolds number based on the mean aerodynamic chord Re = 2.07 million and a range of angles of attack from -5° to 55°. These results indicated that for an angle of attack less than 12°, for all the configurations, the leading edge did not have an effect. The effect of the leading-edge flap configuration was observed for angles of attack larger than 12°, where some vortices dues to the longitudinal flap gaps were created. Numerical analysis and experimental tests confirmed the very good agreement of these results.

Panagiotou *et al*. (2014) realized a winglet design and optimization methodology for a Medium Altitude Long Endurance (MALE) UAV. This methodology was also applied on to the Hellenic Civil Unmanned Aerial Vehicle (HCUAV). Initially, the wing contribution to the total drag was 40% at a trim condition and between 30% and 70% for angle of attack. The aim of their work was to reduce the drag contribution in order to maximize the flight time and the flight operation range. Six different wing configurations with the winglet were investigated by changing the cant, the toe and the sweep angle of the winglet. For each configuration, a mesh grid of 3,000,000 nodes was generated in order to model the phenomena inside the boundary layer. The aerodynamic calculations were performed using the flow solver ANSYS CFX with the Spalart-Allmaras turbulence model. The study was conducted for the loiter phase condition: range of angles of attack from -8° to 16°, speed, V=140km/h and flight altitude alt = 20,000 m, which corresponds to a Reynolds number of 1.8×10e6 based on the mean aerodynamic chord. A significant increase of the L/D (lift to drag) ratio was achieved. This performance improvement corresponded to an increase of 10% in the total flight time.

Despite the effectiveness of the CFD studies, many physical problems could not be understood. Some examples of these problems include the precise estimation of the thin-airfoil stall characteristics, of the aeroelasticity (Liauzun, 2006), of the flow over a double delta wing at a high angle of attack and the estimation of supersonic flows (Fujii, 2005). In addition to the above lacunae, aircraft geometry complexity, the nature of flow physics and computer performance can limit the accuracy of CFD analysis. These issues have prompted the present

work on a methodology to estimate the aerodynamic coefficients using a low cost and accurate method. For this purpose, a new non-linear Vortex Lattice Method (VLM) was introduced. The methodology was applied to an unmanned aerial system, the UAS-S45, designed and manufactured by Hydra Technologies (Kuitche and Botez, 2017 ; Sugar Gabor, 2015). The UAS-S45 provides surveillance and security capabilities for military and civilian purposes. General information regarding the UAS-S45 is presented in Table 4.1, while the UAS- S45 is shown in Figure 4.2.

Figure 4.2 Hydra Technologies
UAS-S45 Bàlaam

Table 4.1 General Characteristics of the UAS-S45

Specification	Value
Wing span	6.11 m
Wing area	2.72 m²
Total length	3.01 m
Mean aerodynamic chord	0.57 m
Empty weight	57 kg
Maximum take-off Weight	79.6 kg
Loitering airspeed	55 knots
Service ceiling	20, 000 ft
Operational range	120 km

The estimation presented in this paper was carried out with the aim to design an UAS-S45 flight simulator. The aerodynamic coefficients obtained using the new non-linear VLM, and the CFD method were compared to those obtained using the in-house developed Fderivatives code (Anton *et al*., 2010, 2011 ; Anton *et al*., 2009b) at the LARCASE.

This code is based on improvements of the DATCOM procedure aerodynamic formulations and was developed in-house at our Research Laboratory in Active Controls, Avionics and Aeroservoelasticity (LARCASE) of the ETS. Fderivatives code can accurately estimate the aircraft aerodynamic coefficients and their corresponding stability derivatives' from a minimum amount of geometrical data.

Based on the results of the investigation of the flow around aircraft (Boelens, 2012 ; Schütte *et al*.,2012), and by highlighting the necessity of an experimental validation, the numerical procedures thereby established was compared to experimental wind tunnel test results for a reduced scaled UAS-S45 wing.

The non-linear VLM is detailed in Section 4.2. The CFD analysis is explained in Sections 4.2 and 4.3, the experimental procedure in Section 4.4 and the Fderivatives methodology in Section 4.5. The results are presented in Section 4.6, and are followed by the Conclusions in Section 4.7.

4.2 New non-linear Vortex Lattice Method

The classical VLM is based on the resolution of the Laplace Eq. (4.1) for a potential flow by assuming a boundary condition of zero flow in the normal direction to the wing surface.

$$\nabla \left(\boldsymbol{V}_p + \varphi \right) . \boldsymbol{n} = 0 \tag{4.1}$$

where, $\boldsymbol{V}_\mathrm{p}$ is the free-stream flow, φ is the perturbation potential, and $\boldsymbol{n}$ is the vector normal to the wing surface.

In order to compute the aerodynamic forces and moments by using the classical VLM, the wing is initially divided into panels. A vortex ring is placed on the quarter chord of each panel, and a collocation point is placed at 75% of the quarter chord line from the leading edge. The velocity induced by each vortex ring to an arbitrary point is given by the Biot-Savart law:

$$\boldsymbol{V} = \frac{\Gamma}{4\pi} \frac{\boldsymbol{r}_1 \times \boldsymbol{r}_2}{\left|\boldsymbol{r}_1 \times \boldsymbol{r}_2\right|^2} \boldsymbol{r}_0 \cdot \left(\frac{\boldsymbol{r}_1}{\boldsymbol{r}_2} - \frac{\boldsymbol{r}_2}{\boldsymbol{r}_1} \right) \tag{4.2}$$

where Γ is the vortex intensity, $\boldsymbol{r_1}$ is the position vector from the beginning of the vortex line to an arbitrary point, $\boldsymbol{r_2}$ is the position vector from the end of the vortex line to an arbitrary point, and $\boldsymbol{V}$ is the induced velocity.

The unknown velocities of the vortex rings are determined by considering that the Eq. (4.1) is satisfied, which leads to the following equation:

$$\left(\boldsymbol{V}_\infty + \sum_{j=1}^{N} \Gamma_j \boldsymbol{v}_{ij} \right) . \boldsymbol{n}_i = 0 \tag{4.3}$$

where $\boldsymbol{V}_\infty$ is the freestream velocity, N is the total number of the vortex ring, $\boldsymbol{n_i}$ is the surface normal vector computed at the ith collocation point, $\boldsymbol{v_{ij}}$ is the velocity induced by the j^{th} vortex ring at the i^{th} collocation point.

In the new nonlinear VLM (Şugar Gabor *et al*., 2016), the vortex rings intensities are adjusted by using nonlinear viscous data. A correction parameter is thus added to the vortex intensities. The corrected vortex rings intensities are given by:

$$\Gamma_j + \Delta\Gamma_j \tag{4.4}$$

where $\Delta\Gamma_j$ is the correction of the vortex rings intensities.

The addition of a correction on the vortex rings intensities leads to obtaining a second induced velocity field, which converts Eq. (4.3) into following Eq. (4.5):

$$\left(\boldsymbol{V}_\infty + \sum_{j=1}^{N} \left(\Gamma_j + \Delta\Gamma_j \right) \boldsymbol{v}_{ij} + \boldsymbol{V}_i^T \right) . \boldsymbol{n}_i = 0 \tag{4.5}$$

where $\boldsymbol{V}^{\mathrm{T}}_{\mathrm{i}}$ is the surface transpiration velocity. IT is assumed, to simplify the notation, that:

$$\boldsymbol{V}_i^T = \boldsymbol{V}_i^T . \boldsymbol{n}_i \tag{4.6}$$

The following Eq. (4.7) is obtained by combining Eqs. (4.3), (4.5), and (4.7):

$$\sum_{j=1}^{N} \boldsymbol{v}_{ij} . \boldsymbol{n}_i \Delta\Gamma_j = -\boldsymbol{V}_i^T \tag{4.7}$$

A strip analysis of the wing is performed to obtain an additional set of equations needed for the problem resolution (Şugar Gabor *et al*., 2016). This strip analysis was used to calculate a set of nonlinear viscous pressure coefficient distribution. For this purpose, the wing was divided into span-wise panels, on which a control point was defined. The nonlinear viscous pressure coefficient distribution was thus calculated for local flow, for each span-wise strip at its control point by using the two-dimensional viscous flow solver XFoil (Drela, 1989).

$$C_{p,i}^{visc} = f\left(airfoil_i, Re_i, \left\|\boldsymbol{V}_i\right\|, \alpha_i\right) \tag{4.8}$$

In Eq. (4.8), Re_i is the Reynolds number, and $\boldsymbol{V}_i$ is the total velocity at the control point given by:

$$\boldsymbol{V}_i = \boldsymbol{V}_\infty + \sum_{j=1}^{N} \left(\Gamma_j + \Delta\Gamma_j\right) \boldsymbol{v}_{ij} \tag{4.9}$$

where, $\boldsymbol{V}_\infty$ is the free-stream velocity, N is the total number of vortex rings over the wing, $\boldsymbol{v}_{ij}$ is the velocity induced by the unit strength vortex ring j at the i^{th} strip control point, and α_i is the local effective angle of attack of the strip given by:

$$\alpha_i = tan^{-1}\left[\frac{\left(\boldsymbol{V}_\infty + \sum_{j=1}^{N}\left(\Gamma_j + \Delta\Gamma_j\right)\boldsymbol{v}_{ij}\right).\boldsymbol{n}_{s,i}}{\left(\boldsymbol{V}_\infty + \sum_{j=1}^{N}\left(\Gamma_j + \Delta\Gamma_j\right)\boldsymbol{v}_{ij}\right).\boldsymbol{c}_{s,i}}\right] \tag{4.10}$$

In Eq. (4.10), $\boldsymbol{n}_{s,i}$ is a unit vector in direction normal to the chord of the i^{th} strip and $\boldsymbol{c}_{s,j}$ is a unit vector in direction of the chord of the i^{th} strip.

In the case of a large sweep angle, the strip theory analysis is replaced by a sweep analysis (Şugar Gabor *et al*., 2016), and the effective angle of attack is corrected using the iterative methodology defined in (Elham, 2015 ; Mariens *et al*., 2014).

The corrected vortex ring intensities are estimated by assuming that the nonlinear viscous pressure coefficient variation obtained from the strip analysis is equal to the pressure

coefficient variation obtained from the vortex ring intensities for each panel on the wing surface. This assumption leads to the following expression:

$$-\boldsymbol{F}_i.\boldsymbol{n}_i + A_i Q_\infty \Delta C_{p,i}^{visc} = 0 \tag{4.11}$$

where $\boldsymbol{F}_i$ is the aerodynamic force generated by all the vortex lines on the panel, $\boldsymbol{n}_i$ is the surface normal vector, A_i is the panel area, Q_∞ is the dynamic pressure, and $C_{p,i}^{visc}$ is the nonlinear viscous pressure coefficient.

For an arbitrary panel, the projected force $\boldsymbol{F_i}$ onto the direction of the local normal is derived from Eq. (4.11) using the three-dimensional vortex lifting law (Şugar Gabor *et al*., 2016):

$$\begin{aligned} -\boldsymbol{F}_i.\boldsymbol{n}_i = \rho\left[\boldsymbol{n}_i \times \left(V_\infty + \sum_{j=1}^{N}\left(\Gamma_j + \Delta\Gamma_j\right)\boldsymbol{v}_{ij}\right)\right].\left[\left(\Gamma_i - \Gamma_U\right)\gamma_{12} + \left(\Gamma_i - \Gamma_R\right)\gamma_{23}\right. \\ + \left(\Gamma_i - \Gamma_L\right)\gamma_{61} + \left(\Gamma_U - \Gamma_{UR}\right)\gamma_{34} + \left(\Gamma_U - \Gamma_{UL}\right)\gamma_{56} + \left(\Delta\Gamma_i - \Delta\Gamma_U\right)\gamma_{12} \\ + \left(\Delta\Gamma_i - \Delta\Gamma_R\right)\gamma_{23} + \left(\Delta\Gamma_i - \Delta\Gamma_L\right)\gamma_{61} \\ \left. + \left(\Delta\Gamma_U - \Delta\Gamma_{UR}\right)\gamma_{34}\right. \end{aligned} \tag{4.12}$$

where ρ is the air density, γ is the geometrical segment of the vortex segment, the subscript U denotes the direct upstream ring, R and L are the right and left rings, and UR and UL are the upstream-right and upstream left rings, and the subscripts i indicates the current vortex rings.

By introducing Eq. (4.12) into Eq. (4.11) and coupling the result with Eq. (4.7), a system of $2N$ equations is obtained:

$$\boldsymbol{R} = \begin{Bmatrix} \vdots \\ -\boldsymbol{F}_i.\boldsymbol{n}_i + \boldsymbol{A}_i Q_\infty \Delta C_{p,i}^{visc} \\ \vdots \\ - - - - - - - - - \\ \vdots \\ \sum_{j=1}^{N} \boldsymbol{v}_{ij}.\boldsymbol{n}_i \Delta\Gamma_j + \boldsymbol{V}_i^T \\ \vdots \end{Bmatrix} = \boldsymbol{0} \tag{4.13}$$

This system of equations allowed calculating the *N* values of the intensities corrections and of the surface transpiration velocities needed to estimate the aerodynamic forces and moments.

4.3 CFD analysis. Grid generation

The accuracies of a structured and an unstructured mesh were investigated by Rakowitz and Eisfeld (2003). They studied the aerodynamic forces and moments of the DLR-F4 wing-body configuration. The DLR-F4 was meshed with unstructured TAU code (Gerhold *et al*., 1997) and structured FLOWer (Kroll, 1994) code. Three different solver models were used: the Wilcox-kw, the kw-linearized stress and the Spalart-Allmaras models. The numerical data obtained by the use of these models was compared to experimental data collected in first AIAA Drag Prediction Workshop (DPW) in Anaheim, California (Laflin, 2006). The results have shown that for a test case of Mach number M = 0.75 and lift coefficient CL = 0.5, where the influence of the transition was neglected, the unstructured and the structured codes gave almost identical predictions with the three different turbulence models. For a test case of Mach number M = 0.75 at a range of angle of attack from -3 deg to 2 deg with an increment 1 deg, and for which the transition and the turbulence effects were taken into account, the lift coefficient obtained with the structured grid has matched the experimental data, whereas the unstructured grid overestimated the lift coefficient by approximately 15%.

Therefore, when meshing an aircraft for computational analysis, there was a compromise in terms of the phenomena studied, complexity of the objective (the more objective become complex, the more a structured mesh was recommended), computational time, and the required accuracy. For the UAS-S45 evaluated here, a structured mesh was considered in the airfoil analysis to evaluate the flow transition, the pressure distribution and the turbulence. Furthermore, an unstructured mesh has been used for the entire UAS-S45 computational analysis because of the fact that the aircraft flies at subsonic speeds.

4.3.1 Mesh design of the S45 wing airfoil

The first step was the obtention of the aerodynamic coefficients of the airfoil, and the analysis of the flow around it, achieved by means of a 2D study of the UAS-S45 airfoil using ANSYS Fluent. The grid was generated with the Fluent meshing module; a structured mesh was selected rather than an unstructured mesh in order to align the velocity gradient with the mesh, thereby limiting dissipation errors. The use of a structured mesh was preferred, even though it is more difficult to generate it without a grid generator than an unstructured mesh, especially for complex geometry.

The grid was generated using the "edge sizing" method shown in Fig. 4.3. ANSYS provides several options to control the size of the mesh cell, one of them being the "edge sizing". This method is used to specify the size or the number of divisions along an edge, and also the growth rate of the cells away from the edge. The "edge sizing" allows to obtain a sufficiently fine mesh to accurately capture the rapid changes inside the boundary layer. To use the "edge sizing", the distance between the first node of the mesh and the airfoil was calculated (Fig. 4.4). This distance also called "distance to the wall" is important to adequately resolve velocity gradients in the viscous sublayer of the boundary layer. The calculations were based on the flat-plate boundary layer theory from White's *Fluid Mechanics* 5th Edition (White, 2003).

The flow conditions used for the grid generation were: Reynolds number R_e = 8.17×10e6, altitude *alt* =10,000ft, and the Mach number M = 0.18. The characteristic length for the Reynolds number calculation was the mean aerodynamic chord of the airfoil c = 1 m.

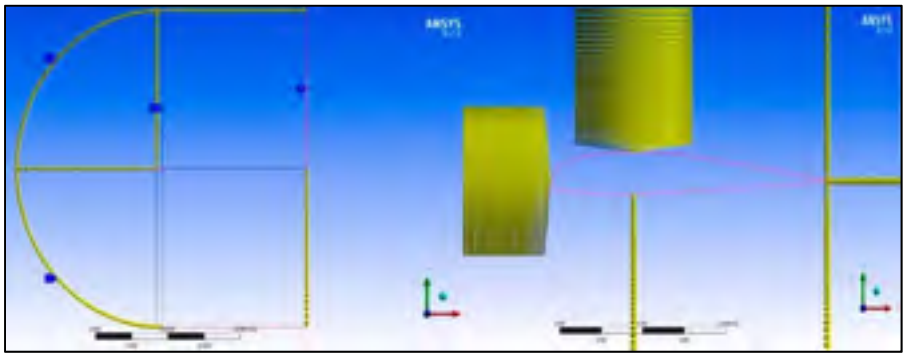

Figure 4.3 Edge Sizing using Fluent

The grid spacing required to observe the turbulent phenomenon occurring around the airfoil for different flow conditions was found using the expressions from (White, 2003):

$$R_e = \frac{\rho U_\infty L}{v} \tag{4.14}$$

$$C_F = 0.026\left(R_e\right)^{-1/7} \tag{4.15}$$

$$\tau_\omega = \frac{C_F \rho {U_\infty}^2}{2} \tag{4.16}$$

$$U_\tau = \sqrt{\frac{\tau_\omega}{\rho}} \tag{4.17}$$

$$h = \frac{y^+ v}{U_\tau \rho} \tag{4.18}$$

By substituting Eqs. (4.14)- (4.17) in Eq. (4.18), Eq. (4.18) becomes:

$$h = \frac{y^+ L}{\sqrt{0.013 R_e^{13/7}}} \tag{4.19}$$

In Eqs. (4.14) –(4.18), ρ is the air density, U_∞ is the freestream velocity, v is the dynamic viscosity, C_F is the skin friction coefficient, τ_ω is the skin shear stress, U_τ is the friction velocity, L is the reference length, in our case, the mean aerodynamic chord, *Re* is the Reynolds number and y^+ is called distance to the wall, that refers to the distance between the first node of the mesh and the airfoil (Fig. 4.4); a small value of y^+ is recommended for boundary or viscous layer analysis but the number of cells of the mesh is increased.

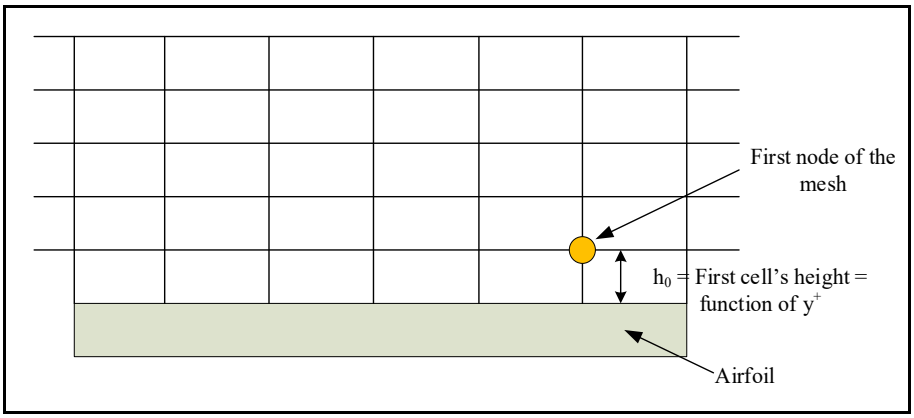

Figure 4.4 First node and cell's distance definition

The first cell's height influences the value of y^+. To calculate the first cell's height, h_0, $y^+ = 1$ should be considered. However, because the Reynolds number is very high, a very small h_0 = 8.12 ×10e-6 m was obtained (Eq. (4.19)), which led to a high number of cells and thus, an increase calculation time. Therefore, it is acceptable to consider $y^+ > 1$ to reduce the computation time.

Furthermore, in order to fully analyze all the disturbances, and especially the phenomenon of separation, it is essential that y^+ lies in the viscous sub-layer which corresponds, for a flat plate, to $0.1 > y^+ > 8$ according to the wall law (Fig. 4.5).

According to the Fluent theory guide (ANSYS, 2013), with the chosen turbulence model, a value of $y^+=5$ was chosen, which corresponds to a first cell distance of h_0=4,1×10e-5 m. The mesh was constructed so that the first cell was located at 0.04 mm from the airfoil, and the growth rate of the cells height never exceeded 1.2. Figure 4.6 shows the mesh around the airfoil.

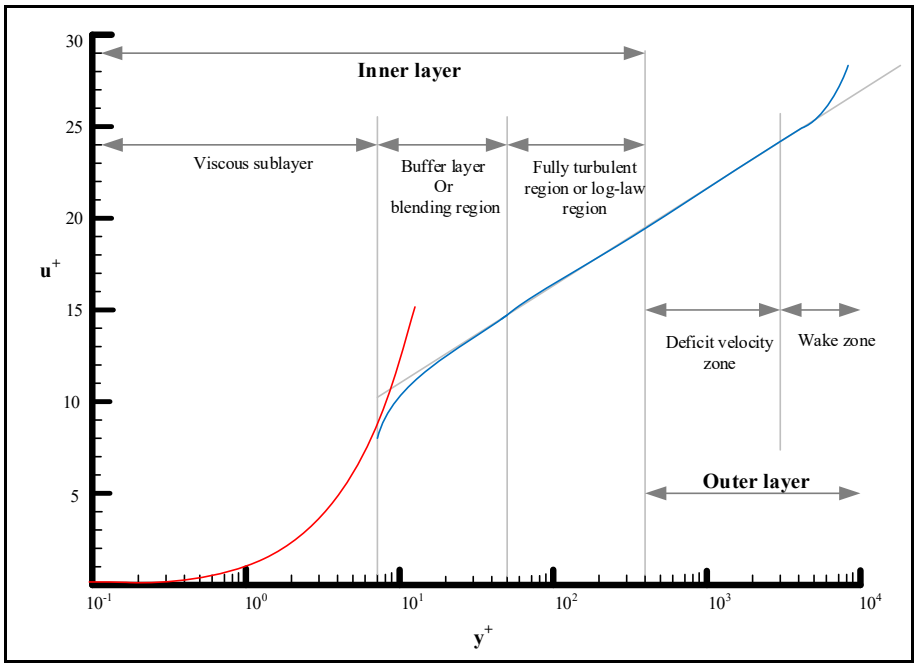

Figure 4.5 Law of the wall (Von Kármán, 1931)

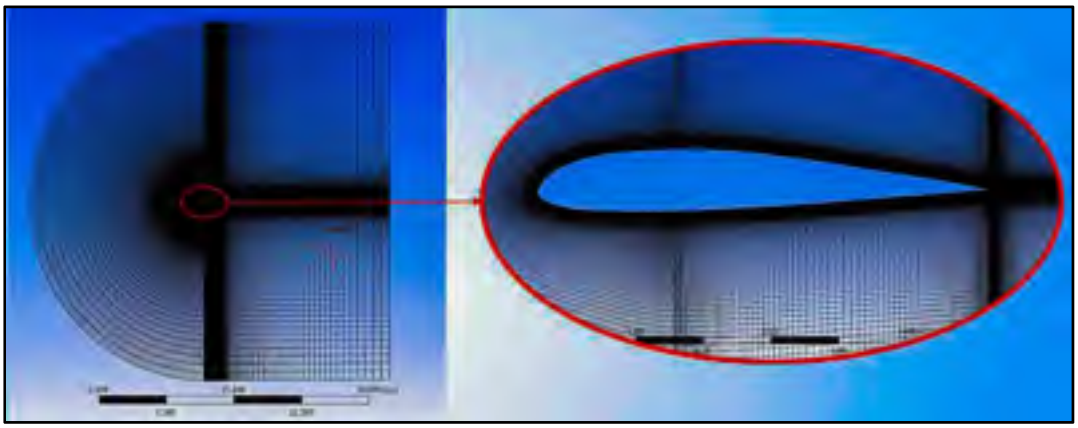

Figure 4.6 Structured mesh grid around an S45 airfoil

The mesh was validated by checking the orthogonal quality and skewness of its cells that are two very good indicators of its quality. The orthogonality is the measure of how close the angles between adjacent element faces are close to an optimal angle (ANSYS, 2013) (90° for quadrilateral faces elements). A value close to 1 corresponds to a good orthogonality. The skewness is the measure of the difference between the shape of the cell and the shape of an

equilateral cell of equivalent volume (ANSYS, 2013). A value close to 0 corresponds to a good skewness. For the case of the UAS-S45 airfoil, the orthogonal quality was 0.978, while the skewness quality for the generated grid was 0.056 which indicate a good quality of mesh.

4.3.2 Mesh design of the entire S45-UAV

In the case of the entire UAS-S45, a grid convergence study was performed to evaluate the mesh density required for the aerodynamic coefficient estimations. Five mesh models were generated; each mesh was analysed at a Mach number of 0.14, an altitude of 0 ft and an angle of attack of 0 deg. Table 4.2 presents the statistics and the inflation parameters of each of the five generated meshes. The statistics parameters show the number of cells and node of the mesh and therefore give an overview of the complexity of the mesh and the calculation time needed to obtain a solution. The inflations parameters show the 1st layer thickness and the maximum layers. The values of these parameters depend on the phenomena studied. For example, a small value of the 1st layer thickness is recommended for boundary layer analysis.

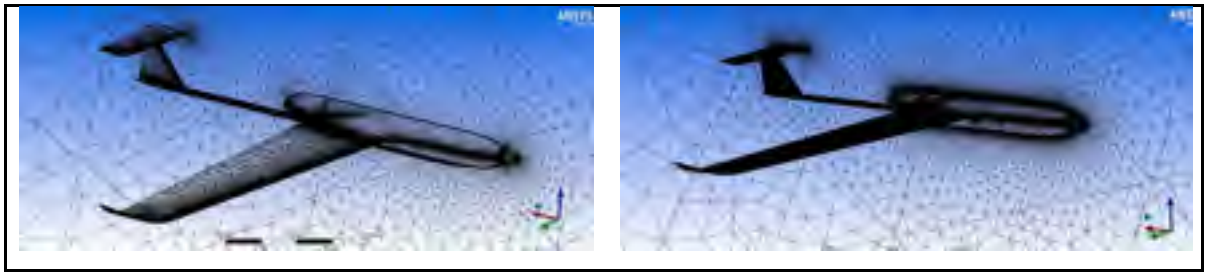

Figure 4.7 UAS-S45 Mesh grid variation

Table 4.2 Parameters of the generated meshes

	Statistics parameters		Inflation parameters	
Mesh	**Number of cells**	**Number of nodes**	**1st layer thickness (m)**	**Maximum layers**
Mesh 1	1,765,718	413,215	0.0006	8
Mesh 2	2,989,591	847,864	0.002	5
Mesh 3	3,349,435	922,813	0.002	5
Mesh 4	3,942,176	1,173,134	0.0006	8
Mesh 5	10,158,869	2,722,846	0.00006	8

Table 4.3 Results obtained for the grid convergence study

	Aerodynamic coefficients			Orthogonal quality of meshes	
Mesh	**CL**	**CD**	**Cm**	**Min**	**Average**
Mesh 1	0.167	0.019	-0.024	0.030514	0.84961
Mesh 2	0.161	0.020	-0.025	0.017939	0.85038
Mesh 3	0.166	0.020	-0.027	0.01305	0.85291
Mesh 4	0.162	0.019	-0.023	0.020536	0.8486
Mesh 5	0.167	0.019	-0.020	0.027141	0.83742

The aerodynamics lift and drag coefficients and the orthogonal qualities for each mesh model were calculated and further presented in Table 4.3. This table shows the differences in aerodynamic coefficients values obtained with mesh 5 versus the aerodynamic coefficients calculated with other meshes. Mesh 5 was selected as a reference mesh because of the fact that it contains the highest number of cells. A maximum relative error of 3% in C_L and C_D was found.

For the design of an aerodynamic model of the UAS-S45, the first cell of the mesh may not be located in the viscous sublayer of the boundary layer. In fact, according to Eq. (4.19) for *h,* and

for flight cases: Mach number M= 0.14, altitude alt =10,000ft, and wall distance of y^+=1, in order to resolve the viscous sublayer, the first cell should be located at 9.5×10e-6m from the aircraft, which is a very small value. This arrangement will result in a decrease in mesh quality and in a divergence in the simulation for a fixed number of cells because the phenomena complexity is increased but the number of cells is the same.

To avoid reducing the mesh quality, an appropriate sizing is required in order to create very small cells close to the aircraft, therefore an increase in the number of cells must be considered as well as the increase of the total simulation time.

Therefore, as a compromise between the mesh quality and the number of cells, **mesh 2** was selected. Mesh 2 corresponds to a wall distance of y^+=200.

To reduce computing time, the number of cells has been reduced without decreasing the quality of the mesh by transforming the tetrahedral mesh into polyhedral mesh (Fig. 4.8). In some cases, the transformations can increase the quality of some cells located out of the boundary layer, but the cells of poorer quality (in general those in the inflation) remain unchanged since the transformation does not affect inflation. Table 4.4 shows the mesh model parameters used for the aerodynamics calculations.

Table 4.4 UAS-S45 mesh 2 model parameters

Parameter	**Number of cells**		**1st layer height**	**Number of layers in the inflation**	**Orthogonal quality average**	**Skewness average**
	Tetrahedral	**Polyhedral**				
values	3,349,435	1,049,508	0.002m	10	0.85291	0.26897

a)

b)

Figure 4.8 Tetrahedral mesh (a), Polyhedral mesh (b)

4.4 CFD analysis. Flow solver

4.4.1 General description of the flow solver

ANSYS Fluent software (2013) was used to describe the pattern flow around the UAS-S45. ANSYS Fluent is capable of solving the Navier-Stokes equations for a wide range of incompressible and compressible, laminar and turbulent fluid flows. The software is useful to solve flow problems for various types of meshes, including unstructured meshes that can be generated about complex geometries relatively easy. Time integration is carried out using a three-stage explicit Runge-Kutta scheme. For steady-state flow simulations, convergence acceleration is achieved using local time stepping, residual smoothing, and a full-approximation storage multigrid.

Setting the fluid flow for aerodynamic analysis using ANSYS Fluent includes defining the boundary conditions and the turbulence model.

4.4.2 Boundary conditions

As a boundary condition for solving the UAS-S45 aerodynamics, the fluid is assumed to stick to the wall, and to move with the same velocity as it. Therefore, a no-slip condition was

selected. A symmetry condition was also used at the symmetry plane of the UAS to reduce computation time.

4.4.3 Turbulence model

By considering a turbulent flow, viscosity is assumed to not affect the larger-scale eddies, with the exception of the viscous sublayer in the boundary layer. The effects of the density fluctuations on the turbulence are assumed to be small. Thus, the direct effect of viscosity and compressibility on turbulence can be neglected (Argyropoulos and Markatos, 2015) . The flow variables can be decomposed into their time-average values and their fluctuating components. These assumptions lead to the Reynolds-Averaged Navier-Stokes (RANS) equations. The Boussinesq eddy-viscosity hypothesis was used to solve the problem of "closure" by relating the Reynolds stress tensor and the turbulent heat flux to the average flow variables. The following equations are obtained:

$$\frac{\partial \rho}{\partial t} + \frac{\partial}{\partial x_j}(\rho U_j) = 0 \tag{4.20}$$

$$\frac{\partial}{\partial t}(\rho U_i) + \frac{\partial}{\partial x_j}\left(\rho U_i U_j\right) = -\frac{\partial \mathrm{P}}{\partial x_i} + \frac{\partial}{\partial x_j}\left[\mu_{eff}\left(\frac{\partial U_i}{\partial x_j} + \frac{\partial U_j}{\partial x_i}\right) - \frac{2}{3}\mu_{eff}\frac{\partial U_k}{\partial x_k}\delta_{ij}\right] \tag{4.21}$$

$$\begin{aligned} &\frac{\partial}{\partial t}\left(\rho H\right) - \frac{\partial P}{\partial t} + \frac{\partial}{\partial x_j}\left(\rho U_j H\right) = \frac{\partial}{\partial x_j}\left[\lambda\frac{\partial T}{\partial x_j} + \frac{\mu_t}{Pr_t}\frac{\partial h}{\partial x_j}\right] + \\ &\frac{\partial}{\partial x_j}\left\{U_i\left[\mu_{eff}\left(\frac{\partial U_i}{\partial x_j} + \frac{\partial U_j}{\partial x_i}\right) - \frac{2}{3}\mu_{eff}\frac{\partial U_k}{\partial x_k}\delta_{ij}\right] + \mu\frac{\partial k}{\partial x_j}\right\} \end{aligned} \tag{4.22}$$

where ρ is the fluid density, U_i are the velocity components, P is the sum of the static pressure, μ_{eff} is the effective viscosity, which is the sum of the molecular viscosity μ and the turbulent viscosity μ_t, H is the total enthalpy, T is the fluid temperature, δ_{ij} is the Kronecker delta function, λ is the thermal conductivity, Pr_t is the turbulent Prandtl number, h is the static enthalpy and k is the turbulent kinetic energy (Şugar Gabor *et al*., 2016).

For the UAS-S45 aerodynamic analysis, two turbulence models were added to the Reynolds-Averaged Navier-Stokes equations: the Spalart-Allmaras model for the entire UAS and the *k-ω* model for the UAS airfoil.

The single-equation Spalart-Allmaras model was used to estimate the turbulence kinetic energy, *k*. This model was designed and optimised for flows past wings and airfoils, and can be implemented for any type of grid (Argyropoulos and Markatos, 2015). The Spalart-Allmaras model determines the transported variable, $\tilde{\nu}$ which is identical to the turbulent kinematic viscosity except in the near-wall region. Equation (4.5) is thus added to the RANS equations (Spalart and Allmaras, 1992).

$$\frac{\partial}{\partial t}(\rho\tilde{\nu}) + \frac{\partial}{\partial x_i}(\rho\tilde{\nu}U_i) = G_\nu + \frac{1}{\sigma_\nu}\left[\frac{\partial}{\partial x_j}\left\{(\mu+\rho\tilde{\nu})\frac{\partial\tilde{\nu}}{\partial x_j}\right\} + C_{b2}\rho\left(\frac{\partial\tilde{\nu}}{\partial x_j}\right)^2\right] - Y_\nu \qquad (4.23)$$

$$G_\nu = C_{b1}\rho\tilde{S}\tilde{\nu} \qquad (4.24)$$

$$Y_\nu = C_{\omega 1}\rho f_\omega\left(\frac{\tilde{\nu}}{d}\right)^2 \qquad (4.25)$$

$$\tilde{S} \equiv S + \frac{\tilde{\nu}}{\kappa^2 d^2} f_{\nu 2} \qquad (4.26)$$

where G_ν is the production of turbulent viscosity, Y_ν is the destruction of turbulent viscosity that occurs in the near-wall region due to wall blocking and viscous damping, ν is the molecular kinematic viscosity, S is the measure the deformation tensor, d is the distance from the wall, f_ω and $f_{\nu 2}$ are empirical function of the turbulence model, $\sigma_{\tilde{\nu}} = 0.66$, $C_{b1} = 0.1355$, $C_{b2} = 0.622$, $C_{\omega 1} = 3.23$, and $\kappa = 0.4187$ are constants.

Since the Spalart-Allmaras model does not calculate the turbulent kinetic energy *k*, the terms related to the turbulent kinetic energy in the RANS equations are neglected. Eqs. (4.21) and (4.22) become:

$$\frac{\partial}{\partial t}(\rho U_i) + \frac{\partial}{\partial x_j}\left(\rho U_i U_j\right) = \frac{\partial P}{\partial x_i} + \frac{\partial}{\partial x_j}\left[\mu_{eff}\left(\frac{\partial U_i}{\partial x_j} + \frac{\partial U_j}{\partial x_i}\right)\right] \tag{4.27}$$

$$\begin{aligned}\frac{\partial}{\partial t}\left(\rho H\right) - \frac{\partial P}{\partial t} + \frac{\partial}{\partial x_j}\left(\rho U_j H\right) = \frac{\partial}{\partial x_j}\left[\lambda\frac{\partial T}{\partial x_j} + \frac{\mu_t}{Pr_t}\frac{\partial h}{\partial x_j}\right] + \\ \frac{\partial}{\partial x_j}\left\{U_i\left[\mu_{eff}\left(\frac{\partial U_i}{\partial x_j} + \frac{\partial U_j}{\partial x_i}\right)\right] + \mu\frac{\partial k}{\partial x_j}\right\}\end{aligned} \tag{4.28}$$

The second turbulence model is the *k-ω* model. The *k-ω* model achieves high accuracy for boundary layers with adverse pressure gradient, and can be easily integrated into viscous sub-layers without any additional damping function (Argyropoulos and Markatos, 2015 ; Boelens, 2012). While the *k-ω* model has some weaknesses in flows with free stream boundaries, it can still give a very good estimation for general subsonic flows.

The *k-ω* model estimates the turbulence kinetic energy *k* and the specific rate of dissipation *ω* by adding two more equations to the RANS equations (Wilcox, 2008; Menter, 1994):

$$\frac{\partial}{\partial t}\left(\rho k\right) + \frac{\partial}{\partial x_j}\left(\rho U_j k\right) = \rho P_k - \beta^* \rho\omega k + \frac{\partial}{\partial x_j}\left[\left(\mu + \sigma_k \mu_t\right)\frac{\partial k}{\partial x_j}\right] \tag{4.29}$$

$$\frac{\partial}{\partial t}\left(\rho\omega\right) + \frac{\partial}{\partial x_j}\left(\rho U_j\right) = \frac{\gamma\omega}{k} P_k - \beta\rho\omega^2 + \frac{\partial}{\partial x_j}\left[\left(\mu + \sigma_\omega \mu_t\right)\frac{\partial \omega}{\partial x_j}\right] \tag{4.30}$$

where, ω is the specific rate of dissipation, P_k is the turbulent kinetic energy due to mean velocity gradients, and $\gamma = 0.52$, $\sigma_k = 0.6$, $\sigma_\omega = 0.5$ and $\beta = 0.06$ are the model's constants.

4.5 Experimental analysis

A wind tunnel experiment was used to validate our computational fluid dynamics methodology. This experiment was performed in the Price-Paidousis low speed wind tunnel

(Communier *et al*., 2015 ; Flores Salinas, 2015). This wind tunnel is composed of a power unit, a settling unit, a contraction unit and a test unit (Fig. 4.9).

The power unit is a room of 80 m² containing a 40hp power direct current motor driving a centrifugal fan. The fluid flow is parallel to the axis of rotation at the inlet of the air intakes, and is perpendicular to the axis of rotation at the outlet of the fan (Flores Salinas, 2015).

The settling unit directs the pressurized air from the power unit to the test chamber while giving it the desired flow characteristics. The settling unit contains a wide-angle diffuser that slows the fluid as much as possible on a short distance to maximize pressure retention. The resulting flow can then be changed and may become turbulent. Five rectifier filters have been re-added to the settling unit to improve the quality of the flow: 1 honeycomb filter to reduce eddies and 4 nylon filters with square pattern holes to produce the desired flow (Flores Salinas, 2015).

The contraction unit is a convergent base of 62.5×91.5 cm² downstream and of 200×200cm² upstream. It is designed to accelerate the fluid in order to reach its maximum speed.

The test unit or test chamber has a length of 182.5 cm, a height of 91.5cm and a width of 62.5 cm. Its size allows reduced scale models of wings to be tested when they are placed in its center.

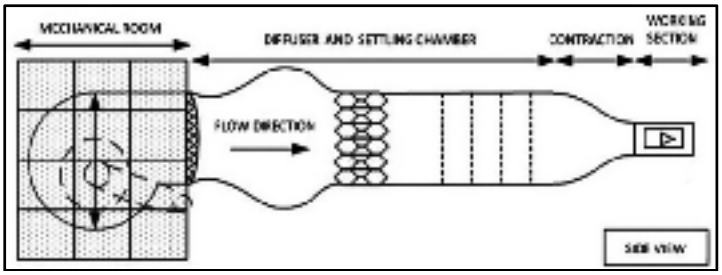

Figure 4.9 Price-Paidousis wind tunnel sections

A wind tunnel calibration was made to determine the air flow conditions in the test chamber using the Log-Tchebycheff (Log-T) method (Fig. 4.10). The accuracy of the estimated local velocities using the Log-T method is often decreased due to Pitot tube measurements uncertainties. Mosbah *et al*. (2013) developed a methodology to cope with this decrease in accuracy. Their methodology used a minimum of dynamic pressure measurements from a Pitot

tube, and estimated the dynamic pressure from a neural network that has been optimized with a great deluge algorithm. This methodology was applied in this work. The calibration of the wind tunnel was made using two airspeeds of: 5.5m/s and 26.5m/s.

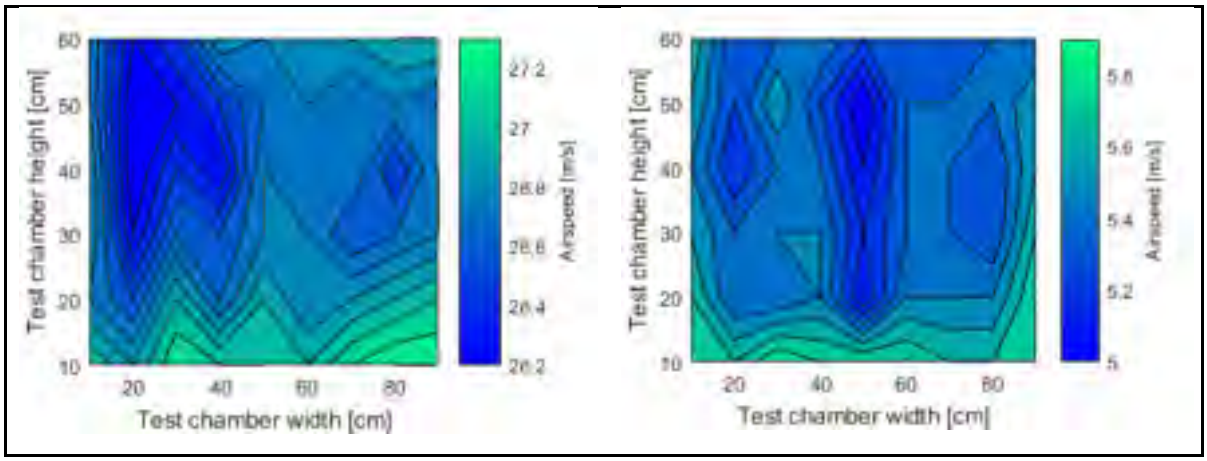

Figure 4.10 Airflows obtained from the Log-Tchebycheff method

Figure 4.10 shows that the flow seems to be uniform in the test chamber. There is a contraction phenomenon at the border of the chamber which causes an acceleration of the fluid. Therefore, the wing model should be small enough to not be in contact with the flow on the border of the test chamber, and big enough to make possible the aerodynamic coefficient measurements.
The wind tunnel wing model was chosen to be a rectangular wing with a chord of 10 inches and a span of 12 inches, which corresponds to 2% of the surface of the test chamber. The wing model was built of wood. Five plywood ribs were cut and assembled using a spar, and the assembly was covered with thin strips of balsa wood. Very small amounts of plastic were then placed to smooth the surfaces and to make them uniform (Fig. 4.11).

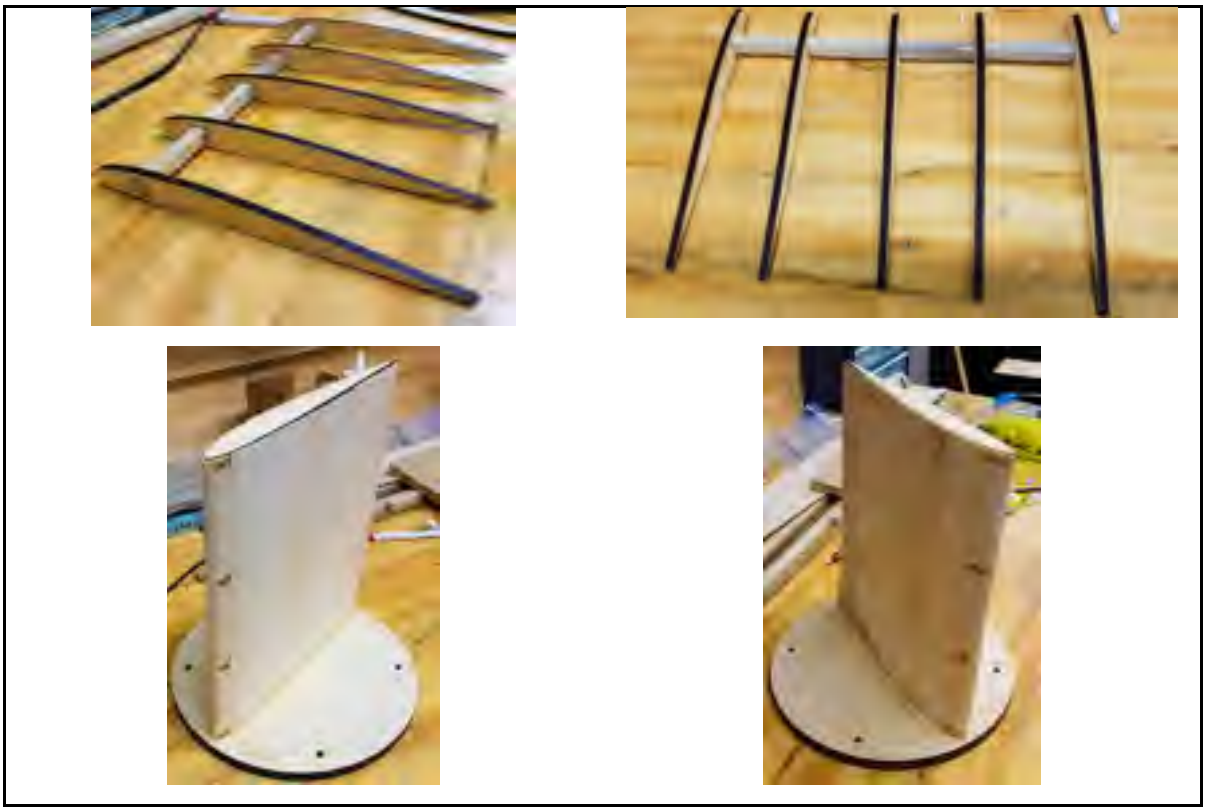

Figure 4.11 UAS-S45 wing model setup

The wind tunnel tests were performed using an aerodynamic scale and a Pitot tube. The scale consists of two plates fixed on a force sensor, one being fixed to the test chamber, the other one being mounted on a gear assembly driven by a servomotor. This servomotor allows the angle of attack to be changed automatically during the test. A mini 40E sensor is connected to a National Instrument acquisition box. The data collected by the box can be directly read and stored with an interface realized using Labview software (Communier *et al*., 2015). The Pitot tube is connected to an FKS 1DP-PBM meter for air pressure, speed and flow measurements (Fig. 4.12). The FKS 1DP-PBM is used to obtain the airflow velocity inside the test chamber knowing the temperature, the humidity, the *K*-factor and the ambient pressure.

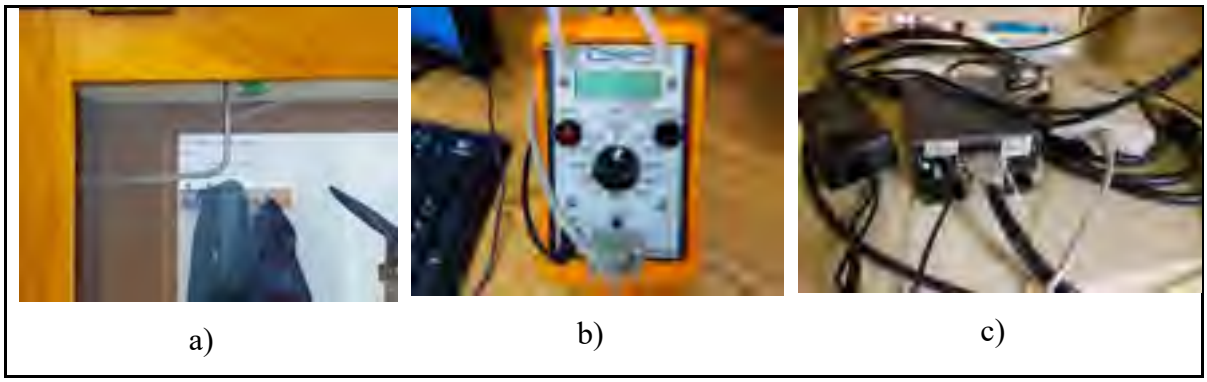

Figure 4.12 Pitot tube (a); FKS 1DP-PBM meter (b); mini 40E (c)

4.6 Fderivatives' methodology

While CFD and experimental methods give accurate results on aerodynamic estimations, they can be very demanding in terms of time and budget. Semi-empirical methods such as our in-house Fderivatives are often used to avoid those drawbacks.

Fderivatives is a collection of methodologies and algorithms for estimating aircraft aerodynamic coefficients and stability derivatives. Primarily designed as an improvement of the classical DATCOM procedure (Williams and Vukelich, 1979), its main improvements are related to the calculation of the aerodynamics characteristics for airfoils, and for entire aircraft in the "Wing-Body-Tail" configuration.

The accuracy of an airfoil's aerodynamic parameters' estimation has a major influence on the aerodynamics results for that aircraft. To validate an airfoil's aerodynamic parameters, Popescu (Popescu, 2009) performed numerical calculations using DATCOM and Fderivatives codes on NACA 4, 5, 6 and 6A digits airfoils. For a collection of 30 airfoils, the estimated the lift curve slope, the zero lift angle of attack and the maximum lift coefficient for a range of Mach numbers from 0.1 to 0.3, and Reynolds numbers from 1×10e6 to 9×10e6. The results gave mean errors of 1.91%, 3.52% and 6.85% between the experimental and the estimated values of the lift curve slope, the zero lift angle of attack and the maximum lift coefficient, respectively.

In the same way, Anton *et al.*(2011) validated the results obtained for an aircraft in a "Wing-Body-tail" configuration. The estimations were performed on a X-31 aircraft. The lift, drag

and pitch moment coefficients obtained experimentally in a wind tunnel were compared to those obtained using Fderivatives, DATCOM and the Jorgensen methods. The calculations were performed for a Mach number of 0.18, a Reynolds number of 2.07×10e7 based on the mean aerodynamic chord, and a range of angles of attack from -2° to 20°. The results have shown a decrease in the estimation errors of 11% by using Fderivatives compared to two other methods (DATCOM and Jorgensen) errors.

The Fderivatives code was used in this paper to estimate the aerodynamic behaviour of the UAS-S45 airfoil, and entire geometry in "Wing-Body-Tail" configuration (Fig.4.13). Compared to other methods, the Fderivatives code used a minimum amount of geometrical data to obtain its results. The wing was represented using its airfoil coordinates at the tip, the MAC and the root position, as well as its aspect and taper ratios, its area, its dihedral and its quarter chord sweep angles. The horizontal and the vertical tail were defined in the same way as the wing.

The fuselage was analysed as divided in 20 elliptical cross sections along the length of the UAS-S45. The nose, the forebody and the afterbody of the UAS were assumed to have conical shapes.

The Fderivatives code does not take into account the geometries of the winglets, the landing gear or the twin vertical tail. Therefore, the winglets and the landing gear were neglected, and the twin vertical tail was replaced by a single vertical tail having twice the area of each of the original tails.

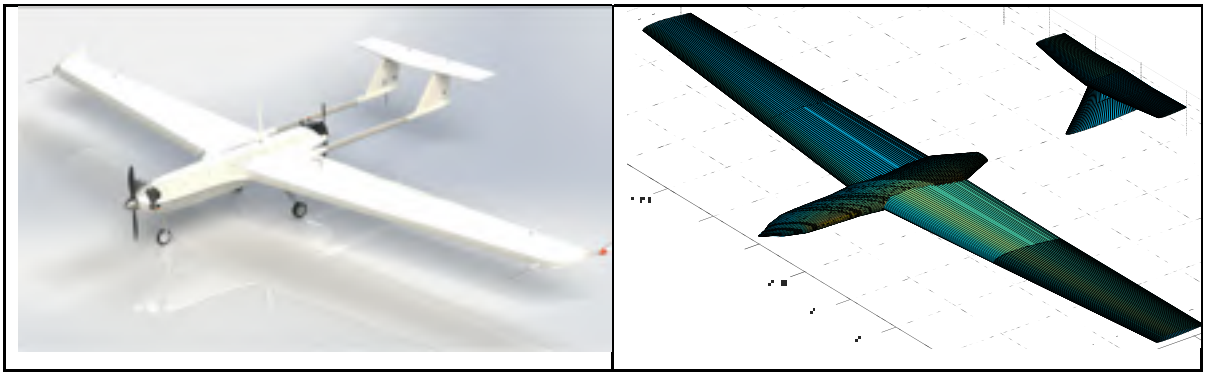

Figure 4.13 UAS-S45 in "Wing-Body-Tail" configuration in Fderivatives

4.7 Results and discussion

In this chapter, the relative error is defined as being calculated between a reference value x_a and an approximated value x_b with the equation $\left|\frac{x_b - x_a}{x_a}\right| * 100\%$.

4.7.1 Validation of the numerical procedure

In order to validate the numerical approach, the CFD and experimental analysis results on a reduced scale model of the UAS-S45 wing were compared. The methodology to obtain the wing model was the same as the methodology described in Section 4.2 for the entire UAS-S45. A polyhedral mesh grid was generated with 4,716,118 cells. Table 4.5 presents the characteristics of the mesh grid model.

Figure 4.14 Mesh grid model
of the UAS-S45 wing

Table 4.5 UAS-S45 wing model mesh parameters

Parameters	**Number of cells**	**1st layer height**	**Number of layers in the inflation**	**Orthogonal quality average**	**Skewness average**
Values	4,716,118	0.002m	10	0.8166	0.37977

The simulation used a k-ω SST model as “turbulence model”. In the wind tunnel test chamber, the flow on the walls was laminar. The wing model was fixed to the test unit floor, and the flow around the wing tip was “laminar”. However, during the numerical simulation of a finite wing, the higher air pressure under the wing tried to move around the tip towards the lower pressure above the wing, and then creates trailing vortices. To cope with this problem in CFD analysis and to obtain the same flow as the one in the experiment analysis, a symmetry condition was added on the wing tip (Fig. 4.15).

Figure 4.15 UAS-S45 wing model symmetry condition

The experimental (Section 4.4) and the numerical analyses were performed for the following specific flow conditions: speeds V =10m/s, 20m/s, 30m/s; altitude alt = 0ft, and for a range of angles of attack between -10° and 10°.

Figure 4.16 shows the lift coefficients obtained using numerical and experimental approaches as functions of speeds. It is obvious that the speed has no significant influence on the results. The non-influence of speed could be explained by the fact that the flow remains subsonic, and the Mach number M remains smaller than 0.2. Thus, the compressible effect of the flow is neglected.

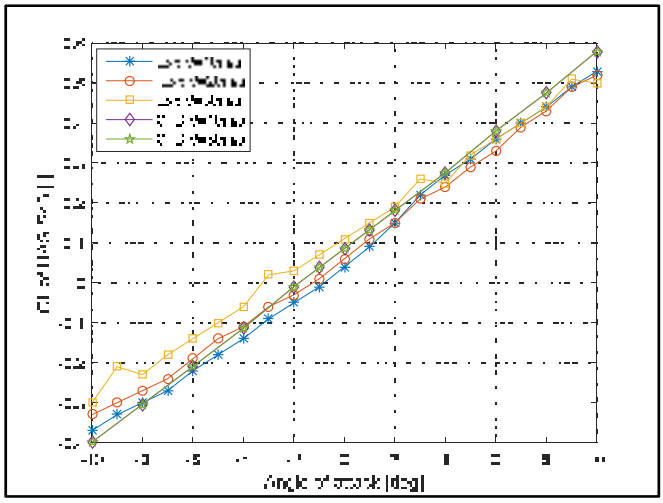

Figure 4.16 Experimental and numerical
lift coefficients' variations with angle of attack
for several airspeeds

Next, the numerical and experimental lift and drag coefficients for varying angles of attack were compared. Figures 4.17 and 4.18 show a test case for the speed v = 30m/s, and altitude alt = 0ft. This test case was selected because this airspeed makes it possible to obtain a drag force much higher than the sensor noise, and thus to facilitate the measurements process. It has been noticed that a very good agreement between the CFD ANSYS Fluent software, the nonlinear VLM and the experimental analysis results for both lift and drag coefficients variations (Fig. 4.17).

However, a small relative error was found between the lift variations with angle of attack) obtained using experimental testing, the numerical CFD and nonlinear VLM theories, as well as the DATCOM and Fderivatives' semi-empirical methodologies (Fig. 4.18).

These differences (relative errors) could be explained by the presence of the "trailing vortices" calculated using the finite wing theory. These trailing vortices were neglected for the case of the CFD analysis, and for the case of the nonlinear VLM these trailing vortices depend on the number of strips considered in the strip analysis. This comparison confirmed the superiority of the CFD theory, as well as of the proposed nonlinear VLM with respect to the other numerical approaches, along with its performance validation with respect to the experimental results values.

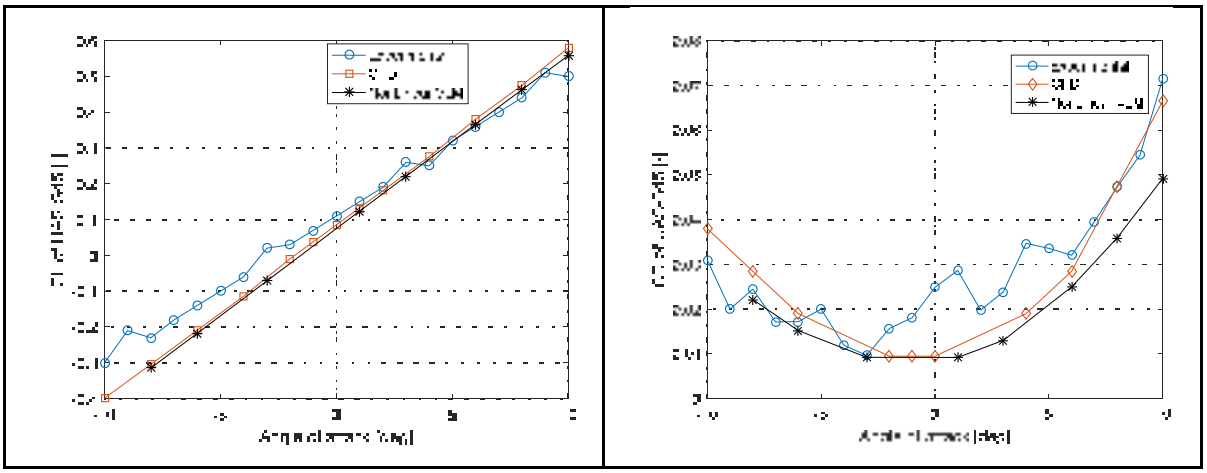

Figure 4.17 Comparison between the lift and drag coefficients' variations with angles of attack obtained with experimental, nonlinear VLM and CFD analyses for V=30m/s

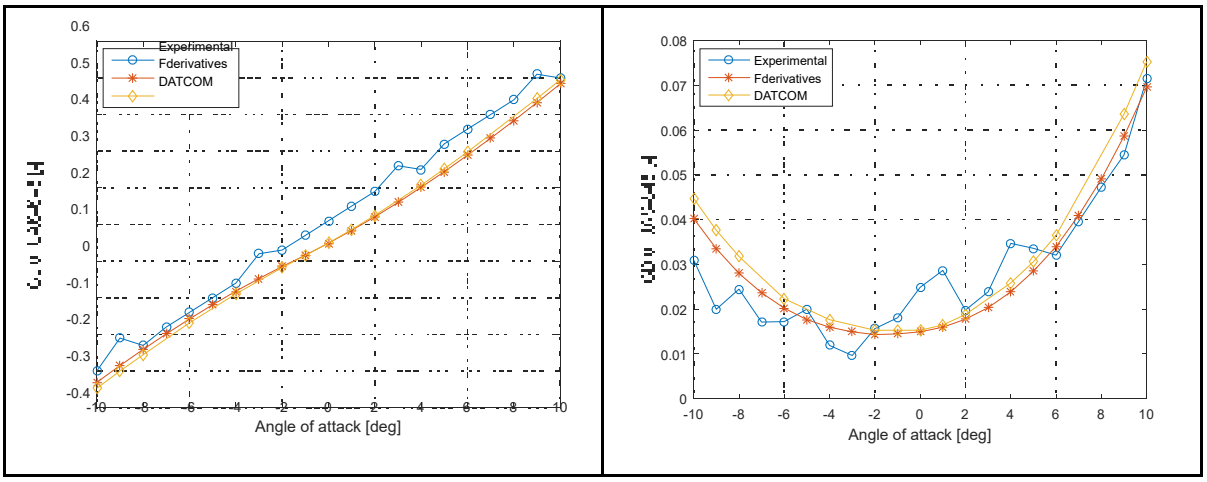

Figure 4.18 Comparison between the lift and drag coefficients' variations with angles of attack obtained with experimental analysis, DATCOM and Fderivatives procedure for V= 30m/s

4.7.2 Airfoil coefficients C_L and C_D comparison

The methodology for estimating the airfoil aerodynamic coefficients using ANSYS Fluent was elaborated in Sections 4.2 and 4.3. The analysis of the S45 airfoil was performed for Mach number 0.18, Reynolds number 1.72×10^6, and a range of angles of attack from -20° to 20°.

Lift and drag coefficients were obtained as well as their corresponding polar curves (C_L vs C_D) (Fig. 4.19).

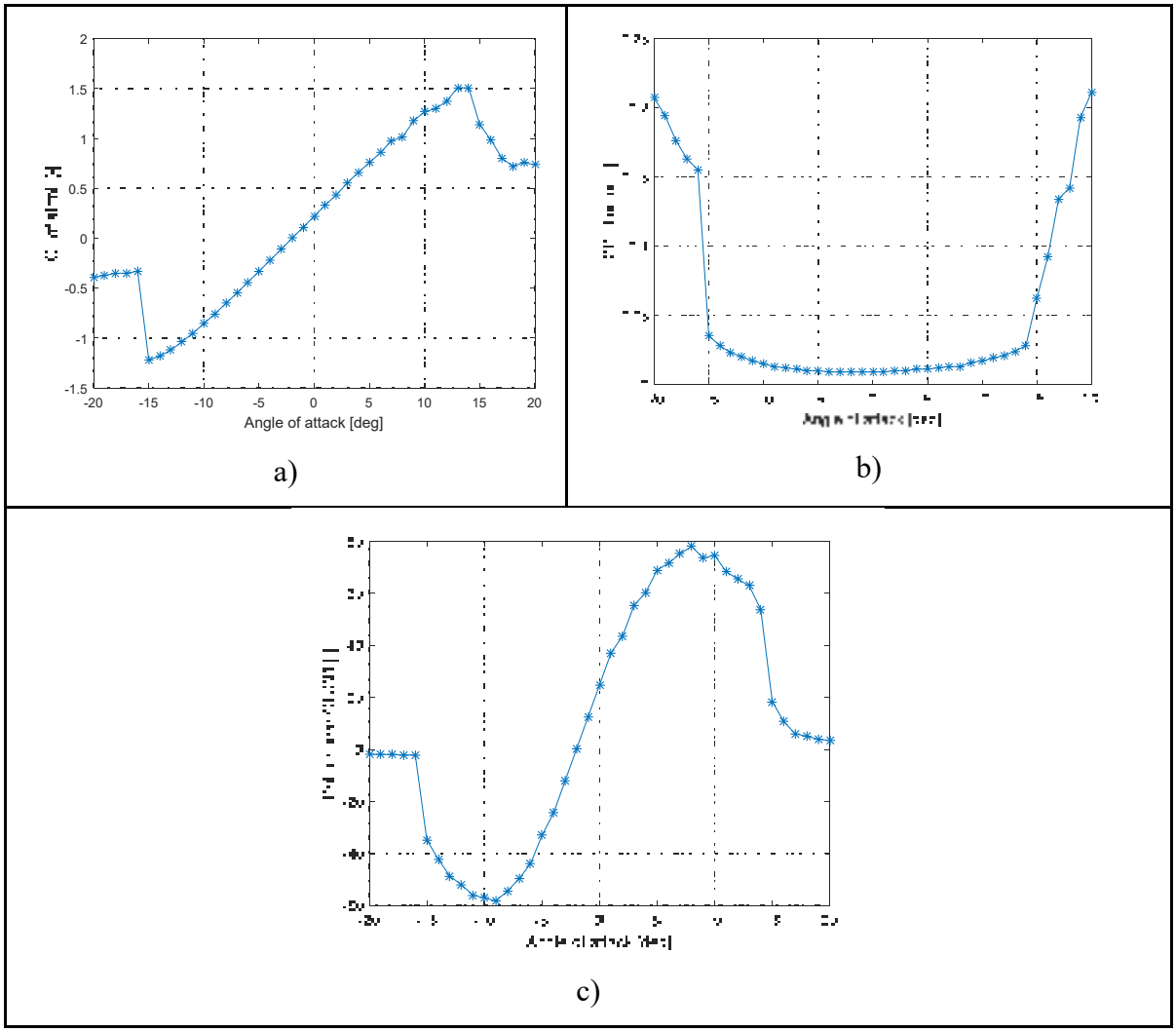

Figure 4.19 UAS-S45 airfoil lift coefficient (a), drag coefficient (b) and polar curve (c) variation with angle of attack for Mach number M=0.18

The evolution of the pressure distribution with angle of attack was also obtained. From Figure 4.20, it can be observed that for an angle of attack equal to 0°, there is a negative pressure on the upper wing surface which is causing the lift force creation. When the angle of attack becomes positive, the pressure on the upper surface decreases, and the pressure on the lower surface increases. Furthermore, for negative angles of attack, the pressure on the lower surface

is less than the pressure on the upper surface. This analysis could be validated from airfoil aerodynamics theory point of view.

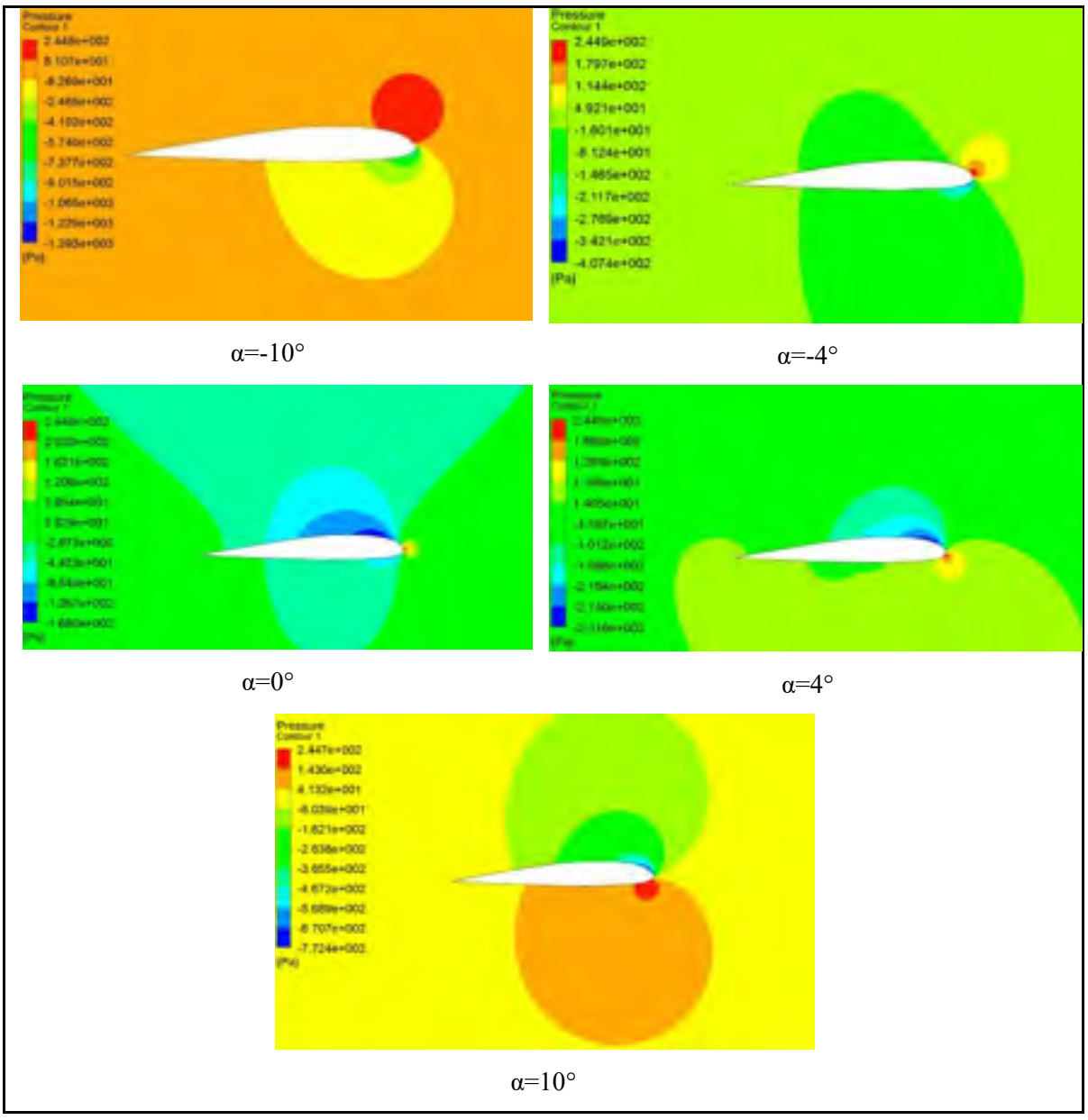

Figure 4.20 UAS-S45 airfoil pressure distribution with angle of attack

The results obtained with ANSYS Fluent were compared with those obtained using Xfoil software (Drela, 1989 ; Morgado, Vizinho, Miguel, AR, & Jose Carlos, 2016). XFoil is a

program commonly used in research to estimate the aerodynamic coefficients of an airfoil for any given Reynolds and Mach numbers. The range of angles of attack was limited to -15° to 15° because of the stall, a phenomenon that is not accurately predicted using XFoil software. The results obtained with the CFD analysis were similar to those obtained with Xfoil for the linear region of the lift coefficient variation with angle of attack (Fig. 4.21). The agreement between results decreases around the angle of attack of 14° because of the beginning of the stall at this angle. Table 4.6 presents a comparison of five main aerodynamic parameters calculated with XFoil and ANSYS Fluent.

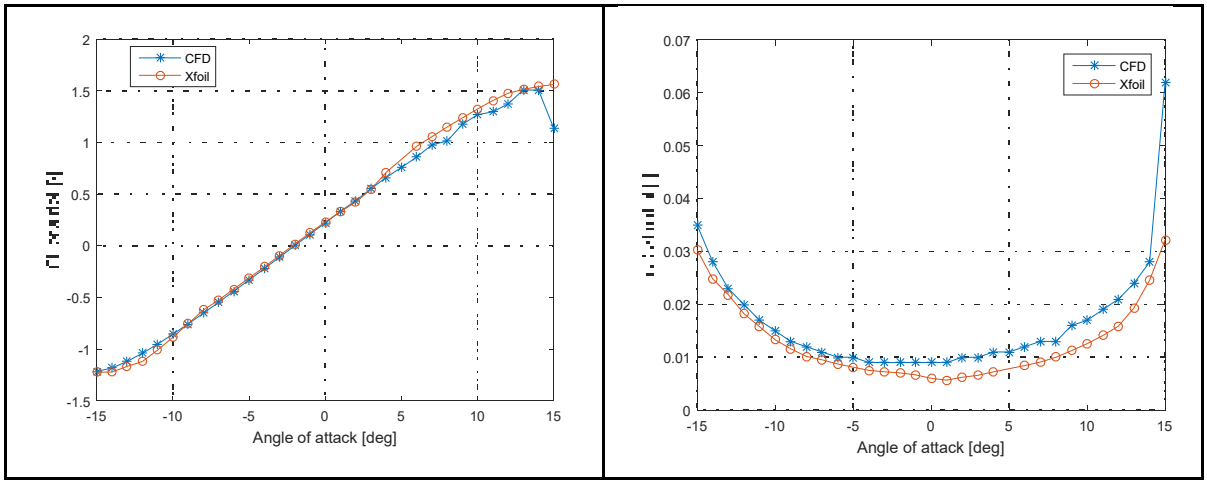

Figure 4.21 UAS-S45 airfoil lift and drag coefficient variation with the angle of attack at Reynolds number = $1.72*10^6$ and Mach number = 0.18

Table 4.6 Airfoil parameter comparison

Parameters	ANSYS Fluent	Xfoil
Minimum drag coefficient, C_{Dmin}	0.009	0.005
Maximum lift coefficient, C_{Lmax}	1.51	1.56
Minimum lift coefficient, C_{Lmin}	-1.22	-1.16
Zero angle of attack lift coefficient, C_{L0}	0.22	0.23
Zero lift coefficient angle of attack, α_0	-2.011	-2.20

4.7.3 UAS-S45 aerodynamic coefficients' comparison

The CFD analysis of the UAS-S45 was designed to establish an aerodynamic model by estimating its aerodynamic coefficients, particularly the lift, drag and pitch moment coefficients. The CFD analysis was performed for several different flight conditions, expressed in terms of Mach number, altitude and angle of attack, and for different aircraft configurations (Wing-Body, Tail, Wing-Body-Tail). The flight test cases are presented in Table 4.7. The results obtained from the CFD analysis using ANSYS Fluent were compared to those obtained using Fderivatives and DATCOM codes.

Table 4.7 Flight test cases for determining the aerodynamic coefficients

Altitude [ft]	Mach number [-]	Angle of attack [deg]
0 – 20,000	0.10 – 0.2	-17 – 17

Figure 4.22 shows a comparison of the three aerodynamic coefficients CL, CD, Cm as function of three Mach numbers and for a range of angles of attack between -10° and 12° for a constant altitude of 10,000 ft. It can be observed that there is no important variation of the aerodynamic coefficients with the Mach number. This variation occurs because of the fact that the Mach number is less than 0.2 (subsonic), and thus the compressibility effects do not apply (Fig. 4.23).

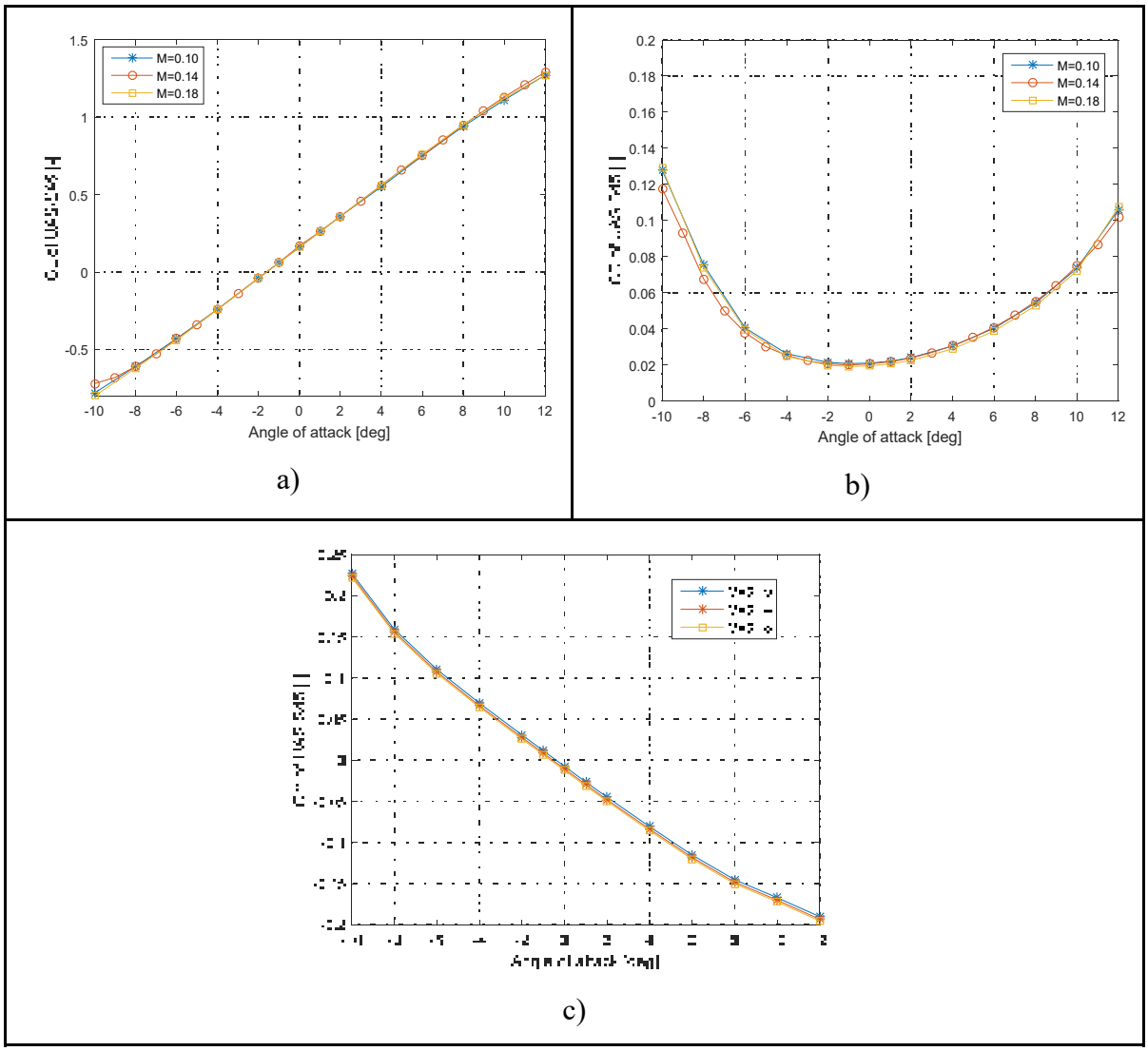

Figure 4.22 Lift (a), drag (b) and pitch moment (c) coefficient variation with the angle of attack for the UAS-S45 at three Mach numbers below 0.2 for Altitude =10,000 ft

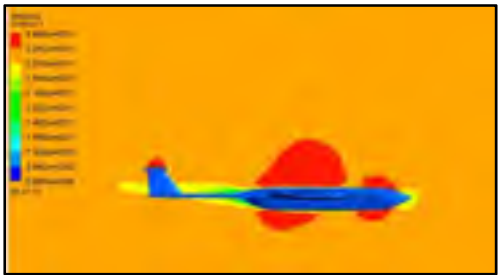

Figure 4.23 Velocity contour around the UAS-S45

The same observation can be made for the drag coefficient variation with three altitudes and for a range of angles of attack between -10° to 12° for a constant Mach number of 0.14 (Fig. 4.24). The minimum drag, also known as the zero lift drag, does not change significantly with the altitude.

Figure 4.25 displays a comparison between the entire UAS-S45 and the UAS-S45 in Wing-Body configuration. As expected, the Wing-Body configuration makes a major contribution to the aerodynamics of the entire UAS (as the variations of their results are very close). The pitch moment coefficient variation with the angle of attack confirmed the necessity of the horizontal tail. The Wing-Body pitch moment coefficient shows that the UAS-S45 in the Wing-Body configuration is nearly stable, and that the horizontal tail (Fig. 4.25) acts as a lever, leading to a decreasing (more stable) pitching moment coefficient variation of the entire UAS-S45 with the angle of attack.

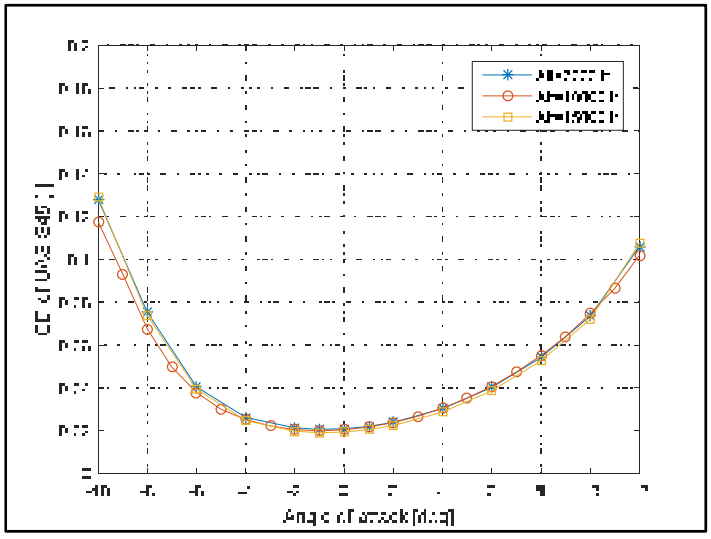

Figure 4.24 Drag coefficient variation with the angle of attack for the UAS-S45 at several altitudes for Mach number = 0.14

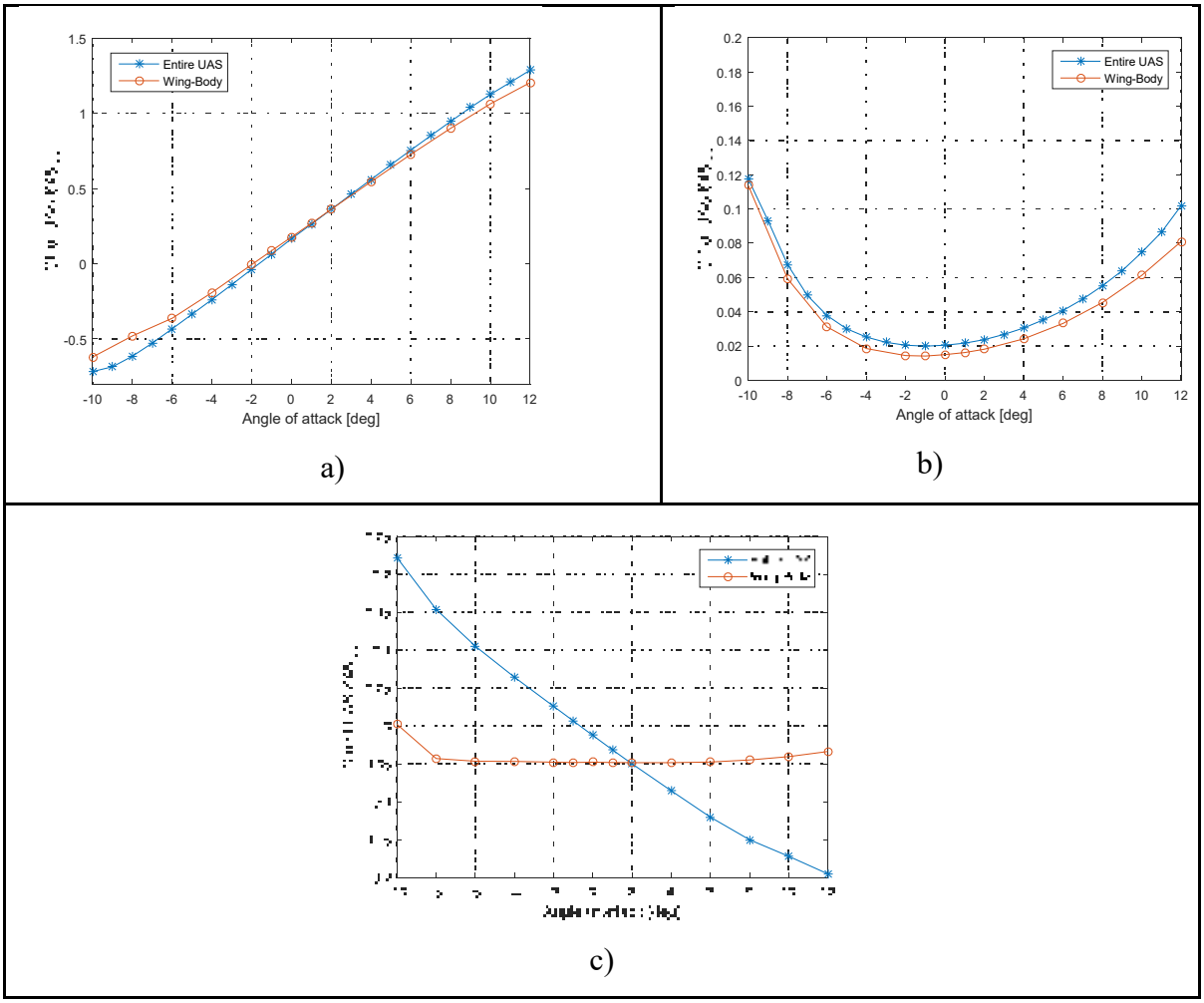

Figure 4.25 Comparison of the lift (a), drag (b) and pitch moment (c) coefficients' variation with the angle of attack for the entire UAS-S45 and the "Wing-Body" configuration

The CFD results were thus compared with the nonlinear VLM results for the flight condition of Mach number = 0.14 and altitude =10,000ft. Fig. 4.26 shows the very good agreement of the results obtained. The zero-lift drag estimated using the nonlinear VLM was lower than the one estimated using the CFD analysis. This relative error was due the number of strips considered in the strip analysis, as the strip analysis was used to calculate the viscous pressure distribution on the wing surface. The increase of the number of strips also increased the computation time. A compromise must be done in fact between the computation time and the needed accuracy.

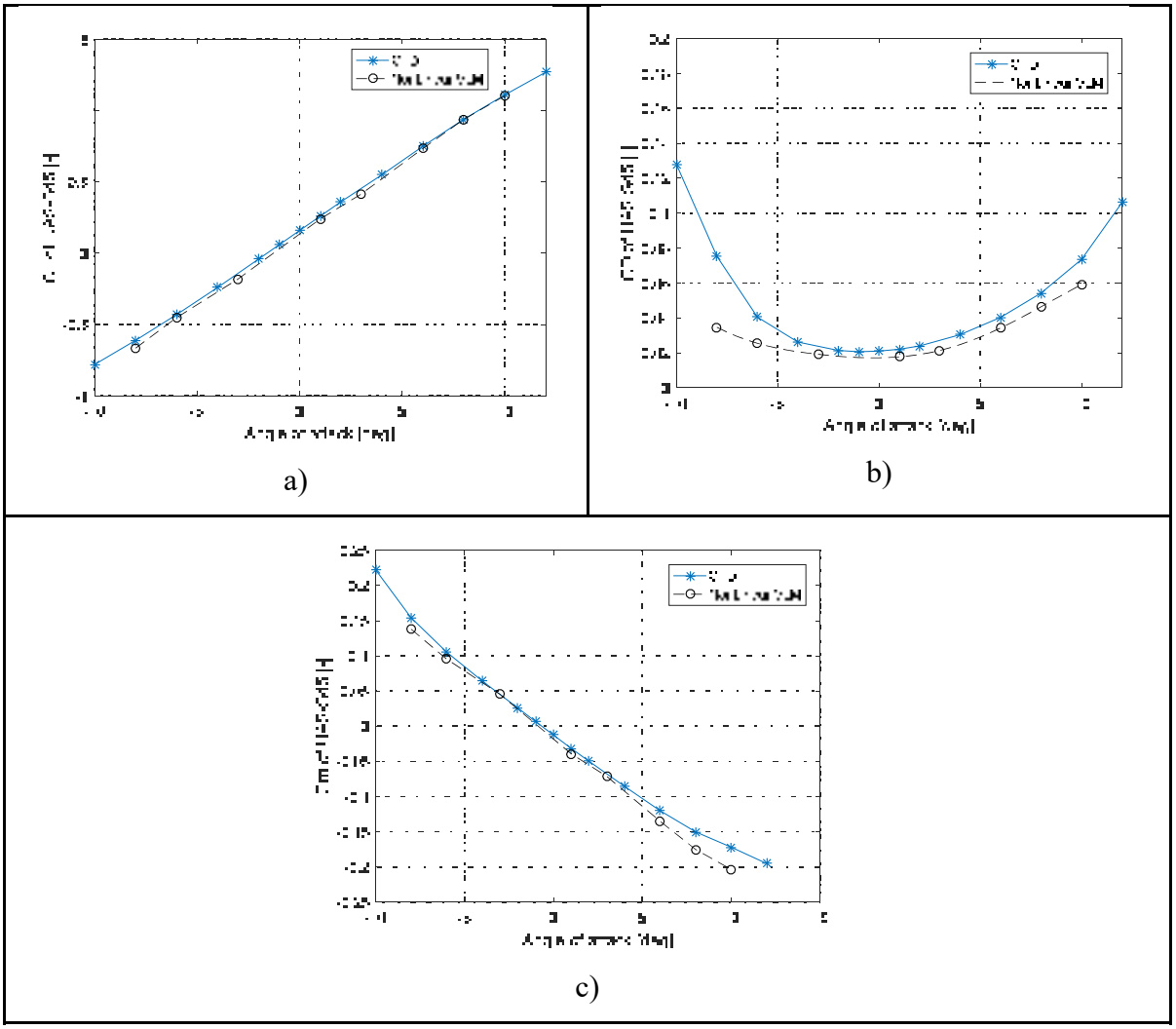

Figure 4.26 Comparison of the lift (a), drag (b) and pitch moment (c) coefficients' variation with the angle of attack for the entire UAS-S45 obtained using the CFD analysis and the nonlinear VLM techniques

The CFD and the nonlinear VLM results were compared to the results obtained from Fderivatives and DATCOM semi-empirical codes. Since no significant variation of the aerodynamic coefficients with the Mach number and the altitude was found, the three numerical methodologies results were shown here only for one flight condition, expressed in terms of Mach number 0.14 and altitude of 10,000 ft (Fig. 4.27).

The graphs shown in Fig. 4.27 clearly show that there is a close agreement for the lift coefficients variations calculated using all four methodologies. The drag coefficients

variations, on the contrary, show a significant difference between values calculated with 3 methods, and values calculated with the CFD analysis, especially for high negative angle of attack values (-10° to -2°).

The CFD analysis predicts the stall at approximately -12°, and therefore the drag coefficient increases rapidly around this value. The nonlinear VLM, Fderivatives and DATCOM codes, however, predict the stall for angles of attack far above 12°, and thus the drag coefficients estimated from these three methodologies maintain do not increase fast.

As expected, the zero-lift drag and the zero-lift pitch moment coefficients variations have different values obtained with Fderivatives, DATCOM and CFD analyses codes (Fig. 4.27). These values differences are small, and are mainly influenced by the airfoil aerodynamics coefficient, are estimated using semi-empirical interpolations in DATCOM and Fderivatives codes. However, the nonlinear VLM predict with a good accuracy the zero-lift pitch because the airfoil aerodynamic coefficient is estimated using Xfoil.

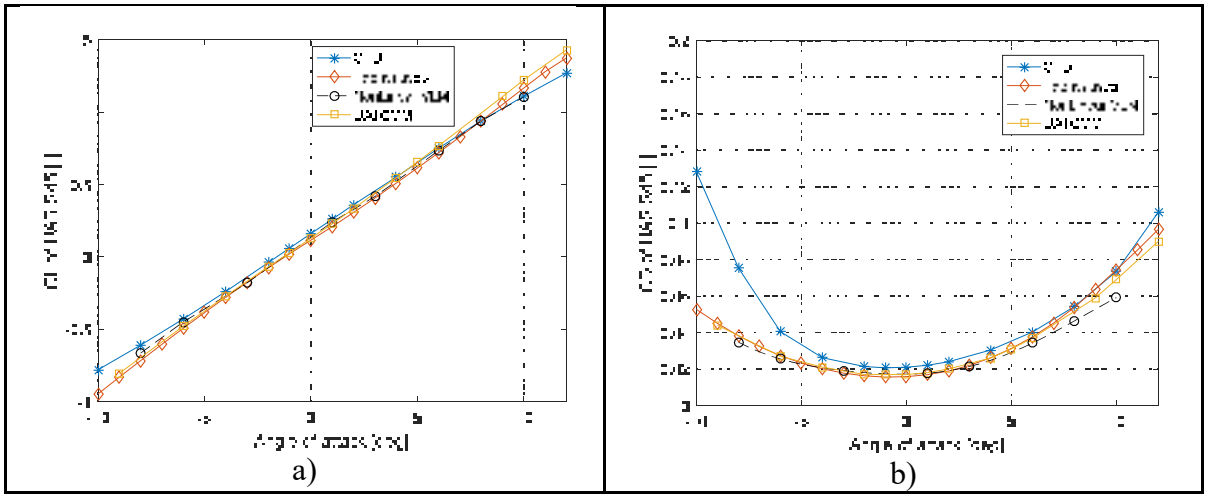

Figure 4.27 Comparison of the UAS-S45 lift (a), drag (b) and pitch moment (c) coefficients' variations with the angle of attack obtained using CFD, nonlinear VLM, Fderivatives and DATCOM theories for $M = 0.14$ and altitude $H = 10{,}000$ft

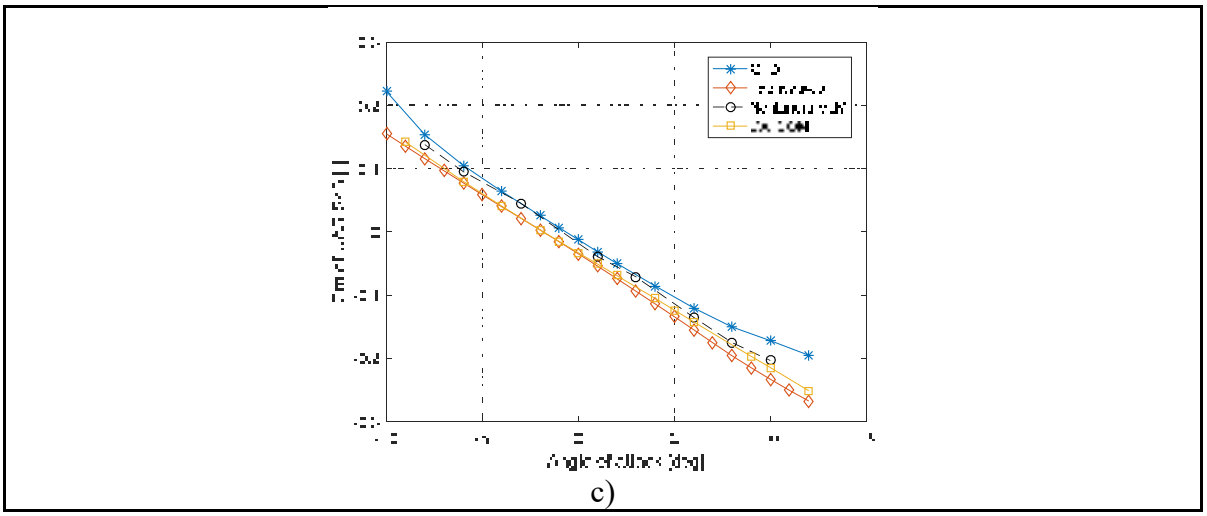

c)

Figure 4.28 (Continued) Comparison of the UAS-S45 lift (a), drag (b) and pitch moment (c) coefficients' variations with the angle of attack obtained using CFD, nonlinear VLM, Fderivatives and DATCOM theories for M = 0.14 and altitude H = 10,000ft

Figure 4.28 shows the longitudinal lift and moment derivatives values with respect to pitch rate, and for a range of angles of attack (-10° to 12°), C_{Lq} and C_{mq} , for the UAS-S45. The estimation was made for a Mach number of 0.14 and an altitude of 5,000ft. The CFD analysis, Fderivatives and DATCOM codes estimated constant lift and moment derivatives with respect to pitch rate C_{Lq} and C_{mq} as shown on Figure 4.27. There is a rather good agreement between the three methodologies results for the moment derivative with respect to pitch rate, C_{mq}, with a relative error 1.3%, and a similar observation on the lift derivative with respect to pitch rate, C_{Lq}, with a relative error of 4.7%.

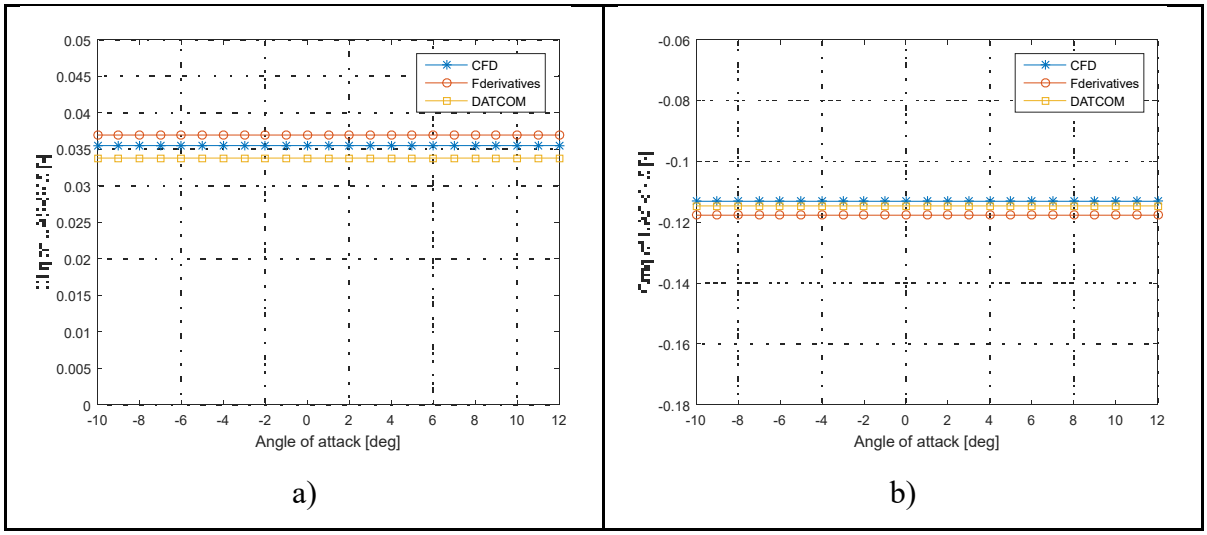

Figure 4.29 Comparison of the lift (a) and moment derivatives (b) with respect to pitch rate variation with the angle of attack of the UAS-S45 obtained using CFD, Fderivatives and DATCOM for M = 0.14 and altitude = 5,000 ft

4.8 Conclusion

This paper presents a methodology designed to predict the aerodynamic behaviour of the unmanned aerial system UAS-S45 of Hydra Technologies. A nonlinear Vortex Lattice Method was introduced. The method consisted in calculating the viscous forces from the strip theory, and the forces generated by the vortex rings from the vortex lifting law. Furthermore, a computational fluid dynamics analysis was applied to the UAS-S45 geometry and airfoil. A structured mesh grid was generated for the UAS-S45 airfoil in order to align the velocity gradient with the mesh and limit dissipation errors. The first layer's thickness, the number of layers and the grid spacing were calculated using the law of the wall in order to study the viscous sublayer. An unstructured grid mesh grid was generated for the entire UAS-S45. A grid convergence study was made and an UAS-S45 mesh model was selected by taking into account a compromise between the accuracy of the results needed as well as the quality of the mesh and the number of cells of the mesh. The Reynolds average Navier-Stokes equations were used to solve the flow equations around the aircraft with the Spalart-Allmaras model and the k-ω model as turbulence models.

These numerical methodologies results were validated with experimental analysis results on a reduced scale model of the UAS-S45. An experimental simulation was made on a 12×10 in wing in the Price-Paidoussis wind tunnel. The lift and drag coefficients obtained were compared to those from a computational fluid dynamics analysis of the same wing. The comparison shows a good agreement of the results.

Finally, the results obtained from numerical simulation of the airfoil and of the entire UAS-S45 were compared to results from Xfoil, for the airfoil, and from DATCOM and Fderivatives, for the entire UAS-S45. This comparison reveals that the approaches were highly accurate. Thus, the aerodynamics model obtained using the nonlinear VLM and CFD can be used for efficient flight dynamics and control law modelling and simulation technologies. The next step will be the use of this code in the level D flight simulator design of the UAS-S45.

4.9 Acknowledgements

Special thanks are due to the Natural Sciences and Engineering Research Council of Canada (NSERC) for the Canada Research Chair Tier 1 in Aircraft Modelling and Simulation Technologies funding. We would also like to thank Mrs. Odette Lacasse and Mr. Oscar Carranza for their support at the ETS, as well as to Hydra Technologies' team members Mr. Carlos Ruiz, Mr. Eduardo Yakin and Mr. Alvaro Gutierrez Prado in Mexico for their collaboration.

CHAPTER 5

UAS-S45 BÀLAAM PROPELLER: IMPROVED BLADE ELEMENT MOMENTUM METHODOLOGY AND WIND TUNNEL TEST PERFORMANCE EVALUATION

Maxime Alex Junior Kuitche, Ruxandra Mihaela Botez, Remi Viso, Jean Christophe Maunand, Oscar Carranza Moyao
LARCASE Laboratory of Applied Research Active Controls,
Avionics and AeroServoElasticity,
Ecole de Technologie Supérieure, 1100 Notre Dame West,
Montreal, H3C1K3, Québec, Canada

Article soumis dans *Journal of Aerospace Engineering*, en Septembre 2019

Résumé

L'évolution des aéronefs est étroitement liée à l'étude et à l'amélioration des systèmes de propulsion. Déterminer les performances de la propulsion est un véritable défi pour la modélisation et la conception des avions. En plus des approches théoriques, des procédures expérimentales sont utilisées pour obtenir une bonne estimation des performances de propulsion. Pour évaluer une propulsion de type piston-hélice, plusieurs tests expérimentaux sont nécessaires, ce qui peuvent être très exigeants en termes de temps et d'argent. Cet article présente une procédure permettant d'estimer les performances d'une hélice à partir d'une approche numérique utilisant une théorie améliorée du moment des éléments de pales. La méthodologie utilise un modèle d'effet de rotation et un modèle de correction du coefficient de portance pour des angles d'attaque élevés pour augmenter la précision des résultats. Une analyse CFD (Computational Fluid Dynamics) a également été mise en œuvre. Le maillage polyédrique et le modèle de turbulence k-ε réalisable ont été appliqués pour décrire avec précision le modèle d'écoulement autour de l'hélice. Puis, les équations de Reynolds Averaged Navier-Stokes ont été résolues à l'aide du logiciel ANSYS FLUENT. Ces méthodes ont été appliquées à l'hélice UAS-S45 conçue et fabriquée par Hydra Technologies au Mexique. Une enquête approfondie a été réalisée pour plusieurs conditions de vol, définies en termes d'altitude et de vitesse, dans le but de déterminer le coefficient de poussée, le coefficient de

puissance et l'efficacité de l'hélice. Les résultats de l’analyse de la dynamique des fluides et de la théorie des éléments de pales ont été comparés aux données expérimentales acquises lors d'essais en soufflerie réalisés dans la soufflerie LARCASE Price-Païdoussis. Les résultats de cette comparaison ont démontré que notre approche est très précise.

Abstract

The evolution of aircraft is closely linked to the study and improvement of propulsion systems. Determining the propulsion performance is a real challenge in aircraft modelling and design. In addition to theory-based approaches, experimental procedures are used to obtain a good estimation of propulsion performance. To evaluate piston-propeller propulsion, several experimental tests are required that can be very demanding in terms of time and money. This paper presents a procedure to estimate the performance of a propeller from a numerical approach using an improved Blade Element Momentum Theory. The methodology used rotation effect model and a high angle of attack lift coefficient correction model to increase the accuracy of the results. A Computational Fluid Dynamics (CFD) analysis was also implemented. Polyhedral meshing and the realisable k-ε turbulence model were applied to accurately describe the flow pattern around the propeller. Thus, the Reynolds Averaged Navier-Stokes equations were solved using ANSYS FLUENT software. These methods were applied on the UAS-S45 propeller designed and manufactured by Hydra Technologies in Mexico. An extensive investigation was performed for several flight conditions in terms of altitude and airspeed with the objective of determining the thrust coefficient, power coefficient and efficiency of the propeller. The Computational Fluid Dynamics and blade element theory results were compared with experimental data acquired from wind tunnel tests performed at the LARCASE Price-Païdoussis wind tunnel. The results of this comparison demonstrated that our approach is highly accurate.

5.1 Introduction

During recent years, interest in Unmanned Aerial Vehicles (UAVs) research has increased. The challenge of meeting the increasing demand for UAVs capable of performing dangerous tasks in hostile environments requires a pronounced effort on performance improvement techniques (Concilio *et al*., 2017 ; Koreanschi, 2016 ; Laliberte *et al*., 2000 ; Tuck *et al.*, 2018). Because of the fact that commercial aviation contributes with 2% of the worldwide carbon dioxide emissions (estimated in 2014) (Air Transport Action Group, 2014), technological innovations in this field are mainly focused on protecting the environment through solutions that improve fuel burn efficiency (Ameduri *et al*., 2018 ; Concilio *et al*., 2018 ; Pecora, 2018 ; Şugar Gabor *et al*., 2016). Aircraft propulsion plays a major role in fuel consumption. Since the first flight of the Wright brothers, propulsion systems have evolved in several ways, leading to four principle propulsion systems: piston-propellers, gas turbines, ramjets, and rockets (Picard *et al.*, 2012 ; Rancourt *et al*., 2012). The piston-propeller propulsion systems are mostly used for subsonic flight and thus are used for UAVs. One possibility of achieving the desired fuel burn efficiency for UAVs is by optimizing piston-propeller propulsion system performance. Achieving this goal requires a good understanding of the propeller behaviour.

Researchers have proposed different solutions for obtaining propeller performance along with significant accuracy. Since the early stage of aviation, wind tunnel testing has been the preferred method for propeller performance estimation. Brandt and Selig (2011) performed tests on 79 propellers at the UIUC subsonic wind tunnel aiming to create a large database to help aircraft designers in propulsion estimation. These tests were carried out to quantify the propellers' performance and efficiency for speeds varying from static to windmill state while considering the low Reynolds number effect.

Kamal *et al*. (2015) developed a propeller propulsion system model using propeller performance characteristics obtained from a wind tunnel analysis. The tested propeller was a Master Aircrew 11×6 G/F G3 Nylon propeller. Their experimental setup included a piston engine, an rpm sensor, a 6-component strain gauge sting balance to measure the thrust and a National Instrument data acquisition system to collect the data. The setup was installed in a low speed closed circuit wind tunnel. The experiment was performed from the propeller's static

conditions until the windmill state. The measured static and dynamic performance data were compared to the published data available in the UIUC propeller database (Brandt and Selig, 2015). The results showed very good agreement between the published and measured data for the thrust and the power.

Complex problems can also be examined using wind tunnel testing, including noise reduction, propeller whirl flutter conditions and ice accretion.

Although wind tunnel testing is effective, the resources needed to collect the required data can be huge. Semi-empirical methodologies, such as the Blade Element Theory (BET) (Gudmundsson, 2013b), have been developed to make the compromise between the accuracy of the data and the need to reduce the resources required to collect them.

Benini (2004) studied the accuracy of the blade element theory in the estimation of propeller performance. His methodology combined momentum theory for the calculation of the induced velocities with the blade element theory. The Combined Momentum-Blade Element Theory (CMBET) was applied on the 3-bladed Wageningen B-series marine propeller. Benini showed that the propeller efficiency is well-predicted for the lowest advance ratio (lowest speed) but is over-predicted as the advance ratio increases.

MacNeil and Verstraete (2017) investigated the possible improvement in accuracy when the blade element theory is used on a small propeller. The methods studied were the Ostowari and Naik (1985) and the Viterna and Corrigan (1982) theories to extend aerodynamic coefficients to post stall angles of attack and the theories proposed by Snel *et al*. (1994) and Corrigan and Schillings (1994) for rotation effect correction. Their investigation was made on APC thin electric 10×5, 10×7, 14×12, 17×12, and 19×12 propellers, with all tests performed at low Reynolds numbers. The results showed a significant improvement relative to the classical blade element theory. When combining the Viterna and Corrigan theory on performance at high angles of attack and Corrigan and Schillings' on the rotation effect, the propeller performance has a close match with the experimental data with a maximum error of 5%.

Due to the rapid increase in computing capacity, Computational Fluid Dynamics (CFD) applications have also begun to be considered for propeller analysis. Kutty and Rajendran (2017) performed a numerical prediction on a small APC Slow Flyer propeller blade. They used a Multiple Reference Frame model approach (MRF) by dividing the computational

domain into a stationary domain and a rotating domain to easily predict the flow around the propeller. The mesh model utilized was unstructured and obtained from a grid convergence study. FLUENT (ANSYS, 2013) software was used to solve the PDE of the flow and the standard k-ω turbulence model (Argyropoulos and Markatos, 2015) was used to close the RANS equations. The numerical analysis results were compared with experimental data and showed that the thrust and power obtained numerically are under-predicted for advance ratios of from 0.192 to 0.659. In contrast, the propeller efficiency is over-predicted throughout the whole range of advance ratios.

Carroll and Marcum (2013) developed a surrogate model to correct the time-averaged thrust and swirl produced by each blade element of a propeller. Their model used the local flow of each blade element of the propeller and estimated the local performance of the corresponding blade while considering the tip and hub losses and the elements' interaction. Trained data for the surrogate model were obtained from a 3D CFD method. The simulations were performed using the CHEM CFD software with an unstructured mesh and a Menter's Shear Stress Transport turbulence model. To validate the model, they compared the thrust estimated using the surrogate model and the thrust calculated from a full 3D CFD approach. The results showed a good agreement between the data obtained with a large reduction in computational expense and data obtained when using the surrogate model

Unlike the other methods, CFD gives the possibility to evaluate the whole flow dynamic by solving the complete Navier-Stokes equation, and is thus suitable for more complex problems. Liauzun (Liauzun, 2006 ; Liauzun & Tran, 2002) proposed two CFD techniques to analyse the wind turbine aeroelasticity. The first technique used a classic finite volume formulation to solve the Navier-Stokes equations, and the second technique considered the viscous-inviscid interactions. Both techniques used the Wilcox k-ω turbulence model. These models were applied to the NACA 63-421 airfoil design. The numerical results were very close to the experimental results for a range of angles of attack from 0^{o} to 15^{o}.

This paper intends to investigate the aerodynamic performance of the UAS-S45 Balàam (Kuitche and Botez, 2019) and the UAS-S4 (Kuitche and Botez, 2019 ; Kuitche and Botez, 2017 ; Segui *et al*., 2017) propeller. The main objective is to design propulsion system model of the UAS-S45.

For this purpose, the accuracy and the efficiency of the above methodologies (BEMT, CFD, wind tunnel) were discussed. Thus, an improvement of the Blade Element Momentum Theory was proposed. This improvement was made to provide more accuracy for low advance ratio and to consider the rotational effect.

The paper is organised as follow. Section 5.2 shows how the Blade Element Theory (BET) is applied to the Mejzlik propeller. The momentum theory was added to the BET to estimate the induced velocity. Thus, correction methods for rotational effect and high angle of attack aerodynamic coefficients were presented. Section 5.3 shows an overview of Computational Fluid Dynamics. The multiple reference frame approach is used to cope with the convergence problems. A realisable k-ε turbulence model was applied for the calculation because of its effectiveness in wind turbine simulations. The experimental analysis performed to validate the numerical results is outlined in Section 5.4. Finally, Section 5.5 presents the results and discussion and is followed by a conclusion in Section 5.6

5.2 Blade Element Theory (BET) from 2D simulation and improvements

5.2.1 CAD model creation

This study aims to estimate propeller performance from a numerical procedure useful for the design of an UAS-S45 flight simulator. The UAS-S45 uses a Mejzlik 23X10 carbon fibre propeller (Fig. 5.1a). A reverse engineering technique (Durupt *et al*., 2008) was applied to analyse the propeller performance. The process of reverse engineering begins with collecting points coordinates data from the surfaces of the propeller. The data acquisition was performed using an HS700 scanner. The points cloud obtained (Fig. 5.1b) was imported into CATIA in order to design a 3D model of the propeller. A pre-processing step reduced the number of points in the point cloud. Only 13 profiles were kept, and then Splines were thus drawn with the assumption of circular leading and trailing edges. A curvature analysis was performed to verify the quality of the splines thus obtained (Fig. 5.2). These splines were then bounded by surfaces. The obtained 3D model is shown in (Fig. 5.1c).

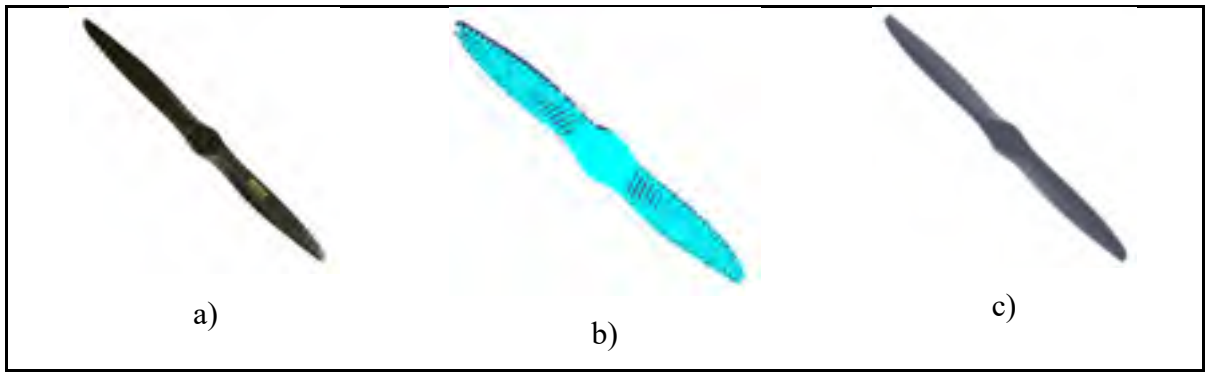

Figure 5.1 Mejzlik propeller: original (a), point cloud (b), CAD model (c)

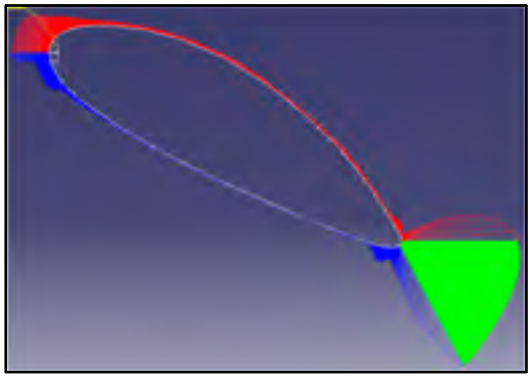

Figure 5.2 Curvature analysis

5.2.2 Classical Blade Element Momentum Theory

First introduced by the Polish scientist Stefan Drzewiecki (Anderson, 2010) , the Blade Element Theory (BET) became more commonly known as the "primitive theory of the blade element" between 1892 and 1920.

This theory estimates the thrust, the torque and the power of a propeller by dividing each blade into several segments called "blade elements". The propellers are usually characterized their complex shapes (curvatures of the blades). The shape of the blade elements changes progressively from “thick” at the level of the hub to “fine” at the end of the propeller. The BET can handle each of these progressive changes. Each element is treated independently, like a two-dimensional wing.

Aerodynamic forces can then be calculated based on the flow conditions of each element. Once the aerodynamic properties have been determined, the properties of the entire propeller are evaluated. Compared to the momentum theory, the BET offers a number of advantages: it can be used for various blade geometries and angles of attack, and it also allows manufacturers to estimate a propeller's torque in order to then estimate the required power. However, the BET remains limited as it assumes that the flow through the stream tube is uniform, which is not the case for deformed stream tubes. The assumption that the forces on each blade element can be estimated using a two-dimensional analysis also neglects the lateral flow. In addition, the BET also assumes that the propeller is rigid, thus ignoring the aeroelastic effects.

In operation, a blade is rotating with an angular velocity ω (n revolutions per second) and is advancing through the air with a relative airspeed V_∞. Each blade element is treated as an airfoil and the aerodynamic lift and drag forces are calculated according to the various flow conditions:

$$dL = \frac{1}{2}\rho V_E^2 c(r) C_l dr \tag{5.1}$$

$$dD = \frac{1}{2}\rho V_E^2 c(r) C_d dr \tag{5.2}$$

where dL and dD are the differential lift and drag forces on the blade element, respectively, $c(r)$ is the chord at the blade station r, ρ is the air density, and V_E is the effective resultant velocity of each blade, given by:

$$V_E = \sqrt{\left((\omega r)^2 + (v_i + V_\infty)^2\right)} \tag{5.3}$$

where ω is the angular velocity of the propeller and r is the distance from the hub to the blade element; V_∞ is the airspeed and v_i is the induced velocity obtained from momentum theory. C_l and C_d are respectively the lift and drag coefficients of the blade element.

The lift and drag coefficient are evaluated at the angle of attack α:

$$\alpha = \beta - \phi - \alpha_i + \alpha_0 \tag{5.4}$$

where β is the angle between the zero-lift line and the rotation plane, also called the pitch angle, α_i is the induced angle of attack obtained from momentum theory, α_0 is the zero-lift angle of attack of the airfoil and ϕ is the helix angle = $\tan^{-1}(V_\infty/V_E)$.

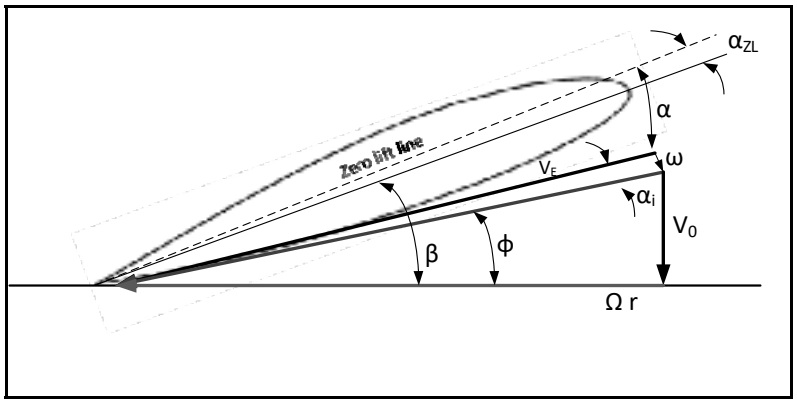

Figure 5.3 Angles and velocities of the propeller

In this paper, an aerodynamic database was constructed for a wide range of angles of attack for each blade airfoil using XFoil software (Drela, 1989). The Prandtl-Glauert correction was applied at each blade section in order to simulate its behaviour for effects of Mach numbers. Figure 5.4 shows the lift and drag coefficient variation with the angle of attack for one of the blades airfoil.

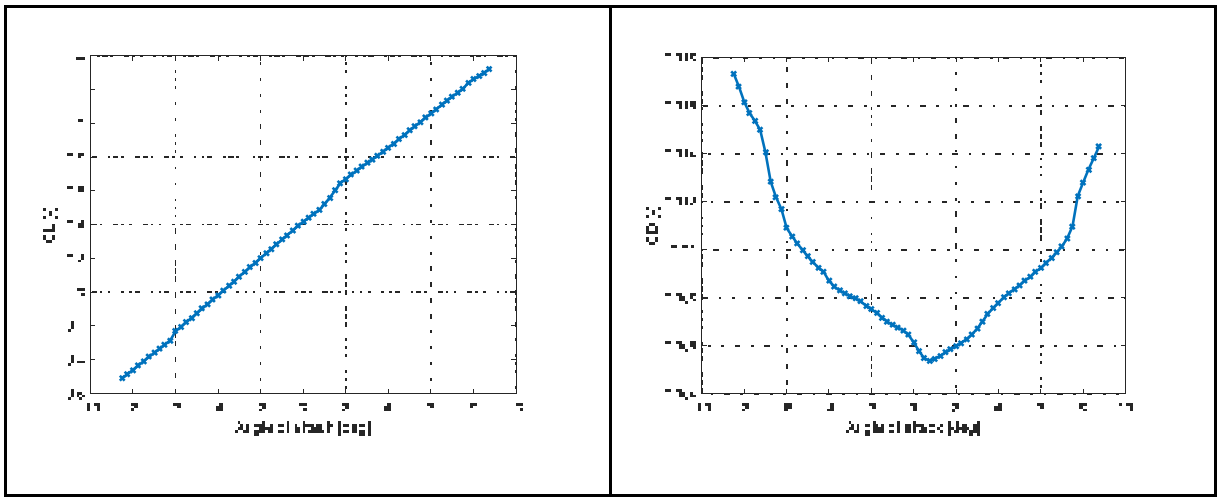

Figure 5.4 Lift and drag coefficient variation with angle of attack for one blade airfoil

The differential thrust and torque are calculated as follows:

$$dT = dL\cos(\phi+\alpha_i) - dD\sin(\phi+\alpha_i) \tag{5.5}$$

$$dQ = r\left[dL\sin(\phi+\alpha_i) + dD\cos(\phi+\alpha_i)\right] \tag{5.6}$$

The thrust ad the torque can be calculated by integrating these differential equations from the hub to the tip of the propeller:

$$T = N_B \int_{R_{hub}}^{R} dL\cos(\phi+\alpha_i) - N_B \int_{R_{hub}}^{R} dD\sin(\phi+\alpha_i) \tag{5.7}$$

$$Q = N_B \int_{R_{hub}}^{R} r.dL\sin(\phi+\alpha_i) - N_B \int_{R_{hub}}^{R} r.dD\cos(\phi+\alpha_i) \tag{5.8}$$

where T and Q are the thrust and torque produced by the propeller, N_B is the number of blades, R is the tip radius, and R_{hub} is the hub radius of the propeller.

The process of estimating the thrust and torque is summarized in Fig. 5.5.

The accuracy of the BET depends mainly on the airfoil aerodynamics coefficients. As introduced above, these coefficients are generally estimated using two-dimensional analysis by neglecting the rotation effect. It results to a maximum lift coefficient lower than the

expectations from experimental measurements. This stall delay is due to the Coriolis force in the cross-flow direction which increase when approaching the rotation axis and modified the centrifugal pumping (Tangler and Selig, 1997). This phenomenon delays the occurrence of separation flow further downstream towards the trailing edge of the airfoil (Breton *et al*., 2008). Several models have been developed to estimate the rotation effect and obtain a three-dimensional corrected lift coefficient. In this work, the method of Corrigan and Schillings was used. The method used a shape function for stall delay to accounts for both centrifugal and pressure gradients effects. Corrigan and Schillings assumed that the centrifugal induced flow is proportional to the ratio of c/r which allows to formulate the shape function in terms of position of the separation point. The stall delay was thus expressed as a shift of the angle of attack:

$$\Delta\alpha = \left(\alpha_{C_{lmax}} - \alpha_{C_{l=0}}\right)\left[\left(\frac{K\,c/r}{0.136}\right)^{n} - 1\right] \tag{5.9}$$

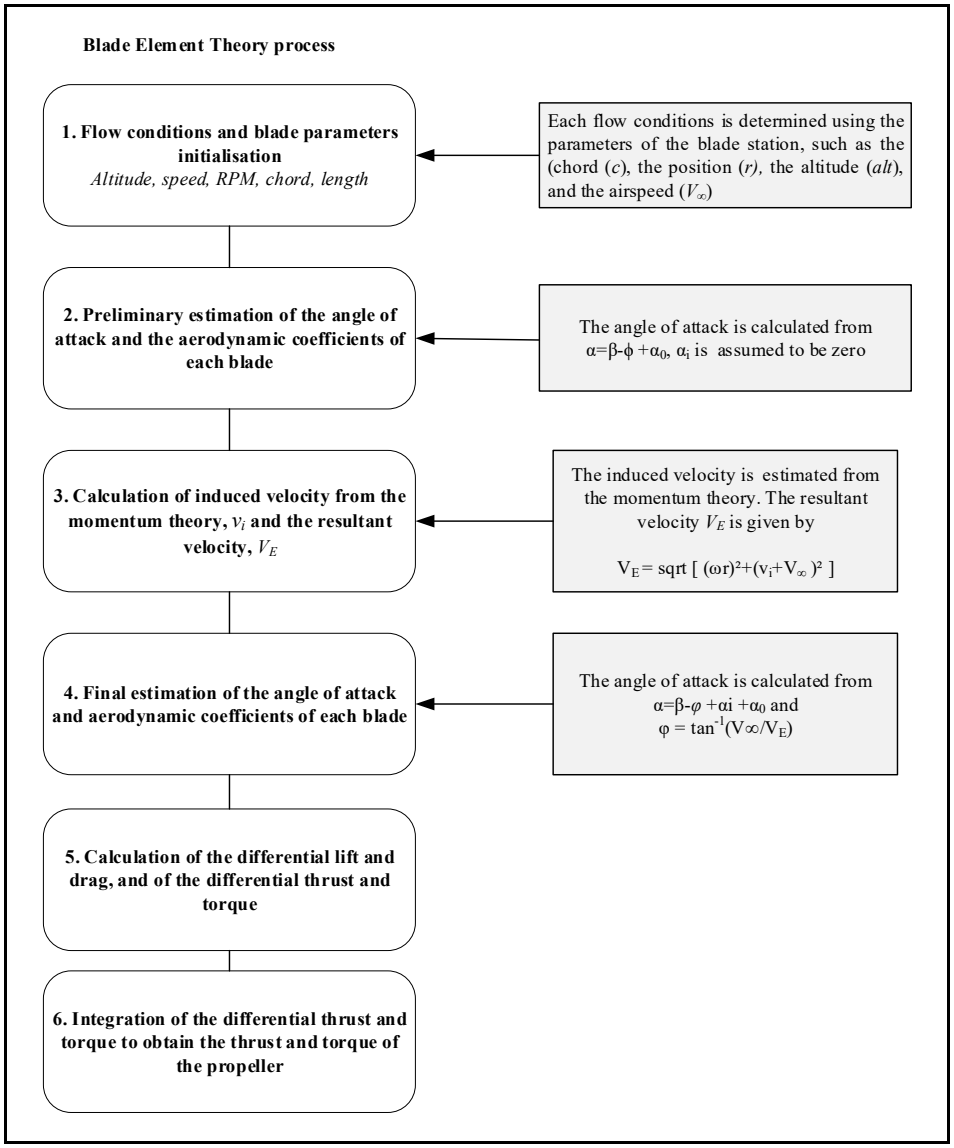

Figure 5.5 BET Calculation Process

where $\alpha_{C_{l_{max}}}$ is maximum lift angle of attack, $\alpha_{C_{l=0}}$ is the zero-lift angle of attack, *c* is the local chord, *r* blade element station, n is relates to the strength of the centrifugal terms which varies from 0.8 to 1.6. In this work, a value of *n*=1 was chosen. *K* is the nondimensional linear adverse velocity gradient given by the following expression:

$$K = \left(\frac{0.1517}{(c/r)} \right)^{1/1.084} \tag{5.10}$$

The lift coefficient is further corrected to obtain a three-dimensional coefficient as:

$$C_{l_{3D}}(\alpha + \Delta\alpha) = C_{l_{2D}}(\alpha + \Delta\alpha) + \left(\frac{\partial C_l}{\partial \alpha} \right) \Delta\alpha \tag{5.11}$$

where $\left(\frac{\partial C_l}{\partial \alpha} \right)$ is lift curve slope of the linear region of the lift.

In this work, the drag coefficient remained unchanged because the effects of rotation did influence the drag.

5.2.3 High angle of attack coefficients calculation

In addition to rotation effect correction, a stall correction was added to the aerodynamic coefficients for high angle of attack. The correction was made to consider the separation on the upper surface of the airfoil for positive angle of attack and on the lower surface of the airfoil for negative angle of attack (Hepperle, 2010). The model is given by the following expression of the corrected lift and drag:

If $\alpha > 0$

$$\begin{aligned} C_{l_{corrected}} &= C_l \left(1 - 0.2 \left(x_{TE} - x_{sep,upper} \right) \right) \\ C_{d_{corrected}} &= Cd + \left| \begin{array}{l} sin^2\alpha \left(x_{TE} - x_{sep,upper} \right)^2 + \\ 0.025cos\alpha \left(x_{TE} - x_{sep,upper} \right)^2 \end{array} \right| \end{aligned} \tag{5.12}$$

If $\alpha < 0$

$$C_{l_{corrected}} = C_l\left(1 - 0.2\left(x_{TE} - x_{sep,lower}\right)\right)$$
$$C_{d_{corrected}} = Cd + \left|\begin{matrix} sin^2\alpha\left(x_{TE} - x_{sep,lower}\right)^2 + \\ 0.025cos\alpha\left(x_{TE} - x_{sep,lower}\right)^2 \end{matrix}\right| \quad (5.13)$$

where α is the angle of attack after the stall, x_{TE} is the trailing edge position, $x_{sep,upper}$ and $x_{sep,lower}$ are respectively the position of the separation point on the upper and lower surface of the airfoil.

The extension to post stall angles of attack is shown in Fig. 5.6.

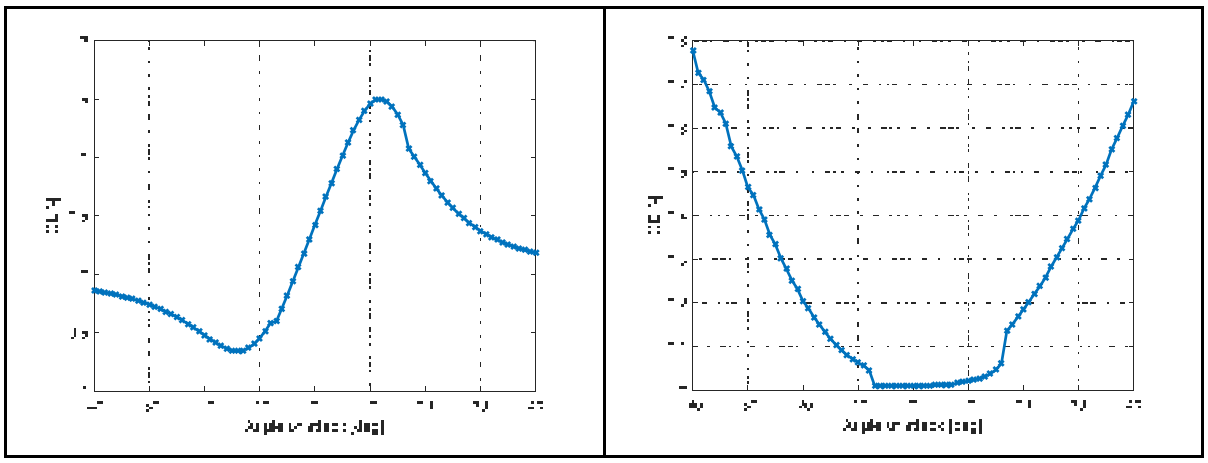

Figure 5.6 Lift and drag coefficient extension to high angles of attack

5.3 Numerical simulation

5.3.1 Mesh generation and grid convergence for the propeller design

A Multiple Reference Frame (MRF) (ANSYS, 2013) was used to estimate the flow around the propeller. MRF is an approach in which individual cell zones move at different rotational or translational speeds. Among the various methods involving both stationary and moving zones, such as the mixing plane method or the sliding mesh method, the MRF approach was chosen because of its simplicity and effectiveness when the flow interaction at the boundary between

the stationary and the moving zones is weak, which is the case in this research. To apply the MRF method, the computational domain was divided into two parts (illustrated in Fig. 5.7):

- A cylindrical rotational domain with a length of 0.4×*D* and a diameter of 1.1×*D*, located inside the stationary domain at 2.5×*D* from the inlet, where *D* is the diameter of the propeller.
- A cylindrical stationary domain with a length of 8×*D* and a diameter of 4×*D*, where *D* is the diameter of the propeller. The inlet and the outlet of the domain are considered far enough apart to avoid the occurrence a reverse flow.

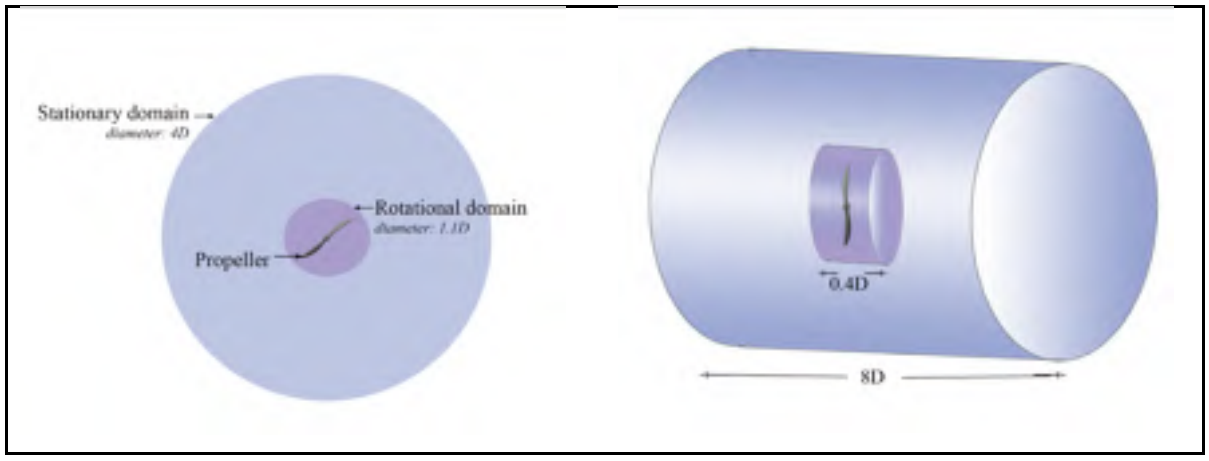

Figure 5.7 The Multiple Frame Reference (MRF) computational domains, cylindrical rotational (left) and cylindrical stationary (right)

The mesh grid was obtained using the ANSYS Fluent meshing module. In the beginning, the first cell's height was calculated. It is an important parameter to estimate as it determines in which part of the boundary layer (laminar, turbulent or transitional) the computation will be made according to the law of the wall (Von Kármán, 1931). The first cell's height was found using the following expressions:

$$Re = \frac{\rho U_\infty L}{\mu} \tag{5.14}$$

$$C_f = \frac{0.026}{Re^{\frac{1}{7}}} \tag{5.15}$$

$$\tau_\omega = \frac{U_\infty^2 \rho C_f}{2} \tag{5.16}$$

$$U_{fric} = \sqrt{\frac{\tau_\omega}{\rho}} \tag{5.17}$$

$$\Delta s = \frac{y^+ \mu}{U_{fric} \rho} \tag{5.18}$$

In Eqs. (5.14)-(5.18), *Re* is the Reynolds number, C_f is the skin friction coefficient, τ_ω is the wall shear stress, U_{fric} is the frictional velocity, Δs is the first cell's height and y^+ is the non-dimensional distance to the wall, U_∞ is the freestream velocity, ρ is the air density and L is the mean chord of the propeller . The distance to the wall was chosen between 10 and 100 to reduce the calculation time and to consider only the region outside of the boundary layer, according to the law of the wall. The value of the first cell's height was found to be 2.8×10^{-6}m. A tetrahedral unstructured mesh was then used, as it is appropriate for complex shapes and is faster to generate than a structured mesh. A mesh grid of 5,306,237 elements was obtained, and then validated using the orthogonal quality and skewness values. A value close to 1 corresponds to a very good orthogonality quality, while a value close to 0 corresponds to a very good skewness. The orthogonal quality obtained for the mesh grid was 0.88 and the skewness quality was 0.03, which both indicates a very good mesh quality of the model.

5.3.2 Flow equation, turbulence and transition model

The rotational motion of the mesh involves transient fluctuation that cannot be neglected. A transient simulation was therefore preferred to a steady simulation. Transient simulation was solved by estimating a solution for many discrete points in time (ANSYS, 2013). The "adaptive

time stepping" method was chosen to set the time step. It allows the time step size to be automatically adjusted from a local truncation error analysis.

The flow was selected to be incompressible and the "pressure based" Navier Stokes solution algorithm was applied. The inlet and outlet velocities were used as the external boundary conditions. The inlet or outlet velocity can only be used if the overall continuity of the domain was fulfilled (ANSYS, 2013) and if its boundaries are far from the object to be studied. In this work, the propeller was located 3.5×D from the inlet and 4.5×D from the outlet, where D is the diameter of the propeller.

ANSYS Fluent was used to simulate the flow around the propeller. ANSYS Fluent can solve a wide range of CFD problems including steady and transient flows, dynamic mesh, laminar and turbulent flows (Aubeelack and Botez, 2019).

ANSYS Fluent uses the Reynolds Averaged Navier-Stokes (RANS) equations (Eqs. (5.19)-(5.21)) to obtain a steady-state flow solution. For transient flow simulations, the interval used for the time averaging of the Navier-Stokes equations was decreased, and the transport equations for the turbulent quantities (such as the kinetic energy and dissipation rate) were time-dependent :

$$\frac{\partial \rho}{\partial t} + \frac{\partial}{\partial x_j}(\rho U_j) = 0 \tag{5.19}$$

$$\frac{\partial}{\partial t}(\rho U_i) + \frac{\partial}{\partial x_j}\left(\rho U_i U_j\right) = -\frac{\partial P}{\partial x_i} + \frac{\partial}{\partial x_j}\left[\mu_{eff}\left(\frac{\partial U_i}{\partial x_j} + \frac{\partial U_j}{\partial x_i}\right) - \frac{2}{3}\mu_{eff}\frac{\partial U_k}{\partial x_k}\delta_{ij}\right] \tag{5.20}$$

$$\begin{aligned} &\frac{\partial}{\partial t}\left(\rho H\right) - \frac{\partial P}{\partial t} + \frac{\partial}{\partial x_j}\left(\rho U_j H\right) = \frac{\partial}{\partial x_j}\left[\lambda\frac{\partial T}{\partial x_j} + \frac{\mu_t}{Pr_t}\frac{\partial h}{\partial x_j}\right] + \\ &\frac{\partial}{\partial x_j}\left\{U_i\left[\mu_{eff}\left(\frac{\partial U_i}{\partial x_j} + \frac{\partial U_j}{\partial x_i}\right) - \frac{2}{3}\mu_{eff}\frac{\partial U_k}{\partial x_k}\delta_{ij}\right] + \mu\frac{\partial k}{\partial x_j}\right\} \end{aligned} \tag{5.21}$$

where ρ is the fluid density, U_i are the velocity components, P is the static pressure and μ_{eff} is the effective viscosity, which is the sum of the molecular viscosity μ and the turbulent viscosity μ_t. H is the total enthalpy, T is the fluid temperature, δ_{ij} is the Kronecker delta function, λ is the

thermal conductivity, Pr_t is the turbulent Prandtl number, h is the static enthalpy and k is the turbulent kinetic energy (Şugar Gabor *et al*., 2016)

The realisable k-ε model was added to the RANS equations to determine the turbulent viscosity and the kinetic energy. This model is an improvement of the standard k-ε model. It has the advantages of the k-ε model for the far wall region prediction, and it gives a very good accuracy to flows involving rotation, boundary layers under strong adverse pressure gradients, separation, and recirculation. The realisable k-ε model is given by the following equations:

$$\frac{\partial}{\partial t}(\rho k)+\frac{\partial}{\partial x_j}(\rho k u_j)=\frac{\partial}{\partial x_j}\left[\left(\mu+\frac{\mu_t}{\sigma_k}\right)\frac{\partial k}{\partial x_j}\right]+G_k+G_b-\rho\varepsilon-Y_M+S_k \tag{5.22}$$

$$\frac{\partial}{\partial t}(\rho \varepsilon)+\frac{\partial}{\partial x_j}(\rho \varepsilon u_j)=\frac{\partial}{\partial x_j}\left[\left(\mu+\frac{\mu_t}{\sigma_\varepsilon}\right)\frac{\partial \varepsilon}{\partial x_j}\right]+\rho C_1 S\varepsilon-\rho C_2\frac{\varepsilon^2}{k+\sqrt{\upsilon\varepsilon}}+C_{1\varepsilon}\frac{\varepsilon}{k}C_{3\varepsilon}G_b+S_\varepsilon \tag{5.23}$$

In Eqs. (5.22) and (5.23), k is the turbulence kinetic energy, ε is the dissipation rate of the turbulence kinetic energy, G_k is the turbulence kinetic energy generation due to the mean velocity gradients, G_b is the generation of turbulence kinetic energy due to buoyancy, Y_M is the contribution of the fluctuating dilatation in compressible turbulence to the overall dissipation rate, σ_ε and σ_k are the turbulent Prandlt numbers, and S_k and S_ε are the source terms and , C_1, C_2, $C_{1\varepsilon}$, and $C_{3\varepsilon}$ are constants.

5.4 Wing tunnel test investigation

5.4.1 Bench test description

For the experimental analysis, a bench test was built to accurately measure the thrust and the power generated by the propeller. Figure 5.8(a) shows a schematic of the bench test used in the present study.

This test bench which is mainly composed of an aluminium plate to fix the motor and the sensor, and also of an aluminium tube with a streamlined cross section. An appropriate sizing step was performed to ensure the structural solidity of the test bench. This sizing step estimated

the diameter of the aluminium tube and screw needed to support the thrust of the propeller (Fig. 5.8b).

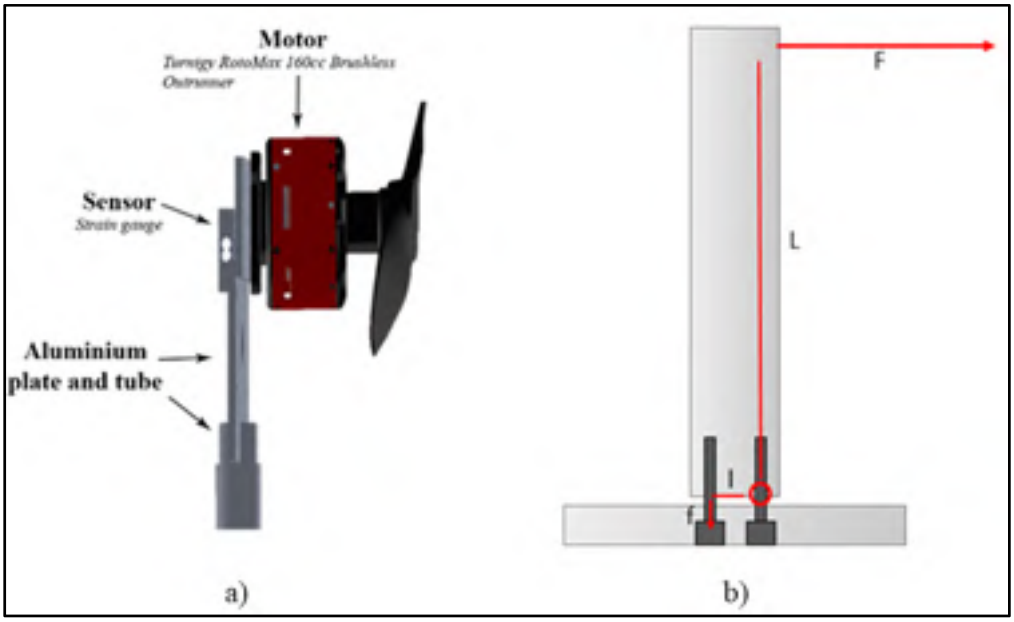

Figure 5.8 (a) Schematic of the bench test; (b) Mechanical structure

The diameter of the tube is given by:

$$D = \sqrt[4]{\frac{64I}{\pi}} \tag{5.24}$$

where I is the inertia of the tube, that is calculated with the next equation

$$I = \frac{FL^3}{3Ef} \tag{5.25}$$

In Eq. (5.25), F is the force produced by the propeller. The maximum force produced by the Mezjlik propeller is around 120 N. A force amount of 150 N (higher than 120 N) was chosen to ensure that the bench test resist to all the mechanic constraint: L is the length of the tube, E is the Young's modulus, and f is the bending moment of the tube. The value of each parameter is given in Table 5.1.

Table 5.1 Parameters of the mechanical structure

Parameter	Value
Length of the tube, L	508 mm
Young modulus, E	69 GPa
Bending moment of the tube, f	0.9 Nm

The aluminium tube was fixed on the support with two screws 20 mm apart as seen in Fig.5.8(b) The force applied on the screws, F_{screws}, was calculated using the moment's equilibrium:

$$F_{screws} = \frac{FL}{l} \tag{5.26}$$

where F is the force produced by the propeller, L is the length of the tube and l is the distance between the two screws. The force applied on the screws was calculated to be 2287.5N. Screws "grade 1 ¼-20 (American Fastener Technologies Corporation, 2013)" were chosen because they can support forces up to 4600 N.

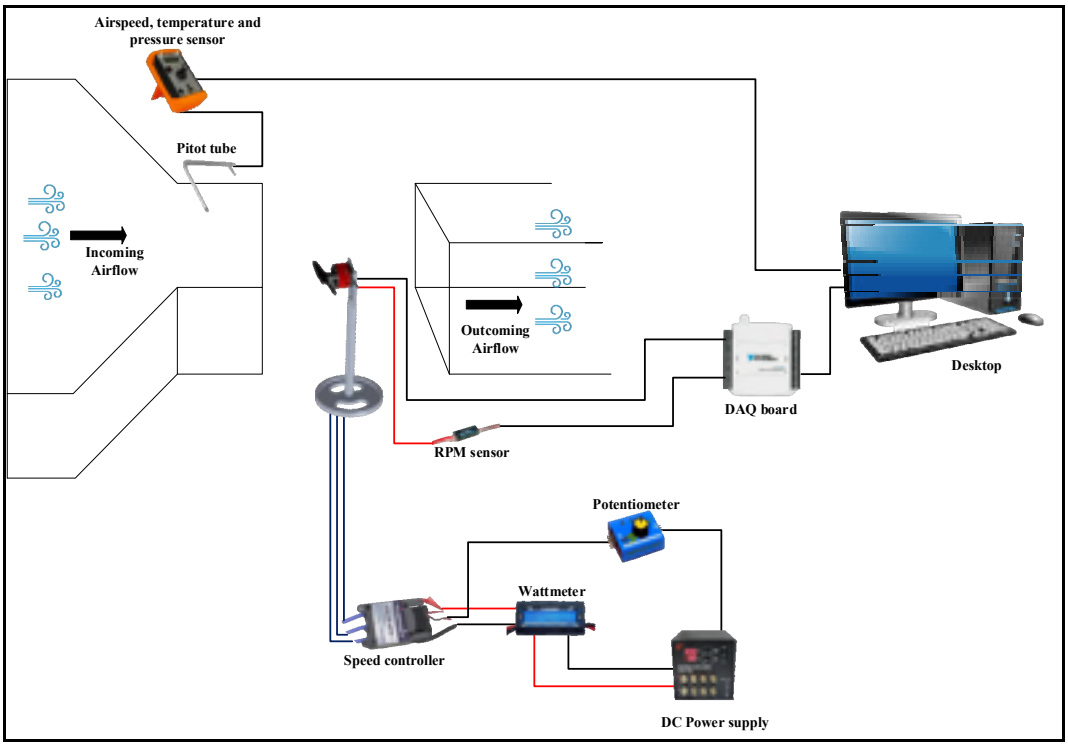

Figure 5.9 Schematics of the experimental setup

A schematic of the experimental setup is presented in Fig. 5.9. During the experiment, the propeller was driven by a direct current motor (Turnigy RotoMax 160cc Brushless Outrunner Motor (Hobbyking, 2010b)) that has the same power as the engine of the UAS-S45. The rotational speed of the propeller was controlled using a potentiometer (Servo Consistency Master Automatic Tester (CCPM, 2010)) in order to obtain a specific rotational speed, in addition a speed controller (TURNIGY K-Force 120A-HV OPTO V2 5-12S Brushless (Hobbyking, 2010a)) was used to keep the rotational speed constant. The rotational speed was monitored using an RPM sensor (Hobbywing, 2010), that generated a pulsed signal. This sensor was connected to an oscilloscope to obtain the frequency. The rotational speed and the frequency are related as given in the following equation:

$$RPM = \frac{120\,f}{p} \tag{5.27}$$

where *RPM* is the rotational speed, *f* is the frequency and *p* is the number of magnetic poles of the motor. A strain gauge was connected by one of its extremities to the aluminium plate, and by the other extremity to the motor. When the propeller produced thrust, it bended the strain gauge, thus provoking a that was further converted into an electrical signal. The electrical signal output was very small and required an amplification. An amplifier (INA 125P (Burr-Brown Corporation, 1997)) was used to increase the electrical signal of the strain gauge, and it required specific wiring, as seen on in Fig 5.10.

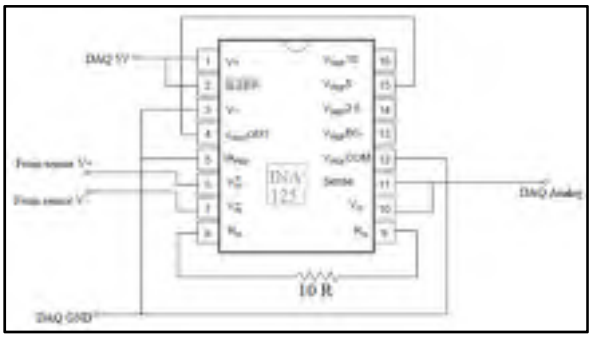

Figure 5.10 INA 125 electric wiring

The thrust was recorded via a National Instrument acquisition box (NI USB-6001 (National Instruments, 2014)). The data collected by the acquisition system can be directly read and stored with an interface developed using Labview software.

5.4.2 Bench Test Calibration

A calibration test was performed to relate the electrical signal read from the Labview interface with the measured actual force. For this purpose, several weights were measured using the bench test. The signals obtained were then used to create a relationship between the measured weights and the signals obtained. Figure 5.11 shows the measured weight variations with the read signal.

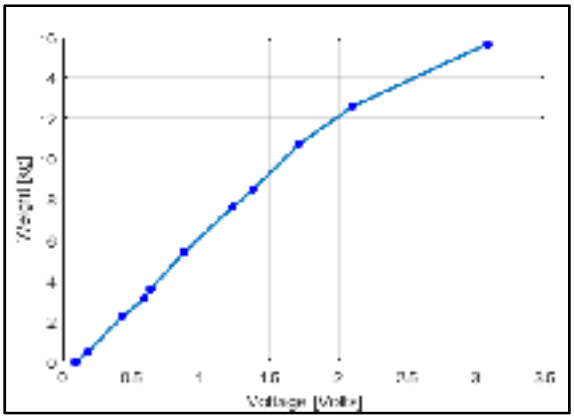

Figure 5.11 Relationship between the read voltage signal and the weights

A validation test was performed to evaluate the error between the actual and the measured weights. The results have shown that the bench test gave an error of 5% for weights between 0 to 50 N, and, 2% for 50 to 150 N. The calibration tests have shown that the bench test could accurately estimate the generated thrust as the relative error was smaller than 5%.

Table 5.2 Calibration Tests

Real value (kg)	Estimated value (kg)	Error (%)
2.75	2.63	4.36
3.18	3.01	5.34
5.92	5.92	0
7.83	7.58	3.19
10.9	11.14	2.20
13.22	13.35	0.98

5.4.3 Experimental Testing

The experimental tests were performed at the Price-Païdousis subsonic wind tunnel (Communier *et al*., 2015 ; Flores Salinas, 2015). This wind tunnel has a maximum speed of 40

m/s. The test unit or test chamber has a length of 182.5 cm, a height of 91.5 cm and a width of 62.5 cm. This test unit is useful for the aerodynamic experimental analysis of reduced-scale objects. When testing a propeller in a closed test section, the velocity of the propeller's slipstream for a positive thrust, will be greater than the airspeed *V* (Fig. 5.12). Since the same air volume passes ahead of and behind the propeller, it follows that the velocity outside the propeller's slipstream is less than the airspeed (Barlow *et al*., 1999). This difference causes the air outside the slipstream to increase its static pressure relative to the wind tunnel flow, and thus increases the pressure in the propeller slipstream. Therefore, the propeller develops more thrust than it would develop in free air.

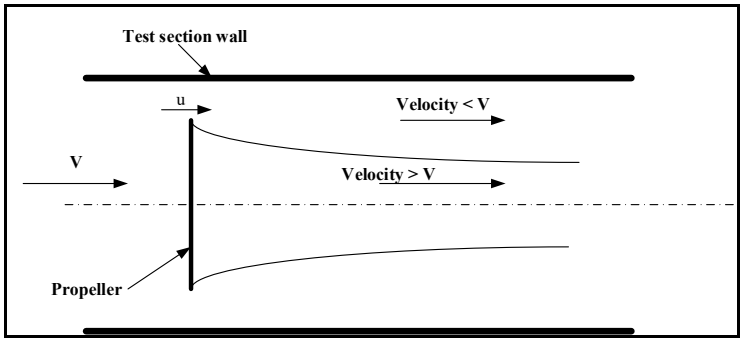

Figure 5.12 Velocities of a propeller in a closed test section

To avoid this problem, the experimental analysis was performed in an open test section. Figure 5.13 shows the test unit with the test bench installed. A wind tunnel calibration was made to verify that the air velocities at the outlet of the first section and at the inlet of the second section were constant. The calibration was also conducted to verify that the velocity distribution in the test section was constant.

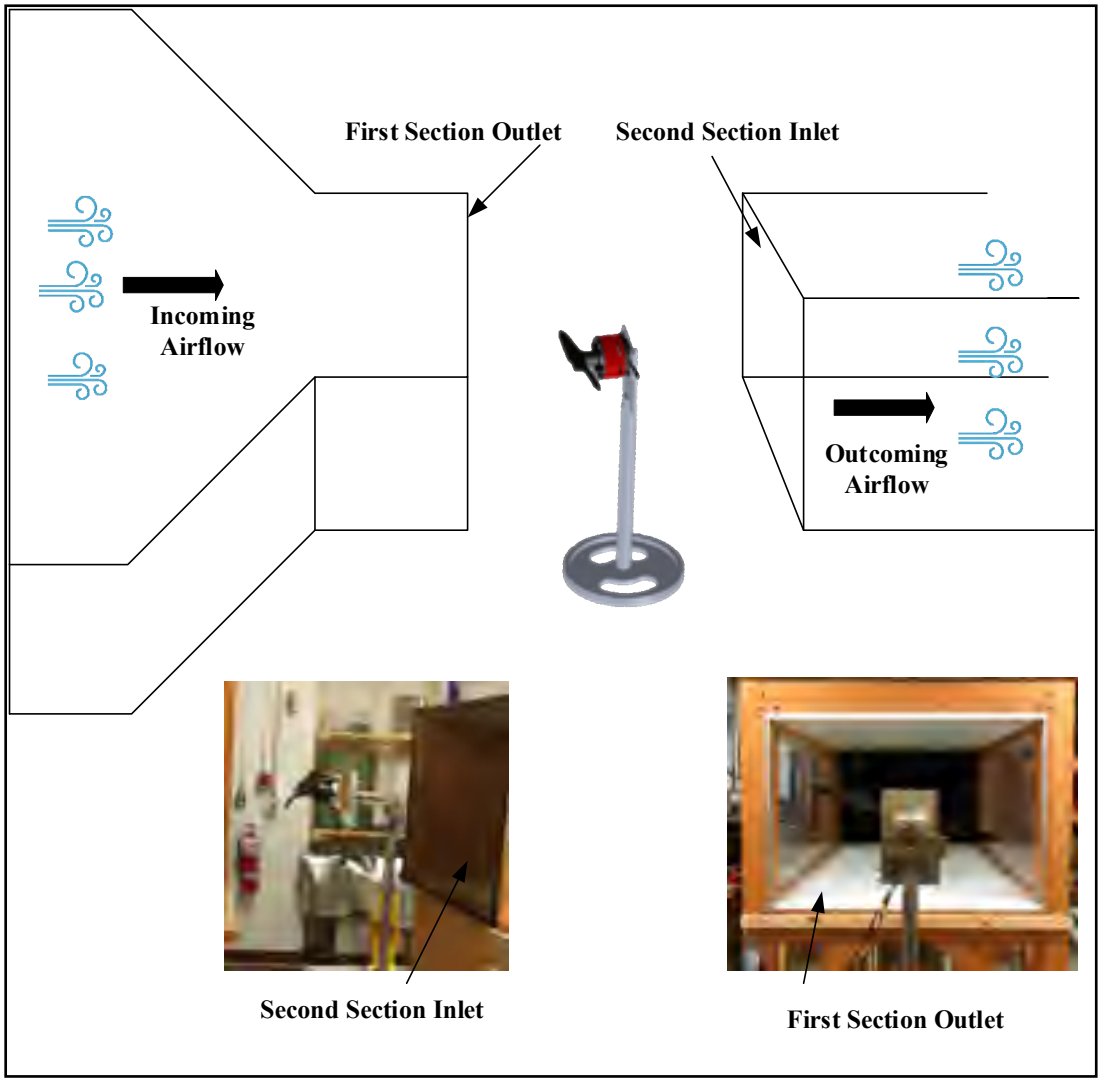

Figure 5.13 Bench Test in the Wind Tunnel Open Section

The wind tunnel calibration was done at two airspeeds: 5.8 m/s and 27 m/s. The air velocity was measured using a Pitot tube connected to a meter for air pressure, speed and flow measurements (FKS 1DP-PBM). The FKS 1DP-PBM Pitot tube uses the temperature, the humidity, the *K*-factor and the ambient pressure in order to obtain the airflow velocity inside a test unit.

Figure 5.14 shows that the flow distribution was uniform in the test chamber. The contraction for the air at the border of each section does not cause too significant acceleration of the fluid. The flow distribution in each section is constant. Also, the air velocity at the outlet of the first

section and at the inlet of the second section, for the two speeds, seems to be constant with a maximum variation of 6% between the first and the second section. The open test section was thus verified as appropriate for the propeller experimental analyses.

5.5 Results and Discussion

The propeller performance was estimated for a range of speeds from 6 m/s to 30 m/s dues to the wind tunnel's limitation speed and the stall speed of the propeller. The experimental and estimated thrust and power were reformulated into non-dimensional parameters. The thrust, C_T, and power, C_P, coefficients as well as the advance ratio, J, and the efficiency, η, of the propeller are given by the following equations:

$$C_T = \frac{T}{\rho n^2 D^4} \tag{5.28}$$

$$C_P = \frac{P}{\rho n^3 D^5} \tag{5.29}$$

$$J = \frac{V}{nD} \tag{5.30}$$

$$\eta = J\frac{C_T}{C_P} \tag{5.31}$$

where n is the rotational speed of the propeller, D is its diameter, ρ is the air density, V is the airspeed, T and P are respectively the thrust and the power generated by the propeller.

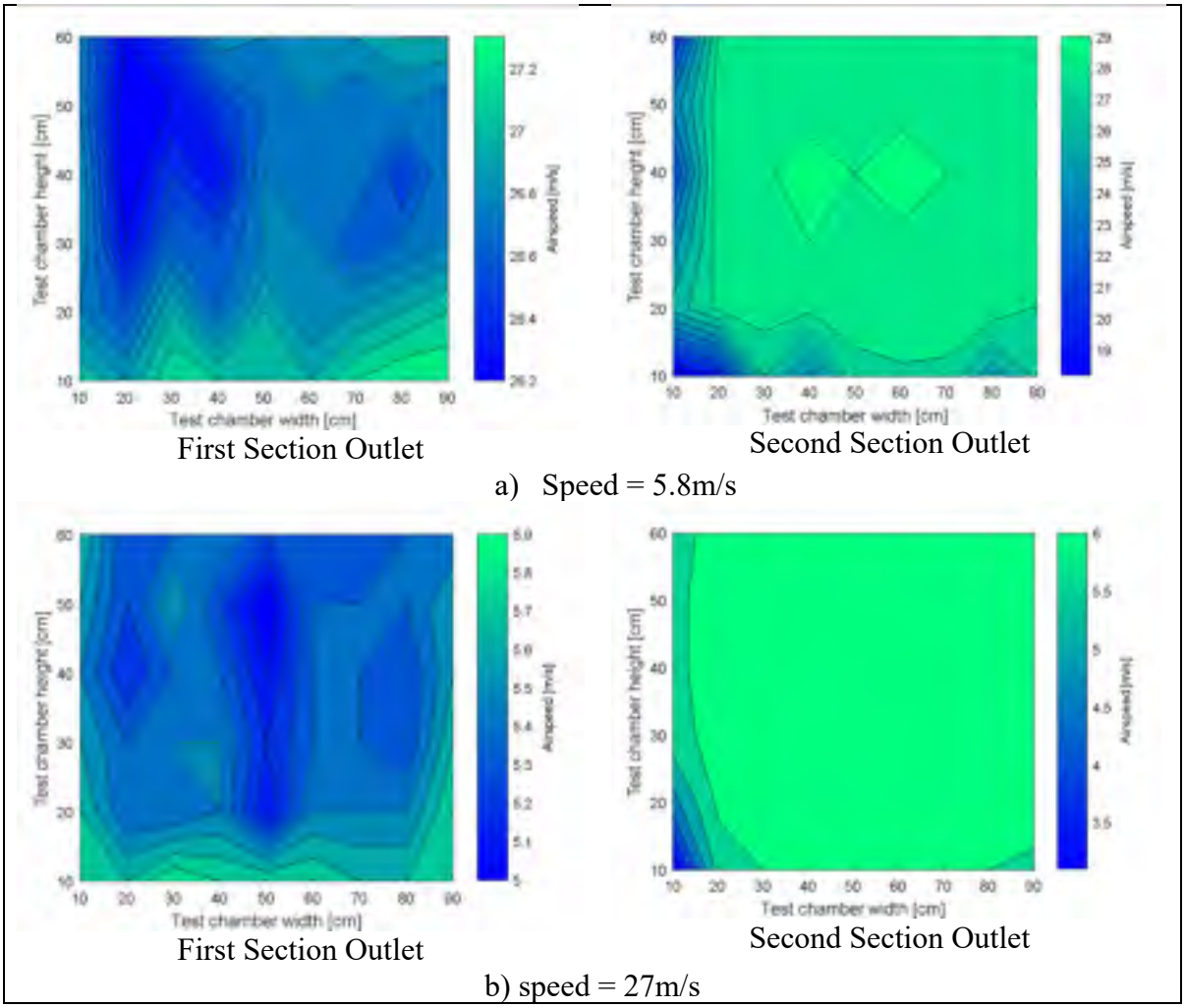

Figure 5.14 Velocity Distribution for the Experimental setup

For the comparison of the measured with the estimated data, the relative error is defined as being calculated between a reference value x_a and an approximated value x_b with the equation:

$$\left|\frac{x_b - x_a}{x_a}\right| * 100\% .$$

To highlight its accuracy, the proposed methodology, was firstly compared to the classical Blade Element Momentum Theory and to the experimental analysis.

The comparison was made for and rotation speed of 5000 RPM and a range of airspeed from 6m/s to 30m/s. Figure 5.15 shows the comparison of the thrust and power coefficients

estimated using these methodologies. The classical BET overestimates the thrust coefficient (Fig. 5.15a) by 26% for all the airspeeds (advance ratio). This overestimation is due to the rotation effect which were neglected in the case of the classical BET. The proposed method in contrary to the classical BET has a good agreement with the experiment analysis for advance ration from 0.25 to 0.6. The rotation of the propeller delays the stall of the aerodynamic lift coefficient which leads to a decrease of the thrust coefficient. For low advance ratio, (from 0.1 to 0.25) the relative error between the thrust coefficients estimate with the proposed method and the experimental analysis increases. The maximum relative error is 12.8% at advance ratio equal to 0.1. This result is due to the high angle of attack coefficient calculation method. For low advance ratio (low airspeed), Eq. (5.4) gives angles of attack beyond the stall angle of attack. Therefore, the accuracy of the high angle of attack coefficient calculation method influence the accuracy of the thrust coefficient. To highlight this influence, the proposed method was compared to a Blade Element Theory with same rotation effect correction and another high angle of attack coefficient calculation method. The Viterna and Corrigan (1982) method was used for this comparison as it is the most frequent in the literature. Figure 5.16 shows that there is a slight improvement of the accuracy for the low advance ratio when using the Viterna and Corrigan method, but overall relative error is increased in contrary to the proposed method which gives a very good accuracy for advance ratio from 0.25 to 0.6.

For the case of the power coefficient, Fig 5.15b shows that both methodologies have the same trend with a mean relative error of 9%. The power coefficient is mainly influenced by the drag. As explained in Section 5.2, the rotation effects do not change the drag polar. Thus, the power coefficient remains unchanged. The difference between the power coefficient estimated with classical BET and the proposed method is due to the high angle of attack coefficient calculation method which increase the values for all the advance ratio. This trend is confirmed in Fig 5.16b with the comparison of the proposed method with the Viterna and Corrigan method.

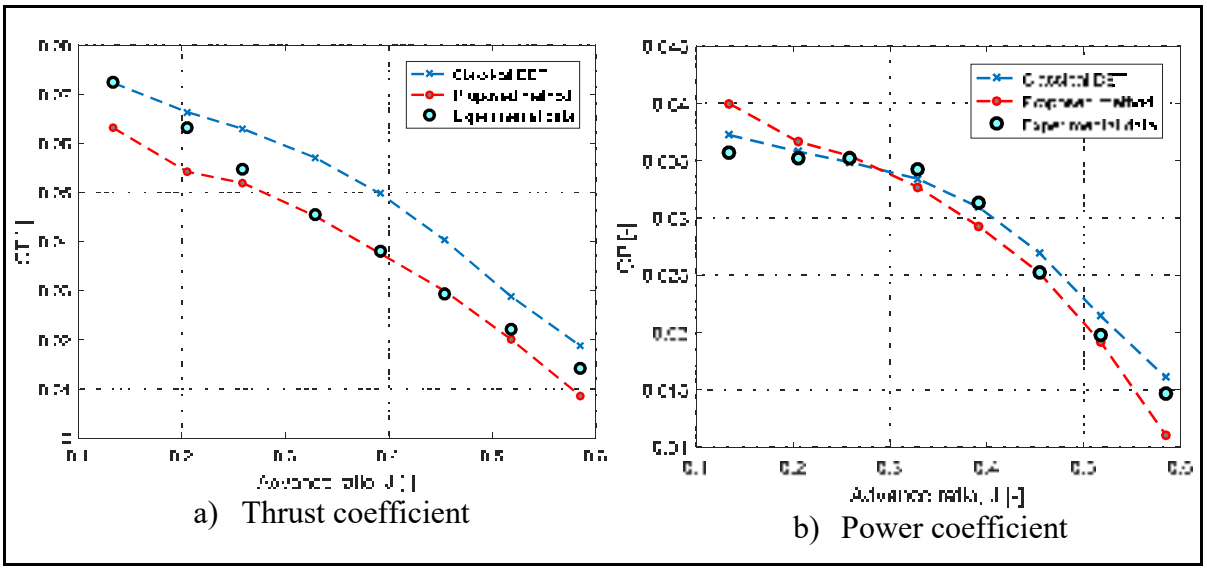

a) Thrust coefficient b) Power coefficient

Figure 5.15 Thrust and power coefficients variation with the advance ratio estimated using the classical BET, the proposed method and the experimental analysis

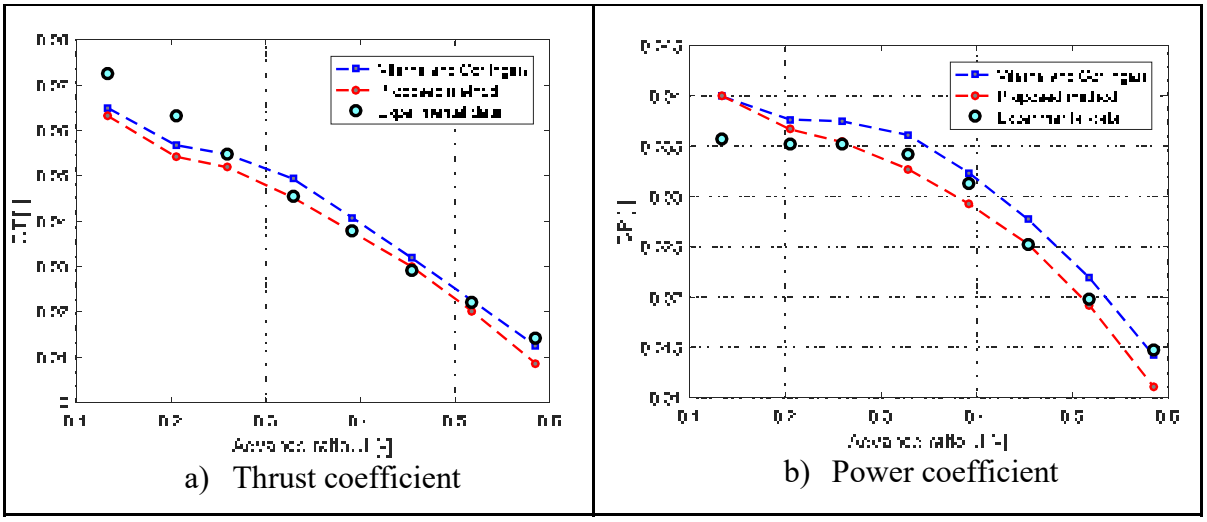

a) Thrust coefficient b) Power coefficient

Figure 5.16 Thrust and power coefficients variation with the advance ratio estimated using the Viterna and Corringan method, the proposed method and the experimental analysis

The CFD analysis was performed for several different flight conditions, expressed in terms of speeds (6-30 m/s) and altitude (0-4,500 m). The rotation speed was also fixed at 5000 RPM. Figure 5.17 shows the thrust and the power of the propeller variation with the advance ratio estimated using the CFD analysis, the proposed method and the experimental analysis. The

results have shown a very good agreement of the thrust estimation from the three methodologies for the thrust coefficient (Fig. 5.17a). The agreement decreases for low advance ratio when using the CFD analysis because the flow is supposed incompressible in this work. But at 5000 RPM the flow at the tip of the propeller is compressible and the high angle of attack aerodynamic coefficient are influenced.

Fig 5.17b shows the power coefficient estimate with the three methodologies. The power coefficient estimated using the CFD analysis gives a maximum error of 8.8%. The slightly diminished accuracy of the power is due to the calculation of the drag created by the propeller, which depends on the mesh quality and the turbulence model and can be difficult to evaluate for rotating motion.

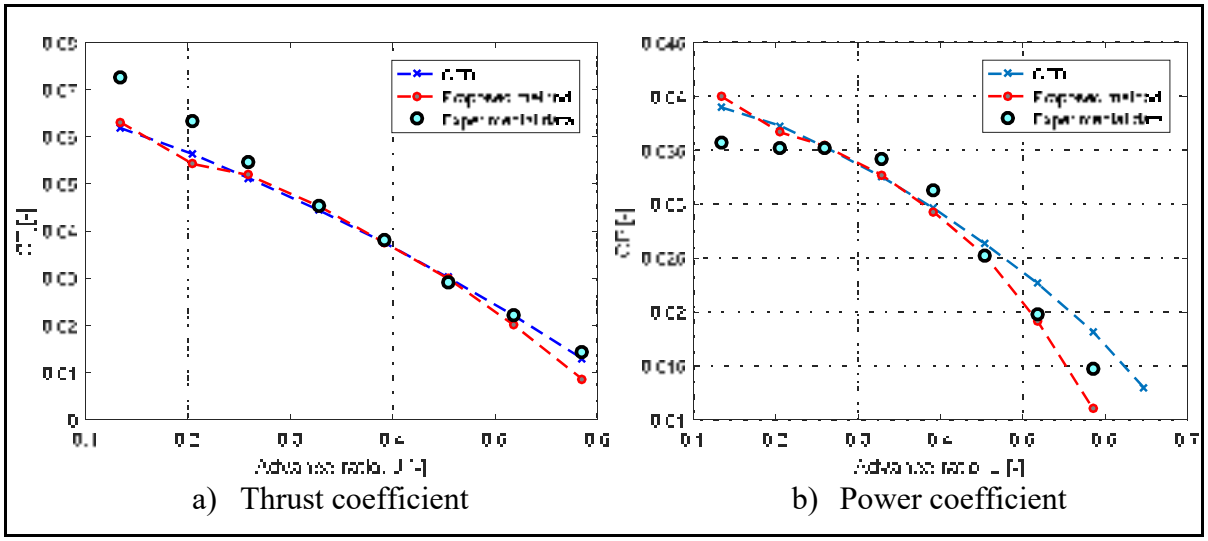

a) Thrust coefficient b) Power coefficient

Figure 5.17 Thrust and power coefficients variation with the advance ratio estimated using the CFD analysis, the proposed method and the experimental analysis

5.6 Conclusion

This paper presents new methodologies to predict the performance behaviour of the unmanned aerial system UAS-S45 propeller. The propeller was originally scanned, and further transformed into a CAD model. A methodology to improve the classical Blade Element Momentum Theory was applied to the propeller. The methodology considered the rotation

effects which result to a stall delay in the lift coefficient polar; and also proposed a high angle of attack aerodynamic coefficient calculation method.

A CFD analysis was also applied to the propeller geometry. The first layer's thickness, the number of layers, and the grid spacing were calculated using the law of the wall in order to study the region out of the boundary layer and to reduce the computation time. These parameters were used to generate a polyhedral unstructured mesh. Reynolds-Average Navier-Stokes equations were used to solve the flow equations around the propeller blade with the realisable k-ε turbulence model.

The proposed methodology compared to experimental results from an experimental testing setup that took place in the Price-Paidoussis wind tunnel and to classical BET. This comparison shows a better agreement of the proposed method with experimental data. Thus, the influence of the high angle of attack aerodynamic coefficient was evaluated. A comparison with the Viterna and Corrigan was made for this purpose.

A comparison of the thrust and power coefficient obtained using the CFD analysis and using the proposed method was made. The limitations of the CFD analysis such as the type of flow, the mesh quality and the turbulence model were revealed in reduce accuracy of the power coefficient variation with the advance ratio.

All these comparisons showed that our numerical approaches were highly accurate. These results also showed the applicability of the numerical methods for efficient flight dynamics and control law modelling and simulation technologies

5.7 Acknowledgements

Special thanks are dues to the Natural Sciences and Engineering Research Council of Canada (NSERC) for the Canada Research Chair Tier 1 in Aircraft Modelling and Simulation Technologies funding. We would also like to thank Mrs. Odette Lacasse for her support at the ETS, as well as to Hydra Technologies' team members Mr. Carlos Ruiz, Mr. Eduardo Yakin and Mr. Alvaro Gutierrez Prado in Mexico.

CHAPTER 6

LOW-ORDER ROBUST CONTROLLER FOR STABILIZATION, TRACKING AND DISTURBANCE REJECTION OF THE UNMANNED AERIAL SYSTEM UAS-S45 BÁLAAM

Maxime Alex Junior Kuitche, Hugo Yañez-Badillo and Ruxandra Mihaela Botez
LARCASE Laboratory of Applied Research Active Controls,
Avionics and AeroServoElasticity,
Ecole de Technologie Supérieure, 1100 Notre Dame West,
Montreal, H3C1K3, Québec, Canada

Article soumis dans *The Aeronautical Journal*, en Septembre 2019

Résumé

Les mécanismes de stabilisation et de contrôle d'un système aérien sans pilote (UAS) doivent être correctement conçus pour garantir des performances de vol acceptables. Au cours de leur fonctionnement, ces systèmes sont soumis à des effets environnementaux inconnus et aléatoires, de sorte qu'il est impératif que toutes les informations disponibles soient prises en compte lors de la conception des mécanismes (par exemple, dynamique du système, actionneurs, conditions de vol et d'autres critères). , tels que les modes long (phugoïde) et court pour les mouvements longitudinaux, et les modes affaissement par roulis, spirale et roulis hollandais pour la dynamique latérale, afin de garantir la stabilité de vol même en présence de ces perturbations. Par conséquent, cet article présente une nouvelle méthodologie pour la stabilisation et le contrôle des mouvements du UAS-S45 Bálaam, conçu et fabriqué par Hydra Technologies. Cette méthodologie utilise des contrôleurs composites combinant des régulateurs linéaires quadratiques à rétroaction (LQR) et des contrôleurs de type proportionnel-intégral avec des contrôleurs de compensation FeedForward de référence (PI-FF) pour les tâches de stabilisation et de suivi, respectivement. Un observateur d'états étendu généralisé a été mis en œuvre pour renforcer la dynamique en boucle fermée en introduisant une compensation de perturbation. En outre, un système d'inférence neuronal floue adaptatif (ANFIS) a été adopté pour effectuer une planification de gain en calculant les gains de chaque

contrôleur composite pour certaines conditions de trim inconnues dans un domaine de vol donné. Enfin, plusieurs évaluations numériques sont réalisées pour mettre en évidence la faisabilité et l'efficacité de la méthodologie proposée.

Abstract

The stabilization and control mechanisms of an Unmanned Aerial System (UAS) must be properly designed to ensure acceptable flight performance. During their operation, these systems are subjected to unknown and random environmental effects, making it imperative that all of the available information should be taken into consideration during the mechanisms' design process (e.g., system dynamics, actuators, flight conditions, and certain criteria requirements, such as long (phugoid) and short modes for longitudinal motions, and roll subsidence, spiral and Dutch-roll modes for lateral dynamics) in order to guarantee flight stability even in the presence of these disturbances. Therefore, this paper introduces a novel methodology for the stabilization and motion control of the UAS-S45 Bálaam, designed and manufactured by Hydra Technologies. This methodology uses composite controllers combining feedback Linear Quadratic Regulators (LQR) and Proportional Integral with a reference FeedForward (PI-FF) compensation controllers for stabilization and tracking tasks, respectively. A Generalized Extended State Observer was implemented to provide robustness to the closed loop dynamics by introducing disturbance compensation. Furthermore, an Adaptive Neuro-Fuzzy Inference System (ANFIS) was adopted to perform a gain scheduling by computing the gains of each composite controller for certain unknown trim conditions within a given flight domain. Finally, several numerical assessments are performed to highlight the feasibility and efficacy of the proposed methodology.

6.1 Introduction

Achieving accurate tracking for Unmanned Aerial Systems is complicated because of many difficulties. The diversity of mission platforms, nonlinear dynamics, resource constraints and unpredictable environmental conditions are some of the main problems inherent to the UAS

control domain. An efficient solution to these problems requires the utilization of flight control systems that are highly resilient and autonomous, capable of guaranteeing constraints satisfaction, robustness and reliability in the range of model dynamics and operating conditions (Eren *et al*., 2017 ; Valyou *et al*., 2013). The recent interest in making Unmanned Aerial Systems (Aubeelack and Botez, 2019 ; Sugar Gabor *et al*., 2015 ; Segui *et al*., 2017) more robust, and in increasing their abilities has led researchers to address these challenging demands using modern controller synthesis approaches.

Optimal control (Botez *et al*., 2015 ; Frost *et al*., 2012 ; Kammegne *et al*., 2016 ; Li *et al*., 2017) is a commonly applied method that seeks to maximize the system outputs for a minimum cost. Zhen *et al* (2015). investigated anti-wing attitude control for the Boeing 707 in the landing phase. The longitudinal attitude control was based on the Proportional Integral Derivative (PID) and the C* inner control, whereas the lateral attitude control was performed using an optimal regulator. In (Vinodh *et al*., 2016), a Linear Quadratic Regulator (LQR) control strategy was applied on a two degree-of-freedom laboratory workstation for pitch and yaw angle control. Their methodology used the adaptive Particle Swarm Optimization (PSO) algorithm to improve the selection of the control gains and guarantee an optimal attitude tracking control. Even if optimal control is considered as the universal solution for the linear control problem (Kálmán, 1960), bibliographical research works (Doyle, 1978 ; Rosenbrock and McMorran, 1971 ; Starr and Ho, 1969) pointed out its poor robustness and its excessive bandwidth.

As a completion of the optimal control, robust control (Balas and Frost, 2012 ; Sadeghzadeh *et al*., 2014) methods may be applied when the aircraft dynamic uncertainties, modeling errors and environment disturbance are considered. Boughari *et al*. (2017) proposed a robust controller based on an optimization using the H_∞ method and the genetic algorithm for the Cessna Citation X. The controller was designed to ensure acceptable flying qualities in the presence of aircraft dynamics uncertainties dues to mass and center of gravity variations. Liu *et al*. (2017) proposed a Model Predictive Control (MPC) based on a Linear Quadratic Gaussian (LQG) approach to compensate for the dynamic gust loads on the flexible aircraft in turbulence conditions. This association of the MPC and the LQG methods makes it possible to manage the problems of dynamics variation and disturbance rejection, and thereby to ensure a

robust performance. The major inconvenient of robust controllers is their high order which makes them impossible to implement in a practical situation without reducing their order (Obinata and Anderson, 2012). However, a reduction of a controller also affects its performance.

Another option is to use intelligent control (Ceruti *et al*., 2002 ; Zhixiang *et al*., 2014 ; Magar *et al*., 2017). (Hušek and Narenathreyas, 2016) presents a longitudinal control based on a Takagi-Sugeno fuzzy model. The controller was applied to the LET L410 to guarantee closed loop stability and pitch angle tracking. Wu *et al*. (2018) developed an adaptive neural network flight control for longitudinal motion control in high angle of attack conditions. Their adaptive neural network was designed using a coupling of a variable separation technique with the Lyapunov–Krasovskii function method. The methodology showed good performance for an uncertain non-strict feedback nonlinear system with distributed time-varying delays. However, neural network architecture design requires a large amount of training data. Furthermore, the neural network weights do not represent physical variables, thus neural network architectures are difficult to adjust in practical situations.

To capture the benefits of each of these control methodologies, and to tackle all the inconvenient associated with them especially for Unmanned Aerial Systems, a design methodology is introduced in this paper. The aim of the approach is to provide a robust low-order controller able to solve a nonlinear control problem.

The overall controller architecture is composed by a Linear Quadratic Regulator (LQR) feedback controller to ensure aircraft stability, and a Proportional-Integral controller combined with reference FeedForward compensation (PI-FF) to provide controllability. This controller can be easily implemented in a practical situation because of its low-order. The proposed methodology allows closed-loop stability and controllability, as well as robustness to soft dynamics variations. As a completion of the robustness improvement especially for disturbance rejection, a Generalized Extended State Observer (GESO) was added to the controller design. The GESO is a good alternative to design a robust controller since it allows the estimation and the compensation of the disturbances and uncertainties. Finally, a Linear Parameter-Varying (LPV) method was applied to provide a nonlinear capability to the controller. The proposed scheme uses a minimum amount of data to handle the nonlinear

problem. The LPV method is based on an Adaptive Neuro-Fuzzy Inference System (ANFIS) which is a combination of a fuzzy theory and a neural network. The fuzzy theory provides additional data to the neural network in order to enhance its ability to produce estimated outputs.

The paper is organized as follows. The UAS-S45 model and its dynamic equations are presented in Section 6.2, followed by the control scheme in Section 6.3. It consists of a Linear Quadratic Regulator (LQR) for stability augmentation, a Proportional-Integral with reference feedforward (PI-FF) for the control augmentation, and a Generalized Extended State Observer (GESO) for improving robustness capabilities. Later, the Linear Parameter-Varying (LPV) based on the Adaptive Neuro-Fuzzy Inference System (ANFIS) method is described in Section 6.4. Finally, Section 6.5 presents and discusses the simulation results, and is followed by Conclusions in Section 6.6.

6.2 UAS-S45 Bálaam dynamic equations

The proposed control methodology was applied to the flight dynamics model of the UAS-S45 Bálaam. The UAS-S45 is an Unmanned Aerial System designed and manufactured by Hydra Technologies to provide surveillance and security capabilities for both military and civilian purposes (Fig. 6.1). Its general characteristics are given in Table 6.1.

Figure 6.1 The UAS-S45 Bálaam

Table 6.1 General Characteristics of the UAS-S45

Specification	Value
Wing span	6.11 m
Wing area	2.72 m²
Total length	3.01 m
Mean aerodynamic chord	0.57 m
Empty weight	57 kg
Maximum take-off weight	79.6 kg
Loitering airspeed	55 knots
Service ceiling	20, 000 ft
Operational range	120 km

Kuitche and Botez (2019) developed a flight dynamics model of the UAS-S45 (Fig. 6.2). Their flight dynamics model was designed to evaluate the performance of a morphing wing technique. Its architecture was divided in four sub-models, each of these sub-models was estimated using numerical and experimental methodologies.

The aerodynamic sub-model is realized by a combination of the contributions of the "Wing part", the "fuselage part", the "tail part", and their interactions. Its estimation was performed using Fderivatives code, which is an improvement of the DATCOM procedure, and a CFD analysis.

The propulsion sub-model is a piston-propeller engine model. The piston engine was designed using equations derived from the ideal Otto cycle, and was optimized using the manufacturer's data. The propeller aerodynamic performance was obtained using a CFD analysis and the Blade Element Theory (BET).

The structural sub-model determines the mass and inertia of the UAS-S45 and was calculated using the Raymer equations and the DATCOM procedure.

The actuator sub-model was estimated using a servomotor model coupled with mechanical calculations.

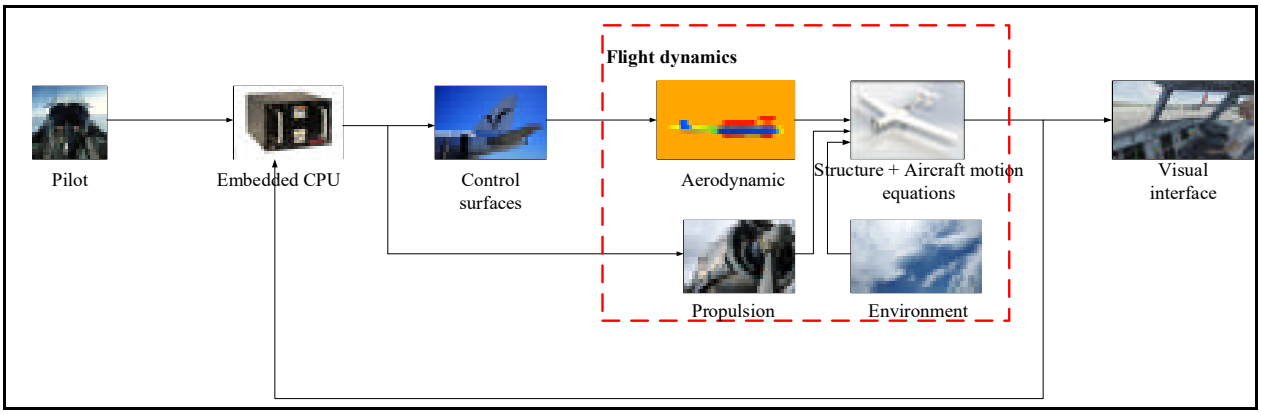

Figure 6.2 The UAS-S45 simulation model

The UAS-S45 flight dynamics model developed by Kuitche and Botez (2019) allows the UAS-S45 flight dynamics to be obtained for several regimes, including cruise, take-off and landing, and so for various flight conditions. This model is therefore used for the purpose of controller design.

Before designing the control system, the UAS-S45 model was linearized for specific flight conditions within its flight domain, as illustrated in Fig. 6.3. For this purpose, a Jacobian linearization of the flight dynamics model of the UAS-S45 was performed around an equilibrium point. The following expression of the linearization process was utilized:

$$f(\theta_e,\delta_{e_e},\delta_{a_e},\delta_{r_e})=0 \begin{vmatrix} v_e=0,u_e=V\cos(\alpha_e),w_e=V\sin(\alpha_e) \\ p_e=q_e=r_e=0 \\ f_e=\psi_e=0,\theta_e=\alpha_e \end{vmatrix} \quad (6.1)$$

where δ_{ee}, δ_{ae}, δ_{re} are the elevator, aileron and rudder angles at the equilibrium state, v_e, u_e and w_e are the speed components at the equilibrium state, p_e, q_e, r_e are the roll, pitch and yaw rates at the equilibrium state, Φ_e, θ_e, ψ_e are the roll, pitch and yaw angles at the equilibrium state, α_e is the angle of attack at the equilibrium state and V is the aircraft airspeed.

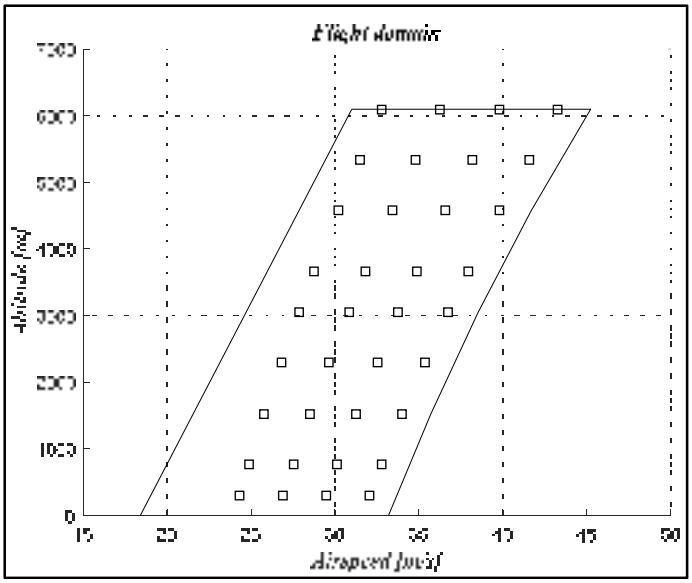

Figure 6.3 The UAS-S45 flight envelope

The coupling effects between the longitudinal and the lateral dynamics were neglected. These assumptions led to the following state-space representations for the longitudinal (Eq. 6.2) and the lateral dynamics (Eq. 6.3):

$$\begin{bmatrix} \Delta\dot{u} \\ \Delta\dot{w} \\ \Delta\dot{q} \\ \Delta\dot{\theta} \end{bmatrix} = \begin{bmatrix} X_u & X_w & 0 & -g \\ Z_u & Z_w & u_0 & 0 \\ M_u + M_{\dot{w}} Z_u & M_w + M_{\dot{w}} Z_w & M_q + M_{\dot{w}} u_0 & 0 \\ 0 & 0 & 1 & 0 \end{bmatrix} \begin{bmatrix} \Delta u \\ \Delta w \\ \Delta q \\ \Delta\theta \end{bmatrix} + \begin{bmatrix} X_{\delta_e} & X_{\delta_T} \\ Z_{\delta_e} & Z_{\delta_T} \\ M_{\delta_e} + M_{\dot{w}} Z_{\delta_e} & M_{\delta_T} + M_{\dot{w}} Z_{\delta_T} \\ 0 & 0 \end{bmatrix} \begin{bmatrix} \Delta\delta_e \\ \Delta\delta_T \end{bmatrix} \tag{6.2}$$

$$\begin{bmatrix} \Delta\dot{v} \\ \Delta\dot{p} \\ \Delta\dot{r} \\ \Delta\dot{f} \end{bmatrix} = \begin{bmatrix} Y_v & Y_p & -(u_0 - Y_r) & g\cos(\theta_0) \\ L_v & L_p & L_r & 0 \\ N_v & N_p & N_r & 0 \\ 0 & 1 & 0 & 0 \end{bmatrix} \begin{bmatrix} \Delta v \\ \Delta p \\ \Delta r \\ \Delta f \end{bmatrix} + \begin{bmatrix} 0 & Y_{\delta_r} \\ L_{\delta_a} & L_{\delta_r} \\ N_{\delta_a} & N_{\delta_r} \\ 0 & 0 \end{bmatrix} \begin{bmatrix} \Delta\delta_a \\ \Delta\delta_r \end{bmatrix} \quad (6.3)$$

where u, v, and w are the velocity components around the body axes, p, q and r are the angular velocity components, θ and ϕ are respectively the pitch and the roll angle, θ_0 is the initial pitch angle, δ_e is the elevator angle, δ_a is the aileron angle, δ_r is the rudder angle, and δ_T is the throttle position. X_u, X_w, X_δ, Y_v, Y_p, Y_r, Y_δ, Z_u, Z_w, Z_δ, L_v, L_p, L_r, L_δ, M_u, M_w, M_δ, and N_v, N_p, N_r, N_δ are the stability derivatives.

Since the UAS-S45 is useful for military purposes, such as intelligence gathering and surveillance, it requires specific flight qualities to guarantee a proper flight performance. The flight quality requirements provided by the *U.S "Military Specification for the Flying Qualities of Piloted Airplanes MIL-STD-1797A"*(Mitchell *et al*., 1994 ; US Military, 1980) defined in terms of damping and natural frequency were therefore used for this analysis. These requirements were chosen by assuming that the UAS-45 is a light aircraft and are listed in Table 6.2 for each dynamic mode response (short period, phugoid, roll subsidence, spiral and Dutch roll), and in Table 6.3 for a tracking step response.

Table 6.2 Stability Augmentation System Criteria

Dynamic mode	**Specifications**
Phugoid	$\xi_{ph} \geq 0.04$
Short period	$0.35 \leq \xi_{sp} \leq 1.30$
Dutch roll	$\xi_{dr} \geq 0.19$ $\omega_{dr} \geq 1.0$ rad/s $\xi_{dr}\,\omega_{dr} \geq 0.35$ rad/s

Table 6.2 (Continued) Stability Augmentation System Criteria

Dynamic mode	Specifications
Spiral	$T_{2s} \geq 12$ s
Roll subsidence	$\tau_{ra} \leq 1.0$s

Table 6.3 Tracking step criteria

Criteria	Specifications
Maximum overshoot (D)	$D \leq 5\%$
Time response at 5% (T_r)	$T_r \leq 6$s
Steady state error (e_p)	$e_p \leq 10^{-2}$

In Table 6.2, ξ and ω are the damping and the frequency, respectively, of the considered mode, τ_{ra} is the time constant, and T_{2s} is the double amplitude time given by:

$$T_{2s} = \frac{-ln(2)}{\xi\omega} \tag{6.4}$$

6.3 Introduction of control schemes in the UAS-S45 flight dynamics model

The state-space representation of the UAS-S45 for its longitudinal and lateral dynamics as described by Eqs. (6.2) and (6.3) can take the form of a Linear Time Invariant (LTI) system (Cook, 2013 ; Phillips, 2009 ; Stevens and Lewis, 2003):

$$\begin{aligned} \Delta\dot{\boldsymbol{x}} &= \boldsymbol{A}\Delta\boldsymbol{x} + \boldsymbol{B}\Delta\boldsymbol{u} \\ \Delta\boldsymbol{y} &= \boldsymbol{C}\Delta\boldsymbol{x} + \boldsymbol{D}\Delta\boldsymbol{u} \end{aligned} \tag{6.5}$$

where A, B, C and D are the system, the input, the output and the feedforward matrices, respectively, x is the state vector, u is the control vector, and y is the output vector.

The low-order UAS-S45 controller to design is given in Eq. (6.6). It is obtained by summing the gains from the LQR, the PI-FF and the GESO methods.

$$\Delta \boldsymbol{u} = -\boldsymbol{K}_x \Delta \boldsymbol{x} - \boldsymbol{K}_i \Delta \boldsymbol{\varepsilon} + \boldsymbol{K}_p \Delta \dot{\boldsymbol{\varepsilon}} + \boldsymbol{K}_{ff} r + \boldsymbol{K}_d \hat{d} \tag{6.6}$$

where K_x is the LQR gain, K_i is the integral gain, K_p is the proportional gain, K_{ff} is the feedforward gain and K_d is the GESO disturbance gain, u is the control input, x is the state vector, ε is the error between input reference and the measure output, r is the reference input and $\hat{d}$ is the estimated disturbance.

Figure 6.4 shows the control architecture for the lateral and longitudinal dynamics of the UAS-S45. The input and the output for the longitudinal dynamics model are respectively given by the elevator δ_e and the pitch θ angles, whereas the inputs of the lateral dynamics model are the rudder and the aileron angles δ_r, δ_a, and its output is the roll angle ϕ.

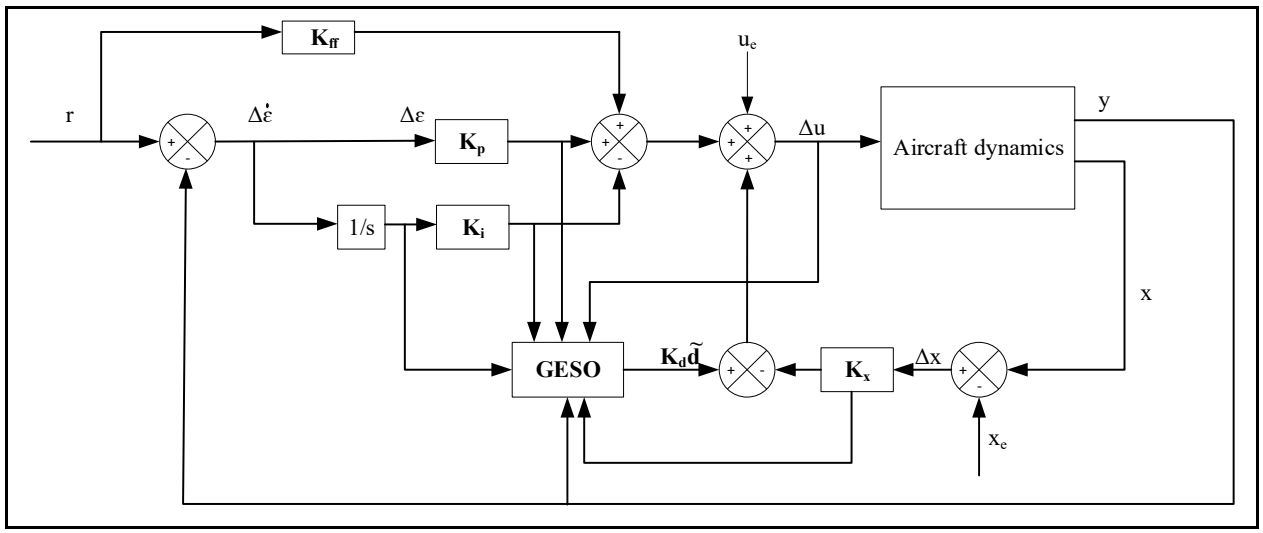

Figure 6.4 The complete UAS-S45 control law

The proposed methods design to obtain the gains K_x, K_i, K_p, K_{ff} and K_d, consists of 3 steps:

Step 1: Design of a Linear Quadratic Regulator (LQR) using a selection technique for the weight matrices. The LQR method was incorporated to give stability to the dynamic mode

(short period, phugoid, roll subsidence, spiral, Dutch roll) of the UAS-S45. An additional state was added to the LTI system described in Eq. (6.5) for considering pitch angle steady-state error, where the following expression is obtained:

$$\begin{bmatrix} \Delta\dot{\boldsymbol{x}} \\ \Delta\dot{\varepsilon} \end{bmatrix} = \boldsymbol{A}_{aug} \begin{bmatrix} \Delta\boldsymbol{x} \\ \Delta\varepsilon \end{bmatrix} + \boldsymbol{B}_{aug}\Delta\boldsymbol{u} + \begin{bmatrix} \boldsymbol{0}_{i\times 1} \\ 1 \end{bmatrix} r \text{ , where } \boldsymbol{A_{aug}} = \begin{bmatrix} \boldsymbol{A} & \boldsymbol{0_{i\times 1}} \\ \boldsymbol{-C} & 0 \end{bmatrix}, \text{ and}$$
$$\mathbf{B_{aug}} = \begin{bmatrix} \mathbf{B} \\ \mathbf{0}_{\mathrm{l}\times j} \end{bmatrix} \tag{6.7}$$

In Eq. (6.7) $\mathbf{A}_{\mathrm{aug}}$ and $\mathbf{B}_{\mathrm{aug}}$ are the augmented matrices, i is the row number of $\mathbf{A}$, and j is the column number of $\mathbf{B}$.

The LQR approach needed to obtain an optimal solution of a control problem is given in (Ashraf *et al*., 2018 ; Choi and Seo, 1999 ; Vepa, 2014). The LQR method is applicable if that the system is controllable. The LQR methodology is based on the minimization of the next cost function

$$J = \frac{1}{2}\int_0^{\infty} \left(\boldsymbol{x}^T \boldsymbol{Q}\boldsymbol{x} + \boldsymbol{u}^T \boldsymbol{R}\boldsymbol{u} \right) dt \tag{6.8}$$

where x is the state, u is the control input, and $\mathbf{Q}$ and $\mathbf{R}$ are the positive weighting matrices.

The optimal $\mathbf{K}$ is thus obtained using the following expression:

$$\boldsymbol{K} = \boldsymbol{R}^{-1}\boldsymbol{B}^T\boldsymbol{P} = \begin{bmatrix} \boldsymbol{K}_x & \boldsymbol{K}_{ss} \end{bmatrix} \tag{6.9}$$

where $\mathbf{P}$ is the Ricatti's matrix, $\mathbf{B}$ is state space input matrix. $\mathbf{K_x}$ is the feedback control gain vector, and $\mathbf{K_{ss}}$ is an integral gain which was replaced by the control augmentation system.

In (Ashraf *et al*., 2018 ; Choi and Seo, 1999 ; Stevens and Lewis, 2003 ; Kumar *et al*., 2016), the weighting matrices $\mathbf{Q}$ and $\mathbf{R}$ of the LQR procedure are manually selected; therefore, it is not guaranteed that the system to be controlled will meet some specific requirements. To ensure that the stabilized UAS-S45 will meet the desired flight qualities, the weighting matrices $\mathbf{Q}$ and $\mathbf{R}$ are selected using an optimisation procedure based on the metaheuristic Particle Swarm Optimisation (PSO) algorithm

The PSO was bounded for the weighting matrices' selection to reduce the search space, and to ensure that the matrices would be positively defined at each iteration. An objective function was proposed to evaluate the convergence of the optimisation algorithms:

$$J = \min_{\boldsymbol{K}} \left[(N - n_c) \times 10^5 + \sum_j \left(\boldsymbol{K}_j \right)^2 \right] \tag{6.10}$$

where N is the total number of requirements for the stability as presented in Table 6.2, n_c is the number of requirements that are met in each iteration, and $\mathbf{K}_j$ represent the j^{th} element in the vector **K**. The expression $\sum_j \left(\boldsymbol{K}_j \right)^2$ is added to the objective function to reduce the size of control vector gains parameters.

The overall process that takes place to obtain the LQR control vector gain is summarized in Fig. 6.5.

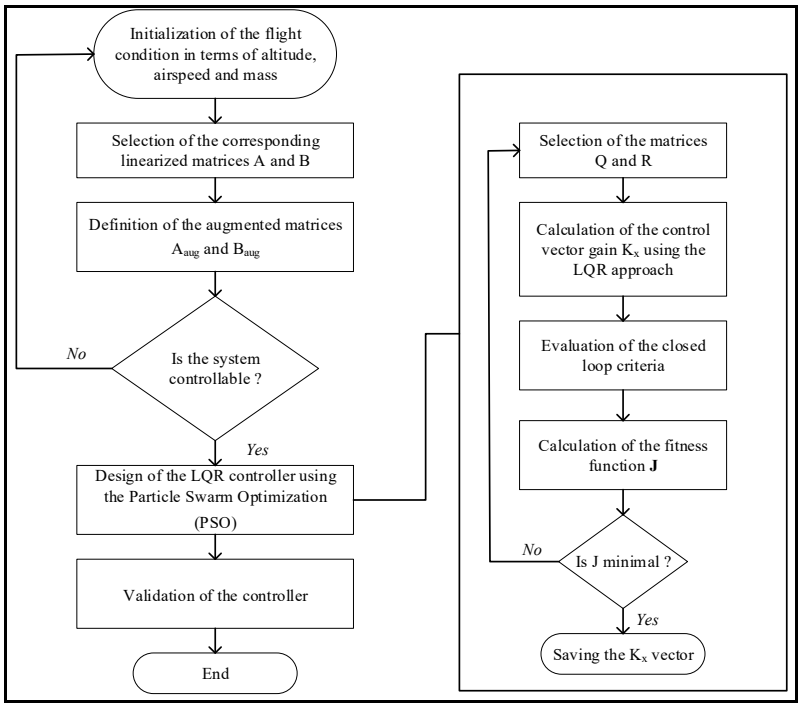

Figure 6.5 LQR control process

Step 2: The Proportional-Integral with reference feedforward (PI-FF) gains are evaluated for the stabilized system. A PI-FF controller was used to address the tracking problems. It is

mainly composed of a Proportional Integral (PI) controller. Due to its stable, reliable and easy-to-adjust structure, PI controller remains as one of the main controller for industrial purposes (Reznik *et al*., 2000). The PI controller is suitable for stabilizing a system and for eliminating the steady state error. Moreover, in order to improve the tracking performance, a reference feedforward compensator was added to the PI controller (Saussié *et al*., 2006). The reference feedforward compensator can anticipate the reference modification before the PI controller and can provide an additional command.

The overall process to obtain the *Ki, Kp* and K_{ff} parameters is summarized in Fig. 6.6.

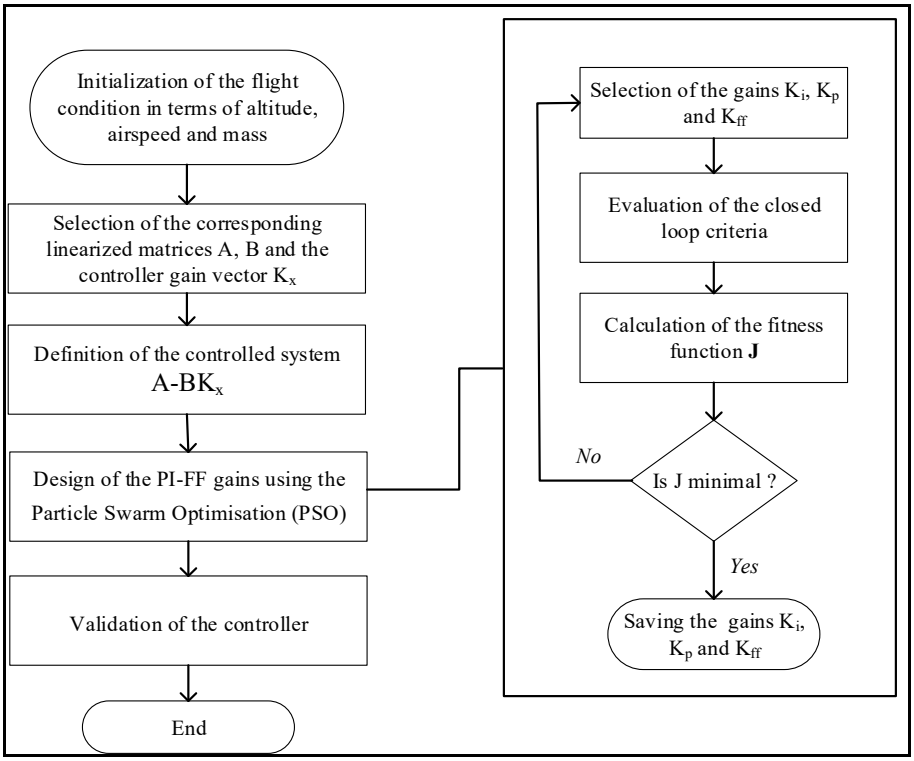

Figure 6.6 PI-FF gains estimation process

Step 3: A Generalized Extended State Observer (GESO) is designed for both disturbances gain calculation and estimation of external disturbances. Then, for the purposes of GESO design, an alternative representation of the augmented model introduced in Eq. (6.7) is considered:

$$\Delta\dot{\boldsymbol{x}}_{aug} = \boldsymbol{A}_{aug}\Delta\boldsymbol{x}_{aug} + \boldsymbol{B}_{aug}\Delta\boldsymbol{u} + \boldsymbol{G}r \tag{6.11}$$

Unmodeled dynamics, parametric uncertainties and external disturbances can then be introduced in the analysis by adding them into the UAS-S45 system model given in Eq. (6.11) as follows:

$$\begin{aligned}\Delta\dot{\boldsymbol{x}}_{aug} &= \boldsymbol{A}_{aug}\Delta\boldsymbol{x}_{aug} + \boldsymbol{B}_{aug}\Delta\boldsymbol{u} + \boldsymbol{G}r + \boldsymbol{b}_d f(x,w(t),t)\\ y_m &= \boldsymbol{C}_m\Delta\boldsymbol{x}_{aug}\\ y_o &= \boldsymbol{C}_o\Delta\boldsymbol{x}_{aug}\end{aligned} \tag{6.12}$$

where $f(x,w(t),t)$ is the uncertainty function, y_m is the measurable output, y_0 is the controllable output, $\boldsymbol{C}_o = \begin{bmatrix}\boldsymbol{C} & 1\end{bmatrix}$ and $\boldsymbol{C}_{\mathrm{m}} = \begin{bmatrix}0 & 0 & 0 & 1 & 0\\ 0 & 0 & 0 & 0 & 1\end{bmatrix}$. For design purposes, let introduce *m* as the row number of $\boldsymbol{A}_{\mathbf{aug}}$, and *n* as the column number of $\boldsymbol{B}_{\mathbf{aug}}$.

Then, by considering the methodology introduced in.(Li *et al*., 2012), the extended state-space system can be expressed as

$$\begin{aligned}\dot{\bar{\boldsymbol{x}}} &= \bar{\boldsymbol{A}}\bar{\boldsymbol{x}} + \bar{\boldsymbol{b}}_u\Delta\boldsymbol{u} + \bar{\boldsymbol{G}}r + \boldsymbol{E}h\\ y_m &= \bar{\boldsymbol{C}}_m\bar{\boldsymbol{x}}\end{aligned} \tag{6.13}$$

Where

$$\bar{\boldsymbol{A}} = \begin{bmatrix}\boldsymbol{A}_{aug} & \boldsymbol{b}_d\\ \boldsymbol{0}_{1\times m} & 0\end{bmatrix}, \bar{\boldsymbol{x}} = \begin{bmatrix}\Delta\boldsymbol{x}_{aug}\\ \Delta x_{m+1}\end{bmatrix}, with\ \Delta x_{m+1} = d = f(x,w(t),t) \tag{6.14}$$

$$\boldsymbol{E} = \begin{bmatrix}\boldsymbol{0}_{m\times 1}\\ 1\end{bmatrix}, \bar{\boldsymbol{b}}_u = \begin{bmatrix}\boldsymbol{B}_{aug}\\ \boldsymbol{0}_{1\times n}\end{bmatrix} \tag{6.15}$$

and

$$\bar{\boldsymbol{G}} = \begin{bmatrix}\boldsymbol{G}\\ 0\end{bmatrix}, \bar{\boldsymbol{C}}_m = \begin{bmatrix}\boldsymbol{C}_m & \boldsymbol{0}_{2\times 1}\end{bmatrix} \tag{6.16}$$

If the pair $\left(\boldsymbol{A}_{aug}, \boldsymbol{B}_{aug}\right)$ is controllable, and $\left(\bar{\boldsymbol{A}}, \bar{\boldsymbol{C}}_m\right)$ is observable, the GESO of system (6.11) can be expressed as:

$$\begin{aligned} \dot{\hat{\bar{\boldsymbol{x}}}} &= \bar{\boldsymbol{A}}\hat{\bar{\boldsymbol{x}}} + \bar{\boldsymbol{b}}_u \Delta \boldsymbol{u} + \bar{\boldsymbol{G}}\boldsymbol{r} - \boldsymbol{L}\left(\hat{\boldsymbol{y}}_m - \boldsymbol{y}_m\right) \\ \hat{\boldsymbol{y}}_m &= \bar{\boldsymbol{C}}_m \hat{\bar{\boldsymbol{x}}} \end{aligned} \tag{6.17}$$

where $\boldsymbol{L}$ is the linear observer gain matrix, and $\hat{\bar{\boldsymbol{x}}}$ is the estimated value of $\bar{\boldsymbol{x}}$ .The same feedback controller introduced in Eq. (6.9) is used, and for disturbance rejection tasks, the next disturbance compensation gain K_d is obtained by solving the following equation:

$$K_d = -\left[\boldsymbol{C}_o\left(\boldsymbol{A}_{aug} - \mathbf{B}_{aug}\boldsymbol{K}\right)^{-1}\boldsymbol{B}_{aug}\right]^{-1}\boldsymbol{C}_o\left(\boldsymbol{A}_{aug} - \boldsymbol{B}_{aug}\boldsymbol{K}\right)^{-1}\boldsymbol{b}_d \tag{6.18}$$

where $\boldsymbol{K}$ is the gain vector introduced in Eq. (6.9). The introduced GESO robust scheme was implemented for both longitudinal and lateral dynamics modeling.

Notice the controller design methodology described in Section 6.3 is applied for a linear state space representation locally defined around an operating point. However, aircraft dynamics can change drastically from one operating flight point to another. Thus, there is a need for nonlinear control laws design that can consider the flight dynamics' variations with the flight conditions.

6.4 Extension of the method for nonlinear problem using an Adaptive Neuro-fuzzy Inference System (ANFIS)

Gain scheduling is an effective method to design nonlinear flight control laws using a linear control technique (Rugh and Shamma, 2000). A specific type of gain scheduling called the Linear Parameter-Varying (LPV) system is utilized in this work. Depending on the variation of the exogenous parameters (generally for their strong variations), the gain-scheduled controller can lose its effectiveness (loss of stability and robustness).

The LPV system is thus restricted to the “slow variation” of parameters (Rugh and Shamma, 2000). Conventionally, the “slow variation” problem is addressed by increasing the number of operating points required for the gain scheduling, which has the consequence of increasing the computational time and the amount of resources needed. The proposed LPV system is based on the Adaptive Neuro-Fuzzy Inference System (ANFIS) (Jang, 1993). This approach reduces the number of operating points required, as it uses a fuzzy logic ability to create data when there is a lack of information.

The Neural Network component in the ANFIS (Grigorie and Botez, 2009 ; Grigorie *et al*., 2012 ; Grigorie and Botez, 2015) thus increases the interpolation capacity of its fuzzy logic technique.

The procedure to obtain a gain-scheduled controller using the ANFIS is composed of four steps:

Step 1: The flight envelope domain takes into consideration several flight conditions. A number of 216 flights conditions were considered in terms of altitude, airspeed and aircraft mass. For each flight condition, a linearization process was performed as the one described in Section 6.2 for the longitudinal and lateral dynamics modeling. Figure 6.7 shows the flight domain as well as the flight conditions, which are listed in Table 6.4.

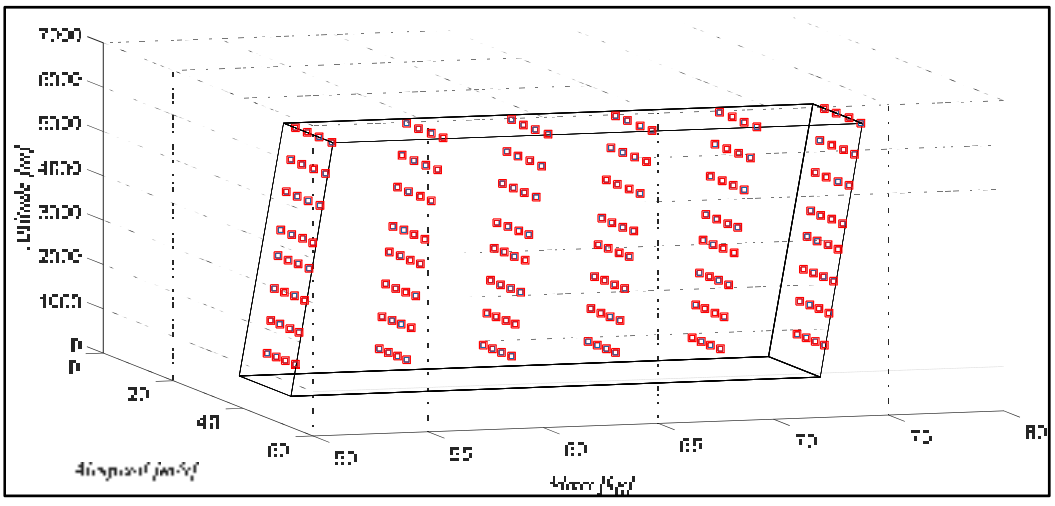

Figure 6.7 Flight domain with the flight conditions for the gain scheduling

Table 6.4 Flight conditions for the gain scheduling method

Altitude [m]	Airspeed [m/s]	Mass [kg]
0-6000	26-45	53-76

Step 2: For each flight condition, a local linear controller, as the one established in Eq. (6.6), was designed following the flight qualities' requirements described in Section 6.2. The gains parameters K_x, K_i, K_p, K_{ff} and K_d were determined, and further mapped as functions of the altitude, airspeed and mass.

Step 3: The scheduling was performed to evaluate the parameters of the controller for an unknown trim condition. The Adaptive Neuro-Fuzzy Inference System (ANFIS) was used for this purpose. The general ANFIS architecture, presented in Fig. 6.8, is based on the Takagi-Sugeno fuzzy inference system (Suparta and Alhasa, 2016) defined that is as:

$$\begin{aligned} &Rule\ 1 = If\ x\ is\ A_1\ and\ y\ is\ B_1, \quad Then\ f_1 = p_1x + q_1x + r_1 \\ &Rule\ 2 = If\ x\ is\ A_2\ and\ y\ is\ B_2, \quad Then\ f_2 = p_2y + q_2y + r_2 \end{aligned} \tag{6.19}$$

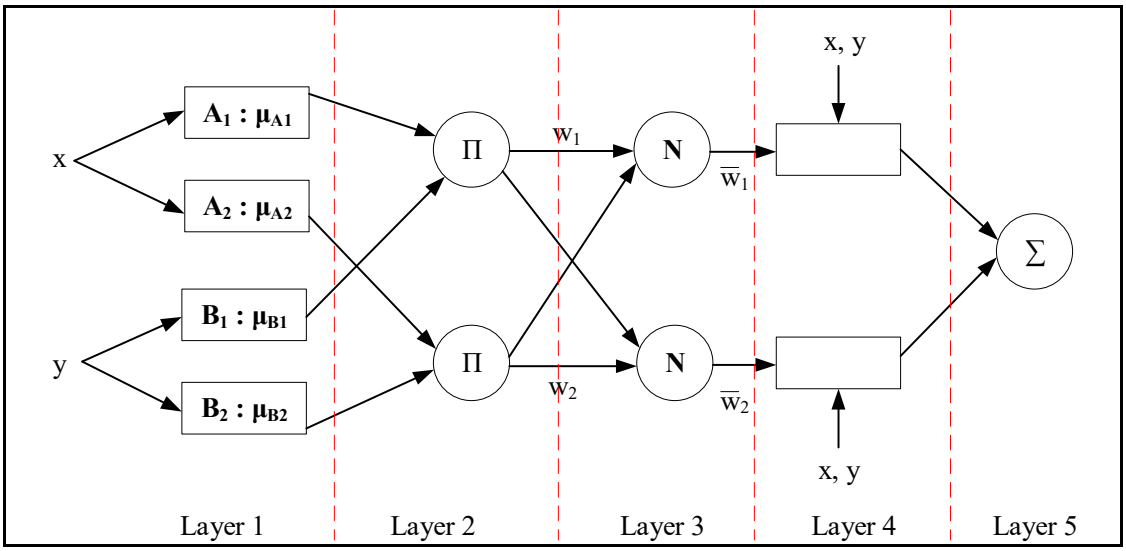

Figure 6.8 General ANFIS Architecture (Suparta & Alhasa, 2016)

The ANFIS architecture has five layers, as shown in Fig. 6.8. In the Layer 1, the output of each node is the membership function μ_{Ai} and specifies the degree to which the given input is similar to A_i. The proposed gain scheduling methodology used four generalized bell-shaped membership functions defined as follows:

$$\mu_{A_i}(x) = \frac{1}{1 + \left| \frac{x - c_i}{a_i} \right|^{2b_j}} \tag{6.20}$$

where μ_{Ai} is the membership function of A_i; and a_i, b_i and c_i are the parameters of the membership function.

The outputs of layer 2's nodes are the products of all the incoming signals. In layer 3, the ratio of each output of layer 2 to the sum of all the outputs of layer 2 is calculated. The output data of layer 3 are called the normalized firing strengths.

In the Layer 4 the output data are defined as:

$$O_{4i} = \overline{w}_i f_i \tag{6.21}$$

where $\overline{w}_i$ is the normalized firing strengths from layer 3 and f_i is the consequent parameter from the Tagaki-Sugeno system Eq. (6.19).

The nodes in the Layer 5 calculate the sum of the incoming signals from layer 4. This layer also computes the overall output of the ANFIS algorithm.

The objective of gain scheduling is to determine the control gains K_x, K_i, K_p, K_{ff} and K_d as function of the altitude, the airspeed and the mass (3-dimensional interpolation). To simplify the learning process in the ANN, the ANFIS was only used for a 2-dimensional interpolation (for airspeed and altitude). A linear interpolation was then used to estimate the control gains as a function of mass.

Step 4: A performance analysis of the gain-scheduled controller is made. The local stability and robustness of the controller was investigated for unknown operating points and the nonlinear performance on the overall UAS-S45 model was tested as explained in Section 6.5.

6.5 Simulation results and discussion

In order to portray the effectiveness of the proposed control schemes, several numerical simulations were performed for each flight condition. A random case defined by airspeed V = 39.76m/s, altitude = 6097m and mass = 53.11 kg, is presented in this section. Such flight condition can be expressed by the following state, control and output matrices, as introduced by Eqs. (6.2) and (6.3):

Longitudinal dynamics model

$$\boldsymbol{A} = \begin{bmatrix} -0.0468 & 0.2359 & -1.8284 & -9.7513 \\ -0.3413 & -3.3721 & 41.1194 & -0.4463 \\ -0.1150 & -1.1861 & 0.3745 & -0.0213 \\ 0 & 0 & 1 & 0 \end{bmatrix} \tag{6.22}$$

$$\boldsymbol{B} = \begin{bmatrix} -0.0085 \\ 0.0424 \\ -0.1413 \\ 0 \end{bmatrix}, \boldsymbol{C} = \begin{bmatrix} 0 & 0 & 0 & 1 \end{bmatrix} \tag{6.23}$$

Lateral dynamics model

$$\boldsymbol{A} = \begin{bmatrix} -0.2423 & 0.2954 & -50.3286 & 9.7613 \\ -0.0619 & -12.8788 & 0.8274 & 0 \\ 0.0870 & -0.2368 & -0.1602 & 0 \\ 0 & 1 & 0.0060 & 0 \end{bmatrix} \tag{6.24}$$

$$\boldsymbol{B} = \begin{bmatrix} 0 & 0.0386 \\ 0.6512 & 0.0074 \\ -0.0078 & -0.1628 \\ 0 & 0 \end{bmatrix}, \boldsymbol{C} = \begin{bmatrix} 0 & 0 & 0 & 1 \end{bmatrix} \tag{6.25}$$

Moreover, consider the next information for longitudinal GESO design,

$$\boldsymbol{b}_d = \begin{bmatrix} \boldsymbol{0}_{3\times1} \\ 1 \\ 0 \end{bmatrix}, i = 4,\ j = 1, m = 5 \text{ and } n = 1 \tag{6.26}$$

and for lateral design,

$$\boldsymbol{b}_d = \begin{bmatrix} 0 \\ 1 \\ \boldsymbol{0}_{3\times1} \end{bmatrix}, i = 4,\ j = 2, m = 5 \text{ and } n = 2 \tag{6.27}$$

Notice in figures that planned reference *r(t)* is expressed as $\Delta\theta^*$ and $\Delta\phi^*$ for pitch and roll angles, respectively

The longitudinal dynamics model was evaluated. For this purpose, the system was assigned to follow the reference profile given by:

$$r(t) = \begin{cases} 0.2\,rad, & 0 \le t \le 30\ sec \\ 0.1\,rad, & 30 < t \le 60\ sec \\ 0.3\,rad, & t > 60\ sec \end{cases}, i = 4,\ j = 2, m = 5 \text{ and } n = 2 \tag{6.28}$$

where step functions were established as references in order to assess the control scheme capabilities. Figures 6.9a and 6.9b show the trajectory tracking and the computed control inputs, respectively; a proper trajectory tracking was achieved under the action of the control input computed by the proposed control approach for an unperturbed motion. In addition to the accurate tracking, the criteria defined in Table 6.3 are also met. Figure 6.10 shows a step response of the UAS-S45. From this figure, the step response parameters are: (time response) $T_r = 5.33$s, (steady state error) $e_p = 10^{-3}$ and (overshoot) $D = 0$ which satisfy the criteria needed.

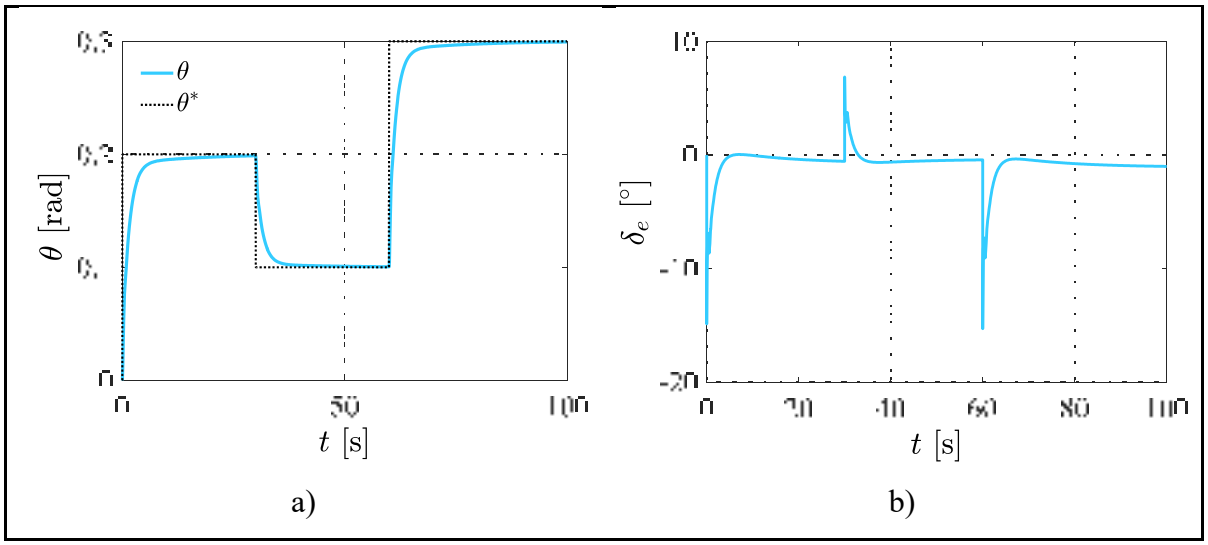

Figure 6.9 Unperturbed pitch motion for the a) trajectory tracking and b) computed control input

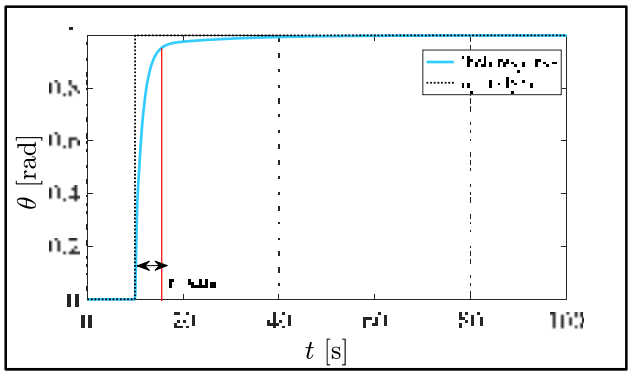

Figure 6.10 Step response of the UAS-S45

The UAS was, thus, commanded to track the reference profile given in Eq. (6.26) while it was subjected to the effects of disturbances. The disturbance affecting the pitch and roll motion are given by d_θ and d_ϕ, respectively; which are assumed to be unknown but bounded quantities. For simplicity, a general model of harmonic disturbance is adopted, that is given for pitch motion as follows:

$$d_q(t) = \begin{cases} 0, & 0 \le t \le 10 \ sec \\ 0.1, & 10 < t \le 30 \, sec \\ 0.5sin(t), & t > 30 \ sec \end{cases}, \tag{6.29}$$

The closed-loop dynamic responses for pitch motion are portrayed in Fig. 6.11. Overall, the results show that the introduced control scheme offers a good performance, but this scheme is not adequate when disturbances are included in the simulation. On the other hand, when the GESO controller is used, an acceptable level of disturbance attenuation is achieved while reachable control inputs are computed. It must be noted that the control inputs effort does not saturate the actuators capabilities, since the maximum and minimum elevator deflections are -40° and 40°, respectively.

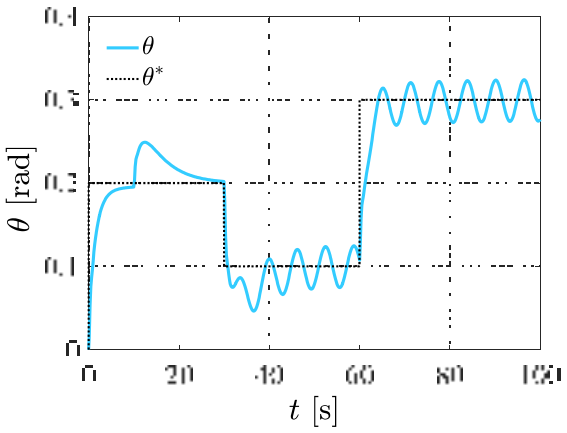

a) Perturbed system without the compensation

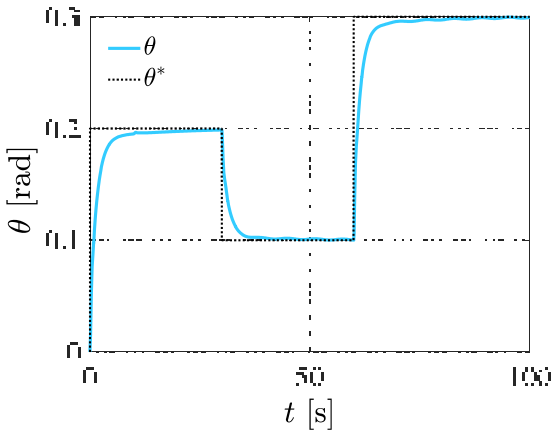

b) Perturbed system with the compensation

Figure 6.11 Pitch trajectory tracking

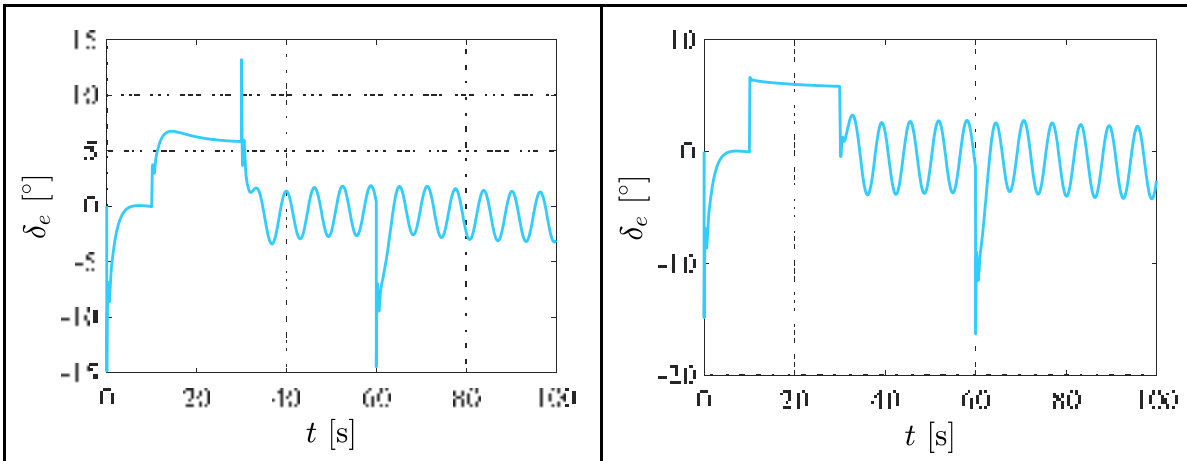

c) Control input without the compensation

d) Control input with the compensation

Figure 6.11 (continued) Pitch trajectory tracking

The real longitudinal disturbances and the disturbances estimated by the GESO are portrayed in Fig. 6.12 in solid and dashed lines, respectively. The ability of the estimated disturbance to track the real disturbance shows that the observer gain introduced in Eq. (6.17) was selected properly.

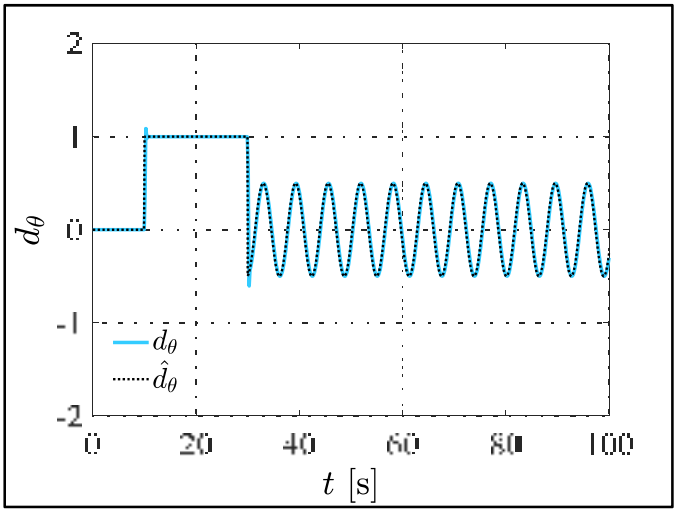

Figure 6.12 Disturbances affecting the longitudinal motion, real (solid line) and GESO-estimated (dashed line).

The proposed control scheme allows the system to deal with the trajectory tracking problem even in the presence of external disturbances, thanks to the action of the disturbance rejection mechanism provided by the GESO.

The control law for the lateral motion of the UAS-S45 was also defined. The scheme allows the aileron and rudder deflections to be used as control inputs for the roll motion (multiple inputs - single output). Two equivalent control laws, as the ones shown in Eq. (6.6), are needed to deal with the trajectory tracking problem and disturbance rejection.

The reference profile defined in Eq. (6.28) is the "planned reference" where, both the δ_a and δ_r control inputs are used to regulate the roll motion.

$$r(t) = \begin{cases} 0.2\ rad, & 0 \le t \le 30\ \ sec \\ 0.1\ rad, & 30 < t \le 60\ \ sec \\ 0.3\ rad, & t > 60\ \ sec \end{cases}, \tag{6.30}$$

The tracking of the roll reference, in which a properly closed-loop system performance was achieved, is portrayed in Fig. 6.13. In the same way, the control inputs vary softly, which avoids actuator saturation. Nevertheless, disturbances were not included in this simulation.

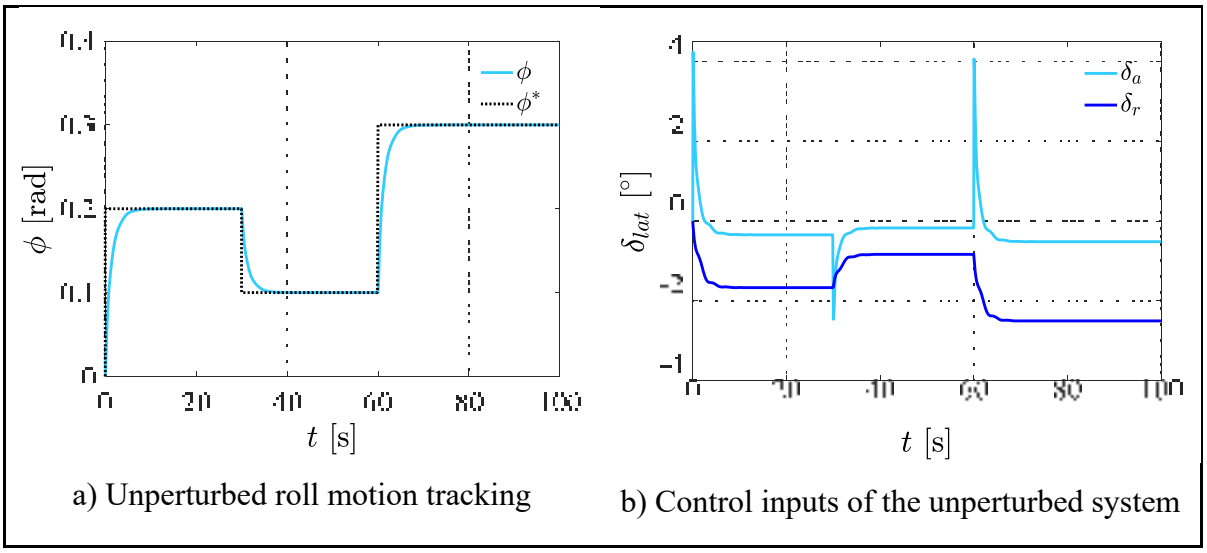

a) Unperturbed roll motion tracking

b) Control inputs of the unperturbed system

Figure 6.13 Unperturbed roll motion.

Next, a random disturbance is injected into the system to prove the robustness of the proposed control scheme, as follows

$$d_f = 0.8\sin\left(\pi\frac{t\text{-}30}{31}\right) + 0.4\sin\left(\pi\frac{t\text{-}30}{7}\right) + 0.08\sin\left(\pi\frac{t\text{-}30}{2}\right) + 0.056\sin\left(\pi\frac{t\text{-}30}{11}\right), \tag{6.31}$$

The system's dynamic response is shown in Fig. 6.14, where the uncompensated (Fig. 6.14a) and compensated (Fig. 6.14b) responses are portrayed. The system governed by the GESO approach guarantees a stable performance and attains a proper trajectory tracking. Furthermore, in spite of an increase in the magnitude of the computed aileron and rudder control inputs, the actuators are not saturated (Fig. 6.14d); this fact means that the proposed robust control strategy is capable of performing the trajectory tracking task in the presence of significant external wind disturbances affecting the UAS-S45's motion.

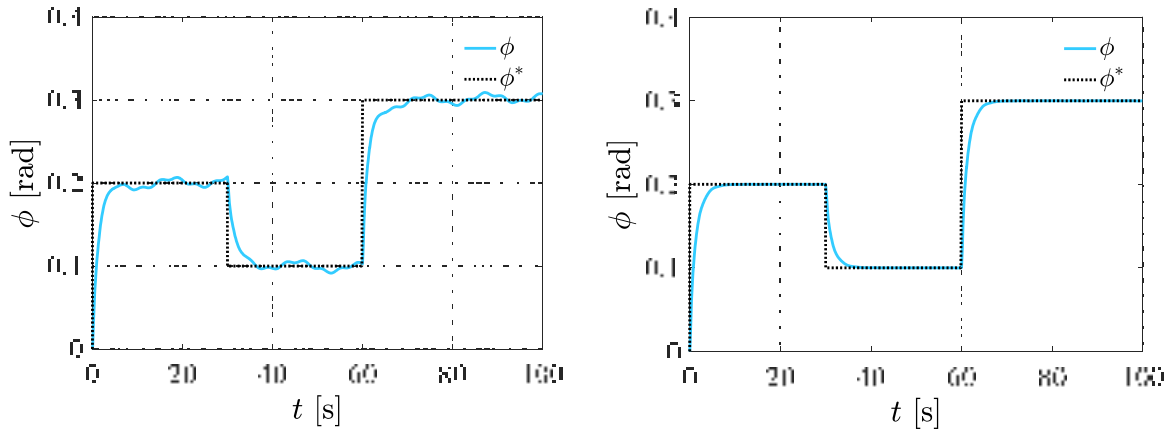

a) Perturbed system without the compensation

b) Perturbed system with the compensation

Figure 6.14 Roll trajectory tracking.

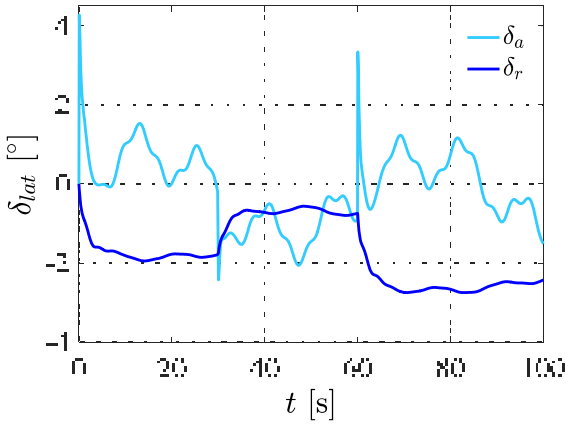

c) Control input without the compensation

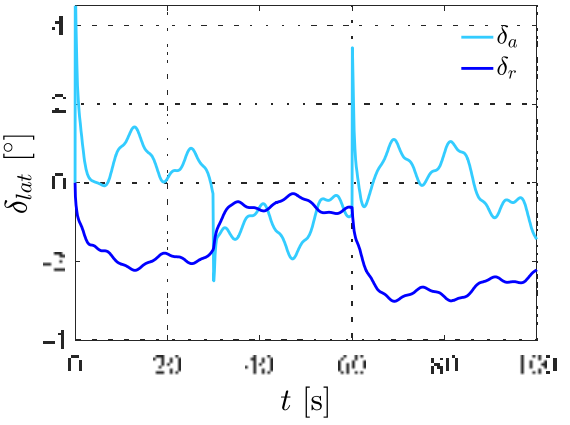

d) Control inputs with the compensation

Figure 6.14 (continued) Roll trajectory tracking.

To analyze the accuracy of the nonlinear controller, a cross validation was performed on the gain scheduling methodology. A set of 50 data points, selected randomly, was used for this validation as illustrated in Fig. 6.15. The interpolation data points shown in Fig. 6.15 represent the data used to train the ANFIS gain-scheduling model. For each validation point (which is a flight condition), the linearized model was obtained, and the controller gains were estimated using the ANFIS model. The data points were considered successful if the controlled system verified all the flight qualities requirements described in Section 6.2. Table 6.5 shows the number and the percentages of the validated data points for the longitudinal and the lateral dynamics model. The results indicate success rates of 84% for the longitudinal dynamics, and 92% for the lateral dynamics models. The failed points are dues to the reduced number of interpolations points and also to the fact that the point to interpolate is close to the limit of the flight envelope. Therefore, a recommendation could be to increase the number of interpolation points close to the boundary of the flight envelope in order to improve the results.

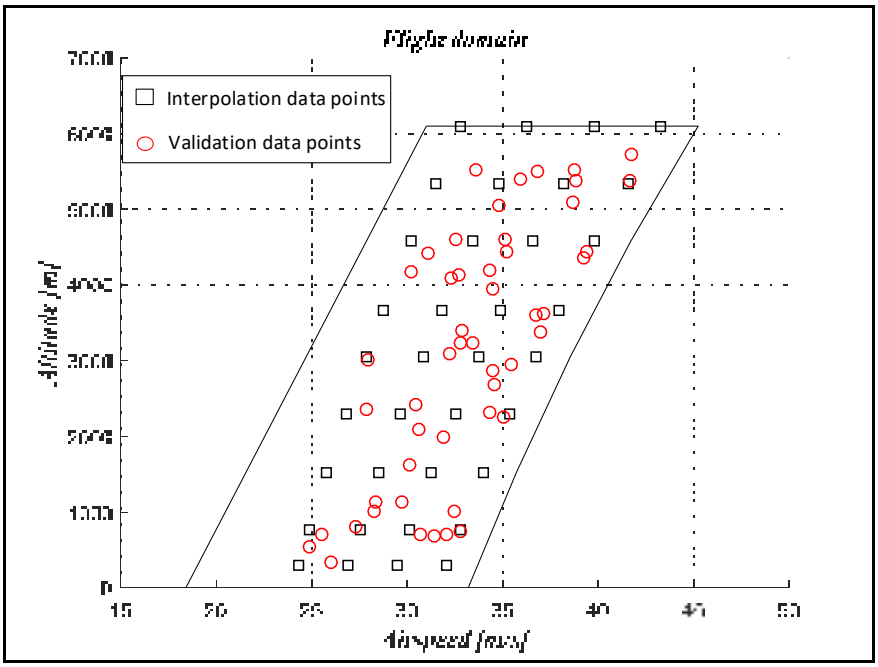

Figure 6.15 Interpolation and validation data points

Table 6.5 Numbers and percentages of interpolation and validation data points

Number of interpolation data points	216
Number of validation data points	50
Success percentage (%) for longitudinal dynamics	84%
Success percentage (%) for lateral dynamics	92%

Figures 6.16a and 6.16b show the pitch trajectory tracking and the control input for a successful validation point. The disturbances calculated in Eq. (6.27) was injected in the longitudinal dynamic model to evaluate its disturbance rejection capability. The results show that the tracking capability as well as the robustness of the nonlinear controller are still highly efficient. Figure 6.16b shows that the control input can reject the sinusoidal disturbance while staying inside the range of the elevator deflection [-40° , 40°].

Figures 6.16c and 6.16d show the roll trajectory tracking and the control input for a successful validation point. The disturbance in Eq. (6.29) was injected in the system to evaluate its

robustness. The results also show a good tracking performance with an efficient disturbance rejection.

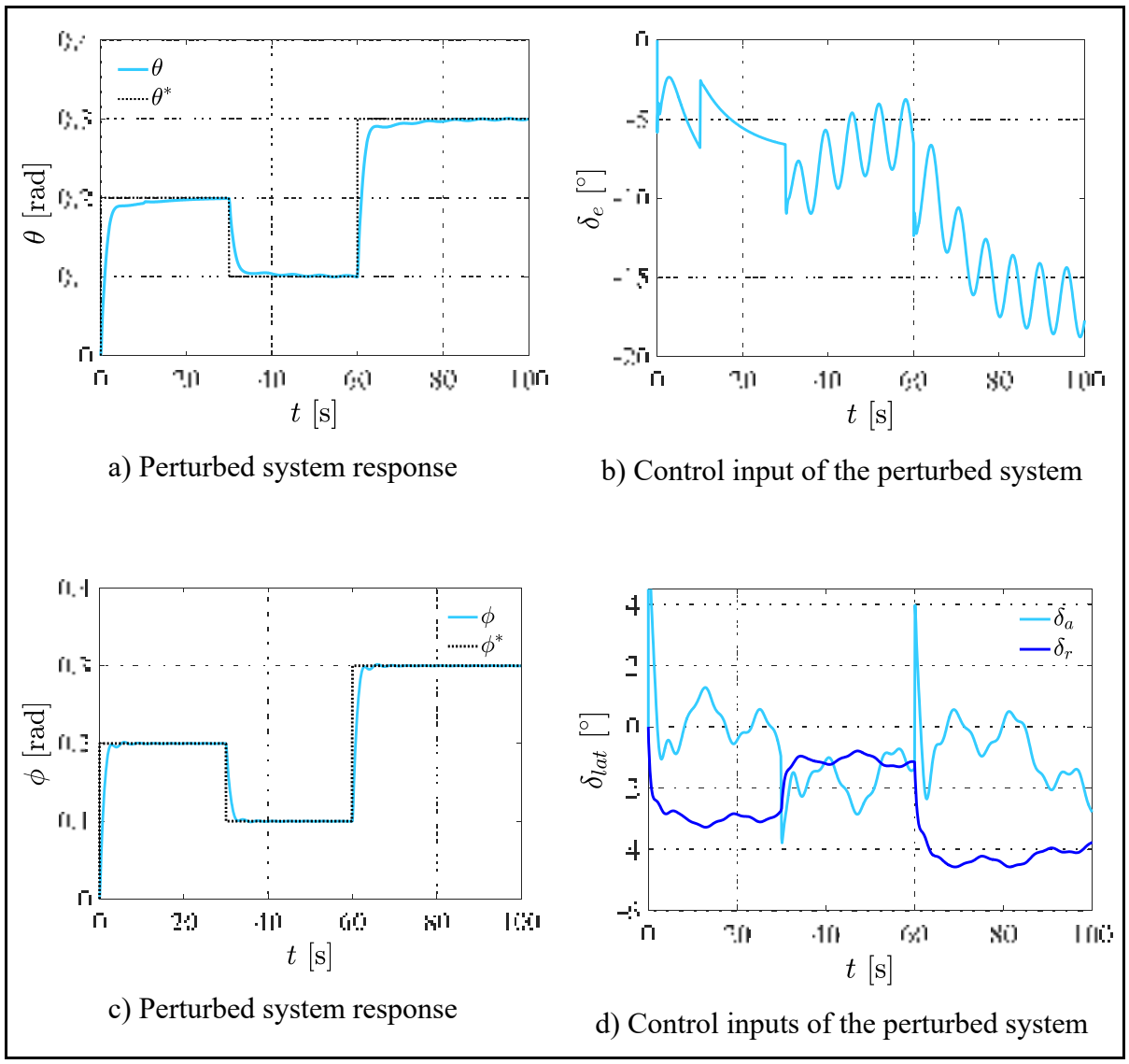

a) Perturbed system response

b) Control input of the perturbed system

c) Perturbed system response

d) Control inputs of the perturbed system

Figure 6.16 Pitch and roll trajectories tracking using the nonlinear controller

6.6 Conclusion

A design methodology to obtain a low-order robust controller was introduced in this paper. The poor robustness and the excessive bandwidth of the optimal controller, the high order of

the robust controller, and the lack of data of the neural network controller were the main problems which needed to be tackled in this work. The methodology was developed in three steps. The first step concerned the design of a Linear Quadratic Regulator (LQR) that used a selection technique for the weight matrices. In the second step, a Proportional-Integral with reference feedforward (PI-FF) was added to the controller in order to provide tracking capability, and slow dynamics variations robustness. In the third step, a Generalized Extended State Observer (GESO) was designed for both disturbances gain calculation, and estimation of external disturbances. The obtained linear controller was thus extended to obtain a nonlinear controller using a Gain Scheduling based on the ANFIS method. Several numerical simulations were performed to highlight the feasibility and efficiency of the proposed methodology. The results obtained showed a very good tracking and stability performance even under disturbances. The nonlinear controller also showed efficient results, but there is a need to increase the number of interpolation points close to the boundary of the flight envelope in order to improve the results. The obtained results, thus, proved that the proposed methodology could be a very good method for the design of a UAS-S45 flight controller.

GENERAL CONCLUSIONS AND RECOMMANDATIONS

The main goal of this thesis was to design a flight dynamics model for Unmanned Aerial Systems S4 and S45. Two research axes were considered: 1) the design of a high precision model to reduce the number of flight tests required for certification, and 2) the integration of a performance improvement technique such as new control laws or morphing wing technology.

Chapter 1 presents a general presentation of UASs, as well as the various methods of their modelling techniques. It was also the opportunity to present the synthesis methodologies of new control laws for UASs. Chapter 2 was devoted to a description of methodologies used for carrying out the research in this thesis.

Chapter 3 covered the modelling of unmanned aerial systems. The journal paper describes in detail the methodology used. The unmanned aerial systems S4 and S45 models were divided into aerodynamic, propulsion, structure and actuator sub-models. Each sub-model was estimated using numerical methods. Experimental tests were conducted to validate the designed sub-models. The results obtained show that the global unmanned aerial system model could be used for the design of a high-level precision flight simulator.

In Chapter 4, a new methodology for obtaining the aerodynamic model of the S45 Balàam unmanned aerial system was presented. This methodology is based on a nonlinear vortex lattice method in which the vortex intensities were calculated using the viscous forces from the strip theory, and the forces generated by the vortex rings from the vortex lifting law. Furthermore, a CFD analysis was performed. Initially, a structured mesh for the airfoil and an unstructured mesh for the complete geometry of the aircraft were obtained. Subsequently, the dynamics of the flow were solved and then analysed using the Reynold Averaged Navier-Stokes equations, the Spalart-Allamars and k-ω turbulence models. A comparative analysis with experimental data and other numerical methods shows the superiority of the proposed methodology.

Chapter 5 described a numerical method as well as an experimental procedure to obtain the propeller performances of the Unmanned Aerial Systems S4 and S45. The numerical method consists of an improved Blade Element Momentum theory and a CFD analysis. Experimental tests were carried out in the Price-Païdoussis subsonic wind tunnel to validate the results

obtained numerically. The proposed numerical methodologies were thereby determined to be very effective.

Chapter 6 addresses the problem of improving the performance of unmanned aerial systems through the design of new control laws. Optimal LQR control, a a Proportional-Integral with reference feedforward (PI-FF) controller and an extended state observer were applied to allow a UAS to satisfy the desired flight qualities. Subsequently, an adaptive fuzzy neural network was used to schedule gains for new flight conditions interpolated among the existing ones. Special attention was given to the low order of the controller and to its ability of the new control law to reject disturbances and to increase its robustness to variations in mass, speed and altitude. The superiority of this methodology over other options available in literature was established in a comparative analysis.

While the methodologies proposed in this thesis do respond to the issues surrounding the unmanned aerial systems, several further studies could be considered, in particular:

- The flight dynamics model can be further improved to study stall phenomena. The random nature of the stall makes it impossible to predict from conventional estimation methods. The research axis could foresee the use of artificial intelligence algorithms that are very promising for the estimation of stochastic phenomena.
- The procedure to estimate the aerodynamic sub-model allowing the integration of a morphing wing technology can be completed. The methodology would consist of designing an algorithm allowing the wing to be modified in real time according to the flight conditions. This algorithm could use a “data mining methodology” that would provide the aerodynamic coefficients of the wing as a function of the desired deformation, while maximizing the aerodynamic lift to drag ratio.
- The realized model can be improved to perform “failure” or “non-conventional geometries” analyses. The purpose of this improvement will be to analyse the flight dynamics of the aircraft when one of its components (the engine, for example) might be damaged. When a crash of an unmanned aerial system would occur, this simulator model could allow all of the prior events that led to its destruction to be studied.

- The realized dynamic model could be integrated into a mission simulation environment. In order to effectively plan its missions, the model could be integrated into a simulation environment to precisely understand the actions to be taken, such as: the landing and take-off conditions, the location of the material, etc.

Finally, it is clear that this thesis has made a significant contribution to the simulation and modelling of UASs.

LIST OF REFERENCES

Air Transport Action Group. (2014). *Aviation Benefits Beyond Borders*. Switzerland : Air Transport Action Group. Taken from https://aviationbenefits.org/media/26786/ATAG__AviationBenefits2014_FULL_LowRes.pdf

Al-Radaideh, A., Al-Jarrah, M. A., Jhemi, A., & Dhaouadi, R. (2009). ARF60 AUS-UAV Modeling, System Identification, Guidance and Control: Validation through Hardware in the Loop Simulation. In *6th International Symposium on Mechatronics and its Applications* (pp. 1-11). https://doi.org/10.1109/ISMA.2009.5164799

Amato, F., & Iervolino, R. (2004). mu Synthesis for a Small Commercial Aircraft: Design and Simulator Validation. *Journal of guidance, control, and dynamics*, *27*(3), 479–490.

Ameduri, S., Concilio, A., Dimino, I., Pecora, R., & Ricci, S. (2018). AIRGREEN2 - Clean Sky 2 Programme: Adaptive Wing Technology Maturation, Challenges and Perspectives. Communication présentée au ASME 2018 Conference on Smart Materials, Adaptive Structures and Intelligent Systems, American Society of Mechanical Engineers Digital Collection. https://doi.org/10.1115/SMASIS2018-8235

American Fastener Technologies Corporation. (2013). ASTM, SAE and ISO Grade Markings for Steel Fasteners. http://www.americanfastener.com. Taken from http://www.americ anfastener.com/astm-sae-and-iso-grade-markings-for-steel-fasteners/

Anderson, J. D. (2010). Brief History of the Early Development of Theoretical and Experimental Fluid Dynamics. In R. Blockley & W. Shyy (Éds), *Encyclopedia of Aerospace Engineering*. Chichester, UK : John Wiley & Sons, Ltd. https://doi.org/10.1002/9780470686652.eae001

Anderson, J. D. J. (2010). *Fundamentals of Aerodynamics* (5 edition). New York : McGraw-Hill Education.

ANSYS. (2013). *Fluent Theory Guide*. 275 Technology Drive Canonsburg : ANSYS, INC.

Anton, N., Botez, R. M., & Popescu, D. (2010). New Methodology and Code for Hawker 800XP Aircraft Stability Derivatives Calculation from Geometrical Data. *The Aeronautical Journal*, *114*(1156), 367-376. https://doi.org/10.1017/S0001924000003821

Anton, N., Botez, R. M., & Popescu, D. (2011). Stability Derivatives for a Delta-Wing X-31 Aircraft Validated using Wind Tunnel Test Data. *Proceedings of the Institution of Mechanical Engineers, Part G: Journal of Aerospace Engineering*, *225*(4), 403-416. https://doi.org/10.1243/09544100JAERO799

Anton, Nicoleta, Botez, R., & Popescu, D. (2009a). New Methodologies for Aircraft Stability Derivatives Determination from Its Geometrical Data. In *AIAA Atmospheric Flight Mechanics Conference* (p. 6046). Chicago, Illinois : American Institute of Aeronautics and Astronautics. https://doi.org/10.2514/6.2009-6046

Anton, Nicoleta, Botez, R., & Popescu, D. (2009b). New Methodologies for Aircraft Stability Derivatives Determination from Its Geometrical Data. In *AIAA Atmospheric Flight Mechanics Conference* (p. 6046). Chicago, Illinois : American Institute of Aeronautics and Astronautics. https://doi.org/10.2514/6.2009-6046

Argyropoulos, C. D., & Markatos, N. C. (2015). Recent Advances on the Numerical Modelling of Turbulent Flows. *Applied Mathematical Modelling*, *39*(2), 693-732. https://doi.org/10.1016/j.apm.2014.07.001

Ashraf, A., Mei, W., Gaoyuan, L., Anjum, Z., & Kamal, M. M. (2018). Design Linear Feedback and LQR Controller for Lateral Flight Dynamics of F-16 Aircraft. In *2018 International Conference on Control, Automation and Information Sciences (ICCAIS)* (pp. 367-371). https://doi.org/10.1109/ICCAIS.2018.8570323

Aubeelack, H., & Botez, R. M. (2017). Accuracy of Two Nonlinear Finite Wing Models in the Aerodynamic Prediction of Wing Sweep Effects. In *35th AIAA Applied Aerodynamics Conference*. American Institute of Aeronautics and Astronautics. https://doi.org/10.2514/6.2017-3259

Aubeelack, H., & Botez, R. M. (2019). Simulation Study of the Aerodynamic Force Distributions on the UAS-S45 Baalam Wing with an Upswept Blended Winglet. *INCAS Bulletin*, *11*(1), 21-38.

Baarspul, M., & Mulder, J.A. (1993). *The synthesis of flight simulation models*. Delft University of Technology. Taken from http://resolver.tudelft.nl/uuid:aebe34a0-7f5f-44ce-b64d-0a7e11bfdcc5

Balas, G. J. (2003). Flight Control Law Design: An Industry Perspective. *European Journal of Control*, *9*(2), 207-226. https://doi.org/10.3166/ejc.9.207-226

Balas, M., & Frost, S. (2012). Robust Adaptative Control With Disturbance Rejection for Linear Infinite Dimensional Systems. In *AIAA Guidance, Navigation, and Control Conference 2012* (Vol. 11). https://doi.org/10.2514/6.2012-4616

Barbosa, R. S., Machado, J. A. T., & Ferreira, I. M. (2004). Tuning of PID Controllers Based on Bode's Ideal Transfer Function. *Nonlinear Dynamics*, *38*(1), 305-321. https://doi.org/10.1007/s11071-004-3763-7

Barlow, J. B., Rae, W. H., & Pope, A. (1999). *Low-Speed Wind Tunnel Testing* (3 edition). New York : Wiley-Interscience.

Ben Mosbah, A., Botez, R. M., & Dao, T. M. (2016). A hybrid original approach for prediction of the aerodynamic coefficients of an ATR-42 scaled wing model. *Chinese Journal of Aeronautics*, *29*(1), 41-52. https://doi.org/10.1016/j.cja.2015.12.022

Ben Mosbah, A., Flores Salinas, M., Botez, R., & Dao, T. (2013). New Methodology for Wind Tunnel Calibration Using Neural Networks - EGD Approach. *SAE International Journal of Aerospace*, *6*(2), 761-766. https://doi.org/10.4271/2013-01-2285

Benini, E. (2004). Significance of blade element theory in performance prediction of marine propellers. *Ocean Engineering*, *31*(8), 957-974. https://doi.org/10.1016/j.oceaneng.2003.12.001

Bertin, J. J., & Smith, M. L. (1998). *Aerodynamics for Engineers*. New Jersey : Prentice-Hall. Repéré à https://infoscience.epfl.ch/record/23088

Blair, G. P. (1996). *Design and Simulation of Two Stroke Engines*. Warrendale, PA : SAE International. https://doi.org/10.4271/R-161

Boelens, O., Goertz, S., Morton, S., Fritz, W., & Lamar, J. (2007). F16-XL Geometry and Computational Grids Used in Cranked-Arrow Wing Aerodynamics Project International. *Journal of Aircraft*, *46*(2), 369-376. https://doi.org/10.2514/1.34852

Boelens, O. J. (2012). CFD analysis of the flow around the X-31 aircraft at high angle of attack. *Aerospace Science and Technology*, *20*(1), 38-51. https://doi.org/10.1016/j.ast.2012.03.003

Boely, N., Botez, R. M., & Kouba, G. (2011). Identification of a non-linear F/A-18 model by the use of fuzzy logic and neural network methods. *Proceedings of the Institution of Mechanical Engineers, Part G: Journal of Aerospace Engineering*, *225*(5), 559-574. https://doi.org/10.1177/2041302510392871

Boerstoel, J. W., Kassies, A., Kok, J. C., & Spekreijse, S. P. (1996). ENFLOW a full-functionality system of CFD codes for industrial Euler/Navier-Stokes flow computations. Repéré à https://reports.nlr.nl/xmlui/handle/10921/1349

Bosch, P. P. J. van den, & Klauw, A. C. van der. (1994). *Modeling, Identification and Simulation of Dynamical Systems*. (S.l.) : CRC Press. (Google-Books-ID: M7oZvR9AMKkC).

Botez, R. M., Kammegne, M. J. T., & Grigorie, L. T. (2015). Design, numerical simulation and experimental testing of a controlled electrical actuation system in a real aircraft morphing wing model. *The Aeronautical Journal*, *119*(1219), 1047-1072. https://doi.org/10.1017/S0001924000011131

Boughari, Y., Botez, R. M., Ghazi, G., & Theel, F. (2017). Flight Control Clearance of the Cessna Citation X using Evolutionary Algorithms. *Proceedings of the Institution of*

Mechanical Engineers, Part G: Journal of Aerospace Engineering, *231*(3), 510-532. https://doi.org/10.1177/0954410016640821

Brandt, J., & Selig, M. (2011). Propeller Performance Data at Low Reynolds Numbers. Dans *49th AIAA Aerospace Sciences Meeting including the New Horizons Forum and Aerospace Exposition*. (S.l.) : American Institute of Aeronautics and Astronautics. https://doi.org/10.2514/6.2011-1255

Brandt, J., & Selig, M. S. (2015). UIUC PDB - Vol 1. *UIUC propeller data site*. Repéré à https://m-selig.ae.illinois.edu/props/volume-1/propDB-volume-1.html

Breton, S.-P., Coton, F. N., & Moe, G. (2008). A Study on Rotational Effects and Different Stall Delay Models Using a Prescribed Wake Vortex Scheme and NREL Phase VI Experiment Data. *Wind Energy: An International Journal for Progress and Application in Wind Power Conversion Technology*, *11*(5), 459-482. https://doi.org/10.1002/we.269

Bryan, G. H. (1911). *Stability in Aviation; an Introduction to Dynamical Stability as Applied to the Motions of Aeroplanes*. London, UK : London, Macmillan and Co., limited. Taken from http://archive.org/details/stabilityinaviat00bryarich

Burns, R. S. (2001). *Advanced control engineering*. Oxford ; Boston : Butterworth-Heinemann.

Burr-Brown Corporation. (1997). Instrumentation Amplifier with Precision Voltage Reference. Burr-Brown Corporation. Taken from http://www.ti.com/lit/ds/symlink/ina125.pdf

Calise, A., & Sharmann. (2001). Neural network augmentation of existing linear controllers. In *AIAA Guidance, Navigation, and Control Conference and Exhibit*. (S.l.) : American Institute of Aeronautics and Astronautics. https://doi.org/10.2514/6.2001-4163

Carroll, J., & Marcum, D. (2013). Local Adaption Capabilities of Momentum Source Surrogate Propeller Models for Propeller-Aircraft Coupled Simulations. *Engineering Letters*, *21*(4), 247-255.

CCPM. (2010). Motor Servo Tester ECS Speed Controller CCPM Servo Consistency Master for Quadcopter, Arduino. www.amazon.com. Taken from https://www.amazon.com/Tester-Controller-Consistency-Quadcopter-Arduino/dp/B01J5D1QS2

Cerulli, C., Schut, E. J., Berends, J. P. T. J., & Tooren, M. J. L. van. (2006). Tail Optimization and Redesign in a Multi Agent Task Environment (TAILORMATE). In *47th AIAA/ASME/ASCE/AHS/ASC Structures, Structural Dynamics, and Materials Conference* (p. 2241). Newport, Rhode Island : American Institute of Aeronautics and Astronautics. https://doi.org/10.2514/6.2006-2241

Ceruti, A., Rossi, V., & Saggiani, G. M. (2002). A Fuzzy Logic Autopilot Development for a Light Twin Engine Aircraft in the Approach Flight Condition. Communication presented at ICAS 2002 Congress.

Chahbani, S. (2015). *Estimation des Masses, des Centres de Gravité ainsi que des Moments d'Inertie de l'Avion Cessna Citation X*. Master. École de technologie supérieure, Montréal. Repéré à http://espace.etsmtl.ca/1455/

Choi, J. W., & Seo, Y. B. (1999). LQR Design with Eigenstructure Assignment Capability [and Application to Aircraft Flight Control]. *IEEE Transactions on Aerospace and Electronic Systems*, *35*(2), 700-708. https://doi.org/10.1109/7.766949

Communier, D., Salinas, M. F., Carranza Moyao, O., & Botez, R. M. (2015). Aero Structural Modeling of a Wing using CATIA V5 and XFLR5 Software and Experimental Validation using the Price- Païdoussis Wing Tunnel. Dans *AIAA Atmospheric Flight Mechanics Conference* (p. 2558). Dallas, Texas : American Institute of Aeronautics and Astronautics. https://doi.org/10.2514/6.2015-2558

Concilio, A., Dimino, I., Pecora, R., & Lecce, L. (2017). *Morphing Wing Technologies, Large Commercial Aircraft and Civil Helicopters* (1re éd.). (S.l.) : Butterworth-Heinemann.

Concilio, A., Lo Cascio, M., Milazzo, A., Dimino, I., Amendola, G., & Arena, M. (2018). Optimization design process of a morphing winglet. In *Bioinspiration, Biomimetics, and Bioreplication VIII* (Vol. 10593, p. 1059305). Denver, Colorado, United States : International Society for Optics and Photonics. https://doi.org/10.1117/12.2297088

Cook, M. V. (2013). *Flight Dynamics Principles* (3rd Edition). (S.l.) : Butterworth-Heinemann. https://doi.org/10.1016/C2010-0-65889-5

Cooper, G. E., & Harper, R. P. (1969). *The use of pilot rating in the evaluation of aircraft handling qualities* (Rapport No. AGARD-567). Neuilly-sur-seine, France : Advisory group for aerospace research and development. Taken from https://apps.dtic.mil/docs/citations/AD0689722

Corrigan, J. J., & Schillings, J. J. (1994). Empirical model for stall delay due to rotation. In *American Helicopter Society Aeromechanics Specialists Conference, San Francisco, CA* (Vol. 21).

Dababneh, O., & Kipouros, T. (2018). A review of aircraft wing mass estimation methods. *Aerospace Science and Technology*, *72*, 256-266. https://doi.org/10.1016/j.ast.2017.11.006

David, D., & Panhaleux, J. (2015). *Les drones civils, enjeux et perspectives* (Rapport No. 008816-01). France : Ministère de l'écologie, du développement durable et de l'énergie. Taken from http://www.ladocumentationfrancaise.fr/rapports-publics/16400 0015/index.shtml

Diston, D. J. (2010). Modeling and Simulation. In *Encyclopedia of Aerospace Engineering*. (S.l.) : American Cancer Society. https://doi.org/10.1002/9780470686652.eae479

Doyle, J. C. (1978). Guaranteed margins for LQG regulators. *IEEE Transactions on automatic Control*, *23*(4), 756–757.

Drela, M. (1989). XFOIL: An Analysis and Design System for Low Reynolds Number Airfoils. In *Low Reynolds Number Aerodynamics* (pp. 1-12). (S.l.) : Springer, Berlin, Heidelberg. https://doi.org/10.1007/978-3-642-84010-4_1

Durupt, A., Remy, S., Ducellier, G., & Eynard, B. (2008). From a 3D point cloud to an engineering CAD model: a knowledge-product-based approach for reverse engineering. *Virtual and Physical Prototyping*, *3*(2), 51-59. https://doi.org/10.1080/17452750802047917

Elham, A., La Rocca, G., & van Tooren, M. J. L. (2013). Development and implementation of an advanced, design-sensitive method for wing weight estimation. *Aerospace Science and Technology*, *29*(1), 100-113. https://doi.org/10.1016/j.ast.2013.01.012

Elham, Ali. (2015). Adjoint quasi-three-dimensional aerodynamic solver for multi-fidelity wing aerodynamic shape optimization. *Aerospace Science and Technology*, *41*, 241-249. https://doi.org/10.1016/j.ast.2014.12.024

Elharouny, A. S., Youssef, A. M., Zakaria, M. Y., & Abdel-Hameed, M. M. (2012). Procedures for Mathematical Modeling for Small Unmanned Aerial Vehicles. Dans *Proceedings of the 15th AMME Conference* (p. 1). Cairo, Egypt.

Eren, U., Prach, A., Koçer, B. B., Raković, S. V., Kayacan, E., & Açıkmeşe, B. (2017). Model Predictive Control in Aerospace Systems: Current State and Opportunities. *Journal of Guidance, Control, and Dynamics*, *40*(7), 1541-1566. https://doi.org/10.2514/1.G002507

Fahlstrom, P., & Gleason, T. (2012). *Introduction to UAV Systems, 4th Edition* (4th Edition). United Kingdom : Wiley-Blackwell; Taken from https://www.wiley.com/en-us/Introduction+to+UAV+Systems%2C+4th+Edition-p-9781119978664

Flores Salinas, M. (2015). *Méthodologies nouvelles pour la réalisation d'essais dans la soufflerie Price-Païdoussis*. masters. École de technologie supérieure, Montréal. Taken from http://espace.etsmtl.ca/1565/

Frost, S., Taylor, B., & Bodson, M. (2012). Investigation of Optimal Control Allocation for Gust Load Alleviation in Flight Control. Communication présentée au AIAA Atmospheric Flight Mechanics Conference, Minneapolis, Minnesota : American Institute of Aeronautics and Astronautics. https://doi.org/10.2514/6.2012-4858

Fujii, K. (2005). Progress and future prospects of CFD in aerospace—Wind tunnel and beyond. *Progress in Aerospace Sciences*, *41*(6), 455-470. https://doi.org/10.1016/j.paerosci.2005.09.001

Gerhold, T., Galle, M., Friedrich, O., Evans, J., Gerhold, T., Galle, M., Evans, J. (1997). Calculation of complex three-dimensional configurations employing the DLR-tau-code. In *35th Aerospace Sciences Meeting and Exhibit* (p. 167). (S.l.) : American Institute of Aeronautics and Astronautics. https://doi.org/10.2514/6.1997-167

Ghazi, G. (2014). *Développement d'une plateforme de simulation et d'un pilote automatique - application aux Cessna Citation X et Hawker 800XP*. masters. École Polytechnique de Montréal. Taken from https://publications.polymtl.ca/1535/

Gibbs-Smith, C. H. (1960). *Aviation: an Historical Survey from its Origins to the End of World War II.* (S.l.) : H.M.S.O. (Google-Books-ID: hxEOAQAAIAAJ).

Gibson, J.C. (1995). *The definition, understanding and design of aircraft handling qualities* (Rapport No. Report LR-756). Delft University of Technology. Taken from http://resolver.tudelft.nl/uuid:a7d15d2e-7075-4487-9ca5-39e93ca93baa

Glatt, C. R. (1974). *WAATS: A computer program for Weights Analysis of Advanced Transportation Systems* (Rapport No. NASA-CR-2420, LTN-01R2). Washington, United States : NASA. Taken from https://ntrs.nasa.gov/search.jsp?R=19740027176

Grey, C. G., & Bridgman, L. (1930). *Jane's All the World's Aircraft 1930. Twentieth Year of Issue*. (S.l.) : Sampson Low, Marston and Company, Ltd.

Grigorie, T L, & Botez, R. M. (2009). Adaptive Neuro-Fuzzy Inference System-Based Controllers for Smart Material Actuator Modelling. *Proceedings of the Institution of Mechanical Engineers, Part G: Journal of Aerospace Engineering*, *223*(6), 655-668. https://doi.org/10.1243/09544100JAERO522

Grigorie, T. L., Botez, R. M., Popov, A. V., Mamou, M., & Mébarki, Y. (2012). A Hybrid Fuzzy Logic Proportional-Integral-Derivative and Conventional on-off Controller for Morphing Wing Actuation using Shape Memory Alloy Part 1: Morphing System Mechanisms and Controller Architecture Design. *The Aeronautical Journal*, *116*(1179), 433-449. https://doi.org/10.1017/S0001924000006977

Grigorie, Teodor Lucian, & Botez, R. M. (2015). Positioning Monitoring Improvement in a Horizontal Plane INS by Using Fuzzy Logic Data Fusion for Denoising of Inertial Sensors in Redundant Clusters. *International Journal of Fuzzy Systems And Advanced Applications*, *2*, 33-40.

Gudmundsson, S. (2013a). *General Aviation Aircraft Design: Applied Methods and Procedures*. Boston : Butterworth-Heinemann.

Gudmundsson, S. (2013b). *General Aviation Aircraft Design: Applied Methods and Procedures*. (S.l.) : Butterworth-Heinemann. (Google-Books-ID: XtU4HVnWeZIC).

Hamel, C. (2014). *Identification d'un Modèle Global Linéarisé De La Dynamique De Vol Du Cessna Citation X À Partir d'essais En Vol* (PhD Thesis). École de technologie supérieure, Montréal.

Hepperle, M. (2010). *Javaprop Users Guide*. (S.l.) : (s.n.).

Hess, J. L., & Smith, A. M. O. (1967). Calculation of potential flow about arbitrary bodies. *Progress in Aerospace Sciences*, *8*, 1-138. https://doi.org/10.1016/0376-0421(67)90003-6

Hobbyking. (2010a). TURNIGY K-Force 120A-HV OPTO V2 5-12S Brushless. *hobbyking.com*. Taken from https://hobbyking.com/fr_fr/turnigy-k-force-120a-hv-opto-v2-5-12s-brushless-esc-1.html

Hobbyking. (2010b). Turnigy RotoMax 1,60 Brushless Outrunner Motor. *hobbyking.com*. Taken from https://hobbyking.com/fr_fr/turnigy-rotomax-1-60-brushless-outrunner-motor.html?___store=fr_fr

Hobbywing. (2010). RPM Sensor For High-Voltage ESC. *HOBBYWING North America*. Taken from https://www.hobbywingdirect.com/products/rpm-sensor

Hodgkinson, J. (1999). *Aircraft Handling Qualities*. Oxford, United Kingdom : AIAA.

Howe, D. (2000). *Aircraft Conceptual Design Synthesis*. London, UK : Professional Engineering Publishing. (Google-Books-ID: QJZTAAAAMAAJ).

Hua, J., Zheng, S., Zhong, M., Wang, G., Eitelberg, G., Hegen, S., & Gebbink, R. (2018). Recent Development of a CFD-Wind Tunnel Correlation Study Based on CAE-AVM Investigation. *Chinese Journal of Aeronautics*, *31*(3), 419-428. https://doi.org/10.1016/j.cja.2018.01.017

Hürlimann, F., Kelm, R., Dugas, M., Oltmann, K., & Kress, G. (2011). Mass estimation of transport aircraft wingbox structures with a CAD/CAE-based multidisciplinary process. *Aerospace Science and Technology*, *15*(4), 323-333. https://doi.org/10.1016/j.ast.2010.08.005

Hušek, P., & Narenathreyas, K. (2016). Aircraft Longitudinal Motion Control Based on Takagi–Sugeno Fuzzy Model. *Applied Soft Computing*, *49*, 269-278. https://doi.org/10.1016/j.asoc.2016.07.038

Jacobs, E. Nw. (1933). *The characteristics of 78 Related Airfoil Sections from Tests in the Variable-Density Wind Tunnel*. Washington, DC, United States : National Advisory Committee for Aeronautics. Taken from https://ntrs.nasa.gov/search.jsp?R=19930091108

Jang, J.-S. R. (1993). ANFIS: adaptive-network-based fuzzy inference system. *IEEE Transactions on Systems, Man, and Cybernetics*, *23*(3), 665-685. https://doi.org/10.1109/21.256541

Jategaonkar, R. V. (2015). *Flight Vehicle System Identification: A Time-Domain Methodology, Second Edition*. Reston, VA : American Institute of Aeronautics and Astronautics, Inc. https://doi.org/10.2514/4.102790

Jeffery, J., & Docksey, P. (2008). Cost Benefits of Aerodynamic Data Generation Techniques for Aircraft Stability and Control Analysis using the J2 Universal Tool-Kit. *SAE International Journal of Aerospace*, *1*(1), 636-656. https://doi.org/10.4271/2008-01-2254

Jodeh, N., Blue, P., & Waldron, A. (2006). Development of Small Unmanned Aerial Vehicle Research Platform: Modeling and Simulating with Flight Test Validation. In *AIAA Modeling and Simulation Technologies Conference and Exhibit* (p. 6261). (S.l.) : American Institute of Aeronautics and Astronautics. https://doi.org/10.2514/6.2006-6261

Jodeh, N. M. (2006). *Development of Autonomous Unmanned Aerial Vehicle Platform: Modeling, Simulating, and Flight Testing* (Master). Air Force Institute of Technology Air University, Ohio.

Kálmán, R. E. (1960). Contributions to the Theory of Optimal Control (Vol. 5, pp. 102-119). Communication presented at Bol. Soc. Mat. Mexicana.

Kamal, A., Aly, A. M., & Elshabka, A. (2015). Modeling and Simulation of Propeller Propulsion Model Using Wind Tunnel. In *AIAA Modeling and Simulation Technologies Conference*. (S.l.) : American Institute of Aeronautics and Astronautics. https://doi.org/10.2514/6.2015-1596

Kamal, A. M., Bayoumy, A. M., & Elshabka, A. M. (2016). Modeling and Flight Simulation of Unmanned Aerial Vehicle Enhanced with Fine Tuning. *Aerospace Science and Technology*, *51*, 106-117. https://doi.org/10.1016/j.ast.2016.01.022

Kammegne, M. J. T., Grigorie, L. T., Botez, R. M., & Koreanschi, A. (2016). Design and wind tunnel experimental validation of a controlled new rotary actuation system for a morphing wing application. *Proceedings of the Institution of Mechanical Engineers, Part G: Journal of Aerospace Engineering*, *230*(1), 132-145. https://doi.org/10.1177/0954410015588573

Katz, J. (1991). *Low-speed Aerodynamics: From Wing Theory to Panel Methods*. (S.l.) : McGraw-Hill. (Google-Books-ID: yzc9PgAACAAJ).

Khan, W., & Nahon, M. (2015). A propeller model for general forward flight conditions. *International Journal of Intelligent Unmanned Systems; Bingley*, *3*(2/3), 72-92. http://dx.doi.org/10.1108/IJIUS-06-2015-0007

Kinsey, D. W., & Bowers, D. L. (1971). *A Computerized Procedure to Obtain the Coordinates and Section Characteristics of NACA Designated Airfoils.* (Rapport No. AFFDL-TR-71-87). Ohio : Air Force Flight Dynamics Lab Wright-Patterson. Taken from http://www.dtic.mil/docs/citations/AD0738623

Kok, J. C. (2000). Resolving the Dependence on Freestream Values for the k- Turbulence Model. *AIAA Journal*, *38*(7), 1292-1295. https://doi.org/10.2514/2.1101

Koreanschi, A., Henia, M. B., Guillemette, O., Michaud, F., Tondji, Y., Sugar-Gabor, O., Flores salinas, M. (2016). Flutter Analysis of a Morphing Wing Technology Demonstrator : Numerical Simulation and Wind Tunnel Testing. *INCAS Bulletin*, *8*, 99-124. https://doi.org/10.13111/2066-8201.2016.8.1.10

Koreanschi, A., Sugar-Gabor, O., & Botez, R. M. (2016). Drag optimisation of a wing equipped with a morphing upper surface. *The Aeronautical Journal*, *120*(1225), 473-493. https://doi.org/10.1017/aer.2016.6

Koreanschi, Andreea. (2016). *Numerical and experimental validation of the optimization methodologies for a wing-tip structure equipped with conventional and morphing ailerons*. phd. École de technologie supérieure, Montréal. Taken from https://espace.etsmtl.ca/1725/

Kostić, I. A., Stefanović, Z. A., & Kostić, O. P. (2014). Aerodynamic analysis of a light aircraft at different design stages. *FME Transactions*, *42*(2), 94-105. https://doi.org/10.5937/fmet1402094K

Kroll, N. (1994). Accurate and Efficient Flow Solvers for 3D Applications on Structured Meshes. In *Computational Fluid Dynamics, March 21-25, 1994*. Taken from https://elib.dlr.de/36208/

Kuitche, M. A. J., & Botez, R. M. (2019). Modeling novel methodologies for unmanned aerial systems – Applications to the UAS-S4 Ehecatl and the UAS-S45 Bálaam. *Chinese Journal of Aeronautics*, *32*(1), 58-77. https://doi.org/10.1016/j.cja.2018.10.012

Kuitche, M., & Botez, R. M. (2017). Methodology of Estimation of Aerodynamic Coefficients of the UAS-E4 Ehécatl using Datcom and VLM Procedure. In *AIAA Modeling and Simulation Technologies Conference* (p. 3152). Denver, Colorado : American Institute of Aeronautics and Astronautics. Taken from https://arc.aiaa.org/doi/10.2514/6.2017-3152

Kuitche, M., Segui, M., Botez, R. M., & Ghazi, G. (2017). New Methodology for Longitudinal Flight Dynamics Modelling of the UAS-S4 Ehecatl towards its Aerodynamics

Estimation Modelling. Dans *AIAA Modeling and Simulation Technologies Conference*. American Institute of Aeronautics and Astronautics. https://doi.org/10.2514/6.2017-0807

Kutty, H. A., & Rajendran, P. (2017). 3D CFD Simulation and Experimental Validation of Small APC Slow Flyer Propeller Blade. *Aerospace*, *4*(1), 10. https://doi.org/10.3390/aerospace4010010

Kwakernaak, H., & Sivan, R. (1972). *Linear Optimal Control Systems* (1 edition). New York : Wiley-Interscience.

Laflin, K. R. (2006). AIAA CFD Drag Prediction Workshop: an Overview (pp. 2-4). Communication presented at 25th ICAS Conference.

Laliberte, J., Poon, C., Straznicky, P. V., & Fahr, A. (2000). Applications of fiber-metal laminates. *Polymer Composites*, *21*(4), 558-567.

Lanchester, F. W. (1907). *Aerial flight*. London, UK : London : Constable. Taken from https://trove.nla.gov.au/version/42762514

Li, B., Zhang, Y., Ge, Y., Shao, Z., & Li, P. (2017). Optimal Control-Based Online Motion Planning For Cooperative Lane Changes of Connected and Automated Vehicles (pp. 3689-3694). Communication présentée au 2017 IEEE/RSJ International Conference on Intelligent Robots and Systems (IROS), Vancouver,BC : IEEE. https://doi.org/10.1109/IROS.2017.8206215

Li, S., Yang, J., Chen, W., & Chen, X. (2012). Generalized Extended State Observer Based Control for Systems With Mismatched Uncertainties. *IEEE Transactions on Industrial Electronics*, *59*(12), 4792-4802. https://doi.org/10.1109/TIE.2011.2182011

Liauzun, C. (2006). Assessment of CFD Techniques for Wind Turbine Aeroelasticity. In *6th FSI, AE and FIV anfd N Symposium* (Vol. 9, pp. 341-350). Vancouver. https://doi.org/10.1115/PV2006-ICPVT-11-93800

Liauzun, C., & Tran, D.-M. (2002). Method of Fluid-Structure Coupling in Time Domain Uisng Linearized Aerodynamics for Turbomachineries. In *Proceedings of the ASME 2002 International Mechanical Engineering Congress and Exposition* (pp. 117-126). New Orleans, Louisiana, USA : ASME. https://doi.org/10.1115/IMECE2002-33046

Liu, X., Sun, Q., & Cooper, J. E. (2017). LQG Based Model Predictive Control for Gust Load Alleviation. *Aerospace Science and Technology*, *71*, 499-509. https://doi.org/10.1016/j.ast.2017.10.006

Liu, Zhixiang, X., Yuan, C., Zhang, Y., & Luo, J. (2014). A Learning-Based Fuzzy LQR Control Scheme for Height Control Of An Unmammed Quadrotor Helicopter (pp. 936-941). Communication presented at 2014 International Conference on Unmanned

Aircraft Systems (ICUAS), Orlando, FL : IEEE. https://doi.org/10.1109/ICUAS2014.6842343

Liu, Zhong, He, Y., Yang, L., & Han, J. (2017). Control Techniques of Tilt Rotor Unmanned Aerial Vehicle Systems: A Review. *Chinese Journal of Aeronautics*, *30*(1), 135-148. https://doi.org/10.1016/j.cja.2016.11.001

MacNeill, R., & Verstraete, D. (2017). Blade element momentum theory extended to model low Reynolds number propeller performance. *The Aeronautical Journal*, *121*(1240), 835-857. https://doi.org/10.1017/aer.2017.32

Magar, K. T., Balas, M., Frost, S., & Li, N. (2017). Adaptive State Feedback - Theory and Application for Wind Turbine Control. *energies*, *10*(12), 2145. https://doi.org/10.3390/en10122145

Mariens, J., Elham, A., & van Tooren, M. J. L. (2014). Quasi-Three-Dimensional Aerodynamic Solver for Multidisciplinary Design Optimization of Lifting Surfaces. *Journal of Aircraft*, *51*(2), 547-558. https://doi.org/10.2514/1.C032261

MathWorks. (2005). *MATLAB The Language of Technical Computing Desktop Tools and Development Environment* (Version 7 edition). (S.l.) : The MathWorks Inc.

Mengali, G. (2000). The use of fuzzy logic in adaptive flight control systems. *The Aeronautical Journal*, *104*(1031), 31-37. https://doi.org/10.1017/S0001924000064125

Menter, F. R. (1994). Two-Equation Eddy-Viscosity Turbulence Models for Engineering Applications. *AIAA Journal*, *32*(8), 1598-1605. https://doi.org/10.2514/3.12149

Mitchell, D. G., Hoh, R. H., Aponso, B. L., & Klyde, D. H. (1994). *Proposed Incorporation of Mission-Oriented Flying Qualities into MIL-STD-1797A.* (Rapport No. TR-1291-1). Systems Technology Inc Hawthorne CA. Taken from https://apps.dtic.mil/docs/citations/ADA294211

Moran, J. (1984). *An Introduction to Theoretical and Computational Aerodynamics*. New York : Courier Corporation. (Google-Books-ID: qEU3oxHBl5kC).

Morgado, J., Vizinho, R., Miguel, AR, S., & Jose Carlos, P. (2016). XFOIL vs CFD Performance Predictions for High Lift Low Reynolds Number Airfoil. *Aerospace Science and Technology*, *52*, 207-214. https://doi.org/10.1016/j.ast.2016.02.031

Morris, A. (2002). MOB A European Distributed Multi-Disciplinary Design and Optimisation Project. In *9th AIAA/ISSMO Symposium on Multidisciplinary Analysis and Optimization* (p. 5444). Atlanta, Georgia : American Institute of Aeronautics and Astronautics. https://doi.org/10.2514/6.2002-5444

National Instruments. (2014). NI USB-6001 Specifications - National Instruments. Taken from http://www.ni.com/pdf/manuals/374369a.pdf

Nelson, R. C. (1997). *Flight Stability and Automatic Control* (2e éd.). Boston : McGraw-Hill Higher Education.

Nelson, T. E., & Zingg, D. W. (2004). Fifty Years of Aerodynamics: Successes, Challenges, and Opportunities. *Canadian Aeronautics and Space Journal*, *50*(1), 61-84. https://doi.org/10.5589/q04-003

Obinata, G., & Anderson, B. D. (2012). *Model reduction for control system design*. (S.l.) : Springer Science & Business Media.

Oliviu, S. G., Koreanschi, A., & Botez, R. M. (2015). Numerical Study of UAS-S4 Éhecatl Aerodynamic Performance Improvement Obtained with the Use of a Morphing Wing Approach. In *33rd AIAA Applied Aerodynamics Conference* (p. 2259). American Institute of Aeronautics and Astronautics. https://doi.org/10.2514/6.2015-2259

Ostowari, C., & Naik, D. (1985). *Post-stall wind tunnel data for NACA 44XX series airfoil sections* (Rapport No. SERI/STR-217-2559, 5791328). https://doi.org/10.2172/5791328

Panagiotou, P., Kaparos, P., & Yakinthos, K. (2014). Winglet design and optimization for a MALE UAV using CFD. *Aerospace Science and Technology*, *39*, 190-205. https://doi.org/10.1016/j.ast.2014.09.006

Pankhurst, R. C. (1944). *A Method for the Rapid Evaluation of Glauert's Expressions for the Angle of Zero Lift and the Moment at Zero Lift*. London : H.M. Stationery Office. (Google-Books-ID: XM3cJAAACAAJ).

Pecora, R. (2018). Multi-Modal Morphing Wing Flaps for Next Generation Green Regional Aircraft: The CleanSky Challenge. In *Smart Materials, Adaptative Structures and Intelligent Systems* (Vol. 1). San Antonio, Texas, USA : American Society of Mechnanical Engineers. https://doi.org/10.1115/SMASIS2018-8108

Pecora, R., & Dimino, I. (2015). SMA for Aeronautics. In *Shape Memory Alloy Engineering* (pp. 275-304). (S.l.) : Butterworth-Heinemann.

Perrin, C., Roger, G., Bockel, J.-M., & VALL, R. (2017). *Drones d'observation et drones armés : un enjeu de souveraineté* (Rapport No. 559 (2016-2017)). Commission des affaires étrangères, de la défense et des forces armées. Taken from http://www.senat.fr/rap/r16-559/r16-559_mono.html

Phillips, W. F. (2009). *Mechanics of Flight* (2nd edition). New Jersey : John Wiley & Sons, Inc.

Phillips, W. F., & Alley, N. R. (2007). Predicting Maximum Lift Coefficient for Twisted Wings Using Lifting-Line Theory. *Journal of Aircraft*, *44*(3), 898-910. https://doi.org/10.2514/1.25640

Picard, M., Rancourt, D., Plante, J.-S., & Brouillette, M. (2012). Rim-rotor rotary ramjet engine, part 2: Quasi-one-dimensional aerothermodynamic design. *Journal of Propulsion and Power*, *28*(6), 1304–1314.

Popescu, D. (2009). *Nouvelle Implémentation de la Procédure DATCOM pour le Calcul des Coefficients Aérodynamiques et des Dérivées de Stabilité dans le Domaine Subsonique de Vol*. Master. École de Technologie Supérieure, Montréal. Taken from http://espace.etsmtl.ca/74/

Pratt, R. W. (Éd.). (1999). *Flight Control Systems: Practical issues in design and implementation: 57*. Stevenage : Institution of Engineering and Technology.

Rakowitz, M., Eisfeld, B., Schwamborn, D., & Sutcliffe, M. (2003). Structured and Unstructured Computations on the DLR-F4 Wing-Body Configuration. *Journal of Aircraft*, *40*(2), 256-264. https://doi.org/10.2514/2.3117

Rancourt, D., Picard, M., Denninger, M., Plante, J.-S., Chen, J., & Yousefpour, A. (2012). Rim-rotor rotary ramjet engine, part 1: Structural design and experimental validation. *Journal of Propulsion and Power*, *28*(6), 1293–1303.

Raymer, D. (1979). A Computer-Aided Aircraft Configuration Development System. Dans *17th Aerospace Sciences Meeting* (p. 64). (S.l.) : American Institute of Aeronautics and Astronautics. https://doi.org/10.2514/6.1979-64

Raymer, D. P. (1989). *Aircraft Design: a Conceptual Approach*. Washington, D.C : American Institute of Aeronautics and Astronautics.

Raymer, D. P., & McCrea, M. M. (2010). Design of Jet STOVL Aircraft using RDS-Professional (p. 8). Communication presented at International Powered Lift Conference 2000 AHS/AIAA/RaeS/SAE, Arlington, Virginia.

Reznik, L., Ghanayem, O., & Bourmistrov, A. (2000). PID plus fuzzy controller structures as a design base for industrial applications. *Engineering Applications of Artificial Intelligence*, *13*(4), 419-430. https://doi.org/10.1016/S0952-1976(00)00013-0

Ritter, R. C. (1960). Rib Weight Estimation by Structural Analysis. Dans *SAWE Paper No. 259*. Hollywood, California : Society of Allied Weight Engineers, Inc.

Rizzi, A. (2011). Modeling and simulating aircraft stability and control—The SimSAC project. *Progress in Aerospace Sciences*, *47*(8), 573-588. https://doi.org/10.1016/j.paerosci.2011.08.004

Rocca, G. L., & Tooren, M. J. L. V. (2009). Knowledge-Based Engineering Approach to Support Aircraft Multidisciplinary Design and Optimization. *Journal of Aircraft*, *46*(6), 1875-1885. https://doi.org/10.2514/1.39028

Rosenbrock, H., & McMorran, P. (1971). Good, bad, or optimal? *IEEE Transactions on Automatic Control*, *16*(6), 552-554. https://doi.org/10.1109/TAC.1971.1099822

Roskam, J. (1985a). *Airplane Design: Preliminary Sizing of Airplanes*. : DARcorporation.

Roskam, J. (1985b). *Airplane Design VII: Determination of Stability, Control and Performance Characteristics: FAR and Military Requirements* : DARcorporation.

Roskam, J. (1998). *Airplane Flight Dynamics and Automatic Flight Controls* : DARcorporation.

Rugh, W. J., & Shamma, J. S. (2000). Research on Gain Scheduling. *Automatica*, *36*(10), 1401-1425. https://doi.org/10.1016/S0005-1098(00)00058-3

Sadeghzadeh, I., Chamseddine, A., Theilliol, D., & Zhang, Y. (2014). Linear Parameter Varying Control Synthesis : State Feedback Versus H∞ Technique With Application To Quadrotor UAV (pp. 1099-1104). Communication présentée au 2014 International Conference on Unmanned Aircraft Systems (ICUAS), Orlando, FL : IEEE. https://doi.org/10.1109/ICUAS.2014.6842362

Salvatore, A., Brindisi, A., Tiseo, B., Concilio, A., & Pecora, R. (2012). Optimization and Integration of Shape Memory Alloy (SMA)-Based Elastic Actuators Within a Morphing Flap Architecture. *Journal of Intelligent Material Systems and Structures*, *23*(4), 381-396. https://doi.org/10.1177/1045389X11428672

Saussié, D. A. (2010). *Contrôle du vol longitudinal d'un avion civil avec satisfaction de qualités de manoeuvrabilité*. phd. École Polytechnique de Montréal. Taken from https://publications.polymtl.ca/396/

Saussié, D., Saydy, L., & Akhrif, O. (2006). Longitudinal flight control design with handling quality requirements. *The Aeronautical Journal*, *110*(1111), 627-637. https://doi.org/10.1017/S0001924000001494

Schut, J., & Tooren, M. V. (2007). Design « Feasilization » Using Knowledge-Based Engineering and Optimization Techniques. *Journal of Aircraft*, *44*(6), 1776-1786. https://doi.org/10.2514/1.24688

Schütte, A., Boelens, O. J., Oehlke, M., Jirásek, A., & Loeser, T. (2012). Prediction of the flow around the X-31 aircraft using three different CFD methods. *Aerospace Science and Technology*, *20*(1), 21-37. https://doi.org/10.1016/j.ast.2011.07.014

Segui, M., Kuitche, M., & Botez, R. M. (2017). Longitudinal Aerodynamic Coefficients of Hydra Technologies UAS-S4 from Geometrical Data. In *AIAA Modeling and Simulation Technologies Conference* (p. 0579). American Institute of Aeronautics and Astronautics. https://doi.org/10.2514/6.2017-0579

Segui, M. M., Ghazi, G., Botez, R. M., & Thompson, E. M. (2018). Design, Development and Validation of a Cessna Citation X Aerodynamic Model using OpenVSP Software. Communication presented at 2018 Modeling and Simulation Technologies Conference, Atlanta, Georgia : American Institute of Aeronautics and Astronautics. https://doi.org/10.2514/6.2018-3256

Selig, M. S. (2012). *Aerodynamic Design Software for Horizontal Axis Wind Turbines*. UIUC Applied Aerodynamics Group Department of Aerospace Engineering University of Illinois at Urbana-Champaign, Urbana : (s.n.).

Selig, M. S. (2014). Real-Time Flight Simulation of Highly Maneuverable Unmanned Aerial Vehicles. *Journal of Aircraft*, *51*(6), 1705-1725. https://doi.org/10.2514/1.C032370

Sensmeier, M., Stewart, B., & Samareh, J. (2006). Rapid Generation and Assessment of Aircraft Structural Topologies for Multidisciplinary Optimization and Weight Estimation. In *47th AIAA/ASME/ASCE/AHS/ASC Structures, Structural Dynamics, and Materials Conference*. Newport, Rhode Island : American Institute of Aeronautics and Astronautics. https://doi.org/10.2514/6.2006-1981

Silisteanu, P.-D., & Botez, R. M. (2010). Transition-Flow-Occurrence Estimation: A New Method. *Journal of Aircraft*, *47*(2), 703-708. https://doi.org/10.2514/1.44698

Snel, H., Houwink, R., & Bosschers, J. (1994). *Sectional prediction of lift coefficients on rotating wind turbine blades in stall*. (S.l.) : Netherlands Energy Research Foundation Petten, Netherlands.

Spalart, P., & Allmaras, S. (1992). A One-Equation Turbulence Model for Aerodynamic Flows. Communication presented at 30th Aerospace Sciences Meeting and Exhibit 30th Aerospace Sciences Meeting and Exhibit, Reno,NV,USA : American Institute of Aeronautics and Astronautics. https://doi.org/10.2514/6.1992-439

Starr, A. W., & Ho, Y. C. (1969). Nonzero-sum differential games. *Journal of Optimization Theory and Applications*, *3*(3), 184-206. https://doi.org/10.1007/BF009294433

Stepniewski, W. Z., & Keys, C. N. (1984). *Rotary-wing Aerodynamics* (Dover Publications) : Courier Corporation.

Stevens, B. L., & Lewis, F. L. (2003). *Aircraft Control and Simulation* (2nd Edition). Hoboken, N.J : John Wiley & Sons.

Sufendi, Trilaksono, B. R., Nasution, S. H., & Purwanto, E. B. (2013). Design and implementation of hardware-in-the-loop-simulation for uav using pid control method. In *2013 3rd International Conference on Instrumentation, Communications, Information Technology and Biomedical Engineering (ICICI-BME)* (pp. 124-130). https://doi.org/10.1109/ICICI-BME.2013.6698478

Sugar Gabor, O. (2015). *Validation of Morphine Wing Methodologies on an Unmanned Aerial System and a Wind Tunnel Technology Demonstrator*. phd. École de Technologie Supérieure, Montréal. Taken from http://espace.etsmtl.ca/1614/

Şugar Gabor, O., Koreanschi, A., & Botez, R. M. (2016). A New Non-Linear Vortex Lattice Method: Applications to Wing Aerodynamic Optimizations. *Chinese Journal of Aeronautics*, *29*(5), 1178-1195. https://doi.org/10.1016/j.cja.2016.08.001

Şugar Gabor, O., Koreanschi, A., Botez, R. M., Mamou, M., & Mebarki, Y. (2016). Numerical Simulation and Wind Tunnel Tests Investigation and Validation of a Morphing Wing-Tip Demonstrator Aerodynamic Performance. *Aerospace Science and Technology*, *53*, 136-153. https://doi.org/10.1016/j.ast.2016.03.014

Suparta, W., & Alhasa, K. M. (2016). Adaptive Neuro-Fuzzy Interference System. In *Modeling of Tropospheric Delays Using ANFIS* (pp. 5-18). Cham : Springer International Publishing. https://doi.org/10.1007/978-3-319-28437-8_2

Tangler, J. L., & Selig, M. S. (1997). *An Evaluation of an Empirical Model for Stall Delay due to Rotation for HAWTS* (Rapport No. NREL/CP-440-23258;CONF-970608-2). Austin, TX, USA : National Renewable Energy Lab., Golben, Co.

Taylor, M. J. H. (1989). *The Aerospace Chronology* (First Edition edition). London : Tri-Service Press Ltd.

Tewari, A. (2011). *Advanced Control of Aircraft, Spacecraft and Rockets*. Chichester, West Sussex : Wiley-Blackwell.

Tondji Chendjou, Y. W., & Botez, R. (2014). Numerical and Experimental Measures of the Unmanned Aerial System UAS-S4 of Hydra Technologies. https://doi.org/10.4271/2014-01-2145

Tondji, Y., & Botez, R. (2016). Semi-empirical Estimation and Experimental Validation of the Mass and the Center of Gravity Location of the Unmanned Aerial System - UAS-S4 of Hydra Technologies. In *2016 International Conference on Unmanned Aircraft Systems (ICUAS)* (pp. 1319-1326). Arlington, VA, USA : IEEE. https://doi.org/10.1109/ICUAS.2016.7502550

Tondji, Y., & Botez, R. M. (2017). Semi-empirical estimation and experimental method for determining inertial properties of the Unmanned Aerial System – UAS-S4 of Hydra Technologies. *The Aeronautical Journal*, *121*(1245), 1648-1682. https://doi.org/10.1017/aer.2017.105

Tondji, Yvan, & Botez, R. (2016). Semi-empirical estimation and experimental validation of the mass and the center of gravity location of the unmanned aerial system — UAS-S4 of hydra technologies (pp. 1319-1326). IEEE. https://doi.org/10.1109/ICUAS.2016.7502550

Torenbeek, E. (2013). The Wing Structure and Its Weight. Dans *Advanced Aircraft Design: Conceptual Design, Analysis and Optimization of Subsonic Civil Airplanes,* (pp. 319-362). Chichester ,UK : John Wiley & Sons, Ltd. https://doi.org/10.1002/9781118568101.ch11

Tsach, S., Tatievsky, A., & London, L. (2010). Unmanned Aerial Vehicles (UAVs). In *Encyclopedia of Aerospace Engineering*. (S.l.) : American Cancer Society. https://doi.org/10.1002/9780470686652.eae385

Tuck, L., Samson, C., Laliberté, J., Wells, M., & Bélanger, F. (2018). Magnetic interference testing method for an electric fixed-wing unmanned aircraft system (UAS). *Journal of Unmanned Vehicle Systems*, *6*(3), 177-194. https://doi.org/10.1139/juvs-2018-0006

Udin, S. V., & Anderson, W. J. (1992). Wing mass formula for subsonic aircraft. *Journal of Aircraft*, *29*(4), 725-727. https://doi.org/10.2514/3.46232

U.S. Army. (2010). *Eyes of the Army. U.S. Army Roadmap for Unmanned Aircraft Systems 2010-2035*. United States -- Albama : U.S. Army UAS center of excellence. Taken from https://www.rucker.army.mil/usaace/uas/US%20Army%20UAS%20RoadMap%202010%202035.pdf

US Military. (1980). *MIL-F-8785C, Military Specification: Flying Qualities Of Piloted Airplanes* (Rapport No. MIL-F-8785C). Taken from http://www.mechanics.iei.liu.se/edu_ug/tmme50/8785c.pdf

Valyou, D., Ceruti, A., Miller, J., Pawlowski, B., Marzocca, P., & Tranchitella, M. (2013). *Design, Optimisation, Performances and Flight Operation of an All Composite Unmanned Aerial Vehicle* (Rapport No. 2013- 01-2192). SAE International.

Vepa, R. (2014). *Flight Dynamics, Simulation, and Control : For Rigid and Flexible Aircraft*. Boca Raton : CRC Press. https://doi.org/10.1201/b17346

Vinodh Kumar, E., Raaja, G. S., & Jerome, J. (2016). Adaptive PSO for Optimal LQR Tracking Control of 2 DoF Laboratory Helicopter. *Applied Soft Computing*, *41*, 77-90. https://doi.org/10.1016/j.asoc.2015.12.023

Viterna, L. A., & Corrigan, R. D. (1982). Fixed Pitch Rotor Performance of Large Horizontal Axis Wind Turbines (p. 17). Cleveland, OH, United States : NASA Lewis Research Center.

Von Kármán, T. (1931). *Mechanical similitude and turbulence* (Rapport No. 611). Washington, D.C : National Advisory Committee For Aeronautics.

Whitcomb, R. T. (1952). *A study of the Zero-Lift Drag-Rise Characteristics of Wing-Body Combinations Near the Speed of Sound.* (Rapport No. NACA-TR-1273). Washington, DC, United States : National Advisory Committee For Aeronautics;

White, F. M. (2003). *Fluid Mechanics*. Boston : McGraw-Hill Publishing Co.

Wilcox, D. C. (2008). Formulation of the k-w Turbulence Model Revisited. *AIAA Journal*, *46*(11), 2823-2838. https://doi.org/10.2514/1.36541

Williams, J. E., & Vukelich, S. R. (1979). *The USAF Stability and Control Digital DATCOM. Volume I. Users Manual* (Rapport No. AFFDL-TR-76-45-VOL-1). McDonnell Douglas Astronautics Company, Air Force Flight Dynamics Laboratory. Taken from http://www.dtic.mil/docs/citations/ADA086557

Winter, F. H. (1980). Ducted fan or the world's first jet plane? The Coanda claim re-examined. *The Aeronautical Journal*, *84*(839), 408-416. https://doi.org/10.1017/S0001924000031407

Wu, D., Chen, M., & Gong, H. (2018). Adaptive Neural Flight Control for an Aircraft with Time-Varying Distributed Delays. *Neurocomputing*, *307*, 130-145. https://doi.org/10.1016/j.neucom.2018.04.038

Zhen, Z., Jiang, J., Wang, X., & Gao, C. (2015). Information Fusion Based Optimal Control for Large Civil Aircraft System. *ISA Transactions*, *55*, 81-91. https://doi.org/10.1016/j.isatra.2014.09.017